

ABSTRACT

TARAFDER, PRITHWISH. Characterization of Mechanical Properties and Evaluation of Methods for Grain Control of Copper Fabricated Using EB-PBF Process. (Under the direction of Dr. Timothy J. Horn and Dr. Russell E. King).

Pure copper with 99.95% relative density, 99.8% relative thermal conductivity, and >100% IACS (International annealed copper standard) electrical conductivity has been fabricated by several research groups using the electron beam powder bed fusion (EB-PBF) process. However, characterization of its mechanical properties is rather incomplete as majority of the existing literature report properties in as-fabricated condition only. In the first phase of this research, uniaxial tensile testing and microhardness measurements of unalloyed copper samples fabricated by three different post-processing conditions (as-fabricated, vacuum annealed, and hot isostatic pressed (HIP)), and two different orientations (parallel and transverse to the build direction) are conducted to characterize the effects of post-processes on the mechanical behavior of copper. Results show that mechanical properties comparable with annealed cast or wrought products can be achieved, while failure is largely controlled by micro-void coalescence resulting into ductile dimples. Additionally, build orientation is found to be one of the most significant factors, which introduces anisotropy in the properties due to epitaxial columnar grains formed along the build direction, as commonly seen in additive manufacturing. Typically, this anisotropy is mitigated by changing the process parameters and/or modifying the solute contents to promote heterogeneous nucleation, thereby increasing the possibility of more equiaxed grain formation. However, in EB-PBF of pure copper, this is particularly challenging because of its high thermal conductivity, and the demand for high purity for its applications. The second phase of this research, therefore, examines the possibility of achieving columnar to equiaxed transition (CET) in copper by first assessing the effects of process parameters of EB-PBF alone, followed by the effects of solute modification of feedstock powder. With the first solution approach, a CET map is developed using the rapid solidification models for the Cu-O system, two most abundant elements found in the powder feedstock, while the EB-PBF process is simulated for different process parameters via a numerical thermal model. The resultant thermal gradient and solidification velocity values are then plotted on the CET solidification map to understand the underlying solidification kinetics that led to the formation of either columnar or equiaxed grains. It is observed that the thermal gradient

obtained from the numerical simulations of process parameters from both literature and present study is too high to result in any equiaxed grains. CET can be theoretically achieved in copper when the melt current, substrate temperature, and scan velocity are high enough to result in low thermal gradients and high solidification velocities, as inferred from the CET and the thermal model. Although these favorable processing conditions can lead to greater undercooling conducive of equiaxed grain formation, defects like swelling due to high energy input prevents the application of such process parameters. Therefore, the alternative approach proposed for microstructure control examines the solutal effect of Cuprous Oxide (Cu_2O) instead of commonly used rare earth element oxides as the former dissociates at high temperature leaving behind pure copper, as observed from the vacuum annealing tests. The CET becomes more probable for higher oxygen content as it restricts the columnar front growth by increasing the constitutional undercooling ahead of the solid liquid interface. Moreover, the ability to process copper at high substrate temperature increases because of the improved flowability of copper powder with high oxygen content. Results show that copper with moderate level of oxygen content produces equiaxed grains along the build direction, and extra oxygen content can be reduced to the ETP copper specification after the vacuum annealing treatment. In effect, it is proposed that oxidized copper powder along with the modified process parameters obtained from the thermal model can be used for grain refinement, ultimately achieving greater isotropy in its properties.

© Copyright 2021 by Prithwish Tarafder

All Rights Reserved

Characterization of Mechanical Properties and Evaluation of Methods for Grain Control of
Copper Fabricated Using EB-PBF Process

by
Prithwish Tarafder

A dissertation submitted to the Graduate Faculty of
North Carolina State University
in partial fulfillment of the
requirements for the degree of
Doctor of Philosophy

Industrial Engineering

Raleigh, North Carolina
2021

APPROVED BY:

Dr. Timothy J. Horn
Committee Co-chair

Dr. Russell E. King
Committee Co-chair

Dr. Ola L.A Harrysson

Dr. Christopher D. Rock

DEDICATION

This dissertation is dedicated to Aylan Kurdi.
May all children inherit a more peaceful world.

BIOGRAPHY

My name is Prithwish Tarafder. I am a PhD candidate in the department of Industrial & Systems Engineering at North Carolina State University. After completing undergraduate studies in Production Engineering, I worked with an automobile manufacturer in India for almost two years. However, I took more interest in academia, and embarked on pursuing a master's degree in Production Engineering at the Technische Universität Berlin, Germany. To continue my career in academia, I joined this department in 2016 as a PhD student. I started developing immense interest in the lab-work and research activities conducted at the Center for Additive Manufacturing and Logistics (CAMAL) housed in the department and chose additive manufacturing of pure copper as my research track.

ACKNOWLEDGMENTS

First of all, I would like to extend my sincere gratitude to the Chairs of my doctoral committee, Dr. Tim Horn and Dr. Russell King for their continued support and critical feedback throughout this research activity. I also acknowledge the invaluable suggestions and guidance provided by Dr. Christopher Rock, Dr. Ola Harrysson, and Dr. Harvey West in various times that kept me motivated in this journey.

I am immensely indebted to all the lab-mates who collectively constitute a great working and learning environment. I would also like to sincerely thank the staff members at the Analytical Instrumentation Facility (AIF) for their immense support and training in the high-end analysis of the fabricated specimens.

Finally, I express my deepest love for my parents and parents-in-law, my sister Dr. Panchali Dasgupta, and my brother-in-law Dr. Anindya Dasgupta for their support and motivation in hard times. And beyond all, I would like to thank my wife Ms. Shreya Das for being the pillar of my strength and success in all times.

TABLE OF CONTENTS

LIST OF TABLES	viii
LIST OF FIGURES	x
1 Introduction.....	1
1.1 Background.....	1
1.2 Research Motivation	2
1.3 Structure of the Thesis	3
2 Mechanical characterization of EB-PBF fabricated copper under different post-processing conditions.....	4
2.1 Introduction.....	4
2.2 Literature Review.....	4
2.2.1 Laser powder bed fusion of copper.....	4
2.2.2 Electron beam powder bed fusion of copper	6
2.2.3 Binder jetting of copper	7
2.2.4 Overall discussion.....	7
2.3 Research Motivation	9
2.4 Materials and Methods.....	11
2.4.1 Powder feedstock	11
2.4.2 Sample fabrication	11
2.4.3 Uniaxial tensile test procedure.....	15
2.4.4 Metallographic analyses and microhardness measurements.....	17
2.4.5 Fractographs and oxides characterization.....	18
2.5 Results and Discussion	18
2.5.1 Powder characterization.....	18
2.5.2 Uniaxial tensile test results	20
2.6 Conclusions.....	33
2.7 Motivation for further research.....	34
3 Grain refinement and Columnar-to-Equiaxed Transition of EB-PBF fabricated copper by modifying process parameters	37
3.1 Introduction.....	37
3.2 Literature Review.....	38
3.3 Research Motivation	39
3.4 Materials and Methods.....	43
3.4.1 Development of Columnar-to-Equiaxed Transition (CET) model.....	43

3.4.2	Sensitivity analysis of the CET model.....	48
3.4.3	Thermal modeling of EB-PBF and process parameter design.....	49
3.4.4	Feasibility study with experimental builds	53
3.4.5	Microstructural and mechanical characterization of the build specimens	56
3.5	Results and Discussion	56
3.5.1	CET of copper-oxygen system.....	56
3.5.2	Sensitivity analysis of non-compositional variables used in the CET model.....	59
3.5.3	Thermal gradient and solidification velocity calculation from thermal model.....	61
3.5.4	CET of copper in PBF process.....	65
3.5.5	Thermal model and CET results of the build specimens (Build 1).....	68
3.5.6	Microstructural analysis of build specimens (Build 1)	69
3.5.7	Microhardness and density results of the build specimens (Build 1)	74
3.5.8	Thermal model and CET results of the build specimens (Build 2).....	75
3.5.9	Microstructural analysis of build specimens (Build 2).....	76
3.6	Conclusions.....	79
3.7	Motivation for further research.....	80
4	Grain refinement and Columnar-to-Equiaxed Transition of EB-PBF fabricated copper by modifying powder chemistry	81
4.1	Introduction.....	81
4.2	Literature Review.....	82
4.2.1	Solutal effect on CET of alloys fabricated by AM processes.....	82
4.2.2	Grain refinement of copper in casting	83
4.3	Research Motivation	86
4.4	Materials and Methods.....	89
4.4.1	CET for different oxygen concentration	89
4.4.2	Thermal analysis of powder using differential scanning calorimetry (DSC)	91
4.4.3	Single layer experiment for process parameter selection	92
4.4.4	Feasibility study via experimental builds with hypoeutectic high oxygen content powder.....	93
4.4.5	Microstructural and mechanical characterization of the build specimens	97
4.4.6	Vacuum annealing of selected build specimens	97
4.5	Results and Discussion	98
4.5.1	Effect of oxygen concentration on CET	98
4.5.2	DSC results of powder with different oxygen concentration.....	103
4.5.3	Single layer pocket experiment results	107

4.5.4	Results of the feasibility study builds	109
4.5.5	Thermal model and CET prediction of selected specimens.....	111
4.5.6	Microstructural analysis of selected specimens	112
4.5.7	Density and microhardness characterization of the selected specimens.....	119
4.5.8	Vacuum annealing of selected specimens.....	121
4.6	Conclusions.....	122
5	Summary of research	124
5.1	Overall research objective.....	124
5.2	Contribution of this research.....	125
5.3	Future work.....	126
	REFERENCES	128
6	APPENDICES	145
6.1	Appendix A.....	146
6.1.1	Literature review of AM of pure copper.....	146
6.1.2	Tensile test data.....	148
6.1.3	Future directions for better understanding of the effects of post-processing.....	150
6.2	Appendix B	153
6.2.1	Analysis of the effect of thermal model assumptions	153
6.2.2	Preliminary observations of correlation between thermal model results and microstructure	156
6.3	Appendix C	159
6.3.1	TEY images of builds	159
6.3.2	Further characterization of equiaxed grains and possible future directions for analysis.....	160

LIST OF TABLES

Table 2-1. EB-PBF melt parameters used to fabricate the specimens used in this study (the parameters shown are specifically those that have been modified from the standard commercial parameter sets for Ti6Al4V, V3.2 SP2).	12
Table 2-2. EB-PBF preheat parameters used to fabricate the specimens used in this study (the parameters shown are specifically those that have been modified from the standard commercial parameter sets for Ti6Al4V, V3.2 SP2).	13
Table 2-3. Summary of the location, orientation, and post-processing condition of the samples tested in this study. (AF= As-fabricated, HIP= Hot isostatic pressed, VA= Vacuum annealed; B= Bottom, M= Middle, T= Top).	15
Table 2-4. ICP-MS analysis of feedstock unalloyed copper powder prior to the first build. Values are reported in wt. ppm.	20
Table 3-1. Summary of grain refinement studies in AM by changing process parameters.....	41
Table 3-2. Nomenclature of symbols used in the CET model and their values.....	42
Table 3-3. Selected CET model input variables and their levels used in sensitivity analysis; values in bold letters indicate their nominal level.	49
Table 3-4. Thermal model variables: their meaning and values; All values are in SI unit; Response = response variable; Varied = values are varied within simulation experiments.	51
Table 3-5. Process parameter design of the first experimental feasibility study build with a layer thickness of 50 μ m (Note: Focus offset for melt current 20 mA and scan speed 1200 mm/s is changed to 26 mA during the build to avoid swelling of the part due to high input energy density).	54
Table 3-6. Process parameters of fabricated blocks in the second experimental feasibility study build with pure copper powder.....	55
Table 3-7. Melt pool characteristics for representative process windows to show individual effect of substrate temperature, scan velocity, and melt current. The models were created in Paraview, and temperature scale is 573 K (blue) to 2100 K (red).....	63
Table 3-8. Microhardness and optical density of build specimens.	74
Table 4-1. Melt current and scan velocity values for the pocket experiment at different substrate temperatures.....	93

Table 4-2. Process parameters used in the fabrication of blocks during the feasibility study builds. Blocks that are turned off due to defects are given in italics fonts.	95
Table 4-3. DSC results of copper powder with different oxygen concentration and different particle size distributions.	104
Table 4-4. Relative density and microhardness values of selected specimens from feasibility study build.....	119
Table 6-1. EB-PBF processing of pure copper.	146
Table 6-2. BJ processing of pure copper.	146
Table 6-3. L-PBF processing of pure copper.....	147
Table 6-4. Tensile test sample spreadsheet.....	148
Table 6-5. Variable values used in the sensitivity analysis of thermal model assumptions.	153

LIST OF FIGURES

Figure 2-1. Processing space of PBF fabrication of pure copper [EB-PBF (A), L-PBF (B)] by taking the process parameters used in the literature. Major observations of L-PBF studies are highlighted along with reported solid densities. As majority of EB-PBF reported densities reach >99.5%, bed temperature is highlighted in Figure (A) instead of densities.....	8
Figure 2-2. Processing space of EB-PBF fabrication of unalloyed copper adopted in this study, overlaid on the processing space reported by EB-PBF studies (shown in Figure 2-1 previously).....	12
Figure 2-3. Overall experimental framework highlighting the build layout and sample orientations, treatment conditions, and the ASTM Standard design of the test coupons used in the study.	14
Figure 2-4. Fabricated blocks on a copper substrate (A), Machined tensile sample according to ASTM E8-16 standard (B), Overall tensile test set up showing the arrangement of DIC camera and lighting kits (C), Strain mapping of a Z-oriented vacuum annealed tensile sample in GOM Correlate software in the beginning(D) and the end (E) of the test.	17
Figure 2-5. Particle size distribution of feedstock unalloyed copper powder used across the builds (A), and SEM image of the powder prior to the first build (B); scale bar shows 100 μm	20
Figure 2-6. Plots illustrating the effect of treatment condition on the density (A) and oxygen content (B) of copper produced by EB-PBF. Error bars indicate a 95% confidence interval based on the pooled variance of all samples.....	21
Figure 2-7. Mechanical properties summary and selected statistical observations; Ultimate tensile strength (A), Yield strength (B), Elongation to failure (C), Vickers microhardness (D). Error bars indicate a 95% confidence interval based on the pooled variance of all samples.....	23
Figure 2-8. a. Z-oriented sample, b. X-oriented sample; yellow arrow shows pulling direction; dislocation pile up near GB is shown in red.....	24
Figure 2-9. A-C. Grain morphology of representative specimens along the build direction from different post-processing conditions; D-F. Average grain width measured	

considering all samples for each process condition; scale bar shows 200 μm . Arrow indicates the build direction.....	26
Figure 2-10. Inverse pole figure maps of as-fabricated, HIP, and vacuum annealed specimens along the build direction shown with an arrow alongside the scale bar (A-C); pole figures of as-fabricated, HIP, and vacuum annealed specimens (D-F), respectively. The scale bar is multiple uniform distributions for the pole figures ranging from 1 – 9.....	28
Figure 2-11. Fractographs of tensile specimens; top two rows: Z-oriented specimens (as-fabricated, HIP, and vacuum annealed); bottom two rows: X-oriented specimens (as-fabricated, HIP, and vacuum annealed); Scale bar is linked with respective rows.....	31
Figure 2-12. EDS maps of representative specimens from all processing conditions. Lower magnification EDS map of the vacuum annealed specimen is shown in the right to illustrate the spatial distribution of the oxides. Scale is shown in black bars.....	32
Figure 2-13. STEM EDS maps of representative as-fabricated and HIP specimens illustrating the spatial distribution and size differences of copper oxide inclusions at the grain boundaries. Note the different length scales.	33
Figure 2-14. Comparison of mechanical properties measured in this study and reported in the AM literature of pure copper.	36
Figure 3-1. Schematic representation of MATLAB routine steps for the CET calculation of Cu-O system.....	47
Figure 3-2. Temperature profile distribution for arbitrary timestep in small domain and big domain sized models.....	50
Figure 3-3. Process parameter space of PBF of copper; Hexagonal icons within the rectangle indicate newly investigated simulation process parameter. In this picture, substrate temperature of this parameter set is kept at its present level of 300°C.....	53
Figure 3-4. Increase in substrate temperature as an increase in the number of melting passes on each block.	55
Figure 3-5. CET solidification map of copper (a. linear axis plot, b. conventional log-log plot); c. Dendrite tip radius as a function of growth velocity; d. Dendrite tip	

temperature and concentration at tip profile as a function of growth velocity. Interface growth velocity and solidification velocity are used interchangeably.....	57
Figure 3-6. Liquidus and actual local temperature ahead of dendrite tip for solidification velocities of 0.001, 0.01, and 0.1 m/s; b. Undercooling profile ahead of dendrite tip for solidification velocities of 0.001, 0.01, and 0.1 m/s.	59
Figure 3-7. Thermal gradient values of simulations for different combinations of all three investigated input variables.....	60
Figure 3-8. Elementary effects of each examined variable on Thermal gradient (left hand Y axis) and Total undercooling (right hand Y axis); Bars show the mean EE values, while the one-sided error bars show the standard deviation EE values.....	61
Figure 3-9. Effect of melt current on Thermal gradient at different scan velocity and substrate temperature; d-f. Effect of scan velocity on Cooling rate for different melt current and substrate temperatures; Note that Y-axis value ranges are not similar.	62
Figure 3-10. Effect of scan velocity on temperature profile of the melt pool top. The point simulated in the software is shown schematically in the middle. Substrate temperature is kept at 300°C for both process parameter sets. Temperature axis ranges from 500 K to 2300 K.	64
Figure 3-11. Thermal gradient (G) and solidification velocity (V) for different process parameter sets (from literature and newly designed) of pure copper fabricated in EB-PBF process.....	65
Figure 3-12. CET of copper in powder bed fusion process.	66
Figure 3-13. Top: Melt pool contours from thermal model, Bottom: Undercooling and concentration profile ahead of S/L interface; Respective process parameters are shown at the top of the contour maps; Color bar range: 573 K (blue) to 2100 K (red).....	67
Figure 3-14. Thermal model results of the build specimens predicting the overall microstructure by using the proposed CET map.....	69
Figure 3-15. Modified CET and G-V for the experimented samples for 0.04 wt.% oxygen content.....	70

Figure 3-16. Microstructure of all specimens fabricated in the experimental build. Sample numbers are shown at top left corner on each micrograph. Build direction is shown by the black arrow, and the scale bar in yellow shows 200 μm	71
Figure 3-17. SEM images of representative samples showing the overall grain morphology at different magnification levels. Note the different scale bars (100X= 100 μm , 500X= 50 μm , 1000X= 10 μm).	72
Figure 3-18. Columnar dendrite structure within individual grains seen in Sample 9. Black lines indicate the relative orientation of the dendrites with respect to the build direction.	73
Figure 3-19. Microstructure prediction from the thermal and CET model for the fabricated specimens.	75
Figure 3-20. Optical micrographs showing the microstructure for each specimen from Build 2. Black arrow shows the build direction, yellow line represents the scale bar (1000 μm). Sample number is given in the top left inset of each micrograph. ...	77
Figure 3-21. Optical and Electron microscope microstructure of a selected equiaxed grain region in sample 6. Yellow arrows indicate at the growth directions. Note the different scale sizes.	78
Figure 4-1. Growth restriction factor of different alloying elements of copper at initial concentration of 0.1 wt.%; adopted from (Balart et al., 2016).	88
Figure 4-2. Cu-O phase diagram, adapted from (Davis, 2001).	90
Figure 4-3. a. High speed camera and external light sources set up on Arcam A2 machine; b. Substrate plate with six pockets filled with different powder variants; c. Substrate plate placed inside machine on top of build piston.	93
Figure 4-4. Processing space of the experimental builds in comparison to the literature and the tensile study conducted in the first phase of research.	96
Figure 4-5. Specimens kept on pure copper bars in alumina crucible before vacuum annealing.	97
Figure 4-6. Non-equilibrium Scheil curves for copper with different oxygen concentration; obtained using ThermoCalc.	98
Figure 4-7. Partition coefficient of hypereutectic copper systems from both Scheil and equilibrium phase diagram calculations.	99

Figure 4-8. Tip temperature (blue line) and solute concentration in the liquid at dendrite tip (black line) for different solidification growth velocities. a. Hypoeutectic, b. Hyper-low, c. Hyper-med, d. Hyper-high.....	100
Figure 4-9. Liquidus and local temperature profiles as a function of growth velocities of 0.001 m/s, 0.01 m/s, and 0.1 m/s; a. Hypoeutectic, b. Hyper-med copper oxygen system.	101
Figure 4-10. Total undercooling for different solidification velocities. a. Hypoeutectic, b. Hyper-low, c. Hyper-med, d. Hyper-high.....	102
Figure 4-11. a. Columnar-to-equiaxed transition of all copper-oxygen alloy variants; b. Total undercooling as a function of interface solute concentration and solidification velocity; Color bar represents solidification velocity (0.0001 m/s to 0.2 m/s within the limit of stability).....	103
Figure 4-12. Left: Temperature and undercooling values; Right: Latent heat of solidification (enthalpy of fusion) values of different copper powder samples.....	105
Figure 4-13. Image of solidified copper bead on alumina crucible for qualitative assessment of contact angles; Respective powder size distribution and oxygen concentration in wt. ppm are shown in each image.....	106
Figure 4-14. High-speed image snapshots during the scanning of different powder pockets. Identifier of each image is shown on top of the same, and the respective process conditions can be obtained from Table 4-1	107
Figure 4-15. Microstructure of single solid layer from different powder types. Top row represents SEM images (scale bar 10 μm), bottom row represents optical microscope images (scale bar 100 μm). (a, d): Hyper-low; (b, e): Hyper-med; (c, f): Hyper-high.	108
Figure 4-16. Feasibility studies build powder characterization. a. Particle size distribution and oxygen content of virgin powder, sintered cake around the powder bed, and the final build. b. SEM images of virgin powder at 100 X, 500 X, and 1500 X.	109
Figure 4-17. Picture of the experimental builds.....	110
Figure 4-18. Substrate temperature data from log-files for all experimental builds.....	110
Figure 4-19. A. Process map for the experimental builds. Green circles show selected specimens for microstructural and hardness analyses; red circles show selected	

specimens for thermal model simulation. B. Thermal model results mapped onto the CET map for the selected specimens. Probable outcomes of all other specimens are enclosed in the blue oval shape.	111
Figure 4-20. Optical microstructure of selected specimens from the feasibility study builds. Scale bar shows 200 μm	112
Figure 4-21. Effect of oxygen in restricting the columnar grain growth. Build direction is shown with black arrow; scale bar shows 1000 μm	113
Figure 4-22. SEM images of selected specimens from the feasibility study builds. Note that samples are chosen such that the overall volumetric energy density is covered. Scale bar shows 50 μm	114
Figure 4-23. Optical microscope image montage for the sample with equiaxed grains along the build direction. Scale bar is 1000 μm	116
Figure 4-24. SEM image montage for the sample with equiaxed grains along the build direction. Scale bar is 100 μm	117
Figure 4-25. A. Equiaxed grain region, B. Columnar grain region, C-D. Dendrite structures within equiaxed grains. Yellow arrows show the direction of grain growth, Black arrow in A and B indicates the oxides at the grain boundary, and in C it indicates just the grain boundary. Note the different scale lengths.....	118
Figure 4-26. Influence of volumetric energy density on the microhardness of selected samples.....	121
Figure 4-27. Oxygen content and microstructure of sample 3 from build 3 before and after vacuum annealing process.	122
Figure 6-1. XRD peak profiles for X-oriented samples under different treatment conditions. ..	150
Figure 6-2. Dislocation arrangement in as-fabricated (A) and HIP (B) specimen.	151
Figure 6-3. Misorientation maps of X-oriented representative as-fabricated and vacuum annealed specimen.	152
Figure 6-4. Average temperature profile of the selected spot by considering all 27 simulation results.	154
Figure 6-5. Effect of variables in the thermal model on the temperature profiles. Individual effects are shown in (A-C) for beam radius, emissivity, and thermal conductivity,	

respectively. Coupled effects of Beam radius (D) and thermal conductivity (E) for a given emissivity are shown in (D and E).....	155
Figure 6-6. Melt pool snapshots from thermal model simulation showing the effect of melt current and scan velocity for the fabricated samples in the experimental build. Note: Only half of the melt pool is shown in the snapshots due to their axial symmetry along the beam direction. Color bar represents a range of 573K-2100K. Sample number is given at top left corner in each snapshot.....	157
Figure 6-7. Effect of volumetric energy density and cooling rates on the observed grain size for samples 4 to 9.....	158
Figure 6-8. TEY images of all three builds at two different stages. Yellow arrows show representative defects detected by the in-situ monitoring method.....	159
Figure 6-9. a. Lift out specimen for TEM observation; b. EDS map of the particle outlined by red rectangle that clearly shows to be a copper oxide particle; c. tiled image of the top area shown with yellow rectangle, representing the equiaxed subgrains growing transverse to the build direction. d. further magnified image of such subgrain illustrating the distribution of dislocations within the grain and the boundary formed by dense dislocations. Please note the different length scales.	161

1 Introduction

1.1 Background

Developed in the 1980s, additive manufacturing (AM) is gaining increased attention and interest due to the substantial increase in the demand for high performance materials with added functionalities (such as internal cooling channels, foam, or mesh structures with higher strength to weight ratio etc.), and increased complexities in geometrical design. Some of the AM processes require no post-processing or minimal post-processing, and the produced parts can be directly used in practical applications (Gokuldoss et al., 2017). Because the melting occurs in layers of pre-alloyed/ pure metal feedstocks forming small melt volumes that solidify rapidly, the resulting solid microstructure can achieve unique, directional, and epitaxial microstructural features. The material properties used within specific structural components can also be designed in a location specific manner in order to meet any performance requirement that is not even imaginable with traditional metal forming and subtractive techniques (Francois et al., 2017; Mahamood et al., 2014). There are a few papers that present excellent, general overviews of AM, and are great for acquiring fundamentals of the process (Calignano et al., 2017; DebRoy et al. 2018; Frazier, 2014; Herzog et al., 2016; Horn and Harrysson, 2012; Murr et al., 2012; Sames et al., 2016).

Additive manufacturing (AM) of pure copper and its alloys has been explored for past two decades leveraging the aforementioned advantages to cater to high efficiency electrical, thermal management, electronic, aerospace, and radio frequency (RF) photo-injector industries where the primary requirements from the fabricated components are high thermal and electrical conductivity at par with conventionally produced copper parts (El-Wardany et al., 2018; Frigola et al., 2008; Gamzina et al., 2017; Tran et al., 2019). However, as indicated in the literature, AM processing of pure copper faces different challenges due to its characteristic material properties. For example, the high thermal conductivity of copper readily transfers the heat away from the melt pool leading to high thermal gradients. Fabrication defects such as delamination, layer curling, etc. occur due to induced residual thermal stress because of this rapid heat dissipation. Also, its high affinity towards oxygen even at room and/or low temperature makes the production of AM feedstock difficult with respect to its processing conditions, storage, and logistical methods (Rhodin, 1950; White and Germer, 1942). Specifically, laser powder bed fusion of pure copper is difficult due to

low absorptivity of the bulk material (2 to 6%) for conventional wavelength of over 1 micrometer in economically available laser AM systems (El-Wardany et al., 2018; Jadhav et al., 2019; Tran et al., 2019). Because of this low absorptivity, higher beam power is needed to melt the powder bed, rapidly increasing the liquid temperature due to higher absorptivity of the liquid phase. This mismatch leads to the formation of spatter, keyhole porosities, or other types of defects due to higher recoil pressure and more pronounced Marangoni effects at higher melt temperature (Khairallah et al., 2016; Xie and Kar, 1999). Moreover, the inert atmosphere in a laser powder bed fusion (L-PBF) system can lead to oxidation of the molten metal, and thereby decrease the purity of solid copper upon fabrication. In electron beam powder bed fusion process (EB-PBF), the great mismatch of thermal conductivities between the powder bed and solid copper results in a non-uniform heat dissipation over the build layer, further leading to possible warpage, evolution of thermally induced residual stress etc., as mentioned earlier. Nevertheless, fabrication of copper in EB-PBF is still more favorable than L-PBF because of higher absorptivity of electron beam, and processing under high vacuum conditions that prevents any significant amount of oxygen pick up. Therefore, EB-PBF processing of copper is gaining more research interest to fabricate complex copper components along with the desired property.

1.2 Research Motivation

Although stable process conditions mostly for prismatic part shapes have been achieved in EB-PBF of pure copper via systematic experimentation processes, mechanical and metallurgical characteristics of fabricated components are still under investigation. Specifically, the mechanical properties under common post-processing condition, and microstructural evolution under different solidification conditions are extremely important to understand the holistic behavior of EB-PBF processed copper. In the first phase of this research, mechanical characterization of differently post-processed copper is conducted to understand the effects of selected process conditions. This characterization is helpful for designing the manufacturing process sequence of components aimed at a particular application. In the second phase of this research, theoretical and experimental methods are used to control the microstructure of the solidified material. Preliminary experiments and existing literatures reveal a columnar grain structure along the build direction, which results in the anisotropy of properties. This second phase aims at achieving a transition to equiaxed grains

in parallel to build direction along with the equiaxed grain structure commonly found in transverse to the build direction. The hypothesis is that the resulting isotropy in grain morphology will reduce the anisotropy of properties observed thus far. Altogether, this research work seeks to understand the effects of processing conditions and proposes methods that can fabricate copper components with improved properties.

1.3 Structure of the Thesis

Chapter 2 describes the mechanical characterization of EB-PBF fabricated copper in detail and examines the effects of process-related variables. This chapter presents the effects of selected variables on key mechanical property metrics and serves as the baseline for the next phase of research on grain control. The methods for controlling the microstructure can be divided into two categories. In Chapter 3, the first method is presented, which deals with the modification of process parameters only. A columnar-to-equiaxed transition (CET) model is developed for EB-PBF of copper that can be used for predicting the grain structure for a given process parameter set. However, difficulties in processing within the proposed parameter space led to the research of the second method for grain control, which is presented in Chapter 4. This chapter deals with the solutal modification of copper powder feedstock to achieve heterogeneous nucleation and hence, suitable solidification conditions that can lead to CET in the grain structure. Preliminary experimental results presented in this chapter illustrate the feasibility of this method showing equiaxed grains along the build direction. Chapter 5 submits the future work envisioned for further understanding of the proposed methods of producing pure copper parts with improved properties by the EB-PBF method.

2 Mechanical characterization of EB-PBF fabricated copper under different post-processing conditions

2.1 Introduction

Mechanical characterization of additive manufactured copper has been done primarily in as-fabricated conditions. This precludes the analyses of the effects of different post-processes such as annealing heat treatment, densification, etc., on the resulting microstructure and mechanical properties. Therefore, characterization of such post-processes is required to better understand the expected mechanical behavior of additive manufactured copper processed through different routes. In this chapter, uniaxial tensile test and microhardness measurement of EB-PBF fabricated copper are conducted where different post-processes (as-fabricated, vacuum annealed, and hot isostatic pressing) and different orientations (parallel and perpendicular to build direction) are examined to identify their influences on the mechanical response of the material. First, a brief literature review on AM of copper is presented, followed by the description of methods and materials used for the fabrication purposes. Next, test results are presented and discussed in light of grain size, dislocation features, and second phase oxides that contribute significantly to the observed differences among different post-processes. Besides identifying these factors for different mechanical responses, the result indicates at the need for a reduced columnar grain fraction along the build direction to reduce the morphological anisotropy, and subsequently, to reduce the effect of build orientation.

2.2 Literature Review

2.2.1 Laser powder bed fusion of copper

Most of the publications on the L-PBF of pure copper discuss the process feasibility as a function of process-related parameters, and solid density characterization of prismatic part shapes as the validation criterion. Among those who published experimental data on the mechanical behavior of L-PBF processed copper, Lykov, et al. (2016) were the first to demonstrate an ultimate tensile strength (UTS) of 149 MPa with a relative density 88.1%, processed in a conventional CO₂ L-PBF system. Yan, et al. (2020) conducted a more detailed set of experiments using a range of

melt currents and scan velocities to characterize their effect on mechanical properties. For their best process parameter condition, an average of 99.1% relative density was achieved that also yielded best surface roughness values. As for the tensile tests, the authors reported an UTS of 248 ± 8.5 MPa, and elongation to failure 9.2 ± 2.12 for the best process parameter set. Those values were observed to deteriorate as the process yielded either higher or lower energy densities, both leading to higher porosity fractions in the parts. Moreover, vacuum annealing of samples at 500°C fabricated with the best parameter set resulted in a lower strength and higher elongation, hypothesized to be caused by the coarsening of grains during the heat treatment process. Jadhav, et al. (2021) produced pure copper with 99.8% optical density in a customized laser system equipped with infrared fiber laser at a 1080 nm wavelength. Their study revealed that the maximum density was achieved when the melting process was in a transition between conduction mode and a keyhole mode, whereas, either melting mode led to lack-of-fusion or keyhole induced porosity, respectively, when the melting process operated at those two extreme situations. Mechanical result of the as-fabricated specimens recorded an average UTS of 211 ± 4 MPa, yield strength of 122 ± 1 MPa, and an elongation to failure of $43 \pm 3\%$. While only the specimens with best density were tested for mechanical properties, samples fabricated outside the narrow stable processing window showed large fractions of process induced porosities that would ultimately result in an inferior mechanical and physical properties. Other authors have examined different aspects of process parameters for a better understanding of the resulting physical properties. For example, Colopi, et al. (2018) found that high power densities led to stable and defect-free solids with a relative density of $97.8 \pm 0.4\%$. Ikeshoji, et al. (2018) showed that other than scan velocity and melt current, hatch pitch was an important factor as that controlled the overlap of the incident beam between two neighboring scan lines. A relative density of 96.6% was achieved for a smaller hatch pitch, which resulted in more overlap, and thus, higher average energy input. Jadhav, et al. (2019) obtained an electrical conductivity of $83 \pm 3\%$ to $88 \pm 2\%$ IACS for different process inputs, and achieved a highest relative density of 98%. Silbernagel, et al. (2019) examined the effect of heat treatment on the electrical conductivity, and found that the post-process actually improved the conductivity owing to enhanced fusion between un-melted or un-sintered powder particles. El-Wardany, et al. (2018) investigated the effect of surface oxides on powder feedstock, which showed an increase in density at higher power input when the oxygen content is high. Trevisan, et al. (2017) produced an average relative density of $83.01\% \pm 0.13\%$ with an ultrafine microstructure using a very fine

pure copper powder and high cooling rates. Several other research studies examined the system-related issues, e.g. using ultrashort pulse laser at high frequency (Kaden et al., 2017), blue/green diode laser with shorter wavelengths (Heussen and Bremen, 2017; Masuno et al., 2017; Pelaprat et al., 2018) in an effort to produce a feasible processing space for copper in L-PBF systems.

2.2.2 Electron beam powder bed fusion of copper

In an early process feasibility study of copper in electron beam PBF system, Frigola, et al. (2014) examined the effect of different feedstock materials (99.99% pure and 99.8% pure), and showed that pure copper powder produces equiaxed grains with coherent annealing twins at high processing temperatures. A yield strength of 76 MPa was measured while the electrical and thermal conductivities measured 97% IACS and 390 W/m-K, respectively. Ramirez, et al. (2011) studied a highly oxidized copper powder with 98.5% purity that resulted in an incoherent precipitate of cuprous oxides along the columnar grains. They observed an increase in hardness (72 HV of powder to 88 HV of solid) because of the dislocation loops associated with the precipitates. Moreover, it was noted that hardness of the upper build region was much greater (88 HV) than that of the bottom part (57 HV), indicative of precipitation strengthening of the solid along the build direction. Lodes, et al. (2015) established a stable process window for fabricating 99.94% pure copper at different scan speeds and melt currents, ultimately leading to average relative densities greater than 99.5% with a maximum of 99.95% for their optimal process conditions. Raab, et al. (2016) utilized the process space developed by Lodes, et al. (2015), and characterized its thermal and electrical conductivity that measured 400.1 W/m-K (99.8%) and 55.82 MS/m (96.24% IACS), respectively. On the other hand, Guschlbauer, et al. (2020, 2018) undertook a thorough mechanical study for different powder types (pure and oxidized) to examine the effect of build orientations, process parameters, and second phase copper oxides on the strength and ductility in as-fabricated conditions. Maximum UTS of 231.6 ± 5.4 MPa in transverse to the build direction was obtained, whereas a maximum of 181.3 ± 2.7 MPa was achieved in samples oriented parallel to the build direction. It was shown that increase in strength is associated with a decrease in ductility for all orientations. Fractographic results illustrated that cuprous oxides could act as crack propagation sites because of their brittle behavior compared with the softer matrix. For solids with higher oxygen content, the authors obtained an UTS of 177 MPa for samples that were oriented transverse

to the build direction. It was therefore concluded that oxides deteriorate the mechanical properties in the as-fabricated condition irrespective of their concentration.

2.2.3 Binder jetting of copper

Binder jetting (BJ) of pure copper is attractive as the process does not depend on the thermal or optical behavior of copper, and does not employ a sophisticated energy source requiring expensive tooling systems. Bai and Williams, (2015) experimented with different powder size distributions and sintering conditions to establish the processability of pure copper through binder jetting. Their mechanical study showed 116.7 MPa UTS achieved for samples sintered at 1080°C, whereas, only 8.4 MPa UTS was seen in samples sintered at 1040°C. Kumar, et al. (2017, 2019) took these baseline studies, and employed hot isostatic pressing (HIP) to further densify the solids after sintering in a hydrogen atmosphere. HIP, as suggested by several authors (Atkinson and Davies, 2000; Wei et al., 2008), is a widely used process for removing internal porosities. Kumar, et al. (2019) found that HIP improved the UTS of the samples made from bi-modal powder distribution, similar to Bai, et al. (2017), by 32% with the maximum value of 176 MPa along with an elongation of 67.2%. As for the electrical and thermal conductivities, samples with 97.3% relative density registered 96.6% IACS and 84.5% of theoretical values, respectively.

2.2.4 Overall discussion

A summary of the findings of these available studies is illustrated graphically in Fig. 2-1. Following attributes can be inferred with respect to the processing space, and its influence on the physical and mechanical properties of AM copper.

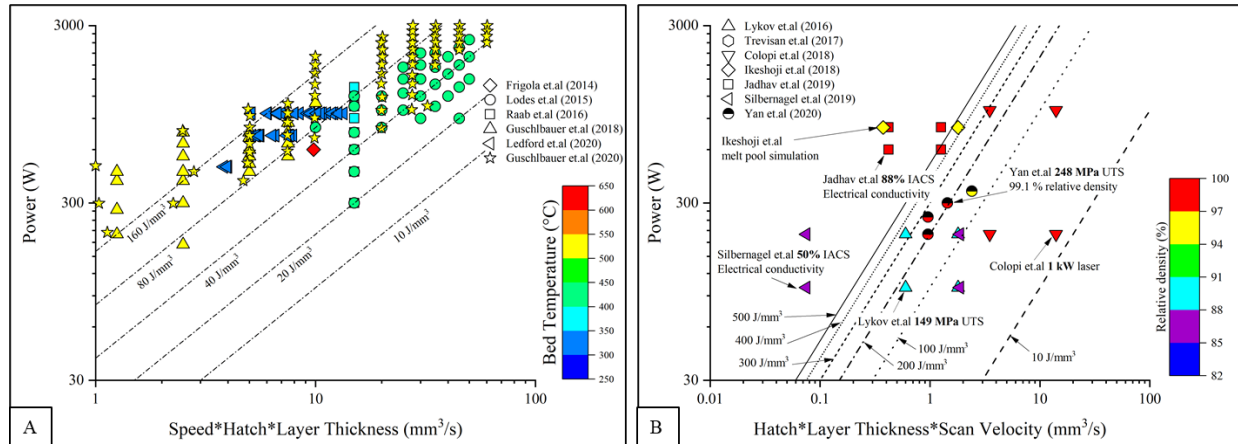


Figure 2-1. Processing space of PBF fabrication of pure copper [EB-PBF (A), L-PBF (B)] by taking the process parameters used in the literature. Major observations of L-PBF studies are highlighted along with reported solid densities. As majority of EB-PBF reported densities reach >99.5%, bed temperature is highlighted in Figure (A) instead of densities.

1. Processing space of copper is different for L-PBF and EB-PBF, primarily due to the difference in thermal response of the powder based on the energy source.
2. The PBF processes are able to achieve >99% relative densities if an appropriate processing space is selected that results into a suitable volumetric energy density.
3. EB-PBF process is reported to achieve >100% IACS electrical conductivity with thermal conductivity close to 393 W/m-K.
4. L-PBF process reports the highest UTS obtained in as-fabricated condition (248 MPa), whereas BJ process achieves the highest elongation to failure in sintered and HIP condition (>67%).
5. BJ produces almost equiaxed grains with grain sizes averaging ~25 μm ; both L-PBF and EB-PBF produce epitaxial columnar grains along the build direction with occasional grain lengths in millimeter range. While no build orientation effect on mechanical property is characterized in BJ and L-PBF processes, EB-PBF reports value differences ranging over 50 MPa in UTS.

Important process parameters and obtained solid densities are presented in Tables 6-1 to 6-3 in the Appendix A for a comprehensive understanding of the state-of-the-art of AM of copper.

2.3 Research Motivation

From the literature review, it is apparent that the mechanical property characterization of PBF fabricated copper is conducted majorly in as-fabricated condition. However, it is well-known that densification methods such as HIP are used as a post-process in AM to improve as-fabricated part densities. Keeping all other factors constant, material density is observed to correlate with strength by power terms (German, 1996, p. 56), and as such, the effect of higher densities are clear in the strength values reported in L-PBF and BJ processes where higher UTS are obtained as the relative density approaches 100%. In EB-PBF process, lack-of-fusion type of defects are common that are formed perpendicular to build direction, and are attributed to behave as stress concentration sites during the plastic deformation process. Such process-related porosities can be reduced or eliminated by using HIP that employs high isostatic pressure at elevated temperature and obtains almost full part density. However, in a review by Seifi, et al. (2016), HIP is seen to have a mixed result in terms of its effect on the mechanical properties. In some material systems higher strength and ductility are obtained along with further densification, whereas in some cases, HIP coarsens the microstructure as a result of thermal activation and subsequently deteriorates the part strength. However, the effect of HIP on PBF processed pure copper is yet not conclusive and needs to be examined to validate its applicability as a post-process.

Besides density, second phase constituents, impurity inclusions, and grain sizes are known to have influences on the mechanical response of materials too. However, purity levels used in most of the PBF fabrication of copper have been >99.9% except for a few studies such as that of Ramirez, et al. (2011) which specifically looked into the precipitate structure of copper oxides with an oxygen level exceeding 2000 wt. ppm. It is found from the literature that oxygen content greater than 300 ppm leads to a significant loss of ductility even at high part densities (Myers and Blythe, 1981). Further, it is reported that oxygen present as a surface layer played a deleterious role in the fatigue life of copper by favoring crack formation during the early stages of the test (Thompson et al., 1956). Although oxygen at low to moderate concentrations is known to have no significant effect on the electrical conductivity (Horn and Gamzina, 2020), process routes to reduce the oxygen content in fabricated specimens is desirable since it improves ductility and fatigue life of copper. It is shown by Nieh and Nix (1981) that annealing copper at 950°C under a vacuum atmosphere for several hours resulted in the dissociation of copper oxide and subsequent release of oxygen from the material owing to its low partial pressure in the system. This method proves

advantageous over other deoxidation processes as it reduces the internal oxygen content without the addition of any other elements, thereby retaining the desired level of purity of the fabricated part. In spite of this benefit, not enough research has been done on employing vacuum annealing as a post-process in AM of copper, although oxygen contents in the ranges of 188 to 545 wt. ppm and 100 to 700 wt. ppm have been reported by Guschlbauer, et al. (2020) and Ledford, et al. (2019) during the EB-PBF processing of copper, respectively. Grain size, on the other hand, influences strength and ductility of pure copper, especially in the low strain range, due to the contribution from the grain boundary fraction that reduces with coarsening of the grains (Carreker and Hibbard, 1953). It is thus expected that the differences in grain sizes produced by the aforementioned post-processes will result in different mechanical properties, necessitating their characterization to understand their overall impact.

However, aspects such as the effects of densification post-process, vacuum annealing on oxide dissociation, change in grain sizes and other microstructural features as a function of post-processes etc. are not well documented for EB-PBF processing of copper. Yet, different processing steps are known to alter microstructural features such as macroscopic grain sizes, dislocations, second phase constituents etc. that ultimately lead to different mechanical properties. For example, Torre, et al. (2004) observed a decrease in dislocation density and partial recovery in cell wall boundaries in equal channel angular extrusion of copper that led to increased ductility and reduced strength at higher number of passes. Hutasoit, et al. (2020) reported an increase in strength and ductility in cold spray additive manufactured pure copper annealed at 400°C for 1 hour in an air environment and attributed the change to the recrystallization and internal strain relieving of the as-deposited grains. On contrary, Yan, et al. (2020) observed a decrease in strength along with an increased ductility when the L-PBF processed copper was annealed at 500°C for four hours under a vacuum environment. Therefore, it is inferred that different post-processes influence the properties differently based on the process history of the material and raise the question as to what mechanical behavior can be expected from differently post-processed EB-PBF copper. Hence, in our study, room temperature uniaxial tensile test and microhardness measurements of copper specimens fabricated with different post-processing conditions are investigated. Some specimens are treated with HIP to examine if the process improves properties by densification or deteriorates them by microstructural coarsening, as mentioned previously. Vacuum annealing is conducted on other specimens to observe its effect on both oxygen reduction and mechanical response, while the

rest of the specimens remain in the as-fabricated condition. The experimental framework along with the description of the selected process-related variables are presented in the next section, and the results are discussed in view of the collective influence of bulk density, grain size, distribution of dislocations, and second phase oxides.

2.4 Materials and Methods

2.4.1 Powder feedstock

Nitrogen gas atomized copper powder screened to -270/+635 mesh is obtained from Sandvik Osprey (Sandvik Osprey OFHC). The initial oxygen content of the powder is 457 ppm, measured using inert gas fusion (LECO OH836, copper protocol). Particle size measurement is carried out on a Microtrac S3500 using laser diffraction technique. The unalloyed copper powder chemistry is obtained using the inductively coupled plasma mass spectroscopy (ICP-MS) method. Powder morphology is observed using a JEOL 6010LA scanning electron microscope (SEM).

2.4.2 Sample fabrication

Five builds, each containing three rectangular blocks measuring 58.5 mm×12.7 mm×58.5 mm are fabricated upon an 86 mm diameter and 40 mm thick oxygen-free copper base plate using a customized Arcam A2 EB-PBF system (Software version 3.2, SP2, Arcam AB), the details of which are described by Ledford et al. (2019). The nominal layer thickness is 40 μm . The powder bed temperature is measured by a thermocouple affixed to the bottom of the build substrate and is observed to be stable throughout the build duration within a range of 290°C-320°C. The vacuum level inside the chamber is maintained at 5×10^{-4} mbar. Table 2-1 and Table 2-2 show the process parameters used to fabricate the samples. As shown in Figure 2-2, this resulted in an average volumetric energy density of 92.3 J/mm³. As shown in Figure 2-3, in the overall experimental plan, the rectangular blocks are oriented 45° about the z-axis. The beam raster patterns are oriented parallel and perpendicular to the x-axis and rotated 90° each layer. The blocks are melted “model-wise”, one by one so that each experienced nearly uniform scan line length (shown schematically on the front block within the build layout) and thermal history. Upon completion, the build volume is allowed to cool to below 30°C prior to removal from the build chamber. The powder cake

surrounding the parts is removed manually in an argon filled glove box maintained with an atmospheric oxygen content below 10 wt. ppm. The powder is passed through a 70-mesh screen to remove large agglomerations and blended with the primary batch prior to each reuse. Powder size and oxygen content of both the reused powder and fabricated solids are measured after each build.

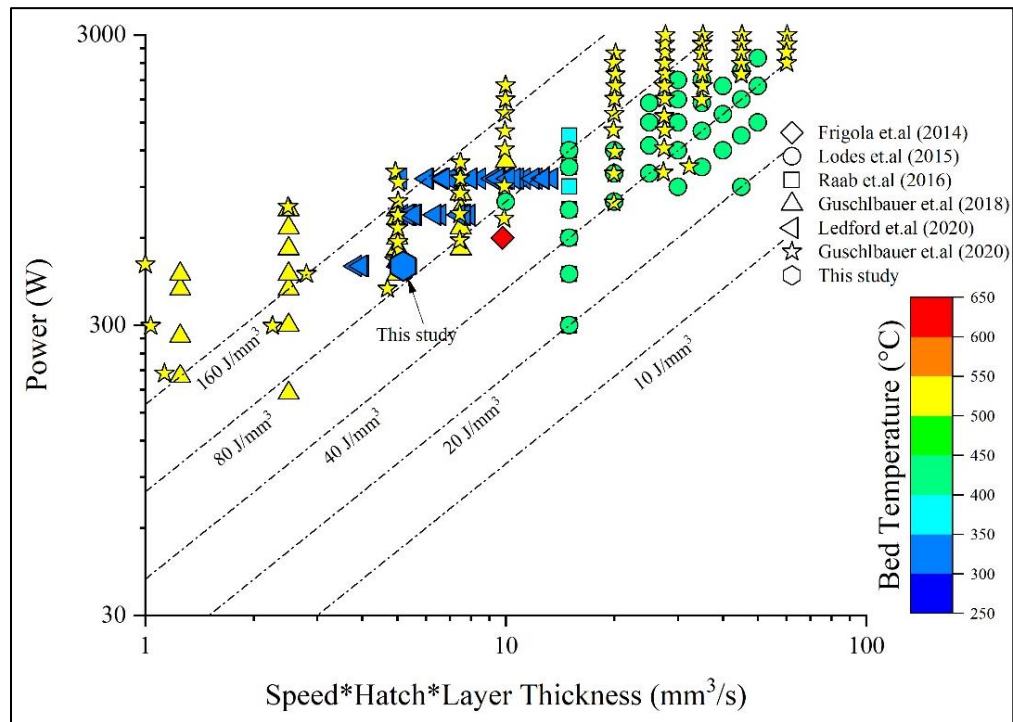


Figure 2-2. Processing space of EB-PBF fabrication of unalloyed copper adopted in this study, overlaid on the processing space reported by EB-PBF studies (shown in **Figure 2-1** previously).

Table 2-1. EB-PBF melt parameters used to fabricate the specimens used in this study (the parameters shown are specifically those that have been modified from the standard commercial parameter sets for Ti6Al4V, V3.2 SP2).

Melting Parameter	Value
Surface Temp (°C)	600
Power Analyze Max Current (mA)	25
Power Analyze Min Current (mA)	8
Beam Speed (mm/s)	1000
Beam Current (mA)	8

Table 2-1. Continued.

Max Current (mA)	8
Focus Offset (mA)	18
Speed Function	20
Line Offset (mm)	0.13
Change for Each Depth (mm)	0.02
Heating Enable	TRUE
Max Heat Time (s)	5
Melt Heating Use Process Power	TRUE
Heating Between Models	TRUE

Table 2-2. EB-PBF preheat parameters used to fabricate the specimens used in this study (the parameters shown are specifically those that have been modified from the standard commercial parameter sets for Ti6Al4V, V3.2 SP2).

Parameter	Value
Focus Value (mA)	70
Focus Value Heater (mA)	150
Box Enable	TRUE
Box Size (mm)	85
Offset to Part (mm)	0.1
Max Current for Box (mA)	22.5
Jump Safe Sweep Max Current (mA)	13.5
Jump Safe Sweep Min Current (mA)	0.1
Jump Safe Sweep Speed (mm/s)	14600
Jump Safe Sweep Total Repetitions of Sweep	40
Jump Safe Sweep Max Number of Sweeps	40
Heating Enable	TRUE
Max Heat Time (s)	5
Heating Between Models	TRUE

Figure 2-3 illustrates the experimental design. The orientation of tensile bars within each block is randomly assigned subject to the constraint that only specimens with a single orientation could be extracted from any one block. As illustrated in the figure, each as-fabricated block is cut into four tensile blanks using a bandsaw assigned as Z when the blank is cut with the long sample axis parallel to the build direction and X when the long sample axis is perpendicular to the build direction using ASTM 52921 nomenclature. Throughout this chapter, Z-oriented or vertical and X-oriented or horizontal are used interchangeably. Each of the tensile blanks is then randomly assigned to one of three treatment groups. Samples in the as-fabricated group are tested without

treatment, samples from the HIP group are subjected to HIP using a QIH15LMURC high pressure furnace (Quintus Technologies) with a heating rate of 10°C/min to 950°C, a dwell of 2 hours, and cooling at a rate of 10°C/min. The pressure is proportional to the temperature, and at 950°C is 165 MPa. Several preliminary experiments were conducted at Quintus Technologies to identify this particular parameter that yielded high densities. Samples assigned to the vacuum annealing group are subjected to the same temperature profile in a tube furnace (Thermo-Scientific Lindberg/Blue M HTF55322C), but under vacuum at 5×10^{-5} mbar (5×10^{-9} MPa). After treatment, all samples are machined into ASTM E8 subsize specimens (specimen type 4). The surface finish of the machined specimens in the gauge region measured an average of 16 $\mu\text{in } R_a$ using a stylus profilometer (Mitutoyo SurfTest SJ210).

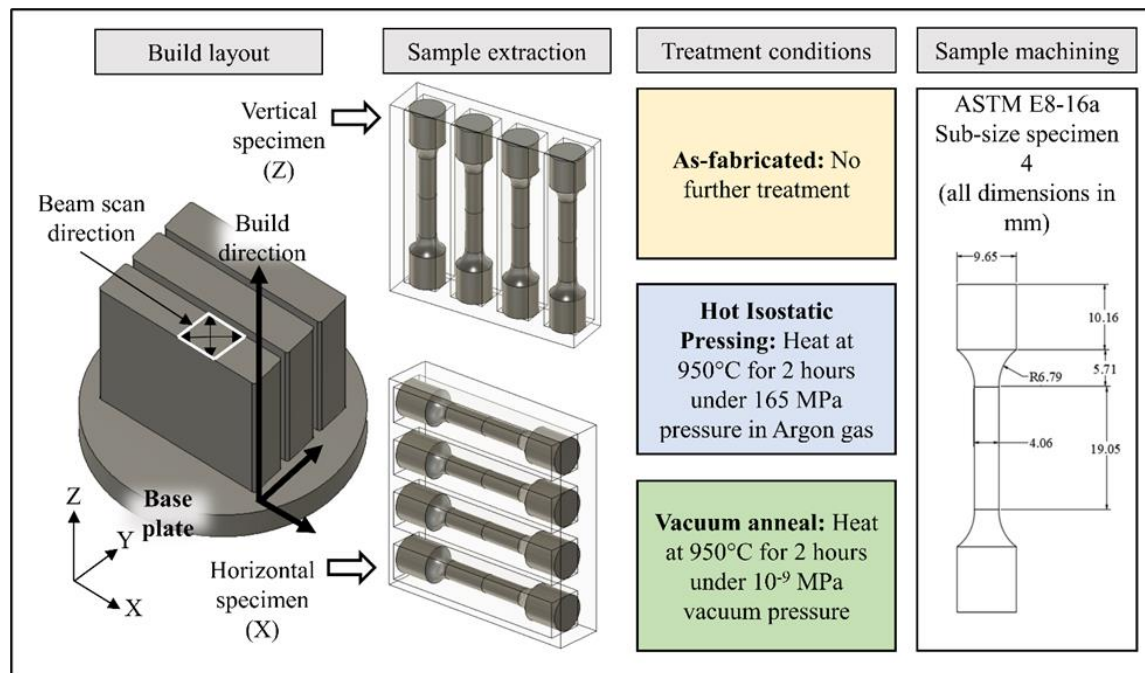


Figure 2-3. Overall experimental framework highlighting the build layout and sample orientations, treatment conditions, and the ASTM Standard design of the test coupons used in the study.

A summary is given in Table 2-3 that describes sample location, orientation, and post-processing conditions for the tested samples. For a given process condition, recorded strength and part density values are seen to change by only $\pm 5\%$ of the average value for different location and builds, and thus, the effect of sample location and build number are not discussed within the scope

of the present study. However, it should be noted that several samples are lost during the machining process due to operational and tooling error, reducing the overall sampling space of different process conditions investigated in this first phase of research. Nevertheless, as the machining failure is not caused by any material-related irregularities, analysis of the rest of the samples remains valid and pertinent to the experimental hypothesis.

Table 2-3. Summary of the location, orientation, and post-processing condition of the samples tested in this study. (AF= As-fabricated, HIP= Hot isostatic pressed, VA= Vacuum annealed; B= Bottom, M= Middle, T= Top).

Build number	Z-oriented samples			X-oriented samples (locations)		
	AF	HIP	VA	AF	HIP	VA
1	3	2	-	1 (B)	-	-
2	1	2	-	3 (B, M, T)	-	2 (B, T)
3	2	-	2	-	4 (B, M, T)	-
4	-	1	2	-	3 (B, M, T)	-
5 ¹	-	-	-	1 (B)	1 (T)	3 (M, M, T)

2.4.3 Uniaxial tensile test procedure

After machining, each tensile sample is rinsed in ethanol and acetone to remove the surface machining contaminants. Specimens are mounted within a wedge grip in an ATS 1620C universal testing machine, pulled with constant crosshead speed of 0.254 mm/min (according to ASTM E8-16a standard) using a load cell of 5 kN. Load displacement data are taken via TestVue® software for the entire duration of the test. For the measurement of elongation to failure, digital image correlation (DIC) is used alongside the conventional measurement of fracture length between two gage marks done for all samples. Although DIC is capable of measuring strain on a granular level based on the camera resolution (Lord et al., 2010; Pankow et al., 2010; Verhulp et al., 2004), the method largely depends on proper adherence of the speckle material onto the test material so that there is no relative motion between them. For materials that show small elongation to failure, DIC can be successfully employed for in-depth micro-strain analysis, as done by Karlsson, et al. (2014) for instance on additively manufactured Ti-6Al-4V tensile specimens. However, for EB-PBF

¹ Build was stopped due to powder shortage before it reached the height required for vertical samples.

processed copper, DIC is difficult because elongation of copper is high, and commercially available paint speckles tend to flake off of the specimen at these high elongations, lending the image analysis erroneous at those points. Moreover, as the specimens are of cylindrical cross-section, the use of 2D-DIC relies upon a frontal rectangular strip data only, which may lead to directional strain anomaly in micro scales. Samples are ultrasonically rinsed in ethanol and acetone before they are painted with a white background coating and black speckles. As the elongation specification of dried paint is below that of copper, the paint is allowed to only settle under a dry cold air gun before the beginning of the test. This wet painting technique has been useful in polymeric materials and is seen to produce better results in copper than its dried state. As per the DIC setup, a 12.3 MP FLIR Grasshopper USB 3.0 camera with a pixel size of 3.45 μm is used along with a Canon 100 mm lens under appropriate illumination conditions obtained using two F&V K4000S bi-color studio lighting kits. Strain field mapping and elongation measurement are carried out using GOM Correlate software (2018 Hotfix 6, Rev. 117418), where selected speckles are tracked for making strain measurements. Figure 2-4 (D-E) show an example of such strain field mapping of a Z-oriented vacuum annealed specimen in the beginning and end of the test. The yield stress is calculated from a 0.2% offset from the linear portion of the stress-strain curve. The mechanical properties results are compared using ANOVA (JMP Pro 15. Ink) with pooled variance. Prior to analysis, the data are tested for normality using the Shapiro-Wilk test with the α -value of 0.05.

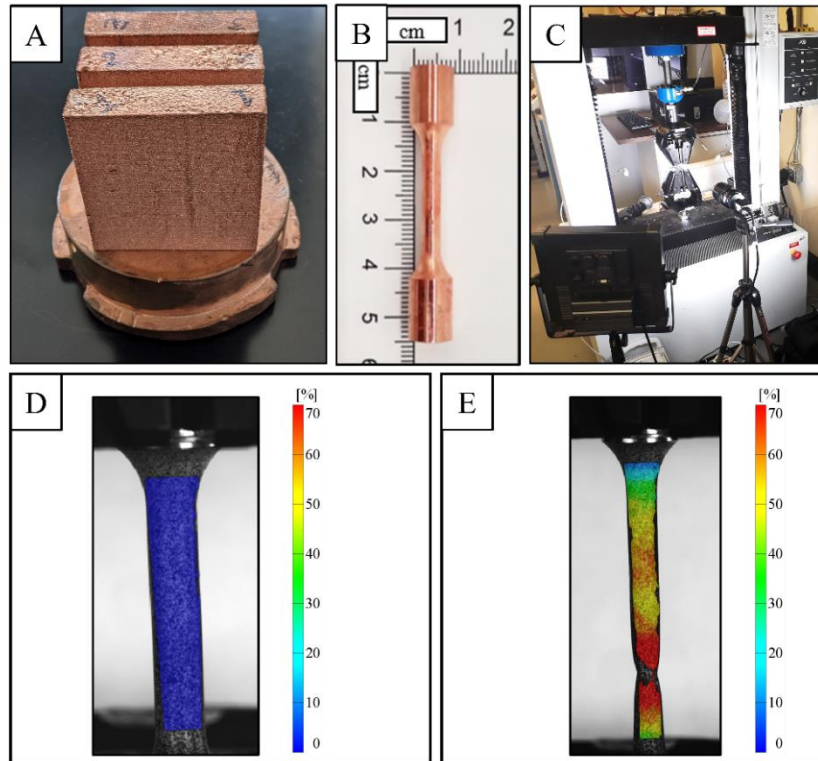


Figure 2-4. Fabricated blocks on a copper substrate (A), Machined tensile sample according to ASTM E8-16 standard (B), Overall tensile test set up showing the arrangement of DIC camera and lighting kits (C), Strain mapping of a Z-oriented vacuum annealed tensile sample in GOM Correlate software in the beginning(D) and the end (E) of the test.

2.4.4 Metallographic analyses and microhardness measurements

The grip section of each tensile bar is cut perpendicular to the longitudinal axis approximately 10 mm from each end. These samples, in turn, are sectioned longitudinally with a low-speed diamond saw (Buehler Isomet). The cut face is potted in phenolic resin and progressively ground using 400,600,1000,2000 and 4000 grit SiC paper with water lubricant. Samples are polished with 1 micron, 0.3 micron, and 0.05-micron alumina slurry, and etched with Ammonium Persulphate solution by submersion/swabbing for 10 seconds and rinsed to reveal grain structure under a Hirox KH7700 optical microscope. Four micrographs along the build direction are taken from each sample, and grain width is measured by the number of intersecting grains for a fixed length of line. For each image, ten equidistant lines are drawn, and the average values are taken for the determination of grain sizes. These same samples are indented for Vickers

microhardness measurements in a LECO M400 hardness tester under 100 gf load for a dwell time of 10 seconds. A total of ten indentations, 500 μm apart, are made along the direction of tension for both types of sample orientation, and the average values are reported. The sectioned grip end not used for metallographic analysis is used to measure the density of the sample using gas pycnometry (Quantachrome Ultrapyc 1200E according to ASTM B923-16 standard). Approximately 1 +/- 0.0002g of the same is sectioned longitudinally for oxygen content measurement with inert gas fusion (mentioned in §2.4.1). After tensile testing, a thin slice of the grip end along the build direction is cut and polished for as-fabricated, HIP, and vacuum annealed X-oriented samples for electron backscatter diffraction (EBSD) which is performed on the FEI Quanta 3D Field Emission Gun (FEG) equipped with an Oxford Instruments EBSD detector on a 3mm \times 3mm area on samples extracted with a X-oriented orientation. Inverse pole figure maps and pole figures are generated with Channel 5 Tango and Mambo software, respectively.

2.4.5 Fractographs and oxides characterization

In order to reveal the overall fracture morphology, fracture surfaces of the tensile specimens are viewed under the SEM using standard operating conditions to understand the effects of the process-related variables. Representative specimens from each processing condition are further analyzed in a variable pressure scanning electron microscope (VPSEM) Hitachi S3200N under an acceleration voltage of 20 kV to obtain electron dispersive X-ray spectroscopy (EDS) maps of the specimen surface. Characterization of grain boundary oxides is carried out with STEM-EDS using a ThermoFisher Talos F200X TEM. The TEM samples are prepared with a Hitachi Ar-blade 5000 ion mill for 15 minutes prior to sample lift out, thinning and mounting with the FEI Quanta 3D FEG.

2.5 **Results and Discussion**

2.5.1 Powder characterization

Figure 2-5A depicts the particle size distribution of the powder used in this study with a d10-d90 size range of 22 – 63 μm and d50 value of 39 μm and demonstrates no significant change in particle size with reuse over the course of this study. Table 2-4 shows the chemistry of the initial

feedstock as measured by ICP where no significant contamination is detected. The oxygen content of the powder does show an increase during the study from an initial 457 ppm to a final value of 630 ppm after the fifth run. While the raw material used to produce the powder is oxygen free (ASTM B170-99 class 1 OFE copper, C10100) with <5 ppm oxygen; the measured level of oxygen in the powder is similar to that of electrolytic tough pitch (ETP), C11000 with approximately 400-600 ppm oxygen (Horn and Gamzina, 2020), and can be attributed to the thin layer of non-passivating cuprous oxide and the high specific surface area of AM powders. This oxygen pickup can be difficult to avoid in practice and originates in the screening of powder to size fractions suitable for AM as well as from build-to-build powder handling. It is likely that special handling and monitoring, or techniques to reduce surface oxides may be required. While the oxygen is elevated in the feedstock powder, it is within the range of recent reports for 3D printed copper powder (Guschlbauer et al., 2020; Ramirez et al., 2011; Yan et al., 2020), where no AM related study has reported oxygen values for copper powder that approach the values of C10100.

The SEM image shown in Figure 2-5B illustrates chiefly spherical morphology with scattered satellite particles attached to the powder surfaces, a typical feature of gas atomized metal powder. While the powder distribution is lower than that typically used by EB-PBF (45-106 μm), no detrimental effects on powder bed formation or electrostatic charging due to the size distribution are observed. It should also be noted that the higher electrical conductivity of copper mitigates the charge induced scattering common in other AM materials (Cordero et al., 2017). Horn, et al. (2018) also previously demonstrated improvements in the surface finish of EB-PBF produced copper associated with finer powder size distributions.

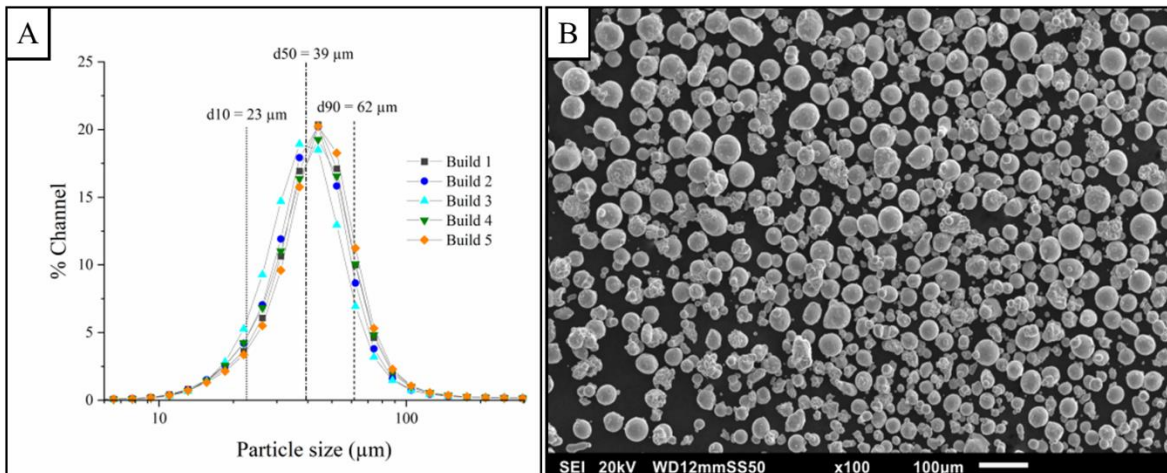


Figure 2-5. Particle size distribution of feedstock unalloyed copper powder used across the builds (A), and SEM image of the powder prior to the first build (B); scale bar shows 100 μm.

Table 2-4. ICP-MS analysis of feedstock unalloyed copper powder prior to the first build. Values are reported in wt. ppm.

Ag	Cd	N	P	Pb	S	Sb	Sn	Zn
10	<1	2	5	2	8	<1	<1	<1

2.5.2 Uniaxial tensile test results

Figure 2-6A reports the density of samples from each treatment condition. The error bars shown represent a 95% confidence interval based on pooled variance of all samples. Within each treatment group no difference in specimen density is detected based on sample orientation, build number or location within the build. Mean density of the specimens ranges from 8.88 g/cm³ to 8.92 g/cm³ (99.4 to 99.9% of theoretical). Specimens subjected to both vacuum anneal heat treatment and HIP exhibit a slightly higher density (8.91±0.01 g/cm³ and 8.92±0.01 g/cm³, respectively) compared to as fabricated samples (<p=0.0001), however no significant difference in density is detected between the HIP and vacuum annealed specimens (p=0.084). It should also be noted that the overall densification is relatively small from the as fabricated to treated conditions (only 0.45%) as the as-fabricated density is already 8.88±0.1 g/cm³.

Figure 2-6B shows the effect of oxygen on post treatment. As noted previously, the oxygen content of the powder trended upward from build 1 to build 5, while within each build there is no

difference between the oxygen content of the powder and the solid specimens prior to treatment, and no difference in oxygen content is detected as a function of sample orientation. The as-fabricated specimens and specimens subjected to HIP show no difference in oxygen content across all builds with average values of 468 ± 47 wt. ppm and 466 ± 43 wt. ppm, respectively. Specimens subjected to the vacuum annealing treatment are significantly different that the other groups, with an average oxygen content of 280 ± 51 wt. ppm. With a vacuum annealing heat treatment of 950°C for 12 hours, EB-PBF produced copper specimens were previously shown to be reduced from 500 wt. ppm to 30 wt. ppm (Horn and Gamzina, 2020). Nieh and Nix, (1981) had previously shown that annealing copper at 950°C under a vacuum environment resulted in the dissociation of copper oxide and subsequent evaporation from the surface. In this study the vacuum annealing time is limited to match the time and temperature profile of the HIP treatment. These data support previous results suggesting that vacuum annealing may be an effective method of removing oxygen from AM copper. Based on the low diffusion coefficient of oxygen in copper, however, wall thickness may be a practical limitation where high isothermal holding time and increased processing temperature will be required to promote the oxide dissociation (Magnusson and Frisk, 2013).

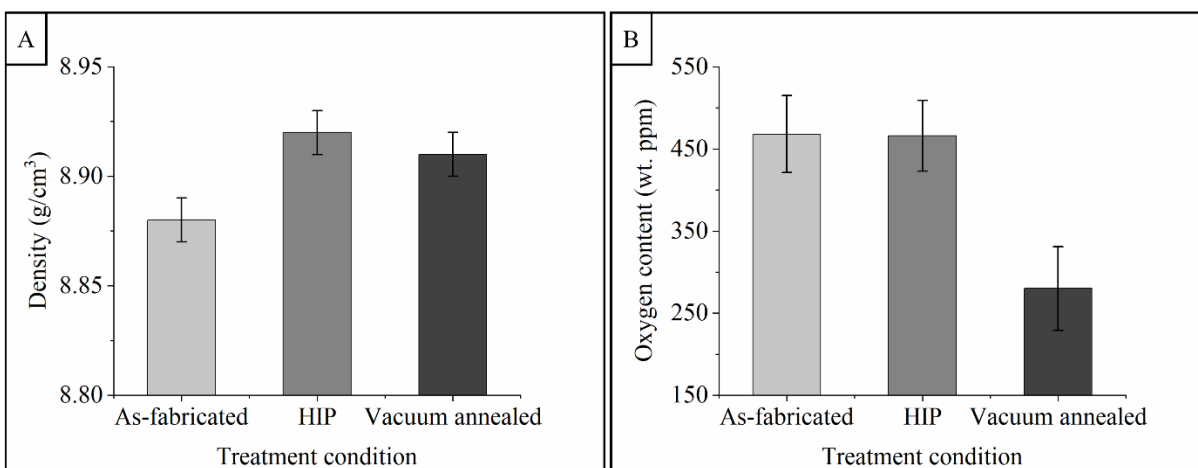


Figure 2-6. Plots illustrating the effect of treatment condition on the density (A) and oxygen content (B) of copper produced by EB-PBF. Error bars indicate a 95% confidence interval based on the pooled variance of all samples.

The plots in Figure 2-7 report the measured mechanical property results from the experiments, including UTS, yield, elongation, and microhardness in the as-fabricated condition

and after post processing conditions for each orientation. ANOVA fails to detect any significant difference in UTS, yield, or elongation within each treatment group associated with the sample batch number ($p > 0.15$), the block number from which the samples are harvested ($p > 0.41$). These trends are observed in Figure 2-7 where the mechanical properties data are plotted with test orientation and treatment condition.

The X-oriented specimens exhibit higher UTS compared to Z-oriented specimens for all three processing conditions, as-fabricated with 211.2 ± 14.7 MPa and 177.2 ± 8.5 MPa ($p = 0.0003$), HIP with 195.7 ± 2.2 MPa and 175.3 ± 4.3 MPa ($p < 0.0001$), and vacuum annealed with 195.5 ± 3.8 MPa and 166.2 ± 17.6 MPa ($p = 0.0007$), respectively (see Figure 2-7A). The average yield stress, measured from a 0.2% offset from the linear portion of the stress-strain curve, is observed to vary between as-fabricated, HIP, and vacuum annealed specimens, regardless of orientation, as illustrated in Figure 2-7B. No significant difference is detected in the measured yield stress between the X and Z specimens in the as fabricated condition with 101.4 ± 27.9 MPa and 102.5 ± 19 MPa ($p = 0.931$) respectively, after HIP 87.3 ± 9.9 MPa and 74.5 ± 7.6 MPa ($p = 0.0475$), or after vacuum annealing, 56.7 ± 9.4 MPa and 52.2 ± 12.3 MPa ($p = 0.42$). The as-fabricated samples consistently have the highest yield values, averaging just over 100 MPa, but also the widest variance due most likely to residual defects such as localized un-healed layer defects. The HIP treatment has an average midrange value for yield stress, ~20% lower than the as-fabricated condition, and a reduced scatter for both orientations ($p = 0.0016$). Consistently low yield stress values are observed in the vacuum annealed samples, ~46% lower than the as fabricated-condition ($p < 0.0001$) and ~32% lower than the HIP condition ($p < 0.0001$).

While the strength values are observed to be influenced by harvest orientation (UTS) and post-treatment condition (0.2% yield); the most obvious property affected is elongation, as shown in Figure 2-7C. On average, the elongation of the Z-oriented specimens ($53.9 \pm 13.4\%$) is 93% higher than the X-oriented specimens ($27.9 \pm 5.5\%$) in the as-fabricated condition ($p = 0.0005$), 77% higher ($63 \pm 9.7\%$ Z-oriented, $35.5 \pm 4.1\%$ X-oriented) in the HIP condition ($p < 0.0001$), and 56% higher ($62.5 \pm 14.8\%$ Z-oriented, $40 \pm 5.2\%$ X-oriented) after vacuum annealing ($p = 0.0018$). The elongation of the as-fabricated Z-oriented specimens approaches the expected values for annealed copper (Davis, 2001; Guschlbauer et al., 2020). The mechanical properties of the as-fabricated specimens in Figure 2-7 are similar to those reported by Guschlbauer, et al. (2020, 2018) for specimens at 99.5% density and 188 ppm O₂. Their reported as-fabricated samples had UTS of

231.6 MPa (X-oriented) and 177 MPa (Z-oriented), yield 149.8 MPa (X-oriented) and 78 MPa (Z-oriented), and elongation ranging from 56.2-59.3 %. The microhardness data in Figure 2-7D show a similar trend to the yield data. The mean data and confidence interval values do not exhibit strong separation between sample treatment or harvest orientations, where all mean values exceed 50 HV reported for annealed copper (Davis, 2001). The hardness data are also similar to two reported hardness values of pure copper processed by EB-PBF. The hardness in this study is greater than that of Guschlbauer, et al. (2018) reported at 57.3 to 57.8 (HV0.05), whereas higher hardness reported by Ramirez, et al. (2011) at 88 (HV0.1) is possibly due to high oxygen content powder used in their study.

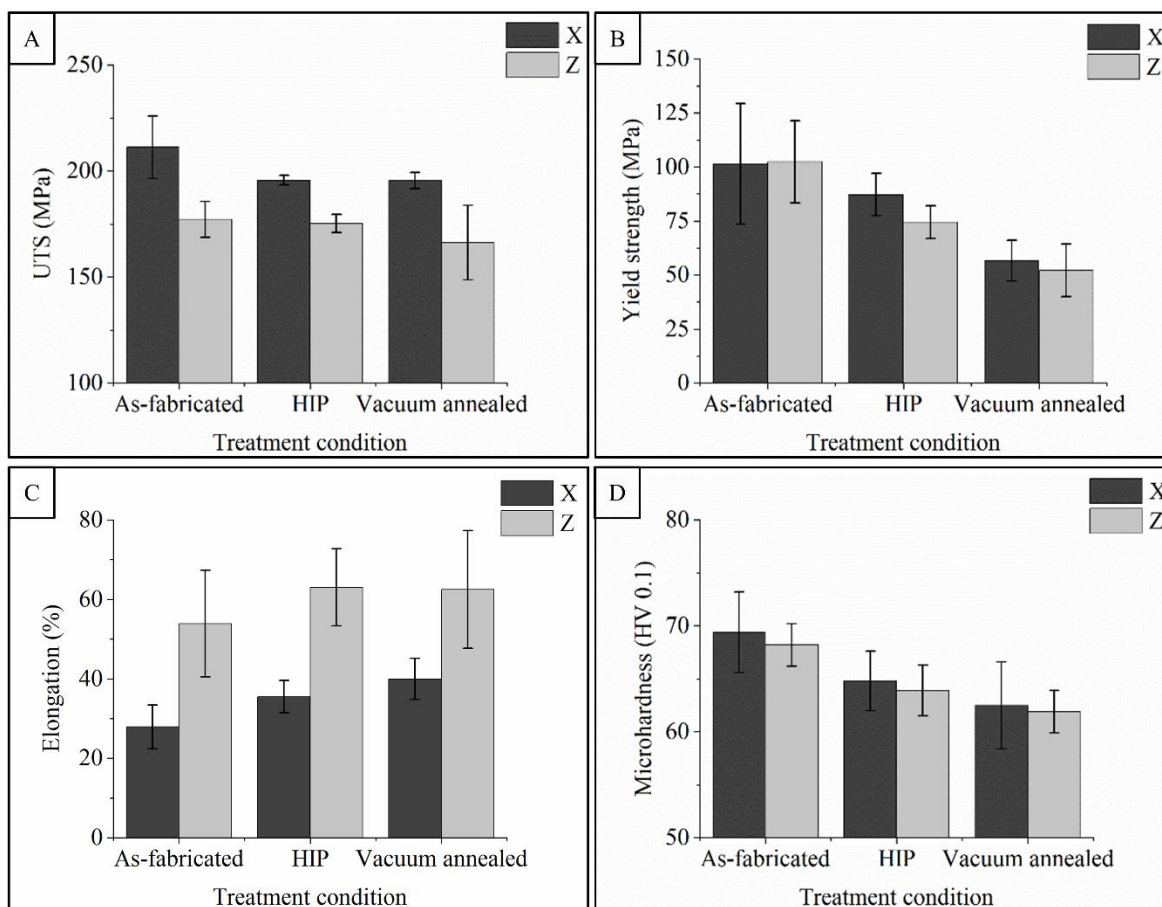


Figure 2-7. Mechanical properties summary and selected statistical observations; Ultimate tensile strength (A), Yield strength (B), Elongation to failure (C), Vickers microhardness (D). Error bars indicate a 95% confidence interval based on the pooled variance of all samples.

From Figure 2-7, it is seen that the build direction of the specimen significantly influences the mechanical properties because of the epitaxial columnar grain structure formed along the build direction. AM parts develop such wiggling columnar microstructure along the build direction because of the periodically changing direction of the scanning beam and resultant heat flow gradients within the melt pool of adjacent layers, as noted by several authors (DebRoy et al., 2018; Rafi et al., 2013). Based on the build orientation of the specimen, this columnar microstructure is differently loaded along their grain boundaries. In case of vertical specimens, pulled parallel to build direction, the grain boundaries lie parallel to the loading direction and dislocations can move along the boundaries with less impediment effects. This leads to easier dislocation pile up and considerably larger plastic flow of the material, without considering the other stress concentration factors such as inclusion particles and lack of fusion defects, etc. In contrast, the horizontal specimens have the dislocations moving perpendicular to the grain boundaries that require more force to propagate, and hence, the higher UTS values. However, the overall plastic deformation is less than that of the vertical specimens due to shorter dislocation movement, as schematically shown in Figure 2-8.

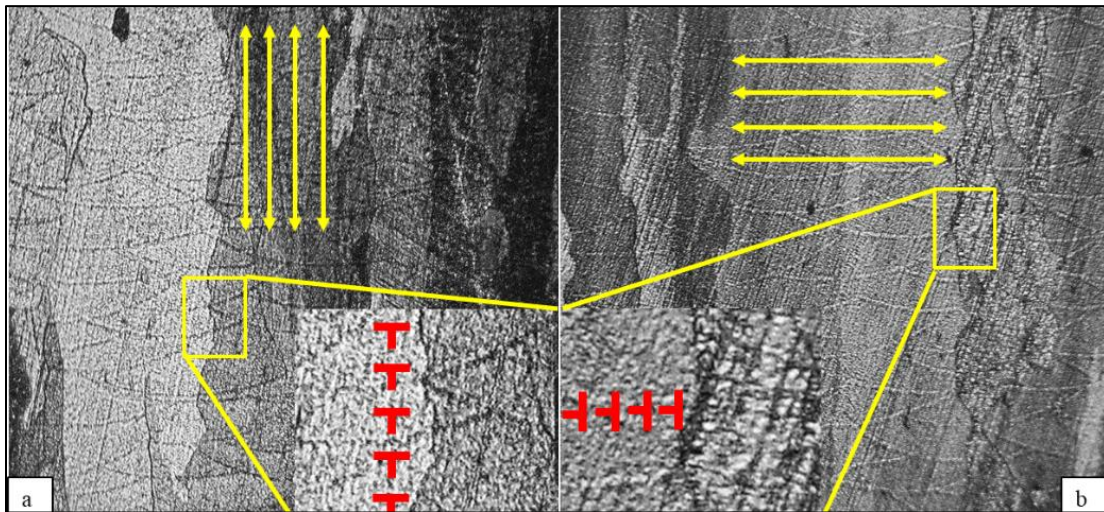


Figure 2-8. a. Z-oriented sample, b. X-oriented sample; yellow arrow shows pulling direction; dislocation pile up near GB is shown in red.

Figures 2-9 (A-F) show the etched microstructure of representative as-fabricated, vacuum annealed, and HIP specimens along the build orientation denoted by the yellow arrow. Such

epitaxial columnar grains result in a contrasting fraction of grain boundaries between the vertical and horizontal specimens, ultimately leading to the significant difference in strength and ductility observed between two orientations. Grain size measurement by linear intercept method shows a slight coarsening in grain width and length as specimens are heat treated either via vacuum annealing or HIP. The average grain widths of HIP and vacuum annealed specimens are $\sim 110 \mu\text{m}$ and $\sim 120 \mu\text{m}$, compared to $\sim 90 \mu\text{m}$ in the as-fabricated condition. However, because of grain epitaxy, length varies between $600 \mu\text{m}$ and $1000 \mu\text{m}$ among the treatment conditions. Although the temperature used in HIP and vacuum annealing is almost $0.9 \times T_m$, it has been shown in other material systems fabricated via AM methods that high temperature heat treatment do not lead to significant change in grain structure or a complete recrystallization (Molinari et al., 2010; Saeidi and Akhtar, 2018; Shamsujjoha et al., 2018).

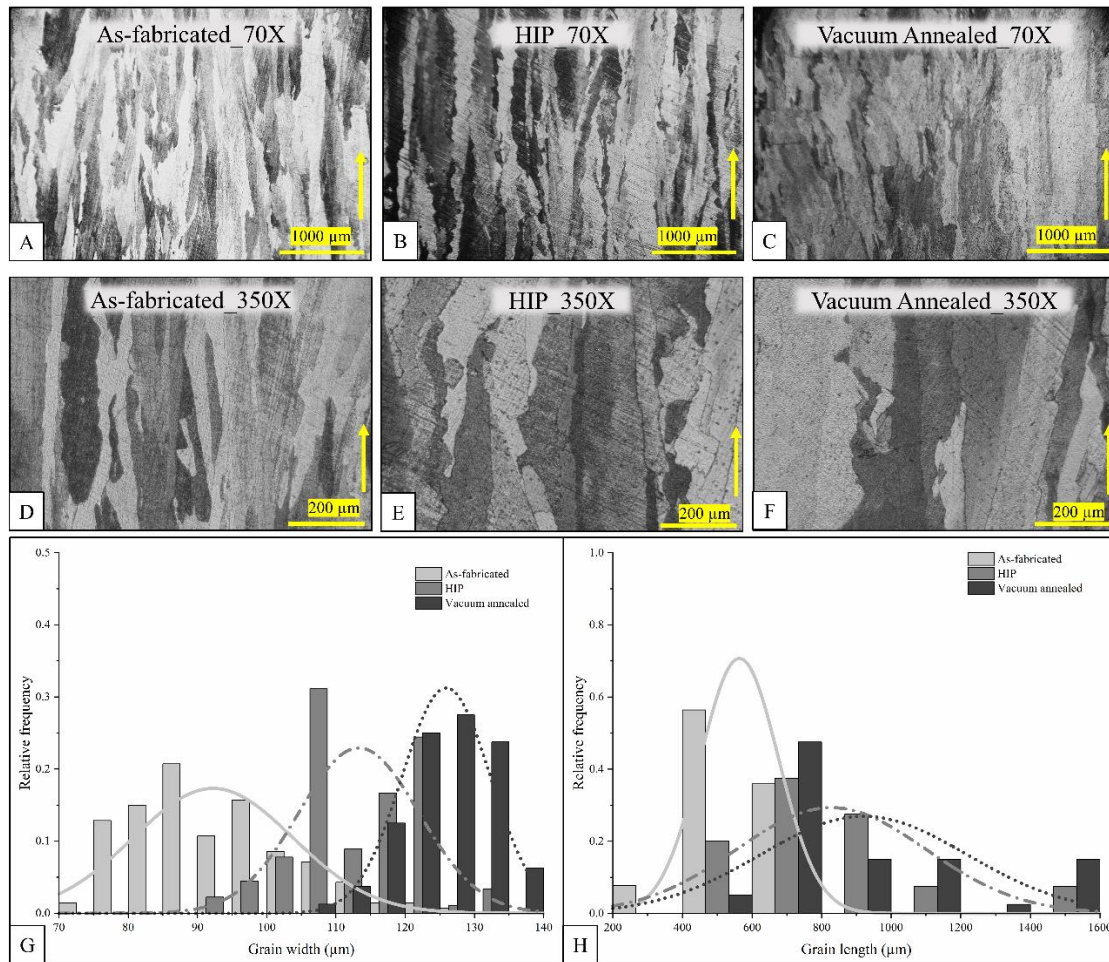


Figure 2-9. A-C. Grain morphology of representative specimens along the build direction from different post-processing conditions; D-F. Average grain width measured considering all samples for each process condition; scale bar shows 200 μm . Arrow indicates the build direction.

For metal or metal alloys which tend to form such columnar anisotropic microstructures, fabricated by processes such as drawing, rolling, forging, or additive manufacturing, it is generally accepted that the properties differ by orientation due to the anisotropy (DebRoy et al., 2018; Dieter, 1976; Guschlbauer et al., 2018; Kok et al., 2018; Lewandowski and Seifi, 2016; Mooney et al., 2019; Reed-Hill, 1973; Shamsujjoha et al., 2018; Yang et al., 2018a). Therefore, EBSD is performed on selected samples fabricated in this study to explore the influence of crystallographic texture of EB-PBF processed unalloyed copper. Figure 2-10 shows reconstructed IPF maps and pole figures, respectively, for A, D) as-fabricated, B, E) HIP and C, F) vacuum annealed samples harvested in the X direction.

The reconstructed EBSD maps in Figure 2-10 (A-C) illustrate columnar grains and a mix of crystallographic orientations. The pole figures for (100), (110) and (111) planes in the as-fabricated X-oriented specimen shows no strong texture at (100) projection in Figure 2-10D, which is often reported in AM fabricated specimens, regardless of the material system or fabrication process (DebRoy et al., 2018; Guschlbauer et al., 2020). The (110) and (111) pole figures also show no strong texture in the as-fabricated specimens. Guschlbauer et al. showed similar results where an IPF and orientation map with orientation distribution function figures for (100), (110) and (111) showed no observable crystallographic texture (Guschlbauer et al., 2020). Figure 2-10E shows pole figures for the HIP condition revealing an amount of imperfect texture in the $\langle 111 \rangle$ and $\langle 110 \rangle$ directions for the (100) projection and $[1\bar{1}0]$ texture in the (110) projection, however no heavily textured patterns were observed. The pole figures in Figure 2-10F for the vacuum annealed condition reveal virtually no observable texture except for the $\langle 010 \rangle$ direction detected in the (100) projection. The yellow and red (6-8) MUD spots in Figure 2-10 (E-F) are most likely large grains or localized clusters of sporadic measured planes and considered not representative of the entire fabricated specimens.

Most of the literature reported on mechanical properties of PBF and directed energy deposition (DED) are in a narrow material space, often focusing on commercially available alloys such as Ti-6Al-4V, IN718, 304 SS, 316L SS, Co-28Cr-6Mo, among others (DebRoy et al., 2018; Lewandowski and Seifi, 2016). In pure metals and alloys produced by AM, many other factors influence strength and ductility in specimens exhibiting columnar grains and crystallographic anisotropy, which complicate the interpretation of properties results. Reports across a number of alloy systems and AM processes report no clear trends in mechanical properties with test orientation and post-treatments where factors such as porosity, layer-induced defects, residual stress, oxidation, precipitation or allotropic phase changes, localized cracking, among others, can have a significant impact on test results (Barkia et al., 2020; DebRoy et al., 2018; Kok et al., 2018; Lewandowski and Seifi, 2016; Mooney et al., 2019; Thijs et al., 2013; Wang et al., 2016).

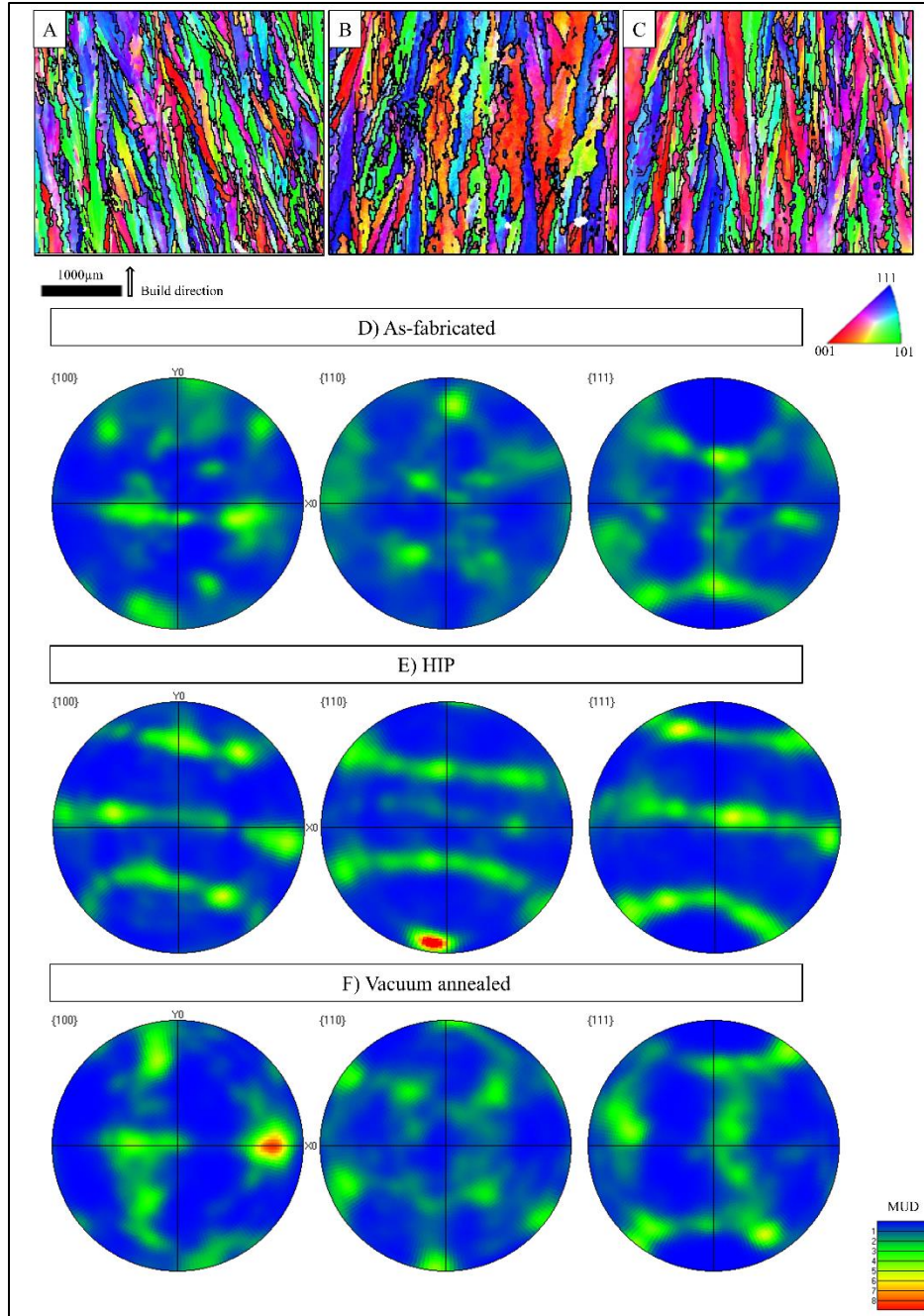


Figure 2-10. Inverse pole figure maps of as-fabricated, HIP, and vacuum annealed specimens along the build direction shown with an arrow alongside the scale bar (A-C); pole figures of as-fabricated, HIP, and vacuum annealed specimens (D-F), respectively. The scale bar is multiple uniform distributions for the pole figures ranging from 1 – 9.

Since our study used unalloyed copper and samples are fabricated to high densities at temperatures exceeding 300°C, some of the effects often reported in PBF and DED studies such as frequent layer defects, residual stress, precipitation, and micro-cracking become less influential. While no cube or strong crystallographic texture is measured by EBSD in any of the X-orientation samples, columnar grains were clearly observed and may explain the differences in our mechanical properties, especially elongation and UTS. In a strain and defect-free pure metal system, dislocation motion in the direction of long, thin grains would have more unobstructed movement in comparison with deformation across narrow grains, experiencing frequent grain boundaries. Therefore, the tensile samples harvested from the blocks in the build direction had significantly higher elongation as compared with the specimens harvested perpendicular to the build direction where fewer grain boundaries and oxides were present to impede deformation. The samples harvested in the X direction had consistently higher UTS compared with those in the Z direction due to significantly more interactions with grain boundaries and oxides during deformation, regardless of treatment. The yield is observed to be influenced by treatment conditions regardless of orientation and most likely is the result of any remaining residual stress which may resist initial deformation. These residual stresses, caused by the numerous thermo-mechanical cycles during the fabrication process, affect the bulk yield strength on a macro-scale where high yield strength values are reported for AM-processed materials with high internal residual stresses (Lewandowski and Seifi, 2016). Heating close to $0.9 \times T_m$ as used in this study for HIP and vacuum-annealed samples and led to residual stress relief, thus resulting in lower yield strength and microhardness values, as shown in Figure 2-7B,D.

Fracture surfaces are observed with SEM to explore the ductile fracture. Figure 2-11 shows representative examples of fracture surfaces for tensile specimens from each post-process condition for both harvesting orientations. The fractography indicates a transgranular fracture mode, forming the ductile dimples distinctive of soft materials like copper. In the case of the as-fabricated specimens, a shear zone at the outer edge is seen, followed by a ductile area in the middle of the sample. The ductile dimples are the manifestation of micro-void nucleation and their coalescence event, while the large size voids are the result of nucleated cavities or process-induced porosities (Ghahremaninezhad and Ravi-Chandar, 2011). Further, the number and distribution of shallow dimples are varied with respect to the orientation of the specimens as observed especially in vacuum annealed and HIP specimens. X-oriented samples show finer dimples more closely

spaced than the Z-oriented specimens where plastic strain is higher, most likely due to the increased length of dislocation mean free path. However, the fractographs of the HIP specimens are markedly different from the as-fabricated conditions due to the presence of micron-scale oxides within many ductile dimples. This is notable because there was no difference in the measured oxygen content between the as-fabricated and HIP specimens, and it suggests that the high temperatures during HIP likely facilitated the mobility of oxygen and a subsequent growth of grain boundary Cu_2O particles. These large scale oxides appear on the dimples due to the stress concentration and dislocation movement around them during the deformation process, similar to what is previously illustrated in as-fabricated EB-PBF copper by Guschlbauer, et al. (2020) and sintered cold-sprayed AM copper by Hutasoit, et al. (2020). However, no feature of brittle failure such as cleavage facets is found in any type of specimen, suggesting that the incoherent copper oxides do not embrittle the copper parts at the concentration levels measured in the specimens. The vacuum annealed samples also exhibited large scale oxides compared to the as-fabricated specimens. However, these tended to be fewer and more widely dispersed along the grain boundaries than the oxides observed in the HIP samples. This is primarily attributed to the dissociation of oxide and low oxygen concentration measured after vacuum annealing.

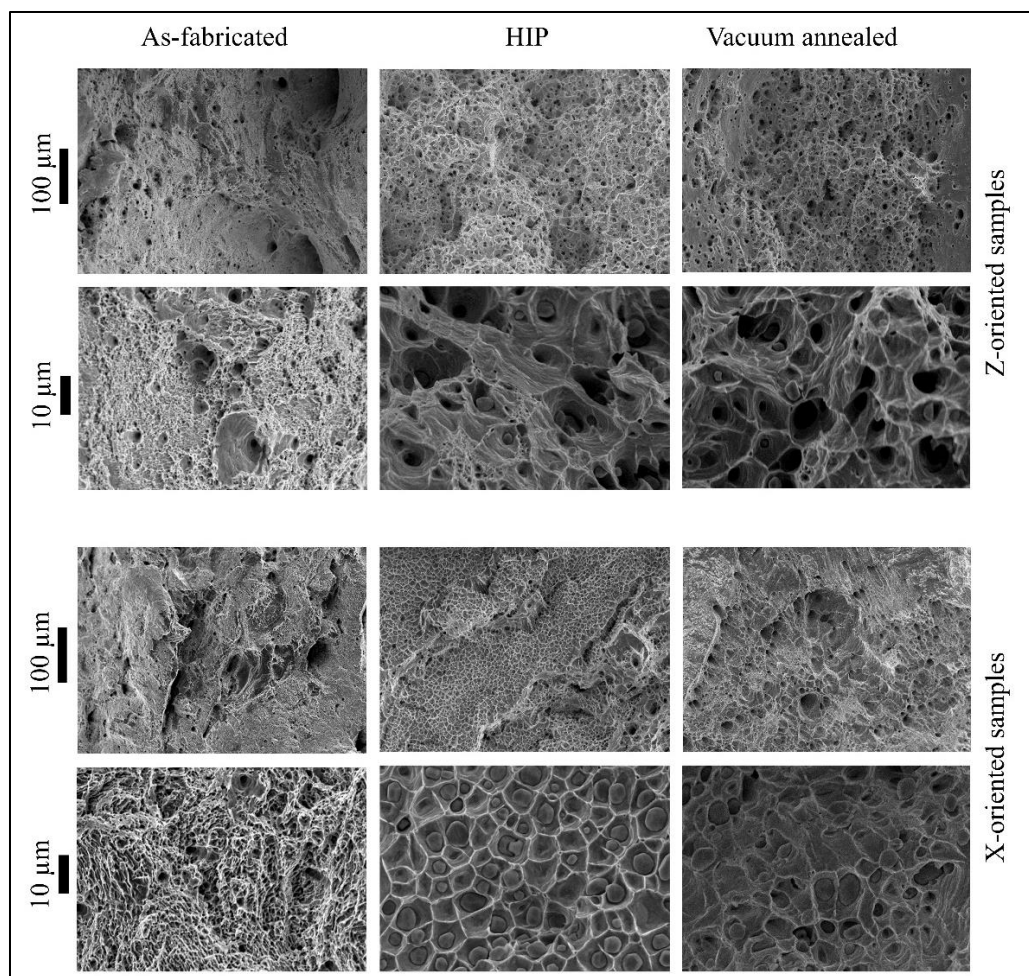


Figure 2-11. Fractographs of tensile specimens; top two rows: Z-oriented specimens (as-fabricated, HIP, and vacuum annealed); bottom two rows: X-oriented specimens (as-fabricated, HIP, and vacuum annealed); Scale bar is linked with respective rows.

In order to confirm that the oxides are native within the material, and not a result of mal-handling after the tensile test, grip sections of representative specimens from each different post-process condition are ion milled and analyzed in the VPSEM as mentioned in §2.4.5. Figure 2-12 demonstrates the EDS maps of all processing conditions where the vacuum annealed, and HIP specimens show the presence of micron-scale copper oxides. However, under similar length scales, the as-fabricated specimen does not reveal any second phase oxides as their size is beyond the sensitivity limit of the EDS detector of the VPSEM instrument. This effect is manifested in the fractographs presented in Figure 2-11 that shows large oxide population for HIP and vacuum

annealed sample, and none for the as-fabricated sample under same magnification level used in the SEM observations.

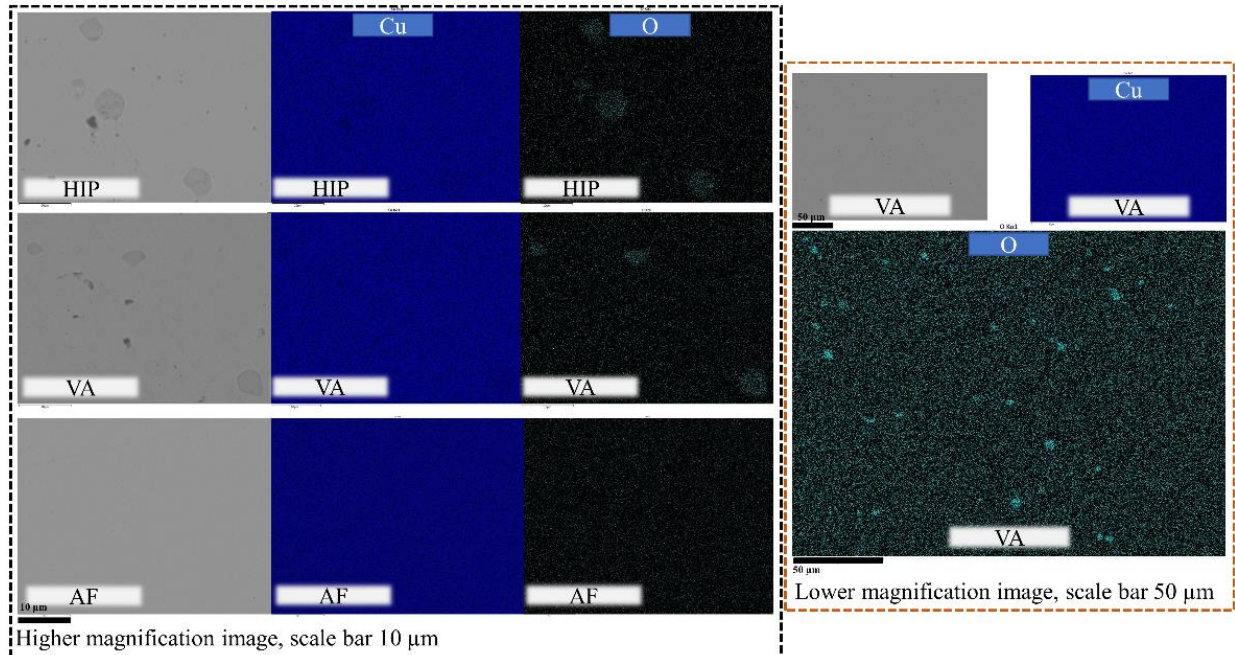


Figure 2-12. EDS maps of representative specimens from all processing conditions. Lower magnification EDS map of the vacuum annealed specimen is shown in the right to illustrate the spatial distribution of the oxides. Scale is shown in black bars.

The STEM EDS maps in Figure 2-13 (A-B) illustrate that the oxides are mostly at nano scales (50-200 nm) formed at the grain boundaries in the as-fabricated sample, whereas in Figure 2-13 (C-D), the oxide particles from the HIP specimen exhibit much larger size scales (2-4 μm). This asserts the coalescence of nano-scale oxides as a result of heat treatment which, in turn, increases the inter-particle spacing between these second phase oxides. As per the recent work of Lu, et al. (2021) on copper alloy processed by EB-PBF, the strengthening effect of second phase precipitates can be modeled using their size scale and inter-precipitate distances, assuming a spherical precipitate morphology. According to this relationship, samples with dense distribution of small-scale oxides will have more strengthening effect than the ones with large-scale and sparsely distributed oxides. Also, this increased spacing between the oxides in HIP and vacuum annealed samples promotes the void sheet formation with increased void spacing, and favor higher

ductility compared to the as-fabricated condition which has oxides at smaller nano-scale sizes with lower inter-particle spacing (Liu et al., 2004).

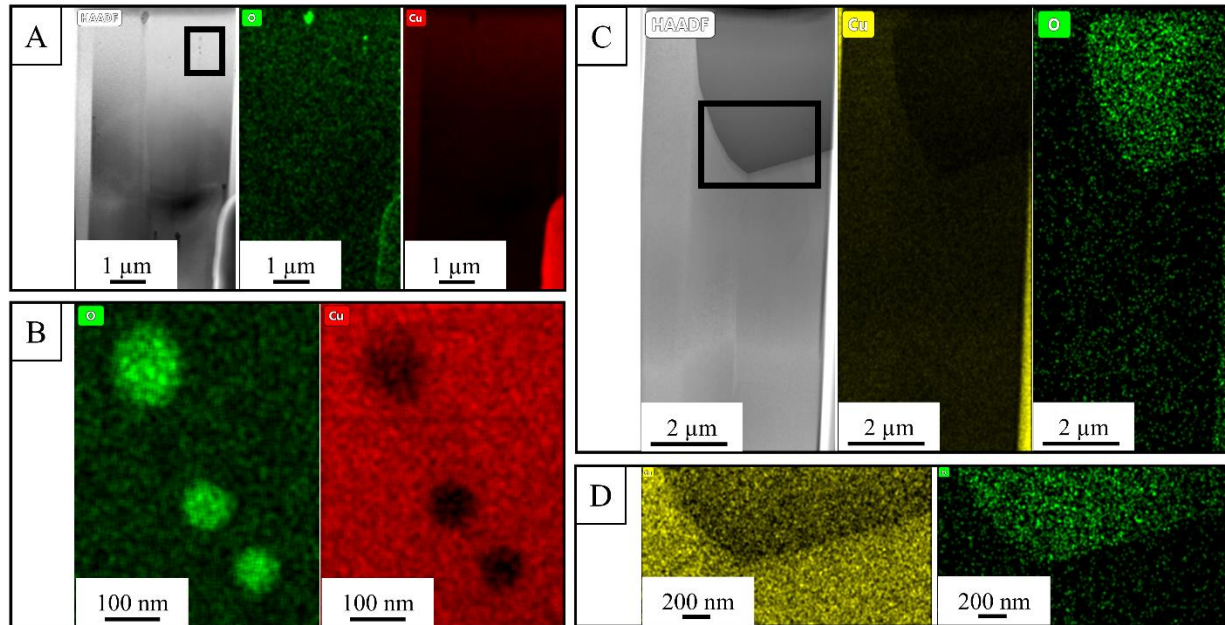


Figure 2-13. STEM EDS maps of representative as-fabricated and HIP specimens illustrating the spatial distribution and size differences of copper oxide inclusions at the grain boundaries. Note the different length scales.

2.6 Conclusions

In this study, the effects of different post-processing conditions on the mechanical properties of EB-PBF fabricated unalloyed copper are characterized and discussed. Rectangular blocks are fabricated with automatic control settings from ~99.95% pure copper powder with a size distribution of 22-63 μm . Tensile specimens are extracted from these rectangular blocks with two different orientations and treated with HIP and vacuum annealing alongside the as-fabricated condition. The following conclusions summarize the major findings of this study:

1. Mechanical properties of the as-fabricated specimens are observed to be similar to unalloyed annealed copper. X-oriented specimens have higher strength values across post-processes than the Z-oriented samples with an average UTS of 211 MPa.

Maximum elongation to failure is recorded for Z-oriented vacuum annealed and HIP specimen that showed average values of ~63%.

2. With the density values reaching close to the theoretical density, the observed differences in UTS and elongation are proposed to be controlled by orientation anisotropy and interdependencies between the grain morphology and dislocation movement. Difference in yield strength is more pronounced between treatment conditions than the specimen orientation and is assumed to be affected by the differences in residual stress as a function of treatment conditions.
3. Density of the specimens increases slightly after the HIP treatment with an associated increase in ductility and decrease in strength. As expected, the vacuum annealing process reduces the oxygen content within the specimen, also resulting in the lowest strength among all treatment conditions.
4. The EBSD maps show no apparent texture in the as-fabricated specimens, and a slight amount of texture in HIP and vacuum annealed specimens. However, the effect of such texture in the mechanical properties is outweighed by morphological anisotropy due to the epitaxial columnar microstructure formed during the fabrication process.
5. While all treatment conditions show a ductile failure mode irrespective of the sample harvesting direction, HIP and vacuum annealed specimens are noticeably different due to the presence of large micron-scale oxide particles within the dimples. It is suggested that the high temperature used in these post-processes promoted the coalescence and growth of grain boundary oxides which are mostly in the nano-scale size in as-fabricated condition. This bigger oxide size led to larger inter-particle distances and resulted in increased void spacing that, in turn, increased ductility in HIP and vacuum annealed condition.

2.7 Motivation for further research

Mechanical property test results demonstrate that the overall strength values are still lower than the conventionally produced and L-PBF processed copper parts while the average elongation to failure is considerably higher. This is primarily due to the processing condition in an EB-PBF system where solidified material stays at an elevated surface temperature for a long duration, which

favors grain coarsening leading to increased grain sizes. A comparison with the mechanical properties of other AM literature of pure copper shown in Figure 2-14 reveals that the grain sizes in this study is considerably higher than the other studies, leading to a lower strength for similar bulk densities.

Nevertheless, this similar effect of grain size on mechanical properties of conventionally produced pure copper has long been reported by several authors in room temperature and elevated temperature tensile tests. Copper parts produced by cold rolling, extrusion or equal channel angular processing tend to have fine or ultra-fine grains that lead to superior strength of the material (Carreker and Hibbard, 1953; Higuera and Cabrera, 2013; Hyun et al., 2001; Jenkins et al., 1957; Kommel et al., 2007; Lassila et al., 1994; Meyers et al., 1995; Sanders et al., 1997; You and Lu, 2015). Annealing of such cold worked copper increases the grain size multifold of the precursor grains and leads to a reduction of strength associated with an improvement in ductility. It is, therefore, apparent that if the grain size in AM fabricated copper can be reduced by refining the microstructure within the process itself, leveraged design complexity of AM parts can still be realized without losing its mechanical strengths. With the goal to investigate the feasibility of grain refinement in copper in EB-PBF system, the next chapters describe the state-of-the-art and the methodologies adopted for this specific material.

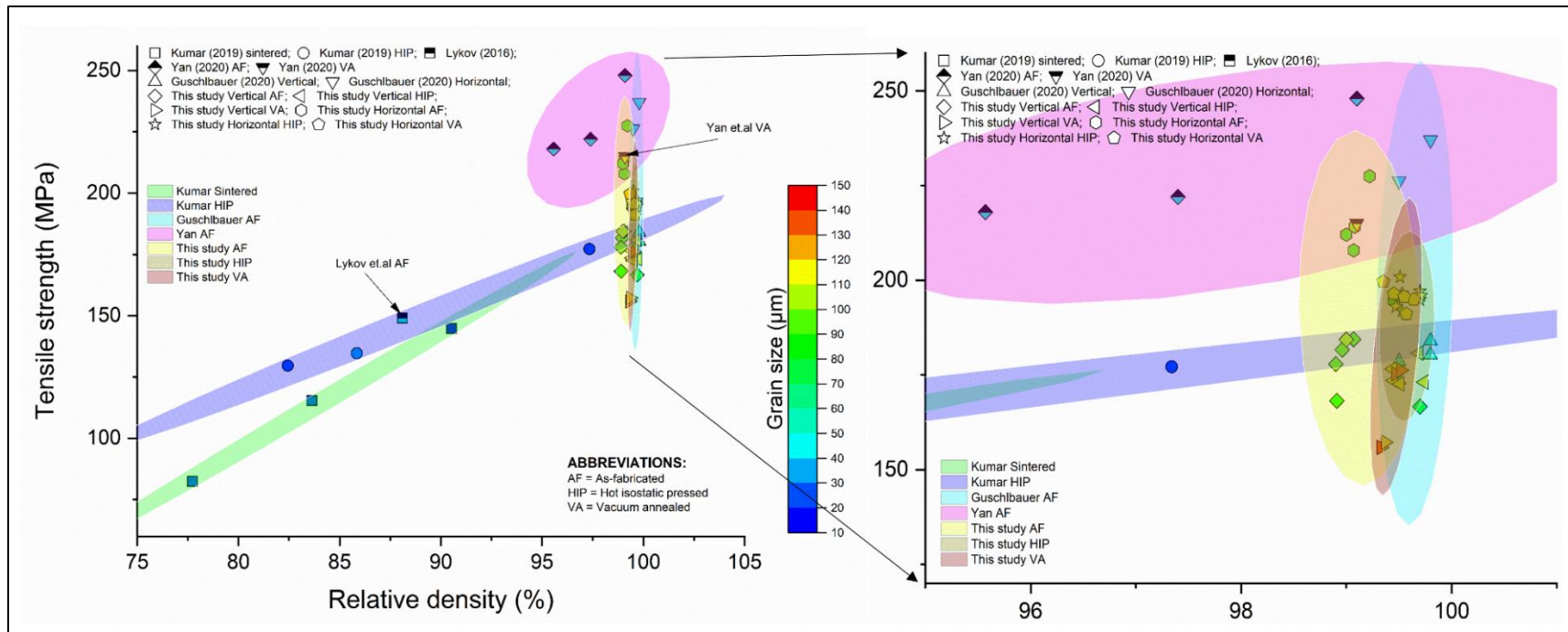


Figure 2-14. Comparison of mechanical properties measured in this study and reported in the AM literature of pure copper.

3 Grain refinement and Columnar-to-Equiaxed Transition of EB-PBF fabricated copper by modifying process parameters

3.1 Introduction

Although the use of grain refinement techniques is common in casting of copper alloys, it is not investigated in the additive manufacturing of pure copper, which in general, results in long columnar grains along the build direction leading to anisotropic properties, as discussed in the previous chapter. As per the literature review of grain refinement of other materials in AM, thermal gradients and the cooling rate are the most critical factors during a solidification process, and these can be altered by modifying the process parameters. Usually, numerical thermophysical models are used to first obtain the thermal gradient and cooling rate specific to a process condition, and are checked with the columnar-to-equiaxed transition (CET) map of the respective materials to predict the grain structure on a macro-scale. However, due to the unavailability of a CET map for copper in the literature, a CET map based on Cu-O system is developed in this chapter since oxygen is the second most abundant element found in the chemical analysis of the feedstock powder. A numerical thermal model is utilized to simulate different process parameter sets reported in the literature to evaluate respective thermal gradients and cooling rates, which are then plotted on the CET map to validate the model assumptions by comparing theoretically predicted and experimentally obtained microstructures. Experiments are conducted to validate the usability of the CET map and the overall approach. The obtained results suggest that a columnar to equiaxed transition is difficult to achieve in EB-PBF processing of pure copper. Microstructural analyses reveal interdependencies among thermal gradient, cooling rate, input energy density, direction of thermal gradient etc. that influence the grain orientations, and subsequently, the grain selection process. However, utilizing the proposed CET map and the numerical thermal model enables a user to predict the obtainable grain structure with sufficient accuracy in the EB-PBF processing of pure copper.

3.2 Literature Review

Grain refinement and CET in AM by modifying process parameter has been reported for IN718 and Ti-6Al-4V alloys by several authors. Raghavan, et al. (2017, 2016) investigated the possibility of site-specific control of microstructure in IN718 by utilizing spot melting strategies in EB-PBF process and observed that columnar grains form at the melt pool bottom at the onset of solidification due to the high thermal gradient and low cooling rate. However, the top surface showed equiaxed grains as the cooling rate increased and the thermal gradient decreased as a result of melt pool shrinkage. It was seen that high melt current, high preheat, and longer beam on time led to the conditions favorable of equiaxed grain formation. Another numerical study by Promoppatum, et al. (2017) on IN718 in the laser-PBF process showed that high melt currents lead to a low thermal gradient because of the larger melt pool size which resulted in less steeper distribution of heat. These aspects of the numerical study were further refined by Liu, et al. (2019, 2018) by taking heterogeneous nucleation, grain selection mechanism, total undercooling, and solute distribution under consideration in a multi-scale phase field model. It was shown that the reason for columnar grains at melt pool bottom or equiaxed grain at melt pool surface could be correlated with the undercooling at respective zones that control the extent of heterogeneous nucleation. The authors confirmed that high scanning speed and high preheat temperature for both spot melting and raster scanning strategies led to increased growth velocities pushing the microstructure more toward the equiaxed zone in the CET map. Helmer, et al. (2016) studied the similar material system in an EB-PBF system for different scan velocity and line offset, and observed that a combination of low line offset and high scan velocity in a raster melt strategy led to greater fraction of equiaxed grains. The equiaxed grain formation was assumed to be caused by the change in the thermal gradient directions between each consecutive layer because of the 90° rotating scan strategy that suppressed the epitaxial grain formation.

For the Titanium alloy systems, Bontha, et al. (2009, 2006) simulated laser engineered net shaping (LENS) using an analytical model originally proposed by Rosenthal, (1946) and a numerical finite element model to examine the effects of melt currents and scan velocities. It was reported that while the thermal gradient decreased with higher melt current, cooling rate decreased too. This competing behavior ultimately resulted in lower solidification velocities at the top surface where big equiaxed grains formed, contrary to the fine equiaxed grains observed in IN718. This led the authors to conclude that CET becomes easier with a higher heat input, although grain

coarsening can take place because of lowering cooling rate. Gockel, et al. (2014) studied the same alloy with a different approach to combine the CET map along with a beam power-beam velocity correlation map, so that computationally extensive numerical simulations could be avoided, and real-time control of microstructure could be achieved by changing beam power or beam velocity. Their experimental study showed that equiaxed grains formed at either high power-low velocity condition, or at low-to-medium power-high velocity condition. However, the technique depended largely on maintaining a constant size melt pool based on beam power and beam velocity modifications, and the approach did not explain the underlying mechanism for equiaxed grain formation.

Several others have examined the effect of processing conditions on grain morphology evolution for different material systems in different AM processes. For example, Q Zhang, et al. (2016) and Q. Zhang, et al. (2016) examined the effect of energy densities on grain evolution in a variant of titanium alloy (Ti-6Al-2Zr-2Sn-3Mo-1.5Cr-2Nb) wherein they found that equiaxed grains formed near the substrate region because of their crystallographic orientation being favorable to a few thermal gradient directions in the melt pool. In another study of titanium alloy processed by laser melting deposition, Wang, et al. (2015) observed that the deposition rate of raw material feedstock significantly impacted the grain morphology if all other process parameters were kept constant. For large deposition rates, more equiaxed grain fraction was achieved owing to enhanced heterogenous nucleation and reduced depth of re-melting penetration. This similar effect of higher feeding rate was observed by several others in a PBF system where increased layer thickness is likely to produce a higher fraction of equiaxed grains, primarily due to the presence of a greater number of un-melted particles which can act as nucleation sites (Birmingham et al., 2020; Gäumann et al., 2001). Summary of some of these studies is presented below in Table 3-1 with reference to the examined process parameter and resulting grain structures to obtain an overall understanding of state-of-the-art of grain refinement in AM by modifying only the process-related parameters.

3.3 Research Motivation

The literature review shows that a combination of a CET solidification map and numerical thermal model can reduce the costly experimental observation by predicting the grain structure for

a given set of process parameters. Yet, to the best of our knowledge, no CET map exists for copper alloys for the elements present in the feedstock powder used in the EB-PBF process. Therefore, in this research, a CET model is developed for Cu-O system because of two reasons: (1) oxygen is the second most abundant element in the powder by weight per cent, (2) cuprous oxide is the only second phase that has significant influences on the properties of the fabricated components. Once the CET model is developed and validated, a numerical thermal model is used to calculate thermal gradient and cooling rate for given process parameter sets, where selected process parameters can be modified like the ones presented in Table 3-1. In this way, while an explanation for a specific microstructure under a given parameter set can be proposed, grain evolution can also be engineered when fabricating pure copper in an EB-PBF process by changing selected variables as required.

Table 3-1. Summary of grain refinement studies in AM by changing process parameters.

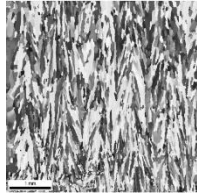
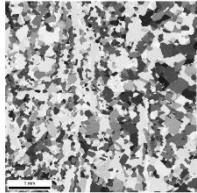
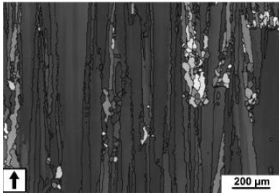
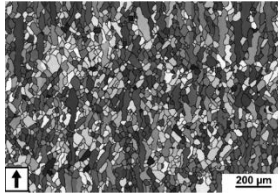
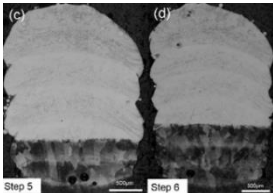
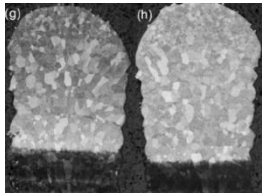
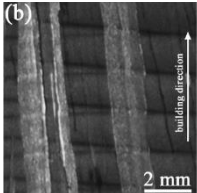
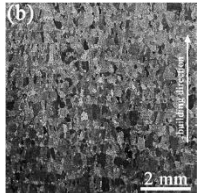
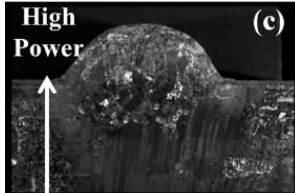
Material System	Investigated build Parameters	Control Grain	Parameter	Examined Parameter Grain	Reference
Nickel alloy: IN718	Beam on time, melt current, preheat temperature				(Raghavan et al., 2016)
Nickel alloy: IN718	Scan velocity, line offset, scan strategy, energy density				(Helmer et al., 2016)
Titanium alloy: Ti-6Al-2Zr-2Sn-3Mo-1.5Cr-2Nb	Beam power, scan velocity, powder feed rate, energy density				(Q. Zhang et al., 2016)
Titanium alloy: Ti-6.5Al-3.5Mo-1.5Zr-0.3Si	Feedstock deposition rate at constant beam power and scan velocity				(Wang et al., 2015)
Titanium alloy: Ti-6Al-4V	Beam power, scan velocity, melt pool dimension				(Gockel et al., 2014)

Table 3-2. Nomenclature of symbols used in the CET model and their values.

Symbols + Meaning (units)	Values
G = Thermal gradient (K/m)	Response
G_c = Concentration gradient (wt.%/m)	Response
V = Interface growth velocity (m/s)	$10^{-5} - 0.15$
V_0 = Velocity of sound in the alloy matrix (m/s)	4600
N_0 = Initial nucleant density (/m ³)	10^{16}
ΔT_N = Nucleation undercooling (K)	0.75
D = Diffusivity (m ² /s)	$1.14 \times 10^{-6} e^{(62500/R_c \times T)}$
C_0 = Initial concentration (wt.%)	0.01
Γ = Gibbs-Thomson parameter	10^{-7}
k_0 = Initial partition coefficient	0.0174
m_0 = Initial liquidus slope	-41.86
a_0 = Characteristic length scale for solute trapping (m)	4.27×10^{-10}
k_v = Velocity dependent partition coefficient	Response
m_v = Velocity dependent liquidus slope	Response
P = Solutal Péclet number	Response
n = Alloy constant	2
C_l = Composition of the liquid at the dendrite tip (wt.%)	Response
ΔT_c = Constitutional undercooling (K)	Response
ΔT_r = Curvature undercooling (K)	Response
ΔT_k = Kinetic undercooling (K)	Response
ΔT_t = Thermal undercooling (K)	Response
a = Thermal diffusivity (m ² /s)	1.11×10^{-4}
R = Dendrite tip radius (m)	Response
P_t = Thermal Péclet number	Response
$Iv(P)$ = Ivantsov function Péclet number	Response
$E1(P)$ = Exponential integral of Péclet number	Response
μ = Linear interface kinetic coefficient	Response
ΔH = Latent heat of fusion (J/kg)	206×10^3
c_p = Specific heat (J/kg K)	385
ΔT = Total tip undercooling (K)	Response
ϕ = Equiaxed grain fraction	0.49
R_c = Universal gas constant (J/mol-K)	8.314
T_m = Melting Temperature	Phase diagram

3.4 Materials and Methods

3.4.1 Development of Columnar-to-Equiaxed Transition (CET) model

The powder feedstock used in the process comprises of pure copper along with some cuprous oxides as the only other principal element having substantial weight per cent (mostly <0.1 wt.%), as shown in the previous chapter. A CET model based on Cu-O system seem scientifically valid since that will most closely capture the melt pool chemistry during its fabrication by the EB-PBF process. What follows next is a step-by-step development of this CET model combining the concepts put forward by several authors, pioneered by Hunt (1984). The nomenclature of the used variables is presented in Table 3-2.

It was pointed out by Hunt (1984) in his work on steady state solidification mechanism that pure metals usually solidify with a columnar structure while adding alloying elements promote growth of equiaxed grains. In his work, Hunt proposed both analytical and numerical solidification models to define the solidification mechanism for growth of equiaxed grains ahead of columnar fronts formed by heterogeneous nucleation. As the nucleation rate I is dependent on the critical Gibbs free energy ΔG_c , which in turn, is related to the undercooling as $\frac{1}{(\Delta T)^2}$, enhanced local undercooling creates greater possibility of forming the equiaxed grains (see Equation 1).

$$I = (N_0 - N)I_0 \exp\left(-\frac{\Delta G_c}{k_B T}\right) \dots eqn(1)$$

Here N_0 is total number of heterogeneous substrate particles originally available per unit volume, N is already nucleated particle number, k_B is Boltzmann constant, and value of I_0 is assumed 10^{20} , a constant for the considered system. During the growth phase, dendrite tip undercooling is dependent on growth velocity V , temperature gradient G , and alloy composition C_0 . However, the $\frac{GD}{V}$ term in Equation 2 is significant if the gradient is very high and velocity is too low; otherwise, it can be neglected (Equation 3) where V_e is the equiaxed interface velocity.

$$\Delta T = \frac{GD}{V} + A'(C_0 V)^{\frac{1}{2}} \dots eqn(2)$$

$$\Delta T = \left(\frac{C_0 V_e}{A}\right)^{\frac{1}{2}} \dots eqn(3)$$

Equiaxed grains grow within the melt at a velocity dependent on the local temperature and their growth will be stopped when the newly formed grains impinge on one another, or a columnar

front pass through them. Under steady state conditions, defined as an unchanged number and size of equiaxed grains in a considerably large area for each temperature point with time as an overlaying constraint, fully equiaxed grains will grow when volume fraction (ϕ) of such will be greater than 0.49, or the extended volume fraction ϕ_E becomes greater than 0.66. In his analytical model of solidification, Hunt (1984) assumed that all nucleation sites operated at the same time as the nucleation temperature was reached, and the evolved heat during grain growth did not change the temperature gradient. Although in his numerical model he did not impose these assumptions, both models showed very similar results. Under the said assumptions, fully equiaxed growth can take place when the extended volume fraction ϕ_E expressed as

$$\phi_E = \frac{4\pi r^3 N_0}{3} > 0.66 \dots eqn(4)$$

is satisfied at the columnar growth front undercooling temperature ΔT_c defined by Equation 3. It is noted that Hunt considered only the effect of constitutional undercooling for nucleation phenomenon, and under this condition, Hunt proposed a solidification criterion for fully equiaxed grain growth as given in Equation 5, which occurs more easily as the value of the quantity $-m(1 - k_0)C_0$, known as growth restriction factor, becomes larger.

$$G < 0.617N_0^{\frac{1}{3}} \left\{ 1 - \left(\frac{\Delta T_N}{\Delta T_c} \right)^3 \right\} \Delta T_c \dots eqn(5)$$

Application of this Hunt criterion shows that as the nucleation undercooling is decreased, for lower thermal gradient, more equiaxed grains can form at a given growth velocity. Also, for an increased number of nucleation sites, CET predicts a higher probability of equiaxed grains for a given thermal gradient and growth velocity. Cantor and O'Reilly (2003, p. 201) supported Hunt's CET model observing that nucleation of new grains started at the constitutionally undercooled region ahead of solidification front, and a decrease in thermal gradient and/or increase in solidification velocity extended the undercooled region and favored the equiaxed grain formation.

However, during a CET solidification scenario, cellular grains do not contribute to the development of a constitutionally undercooled zone and can never result in a CET unless there is external perturbation. Therefore only the columnar dendrite is modeled as the principal driving force that creates an undercooled liquid zone ahead of dendritic front due to its diffusion field and leads to nucleation of equiaxed grains at those sites (Kurz et al., 2001). Modeling of this columnar dendritic growth was done in the Ivantsov-Mullins-Sekerka (IMS) dendritic growth theory which

produced values of concentration and undercooling of a single dendrite tip as per Kurz and Fisher, (1984). However, an elementary model was prescribed by Kurz, et al. (2001) that could be applied to small driving forces and small growth undercooling in casting conditions, and is shown below in Equation 6, where K is an alloy constant and V is growth velocity.

$$\Delta T = K^{\frac{1}{2}} V^{\frac{1}{2}} \dots \text{eqn}(6)$$

However, nucleation and growth depend upon the limit of stability where grain morphologies shift from planar to cellular to dendritic as the growth velocity increases, and then fall back to planar beyond the absolute limit of stability. The Langer and Müller-Krumbhaar (L-M) stability criterion was modified by Kurz and Fisher (1981) to obtain relationships between growth velocity, dendrite tip radius, and thermal gradient for casting conditions (Equation 7).

$$V = \frac{2D(GR^2 + 4\pi^2\Gamma)}{(1 - k_0)(R^3G - 2R^2C_0m_0 + 4\pi^2\Gamma R)} \dots \text{eqn}(7)$$

Although the situation becomes different in AM due to its high growth velocity and high thermal conditions, Kurz's proposed model can be approximated assuming constant solutal partitioning coefficient and liquidus slope. For high velocity conditions, the dendrite tip becomes small, and its power terms can then be neglected when coupled with low-value parameters. Then the above relationship is reduced to Equation 8, as given below (Kurz and Fisher, 1981).

$$V = \frac{4D\pi^2\Gamma}{(k_0 - 1)R^2C_0m_0} \dots \text{eqn}(8)$$

This primary equation proposed by Kurz and Fischer in directional solidification process was further refined by Kurz, et al. (1986) for rapid solidification processes where high growth velocities, high thermal gradient, and large undercoolings rendered the use of previous L-M stability criterion erroneous. Instead, a more involved calculation based on solutal Péclet number, and solute concentration gradient was undertaken to establish the stability criterion. Under such conditions, it was assumed by the authors that stability criterion for a spherical planar interface could be employed which led to the calculation of dendrite tip radius at the limit of stability for a given growth velocity and thermal gradient value. These are shown below in Equation 9-10.

$$R = 2\pi \left(\frac{\Gamma}{m_0 G_c \xi_c - G} \right)^{\frac{1}{2}} \dots \text{eqn}(9)$$

$$\text{where } \xi_c = 1 - \frac{2k_0}{\left\{1 + \left(\frac{2\pi}{P}\right)^2\right\}^{\frac{1}{2}} - 1 + 2k_0}; \quad P = \frac{RV}{2D}; \quad G_c = \frac{C_0}{\frac{R}{2} \frac{D}{V(1-k_0)}} \dots \text{eqn}(10)$$

Based on this new stability criterion, Kurz, et al. (1986) proposed the Kurz-Giovanola-Trivedi (KGT) model of grain morphology transition for alloy systems under rapid solidification processes considering the constitutional and curvature undercooling to be the driving forces for required undercooling of nucleation. Solving for R for a given velocity and thermal gradient predicted the transition event from one grain morphology to another, based on tip temperature and concentration profile at the solid/liquid interface (Equation 11-12).

$$\frac{\pi^2 V^2 \Gamma}{P^2 D^2} + \frac{m_0 C_0 (1 - k_0) \xi_c V}{D [1 - (1 - k_0) Iv(P)]} + G = 0 \dots eqn(11)$$

$$\text{Where } Iv(P) = P \exp(P) E1(P) \dots eqn(12)$$

Gäumann, et al. (1997) employed both the Ivantsov model and the KGT model to obtain the concentration and temperature profile, respectively, ahead of the dendrite tip at the solid/liquid interface for high velocity directional solidification processes like welding or rapid solidification. However, unlike the KGT and Hunt model, Gäumann, et al. (1997) used the velocity dependent partition coefficient and liquidus slopes instead of the constant values used in the previous studies for the stability limit criterion ahead of dendrite tip (Equations 13-15).

$$k_v = \frac{\left(k_0 + \frac{a_0 V}{D}\right)}{\left(1 + \frac{a_0 V}{D}\right)} \dots eqn(13)$$

$$m_v = m_0 \frac{\left[1 - k_v \left\{1 - \ln\left(\frac{k_v}{k_0}\right)\right\}\right]}{1 - k_0} \dots eqn(14)$$

$$C_l = \frac{C_0}{\{1 - (1 - k_v) Iv(P)\}} \dots eqn(15)$$

In this model, Gäumann, et al. (1997) introduced constitutional, curvature, and kinetic undercooling for columnar dendritic growth, whereas in the case of equiaxed dendritic growth, the authors added another thermal undercooling term depending on the thermal diffusivity of the metal alloy. However, thermal undercooling was neglected in analyzing real solidification events (Eskin, 2008; Gäumann et al., 1997) as it was compensated mostly by the thermal effect of latent heat of fusion; and high values of thermal diffusivity of metals resulted in insignificant values of thermal undercooling as the thermal Péclet number is inversely proportional to thermal diffusivities. Nevertheless, in CET models of materials used in AM, all four undercooling entities are used [e.g. (Plotkowski et al., 2017b)] and these are given below in Equation 16-17.

$$\Delta T_c = m_v(C_0 - C_l); \Delta T_r = \frac{2\Gamma}{R}; \Delta T_k = \frac{V}{\mu}; \Delta T_t = Iv(P_t) \frac{\Delta H}{c_p} \dots eqn(16)$$

$$\text{where } \mu = \frac{V_0(1-k_0)}{m_0}; P_t = \frac{VR}{2a} \dots eqn(17)$$

In effect, the total undercooling at the dendrite tip for equiaxed dendritic growth can be expressed as the following equation combining all four undercooling entities. Once this total undercooling becomes larger than nucleation undercooling, heterogenous nucleation within the melt can take place ahead of S/L interface at or below its limit of stability.

$$\Delta T = \Delta T_c + \Delta T_r + \Delta T_k + \Delta T_t \dots eqn(18)$$

Based on these solidification kinetics concepts laid out for rapid solidification processes, the CET model for Cu-O is developed numerically in MATLAB. As the value of dendrite tip radius at the S/L interface is critical for the calculation of growth velocity, Equation 19 is used to calculate R numerically using the well-known bi-section root finding method. Once the value of R becomes known for a given velocity, all other parameters and variable values are then calculated to evaluate the thermal gradient for which equiaxed grains can form (using Equation 20). The CET curve can then be obtained by evaluating G for a range of V , within the limit of stability as established earlier. The entire process of solving these governing equations are shown schematically in Figure 3-1.

$$4\pi^2\Gamma \frac{1}{R^2} + \{2m_v P(1 - k_v) C_l \xi_c\} \left(\frac{1}{R}\right) + G = 0 \dots eqn(19)$$

$$G = \frac{\Delta T}{n + 1} \left(\frac{-4\pi N_0}{3 \ln(1 - \phi)} \right)^{\frac{1}{3}} \left(1 - \frac{\Delta T_N^{n+1}}{\Delta T^{n+1}} \right) \dots eqn(20)$$

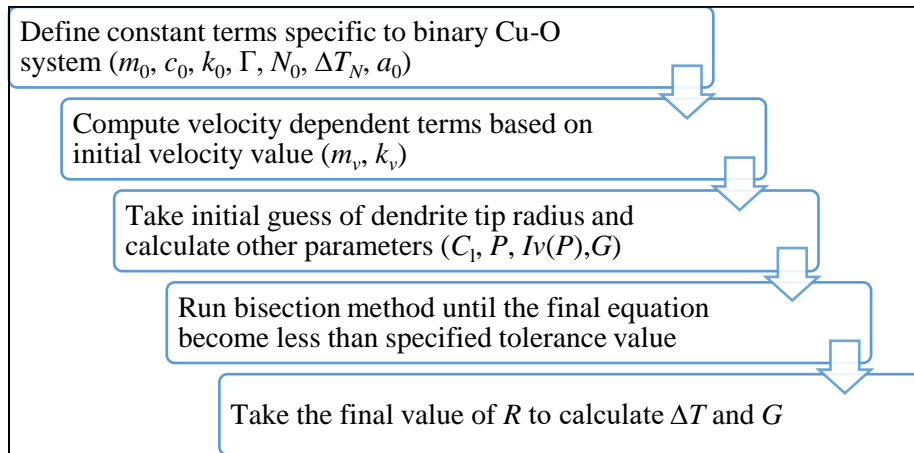


Figure 3-1. Schematic representation of MATLAB routine steps for the CET calculation of Cu-O system.

3.4.2 Sensitivity analysis of the CET model

Although the CET model is extensively used in understanding the phenomenological evolution of grains during solidification, some of its variable values have to be assumed due to the scarcity of experimental data. A sensitivity analysis is therefore necessary to understand the influences of these variables and to validate the underlying assumptions for their chosen values. Since the model is non-linear, a region is chosen from the CET map where the thermal gradient and growth velocity can be approximated as a linear segment when plotted on a log-log graph. From there, the Elementary Effects (EE) method is used to examine the combined effects of selected variables on the model outcome. EE is a commonly used sensitivity analysis method that falls in between a local parametric study such as One-Factor-at-a-Time and its computationally expensive global counterpart such as Uncertainty Quantification (UQ) or other quantitative variance-based methods (Garcia Sanchez et al., 2014; Hu and Mahadevan, 2017). As developed by Morris (1991) and modified by Campolongo, et al. (2007), the EE method utilizes the discretized partial derivative of the response variable with respect to a chosen input variable within the “region of experimentation” where the levels of all input variables have a uniform probability distribution, thus eliminating any stochastic biases in the outcome. In this analysis method if there are k input variables (X) and each variable has p levels, then the region of experimentation becomes a grid of size $(k \times p)$. The elementary effect of each input variable, $d(X_i)$, is then given by Equation 21 (Campolongo et al., 2007) where y is the objective function, and X is the nominal level of the selected variable.

$$d(X_i) = \left(\frac{y(X_1, X_2, \dots, X_{i-1}, X_{i+\Delta}, X_{i+1}, \dots, X_k) - y(X_i)}{\Delta} \right) \text{ for all } i = 1, \dots, k \dots \text{eqn}(21)$$

$$\mu_i = \frac{1}{p} \sum_{j=1}^p d_j(X_i); \sigma_i = \sqrt{\frac{\sum_{j=1}^p (d_j(X_i) - \mu_i)^2}{p-1}} \text{ for all } i = 1, \dots, k \dots \text{eqn}(22)$$

Two useful metrics (μ_i and σ_i) can be extracted for each variable from this analysis which can be used to determine the influence of i -th variable. A low mean value (μ_i) signifies negligible effect of variable X_i , whereas a large value is possible when the effect is linear and additive. The standard deviation (σ_i), on the other hand, implies interaction effects with other input variables, wherein small values signify negligible interaction and large values indicate to more interactions between variables. Although EE gives insight into the influences of significant variables, higher

order global sensitivity analysis is often performed if several input variables have high mean and standard deviation values. Here, the nucleation density, material dependent model exponent, and nucleation undercooling are investigated for their elementary effects on the CET model outcome, and are presented below in Table 3-3. The method itself involves calculations similar to finding the thermal gradient for a given velocity (0.05 m/s in this case, as G and V can be approximated as a linear segment within a velocity range of 0.01 m/s to 0.1 m/s with an R^2 value of 98.17%), and the metrics μ_i and σ_i are easily calculated using Equation 22. However, those standard deviation values will only be helpful for qualitative assertion of interaction. An exemplary discussion is given in (Fezi and Krane, 2016) where the authors used EE method for a thermal model used in direct chill casting.

Table 3-3. Selected CET model input variables and their levels used in sensitivity analysis; values in bold letters indicate their nominal level.

Input variable	Experimented levels	Units
Nucleation density (N_0)	10^{12} , 10^{14} , 10^{16} , 10^{18}	/m ³
Nucleation undercooling (ΔT_n)	0.25, 0.75 , 1.25, 1.75	K
Material dependent exponent (n)	1, 1.5, 2 , 2.5	Unitless

3.4.3 Thermal modeling of EB-PBF and process parameter design

As described in the literature review, understanding the thermal distribution within the build area is crucial for determining the solidification kinetics. A thermal model similar to that of Lee, et al. (2017) and Raghavan, et al. (2016) is utilized to extract spatial and temporal information of thermal profile of a given powder bed area. This is a three-dimensional analysis of temperature distribution by solving heat transfer partial differential equations (PDE) numerically in the FEniCS computing platform. To reduce computational cost, the analysis is restrained to a single layer fabrication within a powder bed envelop of 1.2 mm \times 1.2 mm \times 0.3 mm in XYZ coordinates, divided into a tetrahedral mesh with 10 μ m dimensional resolution. However, both in simulation and experiments, a 10 mm \times 10 mm domain size is used in the literature. Such wide deviation from the standard dimensions is rationalized by the following two aspects of the model.

Within this model, both temperature and thermal gradient data are processed and stored for the total number of timesteps used in the model. The computational time for a $10 \text{ mm} \times 10 \text{ mm}$ domain size is unreasonably high (~ 500 hours) if a spatial resolution of $10 \text{ }\mu\text{m}$ were to be used. Secondly, both thermal gradient and solidification velocity depend on the temperature data of each mesh point at a given timestep. Therefore, if the temperature distribution is the same, the effect of domain size can be minimized for a fixed set of boundary conditions. This is achieved through using a scaling factor within the model that scales the overall temperature distribution based on the domain size and mesh resolution. Finally, this obtained temperature values are then compared with reported substrate temperature of a similar process, and the domain size assumptions are validated if sufficient agreement is found. Therefore, in this study, the scaling factor is modified in such a way that the obtained temperature resembles the temperature values reported by Ledford, et al. (2019), calibrated to the temperature measurements by the in-situ pyrometer. Figure 3-2 shows the temperature output at a given timestep for both domain sizes that illustrates that the maximum temperature for both models is similar. Although several small spikes are seen in the bigger domain sized model, they have values less than the liquidus temperature than the material system, and therefore, do not contribute to the melting process. The similarity in the temperature distribution is taken as a validation of using such unconventional domain size considering the resulting reduced computational time.

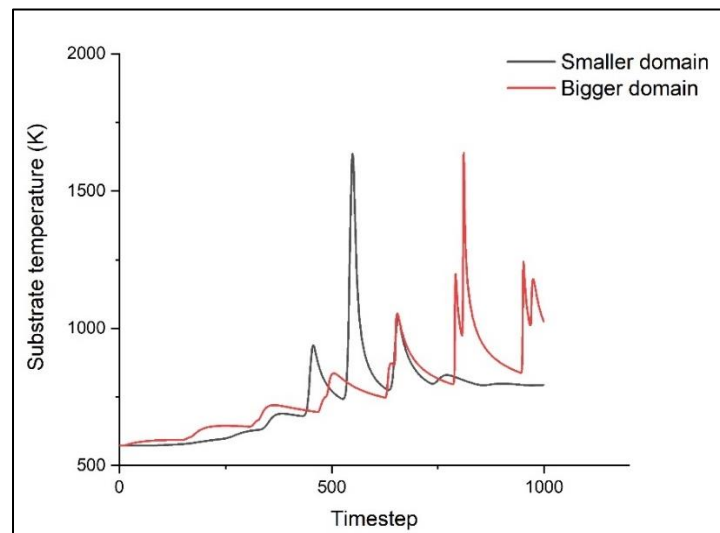


Figure 3-2. Temperature profile distribution for arbitrary timestep in small domain and big domain sized models.

Since thermal conductivity of powder is far lower than the solid bulk material, heat transfer is modeled using only conduction through the substrate plate and radiation through the vacuum of the chamber. The governing equations for this transient heat transfer model are given below (El-Gaaly, 2019; Lee et al., 2017) in Equation 23-25, along with their meaning and values presented in Table 3-4. A sensitivity analysis is conducted for selected variables that investigated the values and their implications chosen in this study (see Appendix 6-B). The model is written in a Python Script and is run in a hyper-computing station that used 70 core processing units, resulting in a running time of ~15 minutes. The processing time also depends on time step resolution of analysis, set at 1 μ s in this model for producing precise temperature data.

$$\rho C_p \frac{\partial T}{\partial t} = \nabla \cdot (k_c \nabla T) + \dot{S} \dots eqn(23)$$

$$\dot{S}(x, y, z) = A_e W \frac{2}{\pi r_b^2 d_p} e^{\left[-2 \left\{ \frac{(x^2 + y^2)}{r_b^2} + \left(\frac{z}{d_p} \right)^2 \right\} \right]} \dots eqn(24)$$

$$q_{radiation} = \varphi \varepsilon (T^4 - T_{vac}^4) \dots eqn(25)$$

Table 3-4. Thermal model variables: their meaning and values; All values are in SI unit; Response = response variable; Varied = values are varied within simulation experiments.

Symbol + Meaning	Value	Symbol + Meaning	Value
ρ = Density	5376.0	t = Time	Response
φ = Stefan-Boltzmann constant	5.67×10^{-8}	$q_{radiation}$ = Radiation loss heat flux	Response
ε = Emissivity	0.5	r_b = Radius of beam	0.0001
\dot{S} = Energy input	Response	d_p = Penetration depth	0.00002
C_p = Specific heat	390.0	T_{vac} = Vacuum temperature	Varied
k_c = Thermal conductivity	50.0	A_e = Effective absorption coefficient	0.9
T = Temperature	Response	W = Beam power	Varied

After the model is run on FEniCS, the output data are exported to the Paraview software for data visualization purposes. The thermal gradient was calculated within the model using Equation 26 for a single timestep at which the beam hits the center of the powder bed. This, on one hand, reduces the computational time of calculating thermal gradient for 10^5 timesteps used in

this study; and takes the overlapping effect of the beam into account where the examined spot is heated on either side when the beam scans its neighbor lines. This thermal gradient is then taken as the average thermal gradient value for the parameter set used in the simulation. Temperature profile pictures for different simulation scenarios (as shown in the next section) were extracted by first taking a 3D clip of the entire volume, and then using the solidus temperature of the system to outline the melt area. The cooling rate was determined in a MATLAB code from the temperature data output using Equation 27. Finally, the growth velocity, V , was calculated using Equation 28 for a given thermal gradient and cooling rate pertaining to a specific process parameter simulation (Raghavan et al., 2016).

$$G = \sqrt{G_x^2 + G_y^2 + G_z^2} \dots eqn(26)$$

$$Cooling Rate = \frac{dT}{dt} \dots eqn(27)$$

$$V = \frac{Cooling Rate}{Thermal Gradient} = \frac{\frac{dT}{dt}}{\sqrt{G_x^2 + G_y^2 + G_z^2}} \dots eqn(28)$$

Utilizing this thermal model to estimate the thermal gradient and solidification growth velocity, parameters used in previous literature and a newly designed set of parameters were simulated to obtain G and V for respective scenarios. Since the thermal conductivity of copper reduces with an increase in temperature (Davis, 2001), processing pure copper powder at high substrate temperature in EB-PBF system is particularly attractive as that reduces the gap of thermal conductivity between powder and solid bulk. In addition, as observed by other authors in other material systems, increased substrate temperatures also help reduce the thermal gradient, an essential condition to achieve CET. Therefore, the newly designed parameter set involves higher substrate temperatures (450°C and 600°C), a range of melt currents starting from 14 mA to 20 mA, and a range of scan speeds from 700 mm/s to 1600 mm/s. This entire process space is selected in such a way that some of it lies within the dense processing space of PBF of copper, as shown in Figure 2-2, while the rest moves further up along energy density coordinate as shown in Figure 3-3 below. However, at higher temperatures, simulations were not done for a scan velocity of 700 mm/s as the initial runs showed that higher velocities result in higher cooling rates. Also, three levels of melt current (16 mA, 18 mA, and 20 mA) were considered for 1300 mm/s and 1600 mm/s scenarios at higher temperatures. At large melt currents, copper tends to swell at the edge because

of great differences of thermal conditions between solidified area and surrounding powder bed. It is assumed that the use of high substrate temperature and high scanning velocity will mitigate this situation by lowering the total volumetric energy density, and thereby reduce the swelling effect. However, copper powder tends to agglomerate and sinter together easily at elevated temperatures which ultimately stalls its flowability, and consequently leads to fabrication failure. This effect could be pronounced at high substrate temperatures such as 600°C investigated in this study, and therefore, a physical build using a comparable parameter set is deemed necessary to check the feasibility of applying such a process window in practice.

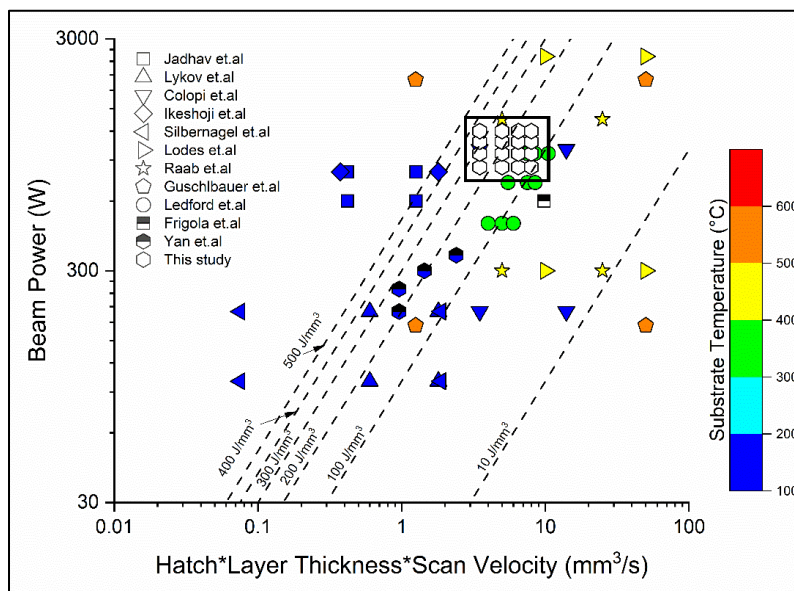


Figure 3-3. Process parameter space of PBF of copper; Hexagonal icons within the rectangle indicate newly investigated simulation process parameter. In this picture, substrate temperature of this parameter set is kept at its present level of 300°C.

3.4.4 Feasibility study with experimental builds

To examine the feasibility of fabricating pure copper at high substrate temperature and high current/ scan velocity settings via the EB-PBF process, an experimental build (Build 1) is conducted at the additive manufacturing unit of General Electric in Garching, Germany. Nine 15×15×15 mm cubes are fabricated in a Q10 Arcam machine (software version EBM Control 5.5.52) on a 99.95% pure CW021A copper plate with 8 mm space in between each cube. Copper powder with 427±9 ppm oxygen content is used, and a raster scan strategy is employed at a

substrate temperature close to 450°C with the following process parameter settings shown in Table 3-5. The values are chosen such that the overall processing space of the thermal model simulation is covered in these nine specimens. Moreover, as the samples are square in the XY plane, the line length will subsequently be the same as the beam rotates; and therefore, the samples are oriented parallel to the rake system.

Table 3-5. Process parameter design of the first experimental feasibility study build with a layer thickness of 50µm (Note: Focus offset for melt current 20 mA and scan speed 1200 mm/s is changed to 26 mA during the build to avoid swelling of the part due to high input energy density).

Sample number	Melt current (mA)	Scan speed (mm/s)	Focus offset (mA)	Line offset (mm)	Volumetric energy density (J/mm ³)
1	12	1000	18	0.1	144
2	16	1100	18	0.1	175
3	20	1200	26	0.1	200
4	12	1400	18	0.1	103
5	16	1500	18	0.1	128
6	20	1600	18	0.1	150
7	12	1800	18	0.1	80
8	16	1900	18	0.1	101
9	20	2000	18	0.1	120

Besides this, another experimental build (Build 2) is conducted in a Q10 Arcam machine (Software version EBM Control 5.2.52) in our laboratory on a stainless-steel base plate. Process parameters for this build are influenced by the results obtained from the previous build. Copper powder used in this build has a size distribution d50 value of 35 µm along with a starting oxygen content of 150 wt. ppm. Thermal conductivity of stainless steel is lower than that of copper, and therefore, the substrate is heated to a thermocouple reading of ~250°C during the build so that excessive heat buildup can be avoided. However, both microstructure analysis and thermal model prediction for previous build specimens showed that the most influential parameter controlling the CET in pure copper is the thermal gradient G , which lowers as both substrate temperature and melt

current increase in a build. To achieve a high local substrate temperature for the fabricated blocks, each block is melted three times with successively more defocused beam. Simulations performed using the thermal model prior to the experiment showed that a higher substrate temperature can be achieved locally if the blocks are scanned multiple times (illustrated in Figure 3-4 below), which ultimately results in a lower thermal gradient than what would have been possible with a single pass at 250°C substrate temperature. However, as high energy input might lead to swelling at the edges, more defocused beam is used for successive melt passes. Relevant process parameters are listed in Table 3-6 used in the fabrication process with 50 μm layer thickness. It is to be mentioned that severe powder flowability issues are encountered during the build owing to several possible reasons, viz. large differences of thermal conductivity between copper and stainless steel, greater powder purity, smaller particle sizes etc. Eventually, the build is stopped at a height of 3.5 mm.

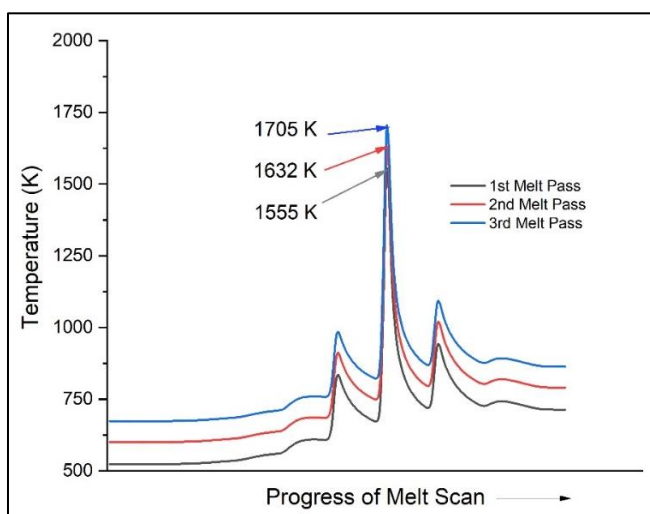


Figure 3-4. Increase in substrate temperature as an increase in the number of melting passes on each block.

Table 3-6. Process parameters of fabricated blocks in the second experimental feasibility study build with pure copper powder.

Sample number	Melt current (mA)	Scan speed (mm/s)	Focus offset (mA)			Line offset (mm)	Volumetric energy density (J/mm^3)
			1 st pass	2 nd pass	3 rd pass		
1	14	1200	18	22	26	0.13	108

Table 3 6. Continued.

2	16	1400	18	22	26	0.13	137
3	20	1800	22	26	30	0.13	133
4	16	1500	18	22	26	0.13	128
5	22	2200	24	28	32	0.13	120
6	30	2600	28	32	36	0.13	138
7	10	800	18	22	26	0.13	150
8	16	1600	18	22	26	0.13	120
9	26	2400	24	28	32	0.13	130

3.4.5 Microstructural and mechanical characterization of the build specimens

Metallographic samples from the first build are prepared from each specimen along the build direction by first cutting the samples in half, and then, mounting, polishing, and etching in Ammonium Persulphate solution. Optical micrographs are taken in a Hirox KH7700 microscope before and after etching the samples. Bulk optical density of the samples is measured using the un-etched images through a MATLAB code by using a suitable threshold value to delineate the internal pores. Further, SEM imaging of selected samples are carried out in a JEOL 6010LA under secondary electron imaging mode to observe the internal grain structure. Grain width is calculated from the etched micrographs by the linear intercept method where ten lines of similar length are drawn on the images, and the number of intersections is measured. Four micrographs of each sample are examined for grain size measurements, and the average number is reported. To obtain the Vickers microhardness of the specimens, ten indentations at 100 gf load for 10 seconds dwell time are made along the build direction, and the average values represent the final microhardness. However, samples from the second build are characterized only for microstructure using optical and electron microscopy as their overall appearance is significantly more porous than the samples fabricated in the first build.

3.5 Results and Discussion

3.5.1 CET of copper-oxygen system

The CET solidification map developed using the equations described previously is shown in Figure 3-5 below. When the actual thermal gradient value is less than the calculated G value

from Equation 20 for a given interface growth velocity, V , the microstructure falls in the region of equiaxed grains (shown in the bottom right area in Figure 3-5a,c). Above this transition line, G exceeds a critical value at the solidification front, and thus, columnar microstructure becomes the dominating grain formation mechanism. Also, it is critical that V is within the limit of stability so that the dendritic growth does not fall back to planar grain growth regime, a characteristic result of either very low growth velocity or very high growth velocity.

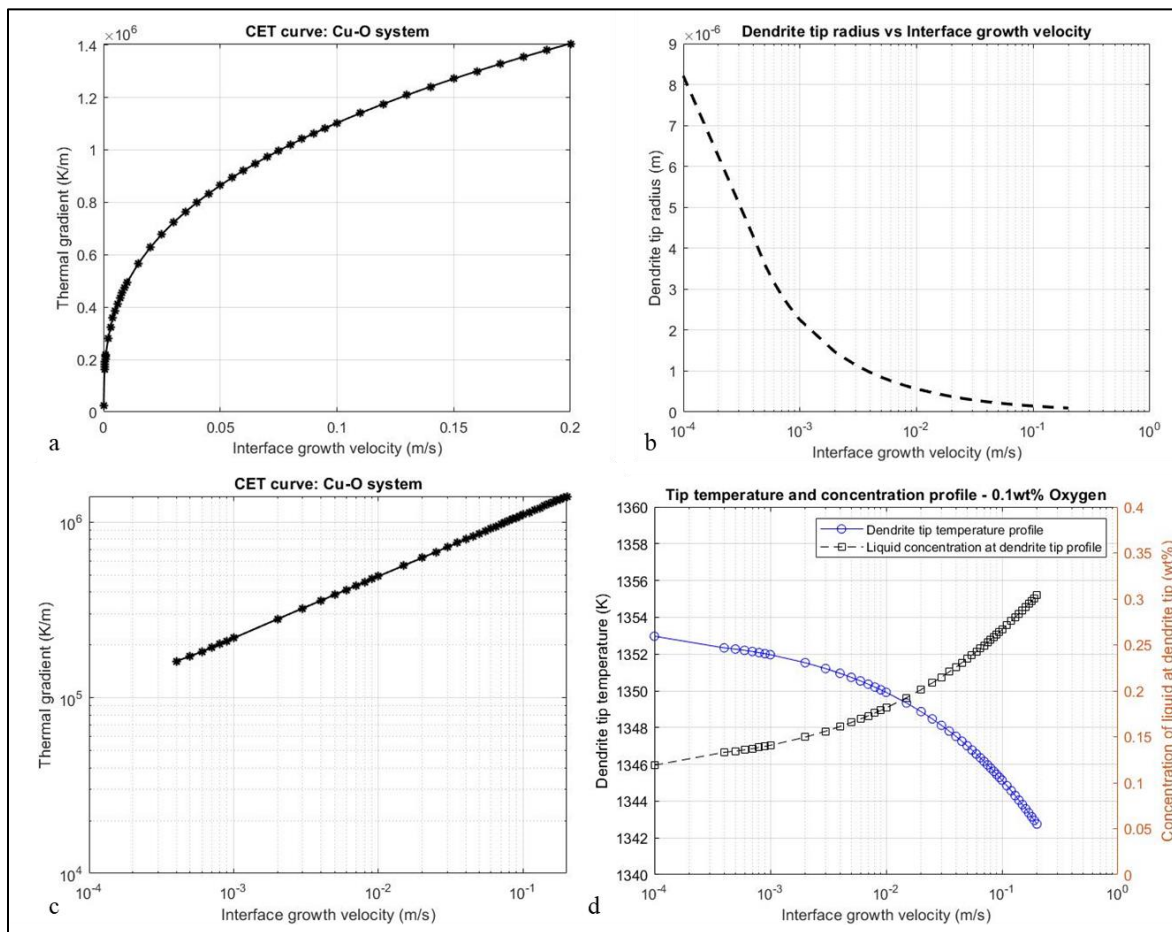


Figure 3-5. CET solidification map of copper (a. linear axis plot, b. conventional log-log plot); c. Dendrite tip radius as a function of growth velocity; d. Dendrite tip temperature and concentration at tip profile as a function of growth velocity. Interface growth velocity and solidification velocity are used interchangeably.

For a given thermal gradient within the velocity range where dendritic grain morphology is prevalent, increasing the solidification velocity results in a greater chance of producing equiaxed grains. This phenomenon is supported with the aid of Figures 3-5b,d which illustrate the effect of growth velocity on dendritic tip radius, and the temperature and composition profile at dendrite tip, respectively. As the tip radius becomes sharper, it can grow much faster and can dissipate more latent heat of fusion with greater efficiency (Kurz and Fisher, 1984) than a dendrite with a large tip radius. This enhanced tip growth raises the solute rejection near the tip, and therefore, creates a more solute-rich region ahead of dendrite tip. This, in turn, is followed by a reduction in tip temperature because of the increased compositional difference between the solid and liquid, and results in more undercooling near the tip. As an undercooled region ahead of solid-liquid (S/L) interface favors the formation of equiaxed grains, the microstructure tends to become more mixed or equiaxed instead of columnar as found at lower velocities. This reasoning can be further elucidated by obtaining temperature and undercooling profiles ahead of the dendrite tip for different interface velocities. Equations 29-32 are used to calculate the liquidus and actual temperature profiles ahead of the dendrite tip, from which, undercooling information is extracted for a given growth velocity (Gäumann et al., 1997).

$$T[z] = T_1 + \frac{(T_{eq} - T_1)E_1 \left[\frac{P(2z + R)}{R} \right]}{E_1(P)} \dots eqn(29)$$

$$\text{where } T_1 = T_m + m_0C_0; \quad T_{eq} = T_m + m_vC_l \dots eqn(30)$$

$$\text{Local temperature } T_q[z] = T_{tip} + Gz; \quad T_{tip} = T_m + m_vC_0 - \Delta T \dots eqn(31)$$

$$\text{Undercooling } \Delta T[z] = T[z] - T_q[z] \dots eqn(32)$$

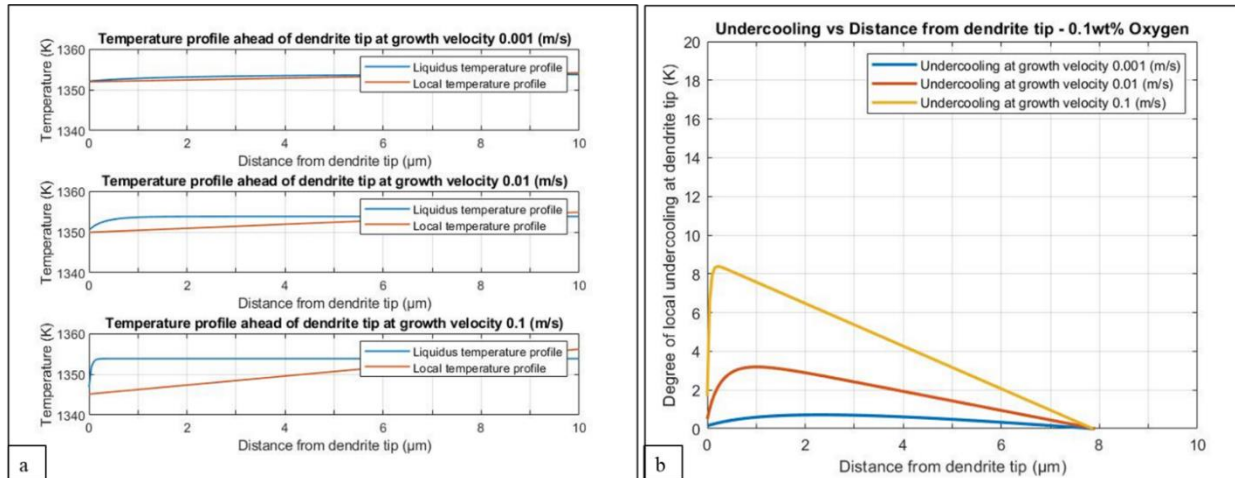


Figure 3-6. Liquidus and actual local temperature ahead of dendrite tip for solidification velocities of 0.001, 0.01, and 0.1 m/s; b. Undercooling profile ahead of dendrite tip for solidification velocities of 0.001, 0.01, and 0.1 m/s.

Figure 3-6a shows the liquidus and local temperature profiles ahead of the dendrite tip for different growth velocities: 0.001 m/s, 0.01 m/s, and 0.1 m/s (all within the range of the limit of stability). It is seen that with increasing growth velocity, the liquidus temperature of the melt ahead of dendrite tip increases due to the enhanced solute rejection (seen from the composition profile with respect to growth velocity in Figure 3-5d). This leads to enhanced undercooling ahead of tip, as illustrated in Figure 3-6b, where the undercooling at the interface for a growth velocity of 0.1 m/s is over 8 K, compared to an undercooling of less than 1 K at a velocity of 0.001 m/s. This enhanced undercooling at increased velocity emphasizes the possibility of achieving the CET, as can be seen in the formulation of CET solidification map in Equation 20.

3.5.2 Sensitivity analysis of non-compositional variables used in the CET model

Elementary effects of the chosen variables used for the sensitivity analysis of the CET model are presented below in Figures 3-7 and 3-8. For the non-composition variables used in the study, these three have higher power effects on the model outcome, and therefore, are considered important factors for the model sensitivity. Because of 4 levels of each variable, a total 64 simulation runs were conducted; and the EE of each variable was calculated with respect to their nominal value using Equation 21. As seen in Figure 3-7, thermal gradient, G , is affected the most

by nucleant density N_0 , and is relatively less influenced by the other two variables. In AM and casting literature, values of N_0 have ranged from 10^9 - 10^{19} /m³ [10^9 (Cziegler et al., 2017; Hunt, 1984), 10^{15} (Anderson et al., 2010; Li and Tan, 2018), 10^{18} (Lian et al., 2019), 10^{19} (Guan et al., 2019)] by fitting the model to experimentally obtained data, and therefore, a range of 10^{10} and 10^{18} /m³ is considered in the sensitivity analysis.

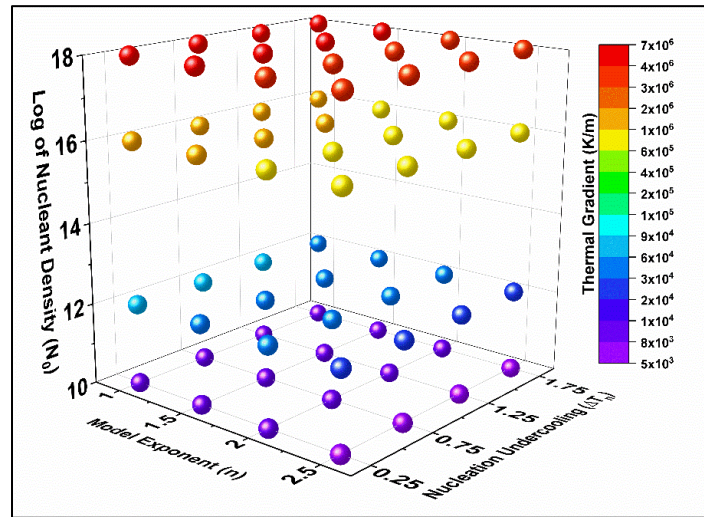


Figure 3-7. Thermal gradient values of simulations for different combinations of all three investigated input variables.

It is also observed that both model exponent n and nucleation undercooling ΔT_n do not significantly impact the model results because of their small nominal values. However, as they control the possibility of heterogeneous nucleation, and a high value of ΔT_n will hinder the formation of new grains, these are rendered important for this analysis. The mean EE metric for each variable is calculated using Equation 22, and is plotted in Figure 3-8 below. It is observed that N_0 has a very high mean effect, in accord with the results shown in Figure 3-7, whereas n and ΔT_n have a low mean effect on the model outcomes. It is also noted that the effect of nucleation density is several orders of magnitude higher than the other two, primarily due to its high-power term value. The overall EE of each variable has a similar effect on total undercooling as presented on the secondary Y axis within the same plot. It is further noted that the effects of each variable increases as the variable departs farther from its nominal level, indicating at the need for choosing the nominal values carefully while fitting the model to experimental data.

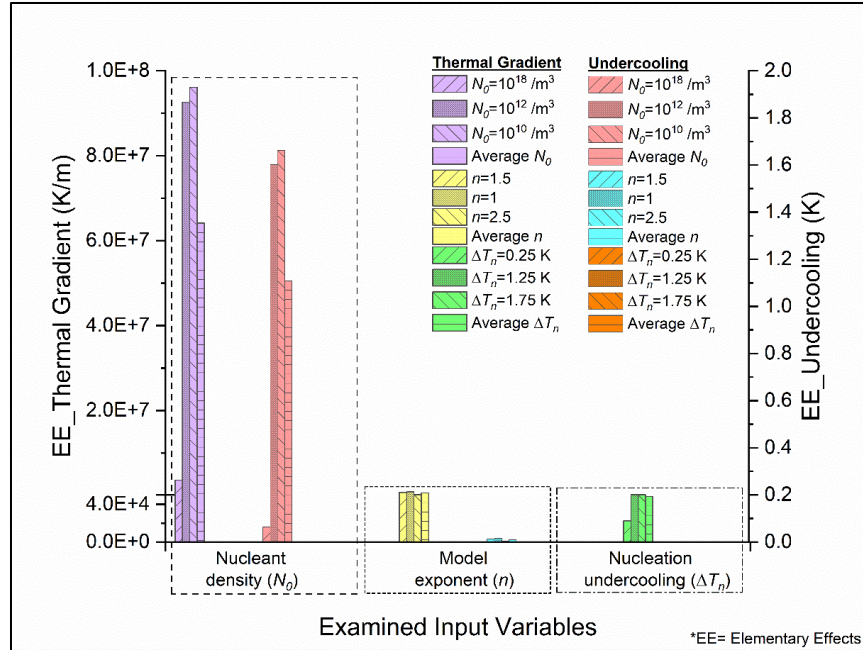


Figure 3-8. Elementary effects of each examined variable on Thermal gradient (left hand Y axis) and Total undercooling (right hand Y axis); Bars show the mean EE values, while the one-sided error bars show the standard deviation EE values.

3.5.3 Thermal gradient and solidification velocity calculation from thermal model

As described in the methods section, thermal gradient and solidification velocity are calculated for the newly designed parameter window by simulating the numerical thermal model. While thermal gradient is calculated directly from the model output, calculation of cooling rate is required prior to obtaining the solidification growth velocity. Therefore, in the following figure, thermal gradient and cooling rate results are shown first for a different set of process parameters. It is seen from Figure 3-9a-c that thermal gradient decreases as the melt current increases for all examined velocities (700 mm/s, 1000 mm/s, 1300 mm/s, and 1600 mm/s) at all substrate temperatures (300°C, 450°C, and 600°C). This decrease in thermal gradient is due to more gradual change of temperature in a wider and larger melt pool, as evidenced from Table 3-7. As the current increases, temperature within the beam incident area increases simultaneously, and the temperature difference between the melt pool top and bottom increases as well. However, the neighborhood powder bed have very close temperature values, which results in a reduced thermal gradient at higher melt currents. Cooling rate (Figure 3-9 d-f), on the other hand, depends more significantly

on the beam scan velocity, and is observed to have a positive correlation. For the same melt current, cooling rate increases as the beam moves faster. This is primarily due to the associated heat dissipation rate which becomes steeper for higher beam velocities. However, increasing substrate temperatures decrease the cooling rate for the same melt current and scan velocity due to a lower temperature difference between the melt pool and its surroundings.

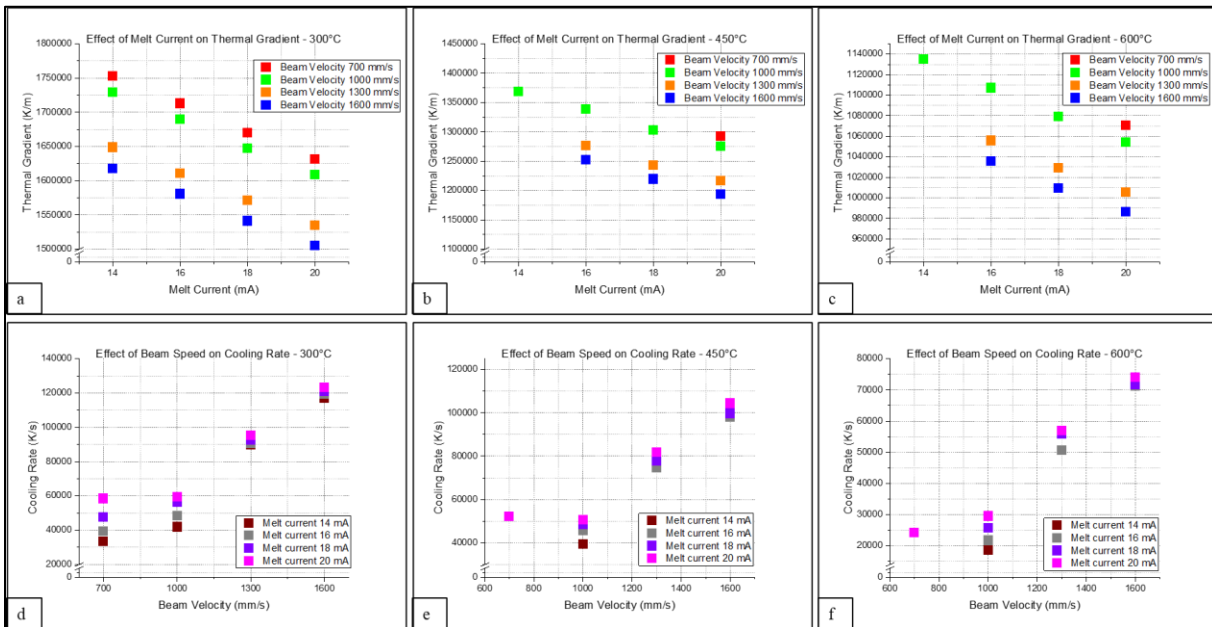
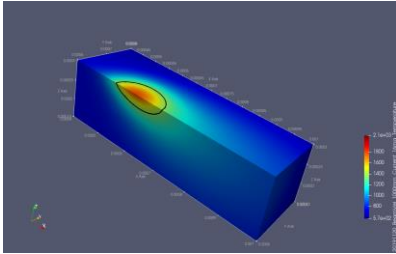
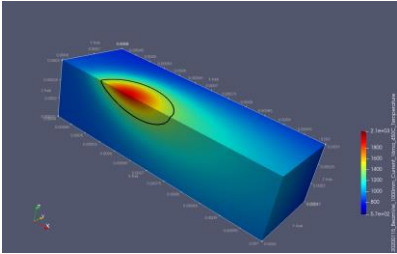
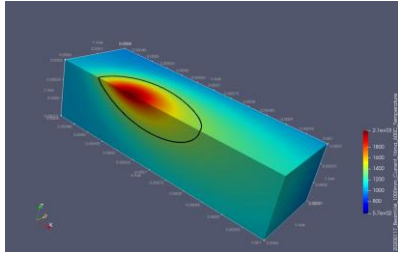
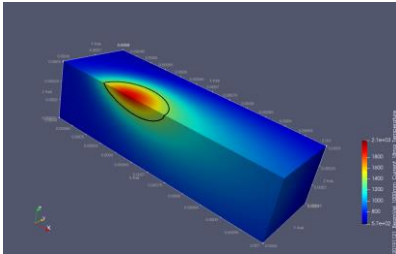
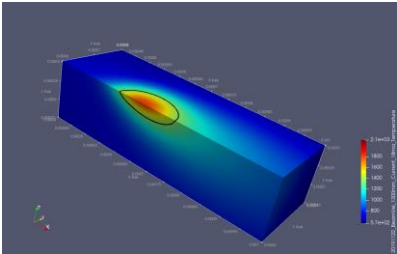
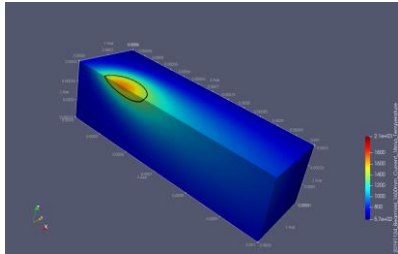
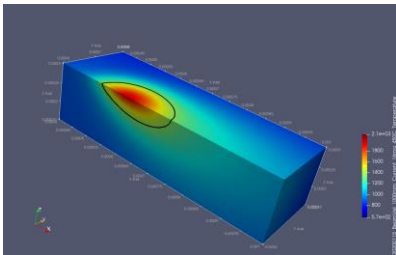
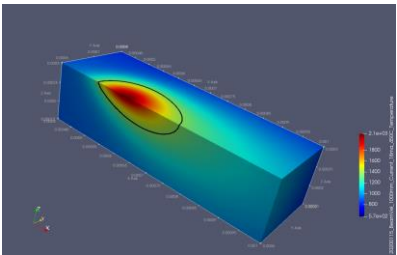
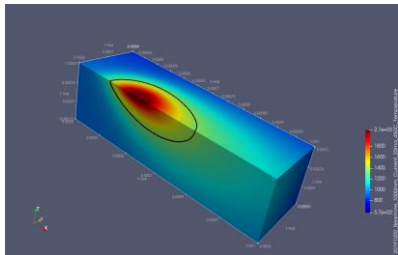


Figure 3-9. Effect of melt current on Thermal gradient at different scan velocity and substrate temperature; d-f. Effect of scan velocity on Cooling rate for different melt current and substrate temperatures; Note that Y-axis value ranges are not similar.

To further investigate these features of Figure 3-9, the melt pools of representative process parameter sets are presented in the table below. These melt pool snippets are taken at a specific timestep when the beam is at the center of the overall domain analyzed in the thermal model. The shape and size of the melt pool (liquidus isotherm line) change significantly when the melt current, scan velocity, and substrate temperature change. For example, when the substrate is heated to a higher temperature, melt pool tends to become wider and longer for same scan velocity and melt current as seen in the first row of Table 3-7. Because of this larger melt pool size and more uniform temperature distribution, thermal gradient reduces as substrate temperature increases.

Table 3-7. Melt pool characteristics for representative process windows to show individual effect of substrate temperature, scan velocity, and melt current. The models were created in Paraview, and temperature scale is 573 K (blue) to 2100 K (red).

Substrate temperature 300°C	Substrate temperature 450°C	Substrate temperature 600°C
1000 mm/s, 16 mA 	1000 mm/s, 16 mA 	1000 mm/s, 16 mA 
Scan velocity 1000 mm/s	Scan velocity 1300 mm/s	Scan velocity 1600 mm/s
18 mA, 300°C temperature 	18 mA, 300°C temperature 	18 mA, 300°C temperature 
Melt current 16 mA	Melt current 18 mA	Melt current 20 mA
1000 mm/s, 450°C temperature 	1000 mm/s, 450°C temperature 	1000 mm/s, 450°C temperature 

A widening melt pool can also be observed in the bottom row with increasing melt current with the other two variables held constant. In the middle row, the consequence of increasing the scan velocity can be seen at constant melt current and substrate temperature where the melt pool length and width decrease as the beam moves faster. Since the local mesh temperature controls

these characteristic features of the melt pool, it is important to extract temperature information for the overall time length of the simulation and compare that for different process parameter sets. Figure 3-10 below illustrates such temperature profiles of a selected point at the top of the melt pool at a given timestep for two different process parameter sets. When scan velocity is low, the spot is heated to a larger extent due to the overlaps of the beam when it scans neighborhood lines on either side. It is also noted that the small spike at the right side is greater than the one on the left, as it retains the heat from two previous raster scans. However, when the scan velocity is high, this overlapping effect of the beam does not raise the temperature as high as before, and hence, results in greater cooling rates.

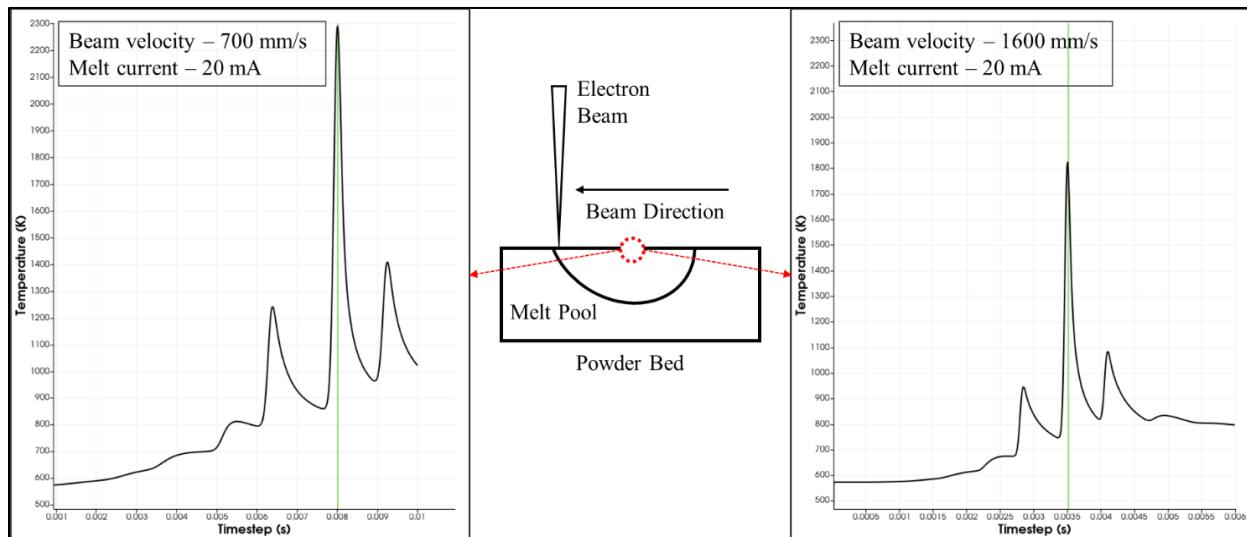


Figure 3-10. Effect of scan velocity on temperature profile of the melt pool top. The point simulated in the software is shown schematically in the middle. Substrate temperature is kept at 300°C for both process parameter sets. Temperature axis ranges from 500 K to 2300 K.

From the obtained cooling rates and thermal gradients, solidification velocity is calculated for each process parameter set. This G - V map hence represents the effects of processing conditions on two critical metrics that impact the solidification kinetics and resulting microstructure, as explained in the literature review. Parameter sets used in other studies were also utilized to calculate the resulting G and V values to compare them with the designed parameter sets. This plot is shown below in Figure 3-11 where it can be seen that the processing conditions that used a combination of high melt currents, high scan speeds, and high substrate temperatures tend to have

lower thermal gradients and higher solidification velocities. In general, EB-PBF processes show lower thermal gradients than the laser-PBF processes due to its substrate plate heating and preheating steps before the actual melting process. The literature used for this G - V map are the following: Laser - (Colopi et al., 2018; El-Wardany et al., 2018; Ikeshoji et al., 2018; Jadhav et al., 2019; Lykov et al., 2016; Silbernagel et al., 2019), EB - (Guschlbauer et al., 2018; Ledford et al., 2020; Lodes et al., 2015; Raab et al., 2016).

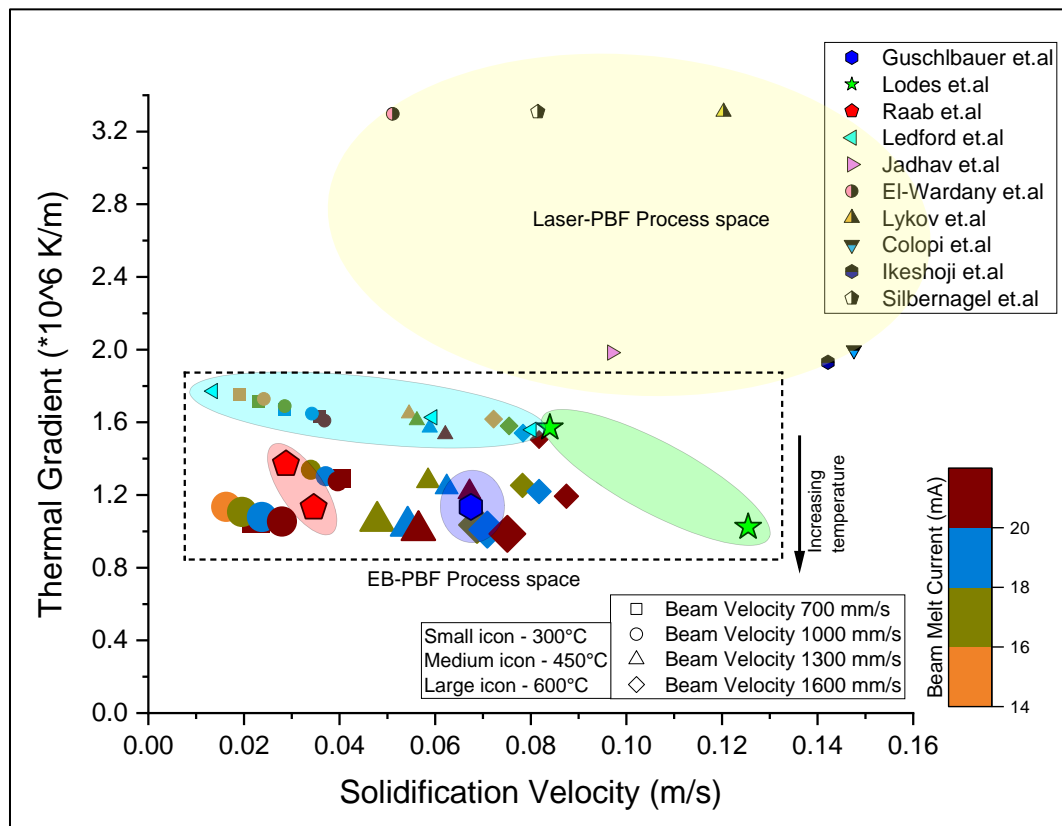


Figure 3-11. Thermal gradient (G) and solidification velocity (V) for different process parameter sets (from literature and newly designed) of pure copper fabricated in EB-PBF process.

3.5.4 CET of copper in PBF process

This section merges the thermal gradient and solidification velocity data obtained through the CET and the thermal model analysis of PBF processing of copper as shown in Figure 3-12. The ultimate aim was to develop an understanding of the resulting microstructure as a function of processing conditions from available literature and the previous tensile study. Figure 3-5a and

Figure 3-11, when superimposed to one another, offer insight as to why the experimentally obtained microstructure is obtained for a specific process parameter set. With due appreciation to all the assumptions taken in the CET model development and processing the thermal model, it is seen that most of the adopted process parameter space in literature leads to columnar grains along the build direction. As the substrate temperature reduces (e.g., room temperature processing in L-PBF or 290°C - 320°C used in the tensile study), columnar grains become more dominating structural factor in the specimens. In order to reach the transition zone, it is imperative to use a combination of high substrate temperature, high melt current, and high scanning velocity. Moreover, from the standpoint of keeping the temperature profile the same throughout the build, preheating condition should also be adjusted such that every new powder layer has a high bed temperature conducive of low thermal gradients.

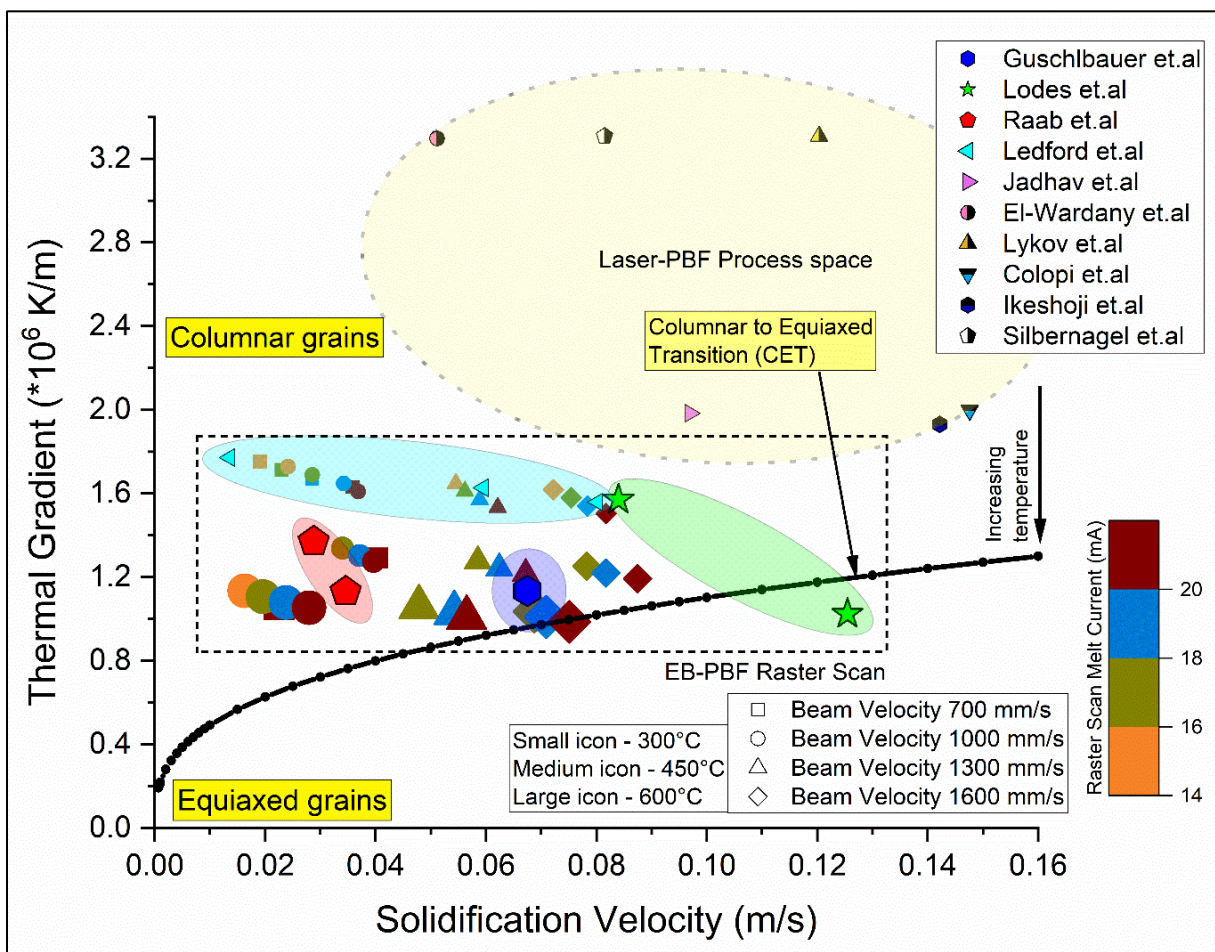


Figure 3-12. CET of copper in powder bed fusion process.

To further establish the relationship between the PBF process conditions and solidification kinetics, the concentration profile and total undercooling ahead of dendrite tip were calculated for representative process parameter sets using the respective solidification velocities obtained from the thermal model simulation. As mentioned previously, columnar-to-equiaxed transition is favorable when undercooling is greater and thermal gradient is lower near the S/L interface. It is observed in Figure 3-13 that increased melt current, substrate temperature, and/or scan velocity result in greater undercooling due to a larger difference between liquidus temperature and actual local temperature, as validated by the peak values of undercooling curves of 4.89 K, 6.56 K, and 7.46 K from Figure 3-13. The local liquid temperature depends on the imposed thermal gradient, dictated by input process parameters; whereas liquidus temperature decreases as more solute builds up near the S/L interface, as validated by the concentration profiles which show a steeper solute concentration gradient closer to the interface with increasing solidification velocity, giving rise to a lower liquidus temperature as opposed to a more gradual change of concentration in low V -high G parameter scenarios. As more solute builds up near the interface, the difference between liquidus temperature and local temperature ahead of dendrite tip increases, which in turn, increases the tip undercooling. This enhanced undercooling ahead of the interface can promote more heterogeneous nucleation resulting in grain refinement.

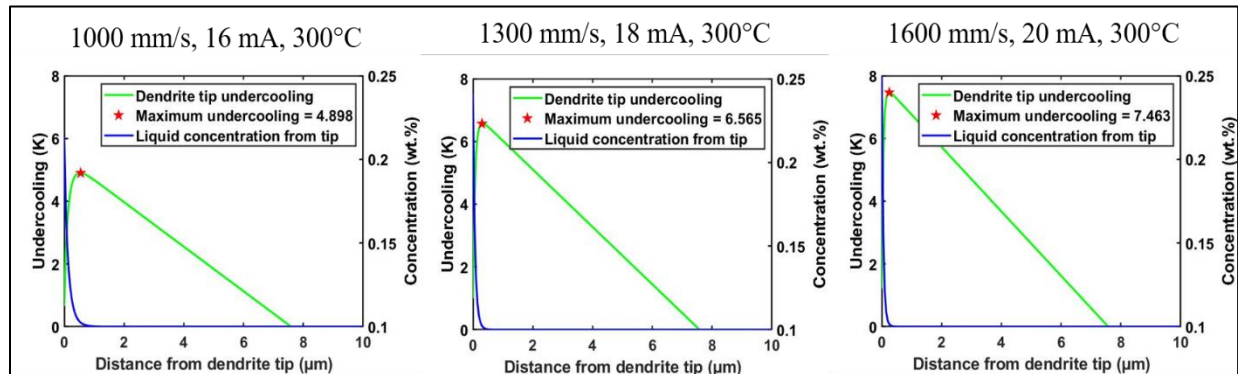


Figure 3-13. Top: Melt pool contours from thermal model, Bottom: Undercooling and concentration profile ahead of S/L interface; Respective process parameters are shown at the top of the contour maps; Color bar range: 573 K (blue) to 2100 K (red).

3.5.5 Thermal model and CET results of the build specimens (Build 1)

Both the numerical thermal model and CET map are used to predict the achievable grain structure of the build specimens fabricated with the process parameters presented in Table 3-5. The chosen parameter set produces a relatively wide range of volumetric energy density for the build specimens within the dense processing space of AM copper, and captures the effects of a range of thermal gradient and solidification growth velocity values. According to the thermal model, higher melt currents result in lower G and higher scan velocities lead to higher V . Therefore, a general trend of refined grain structure is expected from sample 1 to sample 9 in the experimental build. Figure 3-14 shows the resulting G and V for all nine specimens, superimposed on the proposed CET map. All low-melt-current (12 mA and 16 mA) samples have high G and low V values which are not conducive of producing equiaxed grains, and the overall microstructure is predicted to have columnar grains along the build direction. However, for these specimens, higher scan velocities increase the cooling rates, and therefore, a more refined microstructure should be produced with smaller grain widths following the interrelationship between the cooling rate and obtained grain morphology. For 20 mA samples, G is reduced further, and sample 9 lies within the transition region due to its largest V value corresponding to the highest scan velocity used in this experiment.

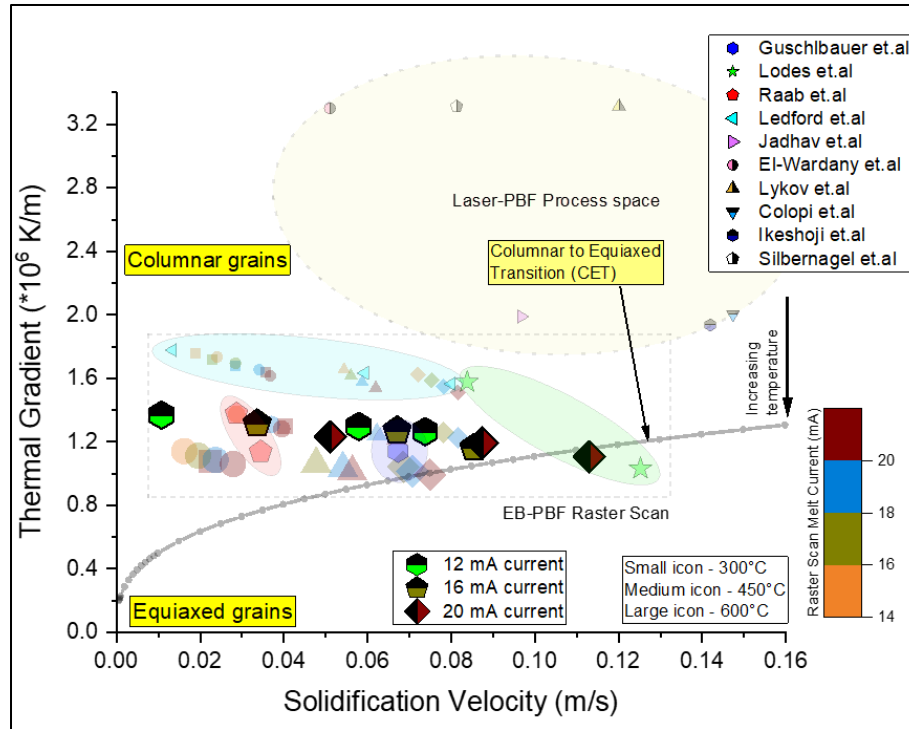


Figure 3-14. Thermal model results of the build specimens predicting the overall microstructure by using the proposed CET map.

3.5.6 Microstructural analysis of build specimens (Build 1)

In compliance with the thermal model and CET map results, the obtained microstructures for each specimen show predominantly epitaxial columnar grains along the build direction, as illustrated in Figure 3-16. In all of the grain structure micrographs, melt pool path can be seen, which is more pronounced in sample 3 that has the highest volumetric energy density. Measured grain sizes are also given for each sample within their respective micrographs, except for sample 2 wherein grain size could not be measured. It is apparent that the grain width reduces as the scanning speed increases for each current setting, primarily due to the increase in cooling rate, and the associated increase in V , as found out in the thermal model results. However, sample 9, predicted to fall in the CET region, does not show equiaxed grain or a substantial transition from columnar grain along the build direction. While there are a few assumptions taken to extract steady state thermal condition that can contribute to this observed discrepancy, the effect of oxygen content is examined here since its amount is significantly different, ~ 0.04 wt.% as compared to 0.1 wt.% used in the CET model. As per the phase diagram of Cu-O system, in the hypoeutectic region,

the liquidus slope m does not change significantly as the initial concentration of oxygen decreases. However, this reduced O_2 concentration decreases the critical thermal gradient required for the transition due to its reduced ability to undercool the liquid, thereby, forcing the grains to be columnar due to a relatively higher thermal gradient calculated for each sample. This is shown in Figure 3-15.

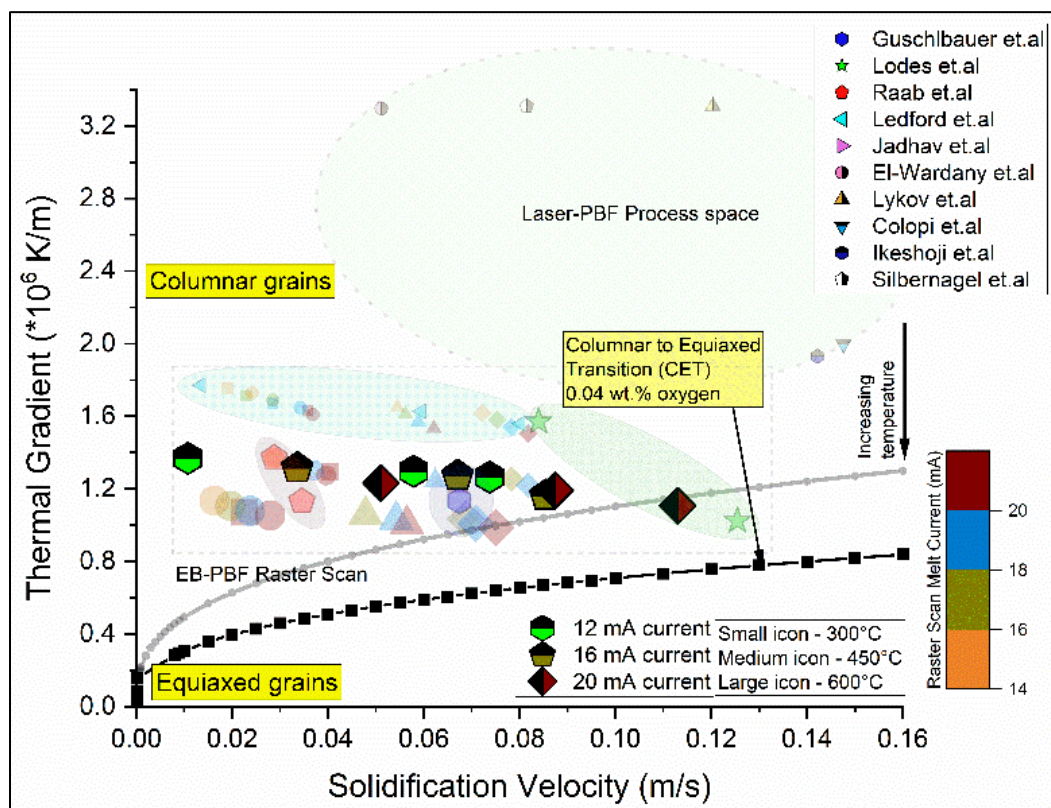


Figure 3-15. Modified CET and G-V for the experimented samples for 0.04 wt.% oxygen content.

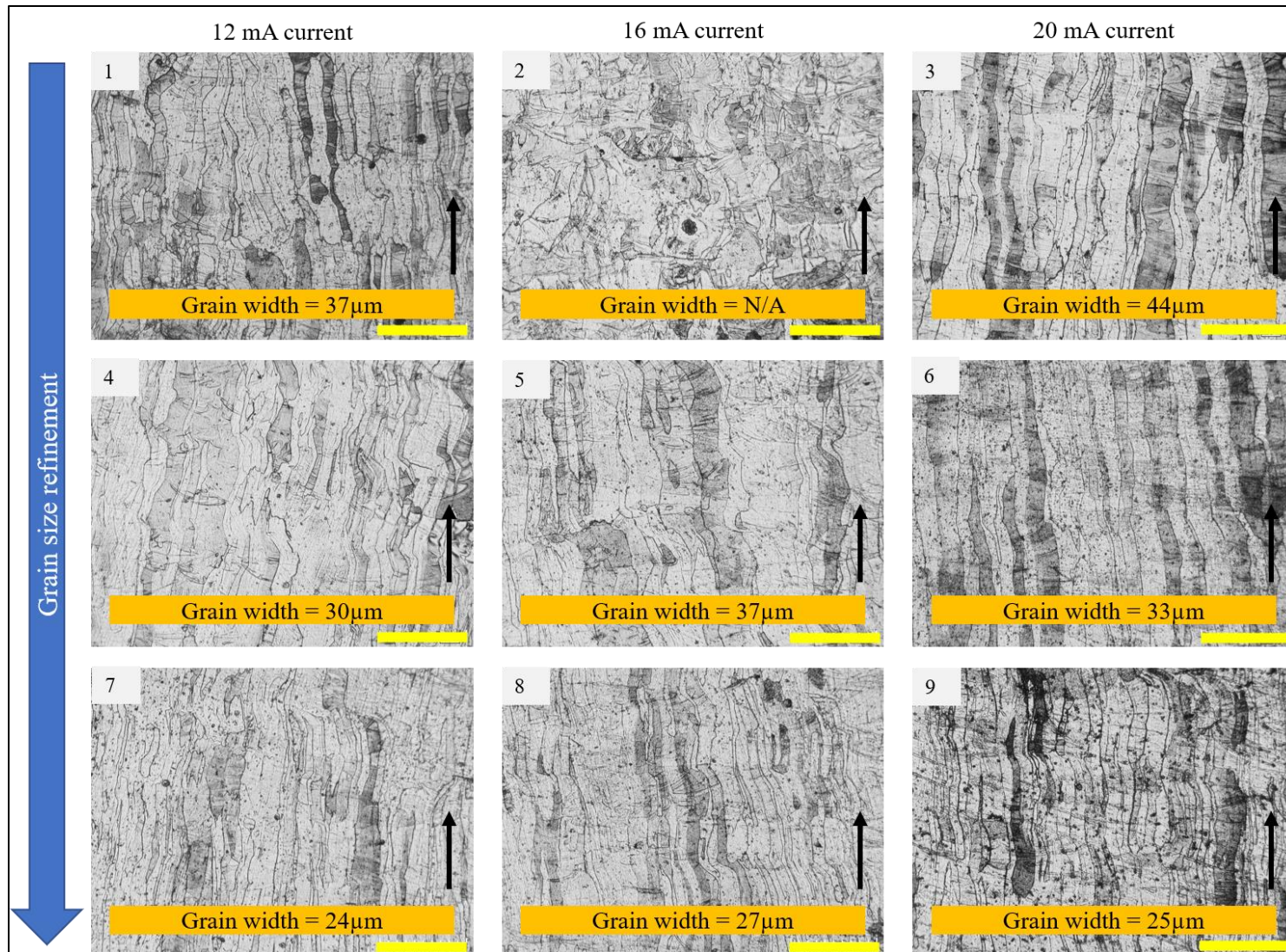


Figure 3-16. Microstructure of all specimens fabricated in the experimental build. Sample numbers are shown at top left corner on each micrograph. Build direction is shown by the black arrow, and the scale bar in yellow shows 200 μm .

To further examine the grain morphology in the fabricated samples, SEM images of selected samples are taken as per the method described in § 3.4.5. Sample 1 and 9 are chosen as they signify the extreme current/velocity conditions for 12 mA and 20 mA current, respectively.

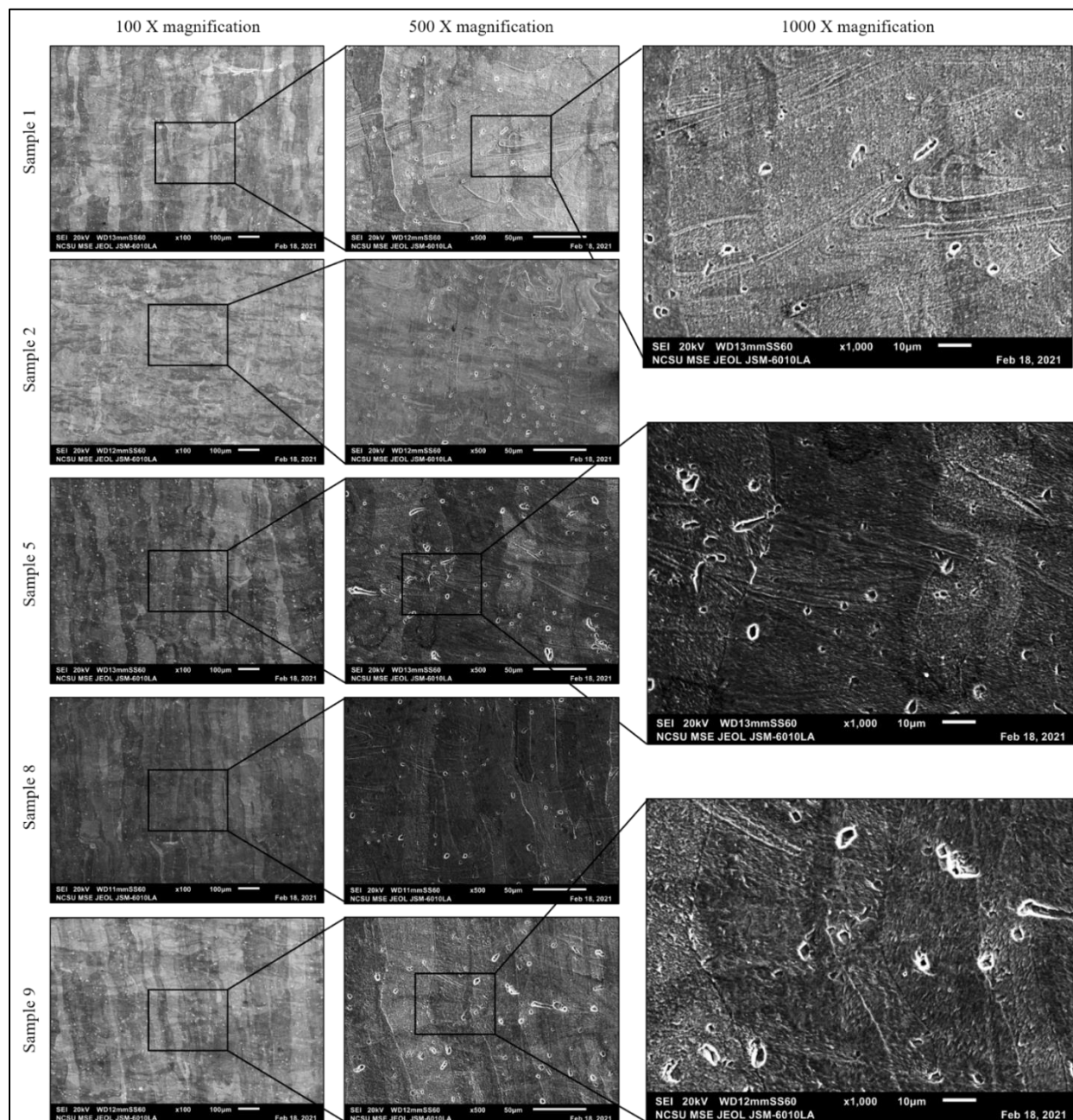


Figure 3-17. SEM images of representative samples showing the overall grain morphology at different magnification levels. Note the different scale bars (100X= 100 µm, 500X= 50 µm, 1000X= 10 µm).

All three from 16 mA samples are selected on the other hand to examine the effect of velocity while keeping the current same. As the samples are etched prior to the SEM imaging, systematic etch pits and inclusions from grinding/polishing are visible in Figure 3-17. Nevertheless, all SEM images show columnar grains with comparable grain sizes measured from the optical micrographs. The higher magnification images clearly show the melt pool boundaries across the grains, with an internal distance corresponding to the layer thickness used during the fabrication process (50 μm). Moreover, orientation of the grain structures can be resolved from these images which showed similarly oriented long-range columnar grain structures within an individual grain. It is well known that grain selection depends on the competition between the direction of thermal gradient and the grain orientation of the preceding layer (Hadadzadeh et al., 2018; Helmer et al., 2016; Liu et al., 2019). Figure 3-18 illustrates this grain orientation of sample 9 along the direction of build that clearly shows how epitaxial grains are formed when influenced by the grain epitaxy of the previous layer.

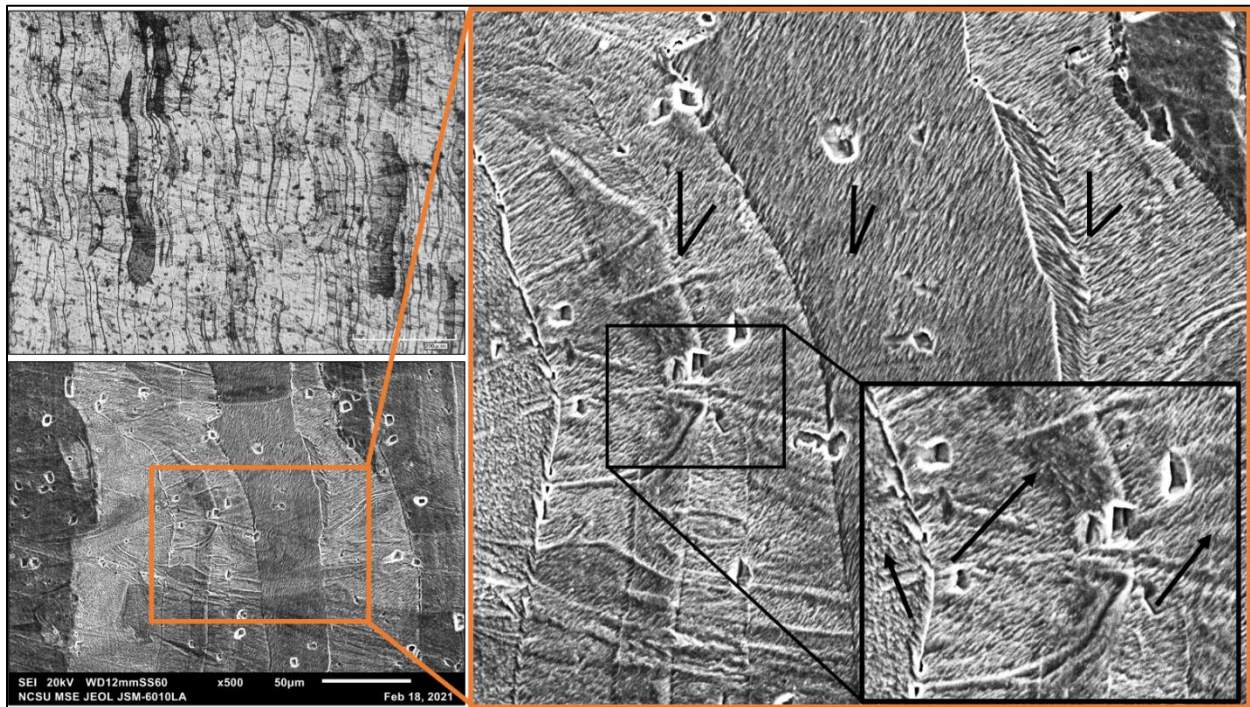


Figure 3-18. Columnar dendrite structure within individual grains seen in Sample 9. Black lines indicate the relative orientation of the dendrites with respect to the build direction.

As seen in the magnified area marked with orange color, columnar dendrites span across the melt pools resulting from melting of each layer, and they grow in the direction dictated by the grains from the previous layer. The orientation angle outlined with the build direction shows that all these columnar dendrites are relatively close to the direction of build, and the direction of growth does not change for long-range lengths even with the change in the direction of thermal gradient corresponding to the scanning rotation in each layer. Moreover, a further magnified snippet of the overlapped melt pool area marked with black color shows that the direction of dendrite growth is the same above and below the melt pool boundary, confirming that the epitaxial solidification conditions. Although reduced G or increased V results in an increase in total undercooling, the obtainable undercooling value for these samples is not very high due to low solute concentration; and hence, the effect of constitutional undercooling in promoting equiaxed grains is not observed in the fabricated samples.

3.5.7 Microhardness and density results of the build specimens (Build 1)

Table 3-8 represents the microhardness and calculated optical density for all fabricated samples from Build 1. The chosen process window is observed to produce copper with relative densities $>99.9\%$ with the highest density of 99.99% in Sample 3. While the density values are relatively independent of the process parameters within the chosen processing space, hardness values show peaks for all 16 mA samples, and a drop on either side of 12 mA and 20 mA samples. This trend is similar to what is observed in the grain sizes. However, a similar trend is observed for the scan velocities for a given melt current, indicating an optimum amount of volumetric energy density within the range of $100\text{-}150\text{ J/mm}^3$ (refer to Table 3-5) for improved hardness of the material.

Table 3-8. Microhardness and optical density of build specimens.

Sample #	1	2	3	4	5	6	7	8	9
Optical density (%)	99.94	99.95	99.99	99.94	99.94	99.96	99.92	99.93	99.96

Table 3-8. Continued.

Microhardness (HV0.1)	69.9	76.6	75.7	75.2	78.9	79.5	73.9	74.4	77.6
-----------------------	------	------	------	------	------	------	------	------	------

3.5.8 Thermal model and CET results of the build specimens (Build 2)

Similar to Build 1, process parameters used for the samples from Build 2 are simulated via the thermal model to obtain representative G and V to predict the obtainable microstructure. It is illustrated in Figure 3-19 that majority of the specimens are still within the columnar region due to high thermal gradient associated with the relatively low starting substrate temperature. Sample 6, however, demonstrates a tendency to lower G because of its high melting current that ultimately can facilitate an equiaxed grain growth along the build direction. Nevertheless, caution should be taken in interpreting the prediction since the transition is calculated for 0.1 wt.% and 0.04 wt.% of oxygen concentration, whereas the oxygen reading of the feedstock powder is ~ 0.015 wt.%.

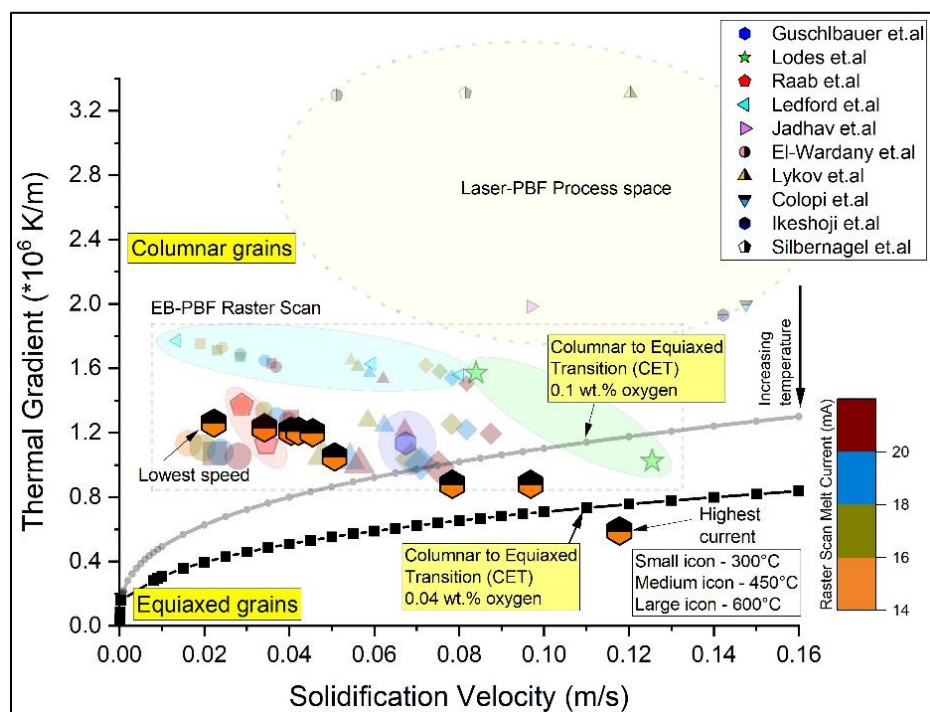


Figure 3-19. Microstructure prediction from the thermal and CET model for the fabricated specimens.

3.5.9 Microstructural analysis of build specimens (Build 2)

Figure 3-20 exhibits the microstructure of each sample under similar magnification levels. It is apparent that adopted processing condition results in instabilities during the fabrication, which manifests into irregular powder spreading, and severe lack-of-fusion type of defects caused by un-melted powder layers. With regard to the microstructure, all samples show predominant columnar grains along the build direction similar to the samples from the previous build. Closer examination reveals formation of equiaxed grains along the first few layers after each un-melted powder layer defect. Such grain formation can be explained by the combined effect of lower thermal gradients due to the presence of powder particles, and lower starting grain sizes comparable with the powder particle size distribution. After these first equiaxed layers, epitaxy again prevails for the remainder height of the sample.

Sample 6 continues to grow equiaxed grains for several layers (~1 mm) from the bottom surface before it shifts to epitaxial columnar grains as the build progresses. This trend of greater equiaxed grain fraction than the other samples is prevalent even when un-melted powder layer defect occurs in sample 6. From the thermal model perspective, the highest melt current (30 mA) used for this sample leads to the lowest thermal gradient of all fabricated specimens, and thus, promotes a solidification condition that is more favorable for equiaxed grain formation. However, when there is no powder layer defect, it is observed that the equiaxed grains ultimately fall back to epitaxial columnar ones, the reason for which is hypothesized to be the superheat effect from the high melting current beam that can increase the local temperature far beyond the liquidus temperature of the feedstock powder, and therefore, can re-melt the previously solidified grains of several layers. This effect was reported by Spittle, (2006) in casting of alloys wherein the fraction of columnar growth increased at the expense of equiaxed grain fraction because of its re-melting caused by a superheated pouring temperature. Nevertheless, this rather unusual approach of fabricating copper blocks by scanning same layer multiple times via EB-PBF process shows a direction toward having a possible CET when other factors such as the melt current, substrate temperature are tuned in favorably that can reduce G almost by half ($\sim 5 \times 10^5$ K/m from $\sim 1 \times 10^6$ K/m).

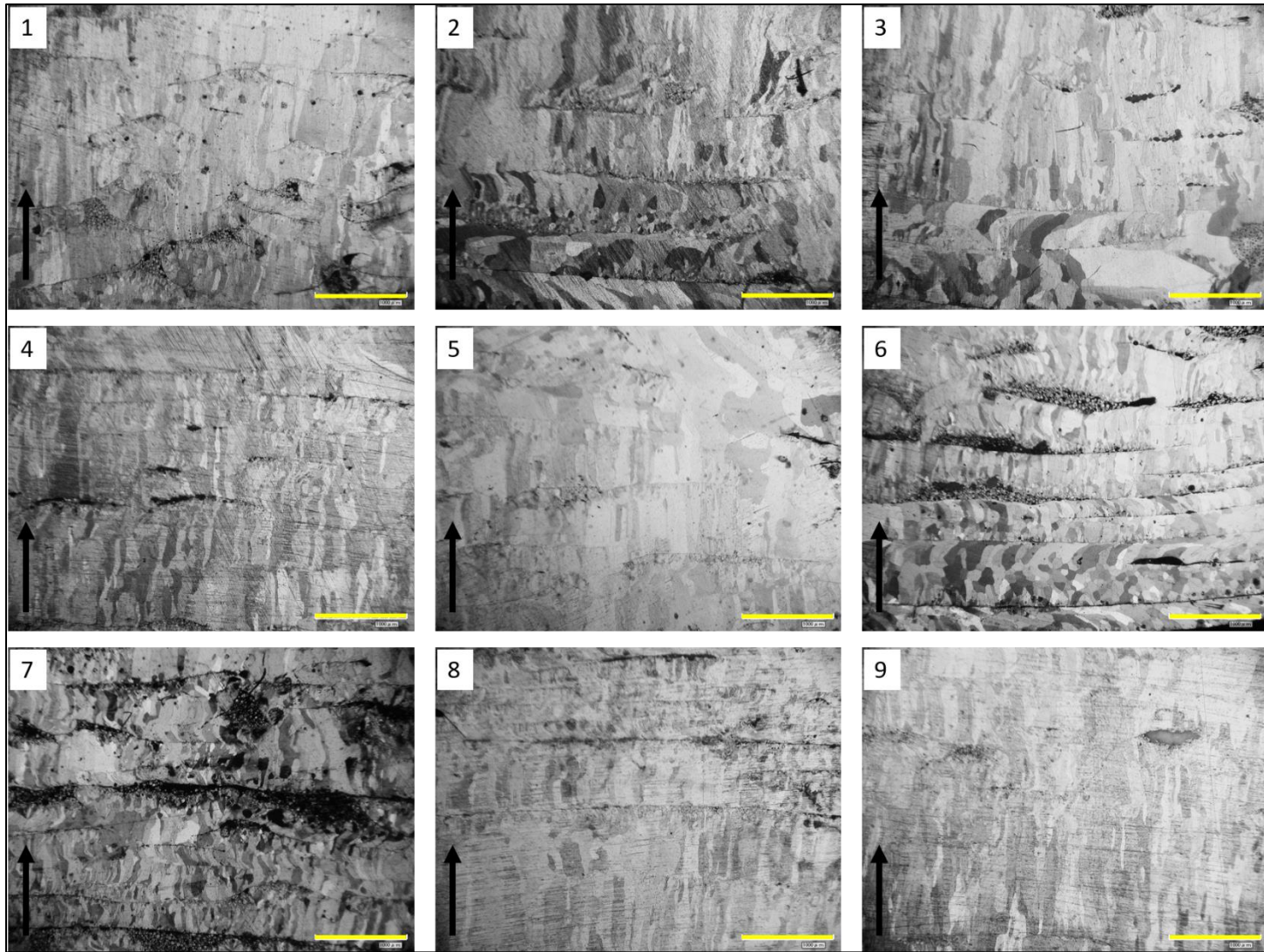


Figure 3-20. Optical micrographs showing the microstructure for each specimen from Build 2. Black arrow shows the build direction, yellow line represents the scale bar (1000 μm). Sample number is given in the top left inset of each micrograph.

A further closer observation of an equiaxed region in sample 6 reveals equiaxed grains with a size scale $\sim 100 \mu\text{m}$ along the build direction. The optical image in Figure 3-21b illustrates equiaxed grains with sharp grain boundaries, clear of any micron-scale precipitate structures. In Figure 3-21c-d, a further magnified optical and SEM image are shown, respectively. It is seen that within the equiaxed grain region, solidified copper dendrites are oriented randomly across different grains, quite in contrast to the columnar region where majority of the grain orientations are in the similar direction, as seen in Figure 3-18. Similar random orientation in the equiaxed grains has been reported in other material systems (Hadadzadeh et al., 2018; Helmer et al., 2016), and is seen in pure copper produced by L-PBF process where randomly oriented nano-scale subgrain structure becomes visible within the micron-scale equiaxed grains (Yan et al., 2020).

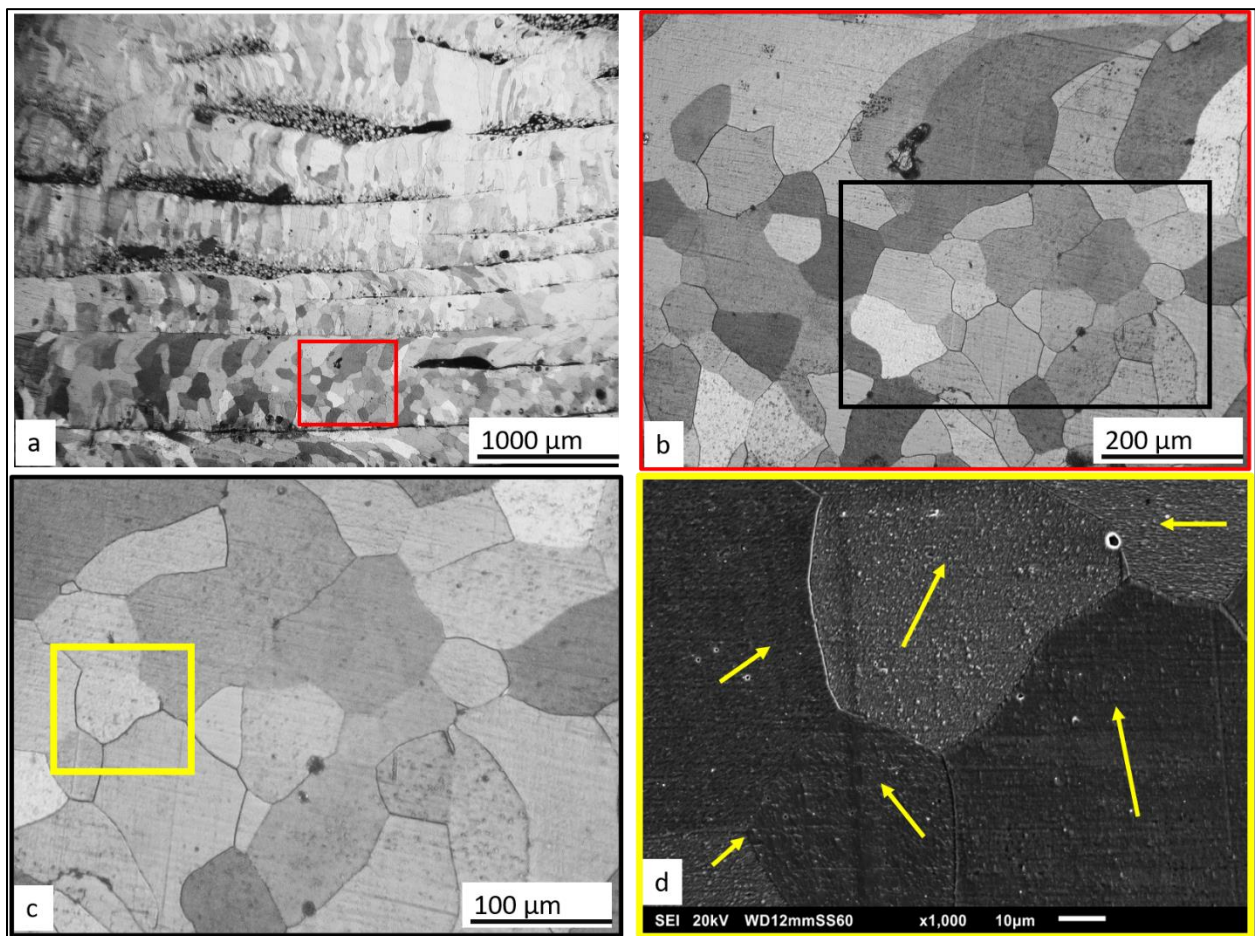


Figure 3-21. Optical and Electron microscope microstructure of a selected equiaxed grain region in sample 6. Yellow arrows indicate at the growth directions. Note the different scale sizes.

3.6 Conclusions

CET solidification map is helpful in understanding the resulting grain structure of materials in any solidification process, and therefore, a CET map is developed based on existing models in this chapter for unalloyed copper fabricated by EB-PBF process. The use of a numerical thermal model enables the user to obtain an average thermal gradient and solidification velocity value of the melt pool for the chosen process conditions. These two aspects are then combined in order to establish a process-structure relationship which suggests that increasing the melt current, scan velocity, or the substrate temperature can lead to the favorable conditions for columnar to equiaxed transition. However, the assumptions made in both CET and thermal model can have implications in the model outcomes, and the overall experimental design thereof. The thermal model assumes values for some variables within the baseline reported in literature, and such assumptions can alter the temperature profile for a given process parameter set. Further, the model assumes homogeneity of the substrate and powder bed, a scenario that deviates significantly in practice. As the powder properties departs from the nominal values used in the model, the outcome becomes less accurate in predicting the process temperatures. This particularly ties up with the calculation of cooling rate and thermal gradient, as they are dependent on the local node temperature values in each simulation result. Therefore, choice and rationality of these variable values are elemental in the thermal model and overall workflow of the method presented in this chapter. Although the model assumptions are not verified experimentally in this study, it is hypothesized that by taking their values from the literature, the overall deviation can be minimized. Additionally, the sensitivity analysis of the thermal model and CET model indicates that the models are sensitive to only one or two parameters that is/are assumed. It is noted from the literature that for similar material system, different values of same variables are used by different authors (e.g. for IN 718, Raghavan, et al. (2016) chose a nucleant density of $2 \times 10^{15}/\text{m}^3$, while Plotkowski, et al. (2017a) chose $10^{11}/\text{m}^3$). Therefore, it is argued that the assumptions taken in the thermal and CET model in this study are reasonable as long as these are used within the same process setup, and modifications need to be made if they are to be used for other material/process system.

Nevertheless, it is seen from the experimental builds that pure copper tends to swell up at the edges when a high melt current is applied due to large differences of thermal conductivity between powder and bulk copper. High substrate temperature is also a challenge in PBF processing of copper as the powder bed tends to sinter easily at that temperature, as mentioned before. The

proposed CET map could only verify the resulting columnar microstructure within the processing space chosen here by considering the aforementioned challenges. The second build examines a different approach by melting individual block multiple times to achieve locally high substrate temperature. Initial results show that processing with such strategies leads to unstable fabrication characterized by irregular powder flows. Further, it remains unclear if the origin of equiaxed grains seen in the sample from Build 2 is lower thermal gradient dictated by the process parameters used, or they are caused by the lack-of-fusion defects. Experiments where top surface temperature is precisely monitored with high acquisition rates can be helpful in correlating process temperature and obtainable thermal gradients. That can validate the approach of predicting microstructure with the help of CET when pure copper is fabricated by EB-PBF process.

3.7 Motivation for further research

It is seen that the adopted processing condition is not well conducive of forming equiaxed grains, as they are not within the favorable G and V zone. It is, therefore, proposed to be necessary to examine the other approach of achieving growth restriction by changing the feedstock powder chemistry, and subsequently obtain an equiaxed grain structure by incorporating the solutal effect in grain refinement, discussed in detail in the next chapter.

4 Grain refinement and Columnar-to-Equiaxed Transition of EB-PBF fabricated copper by modifying powder chemistry

4.1 Introduction

Grain refinement in the EB-PBF fabrication of pure copper by modifying only the process parameters (such as melt current, scan velocity, substrate temperature, hatch depth, hatch spacing etc.) is very challenging in practical scenarios due to the high input energy density and large difference in thermal conductivities between the solidified material and surrounding powder bed. Another method used for grain refinement in materials fabricated by AM processes is to use high solute concentrations in the starting powder which then act as nucleating agents promoting heterogeneous nucleation. However, the use of grain refining solute in copper is restricted due to its demand for high purity, and subsequently, using potent solute for grain refinement of copper in AM is not studied to any appreciable extent. This chapter investigates the effect of oxygen addition in the feedstock powder on heterogeneous nucleation events and seeks to understand a favorable powder chemistry that can lead to equiaxed grain formation. First, a literature review of the current practices of grain refinement for different alloy systems in AM is presented, along with a thorough description of grain refinement of copper in casting that illustrates the effect of adding different solute elements. It is seen from the literature review that the potency of the solute, and the solidification conditions, especially the cooling rate, are the controlling factors which determine the extent of heterogeneous nucleation. Since oxygen is the only second element present in the powder feedstock in abundance, its effect on the CET and related thermodynamic phenomena is examined first. Preliminary experiments are conducted to understand the processability of different powder batches with different oxygen content. Although, the initial results support the hypothesis of refining copper by adding high concentration of oxygen under favorable processing conditions, further experiments were conducted with a powder feedstock having moderate oxygen content. It is observed that equiaxed grains can be achieved in the fabricated solids when moderately high (>1000 wt. ppm) oxygen content and suitable process parameters are selected.

4.2 Literature Review

4.2.1 Solutal effect on CET of alloys fabricated by AM processes

Since solute concentration in alloys plays important role during solidification by creating constitutional undercooling in front of the columnar front, manipulating solute type and its fraction has the potential to produce equiaxed grains and thereby achieving the CET. In both the AM and casting community, the growth restriction factor Q is often used to characterize this undercooling effect, and therefore the potency of the solute element. For example, Bermingham, et al. (2020, 2019) explored different solutes available for the Ti-6Al-4V alloy, and chose Ti-3Al-8V-6Cr-4Mo-4Zr based on their growth restriction factors along with La_2O_3 as a nucleant particle. They observed equiaxed grains with a fraction $>85\%$ when the thermal gradient was kept at the lowest possible value by using very high energy densities. The authors concluded that the equiaxed grain formation by using highly potent solute element and grain refining La_2O_3 is dependent on their orientation relationship with the parent material and the particle size distribution, with bigger particles resulting in higher undercooling and more nucleation during solidification. Zhang, et al. (2019) investigated the grain refinement of Ti-6Al-4V in a laser deposition system by using copper as the solute element, which has a high Q value of 110.5 K. They found that a higher solute content of copper results in more refined equiaxed grains because of the constitutional undercooling due to solute segregation of copper around the β -phase dendrites. Yang, et al. (2018) examined the effect of added solute of 1.08 wt.% Scandium on the microstructure of Al-Mg-Zr alloy during laser melting process. The authors reported a 100% area fraction of equiaxed grains when processed at high substrate temperature and high energy input conditions. High nucleation activity of Scandium at the melt pool boundaries, as seen in the microstructure, was concluded to be an effect of a low nucleation barrier due to the re-melting of previously solidified layer.

In a study of a high entropy alloy, Guan, et al. (2019) observed equiaxed grain fraction over 95% when processed at high beam power conditions. The authors proposed a nucleant density of $3 \times 10^9/\text{mm}^3$, which is far greater than what is commonly observed in AM. However, the authors argued that this high value came from a combination of nucleating particle and dendrite fragments within the melt. Mahbooba, et al. (2017) also reported grain refinement in Ti-6Al-4V alloy using hypoeutectic boron additive in an EB-PBF set up. Although no CET was observed in the fabricated samples, a reduction in the length and width of β -grains and a break-down in the Widmanstätten structure of α -grain colonies was observed when boron addition was high.

4.2.2 Grain refinement of copper in casting

Although pure aluminum or magnesium and their alloys are extensively studied with regard to the formation of equiaxed grains, pure copper and copper alloys has not been explored much, and its mechanism of equiaxed grain formation and grain refinement for different solute types is relatively an open research area for now. For example, at a nano-scale it is found (K. Chen et al., 2016) that iron rich nanoparticles act as potent nucleant at high cooling rates for Cu–10Sn–2Zn–(1–3)Fe–0.5Co alloy when particle diameter is less than 100 nm. At micro and macro scales, several authors have reported grain refinement in copper alloys via alloying or inoculating with potent nucleants, a review of which is given by Czigler and Schumacher, (2016). Yet, for binary copper alloying system, systematic examination of the effects of alloying elements on grain morphology is limited to few research groups, and is mostly aimed at producing commercial grade DHP (Deoxidized High Phosphorus) copper or other types of copper alloys, not focusing on pure oxygen free (OFE) grade copper. For example, Czigler, et al. (2017) investigated the contribution of different alloying elements in grain refinement by comparing their growth restriction factor (Q), which leads to finer grain structure at higher values as a direct result of slower growth rate, slower latent heat release, and higher undercooling. The authors used the free-grain-growth model (Greer et al., 2000) to predict the grain sizes as a function of Q -values for the alloying elements investigated. However, as several parameter values are not available in the literature, the assumed values in the model tend to be erroneous. As a result, the authors could not find good correlation between Q -values and grain sizes and attributed the mismatch to a possible formation of non-metallic or intermetallic impurity as a result of in-situ reactions.

In another study by the same authors (Czigler and Schumacher, 2017a), a more accurate expression for Q , formulated as the rate at which constitutionally undercooled zone is developed ahead of solid liquid interface at zero fraction solid, was used in another attempt to correlate Q with grain sizes for different alloying elements. From their binary phase diagram calculations performed using commercial thermodynamic software packages, it was observed that Niobium, Beryllium and Lithium had very high growth restriction potency while common alloying elements of copper such as Aluminum, Tin, Zinc and Nickel had low Q -values. Oxygen was also reported to have a very high Q -value (38.02 K) at a nominal composition of 1 wt.%, resulting in high grain refinement as found by Kobayashi and Shingu, (1988) in a hypo-eutectic Cu-O system.

Nevertheless, no reliable correlation is found even with the corrected formula of Q , the reason for this is hypothesized to be related with cooling rate of the process and the alloying concentration.

The use of rare earth elements in grain refining of cast copper has been a popular practice. In their study for CET of pure copper with lanthanum addition, Wu, et al. (2018) examined two different alloys containing 0.1 wt.% and 0.2 wt.% lanthanum, and compared with pure copper cast with similar processing conditions at a cooling rate of 50°C/min. They found coarse columnar grains in pure copper which shifted to fine columnar and completely equiaxed in 0.1 wt.% and 0.2 wt.% alloys, respectively. The DSC experiments suggested that the increased addition of lanthanum resulted in greater undercooling ahead of solid liquid (S/L) interface, and thereby, promoted equiaxed grain nucleation. From the DSC test, heterogeneous nucleation temperature was seen to increase with lanthanum addition, which resulted in a higher nucleation rate and lower nucleation undercooling, which then led to the formation of equiaxed grains. The source of nucleation was found to be fragmented copper grains, mostly equiaxed in appearance, floating in the melt. The number of these grains increased with an increase in lanthanum, ultimately leading to a more enhanced grain refinement in copper.

Chen, et al. (2014) also investigated the effects of lanthanum on otherwise pure copper for different lanthanum additions ranging from zero to 0.32 wt.%. As the solid solubility of lanthanum is very low in pure copper, it forms an intermetallic second phase Cu_6La at high lanthanum additions. This second phase then precipitates out to the grain boundaries, and suppresses grain growth by its pinning effect, therefore leading to grain refinement in copper. Two rationales were given for the actual process of equiaxed grain formation: dendritic arm fragmentation with more lanthanum addition, and heterogeneous nucleation of copper around lanthanum-rich particles (Oxides, Sulphides etc.) which have lower lattice dis-registry with copper matrix. Y. Chen, et al. (2016) utilized Burden-Hunt's steady state interface theory to develop an analytical model for the calculation of critical solute concentration and critical radius of particle growth during solidification and verified the sudden CET transition at 0.14 wt.%. These are shown in Equations 1-2 below.

$$R = \frac{mC_0(k-1)}{3Gk} \dots eqn(1)$$

$$C_0 > 1.62 \left(\frac{kG}{m_l(k-1)N_0^{\frac{1}{3}}} \right) \dots eqn(2)$$

Here, R is the radius of equiaxed grain after the completion of solidification, m is the liquidus slope, C_0 is the initial solute concentration (wt.%), G is thermal gradient, k is solute partition coefficient, N_0 is the nucleant density. According to Equation 2, higher solute concentration is essential for CET if the thermal gradient is high or the nucleant density is low. Since such scenarios are common in AM processing of pure materials, the way to achieve CET in such materials is either by using highly potent solute (suggested by Equation 1) that can grow beyond the critical radius during the solidification process, or by using high solute concentrations that lead to higher undercooling. The effect of the solidification front velocity is examined by Tan, et al. (1999) who carried out experiments with pure copper mixed with three different rare earth elements under rapid solidification conditions by the melt spinning method. It was observed that the average grain size decreases when the concentration of the element increases, irrespective of the growth velocities.

Que, et al. (2013) investigated the effect of chromium addition in directional solidification of copper, and observed that for hypereutectic alloy conditions, large primary Cr-rich phases solidified first followed by a halo formation of α -Cu rich phase around them. It was suggested by the authors that high Cr-rich condition of solidified phase created deep undercooling around them and favored the halo formation of Cu-rich phase around them. The eutectic phase of Cu-rich and Cr-rich phases was thereafter solidified within this continuous α -Cu rich phase. It was also noted that higher chromium concentration led to the uniform distribution of Cr-rich phase, which helped in reducing the overall grain size.

Balart, et al. (2015) examined the possibility of refining cast DHP copper by using several alloying elements and their oxides as inoculants in a casting process. In their experiment, copper cast at 1150°C and 1100°C showed coarse and fine equiaxed grains, respectively, due to the presence of native Cu_2O particles (having higher solubility of 0.88% at 1150°C) which could act as nucleation site and grain growth restricting element, as suggested by both Cziegler and Schumacher, (2017a) and Kobayashi and Shingu, (1988). In the case of DHP copper, a specific combination of Phosphorus and Silver was reported by the authors to result in the greatest amount of equiaxed grains due to high solute enrichment at the S/L interface front.

In their seminal work on the hypo-eutectic Cu-O system, Kobayashi and Shingu (1988) examined the effects of solute concentration, solidification time, and growth rate on solidification process and grain structure development of bulk copper in high undercooled condition achieved

by means of glass slag. When bulk copper had an oxygen content of more than 0.015 wt. %, grain refinement could occur due to the long freezing range of the system that permitted dendrite arm coarsening under favorable solidification conditions as investigated by the authors in a mixture of 99.999% pure OFHC copper and cuprous oxide. In their test conditions, grain refinement did not occur for an oxygen content less than 300 ppm at any extent of undercooling, whereas fine equiaxed grain formed for oxygen content of 1260 ppm, 2400 ppm, and 2590 ppm treated at undercooling of 60 K, 130 K, and 125 K, respectively. As oxygen has a low solute distribution coefficient (k) of 0.013, it produces more secondary dendrite arms that have finer neck regions and can detach easily resulting in higher dendrite fragmentation. It also increases the S/L interfacial energy as solutes are rejected sideways around the dendrites creating solute-rich regions within the melt. With higher solute concentration around the dendrite arms, the radius of curvature becomes larger leading to greater probability of fragmentation; and as a result, finer equiaxed grains are formed for higher oxygen contents. Also, it was observed that greater undercooling yielded higher growth rate while greater solidification time resulted in a greater number of equiaxed grains, and both factors became prominent grain refining mechanisms for higher oxygen content in bulk copper melt. This process of fragmentation and equiaxed grain formation is linked by the generation of small-sized fragments that act as heterogeneous nucleation sites; and the equiaxed grains thus formed have comparable grain sizes as that of the initial dendrites.

4.3 Research Motivation

The solutal effect on columnar-to-equiaxed transition is of particular interest when other processing conditions do not favor the formation of equiaxed grains. For different AM material systems, as discussed above, this transition is controlled by adding another alloying element which has low solubility, good lattice registry, and high growth restriction factor (Q). A high Q value means high solute rejection and subsequently, high constitutional undercooling leading to a larger number of active nucleating particles (Eskin, 2008). A high Q also suppresses grain growth, and consequently reduces the release of latent heat ahead of a solid/liquid interface. As undercooling is a net effect of the competition between heat flow and latent heat release, a high Q (having an impact on both nucleation and growth restriction) can drastically change undercooling conditions, and lead to the CET (Cziegler and Schumacher, 2016). As can be seen in Equations 3-4, high

liquidus slope (m) and/or high initial solute concentration (C_0) for a given partition coefficient (k) can lead to a high Q value, which, in turn, can increase the constitutional undercooling (ΔT) and reduce the S/L interface velocity (V_{growth}). Here Ξ is solutal supersaturation and Γ is Gibbs-Thompson coefficient (Eskin, 2008) in the following equations.

$$Q = m(k - 1)C_0 \dots eqn(3)$$

$$V_{growth} = \frac{D\Delta T^2}{Q\Gamma} ; \Delta T = \Xi Q \dots eqn(4)$$

In the incoming copper powder feedstock, the solute elements are mostly within the range of ASTM F68 standard except for oxygen, which is typically within 0.1 wt.% limit. This oxygen is present as cuprous oxide, typically forming either surface oxide scales, or precipitates at the grain boundaries. As mentioned by Kobayashi in their paper (Kobayashi and Shingu, 1988), these oxides can refine the grains when the system is undercooled sufficiently. In their studies of grain refinement of copper, Balart, et al. (2016) and Romero, et al. (2013) gave values for k and m for an initial concentration of 0.1 wt.%, within the hypoeutectic region. Using those values, a Q value of 41.13 is obtained for oxygen, which is far greater than the other solute elements present in the feedstock powder [Ag = 3.66, P = 21.55, Pb = 2.66, S = 23.44, Sb = 4.78, Sn = 5.8, Zn = 0.93 after (Balart et al., 2016)]. Figure 4-1 below shows the growth restriction factor of different alloying elements of copper at similar initial concentration levels where oxygen is marked with a red circle.

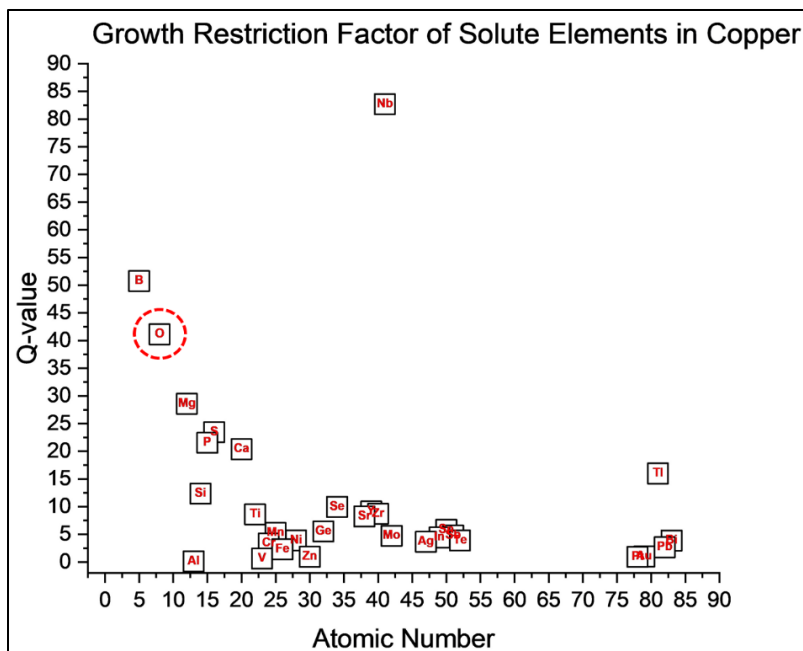


Figure 4-1. Growth restriction factor of different alloying elements of copper at initial concentration of 0.1 wt.%; adopted from (Balart et al., 2016).

Thus, cuprous oxide can be used as a grain growth restricting agent, present in the system as a second phase. As copper is susceptible to oxide formation at elevated temperatures, controlled oxidation of copper powder will result in the appropriate solute concentration, which can be used for grain refinement during the EB-PBF process. As demonstrated in the tensile study, the extra oxide can be reduced by vacuum annealing at 950°C for the amount of time dictated by the initial oxygen content. Therefore, it seems beneficial to use oxygen as the growth restricting and grain refining element in the EB-PBF processing of copper. Besides this beneficial growth restriction influence of oxygen, it also has a negligible solubility in solid copper. When solute concentration exceeds this solid solubility limit, oxygen readily forms cuprous oxide which has a lower density (6 g/cc.) than that of pure copper (8.96 g/cc.), resulting in lower shrinkage defects after solidification (Baker, 1992; Davis, 2001). With respect to the lattice parameters, it is reported by Zhao, et al. (2015) and Zhou (2009) that Cu₂O has a natural lattice misfit of 15.3%-15.4% with copper lattice. While this lattice mismatch prevents the formation of coherent interface, it increases the possibility of epitaxial growth of cuprous oxide on copper by reducing the interfacial energy. However, as the direction of solidification changes at every layer in an EB-PBF process, the growth pattern is expected to change accordingly. Further, as the oxygen content increases in the form of surface oxides scales, it enhances the powder flowability on the substrate plate even at a

high temperature. It is seen from the previous chapter that a higher substrate temperature leads to a more probable formation of equiaxed grains. Therefore, considering all these aspects, it is hypothesized that grain refinement by promoting heterogeneous nucleation and using favorable processing space is possible in the PBF fabrication of copper using cuprous oxide as the refining agent. In the following sections, the associated theory and experiments are described in detail.

4.4 Materials and Methods

4.4.1 CET for different oxygen concentration

In order to establish the advantageous contribution of increasing the initial oxygen concentration, it is necessary to theoretically validate the improvements in solidification kinetics as a function of oxygen content. Current practices of copper fabrication lie within the hypoeutectic region of Cu-O phase diagram (see Figure 4-2) where the solute content is below 0.1 wt.%. As the material system cools down, primary α copper phase solidifies first, followed by cuprous oxide segregating at the grain boundaries. However, as partition coefficient is quite low at this region, high undercooling values are not possible for a given liquidus slope and initial concentration, and therefore, the number of nucleation events remains limited. However, in the hypereutectic region of the phase diagram, high undercooling can be achieved owing to high partition coefficients and high liquidus slopes. Moreover, the primary phase of cuprous oxide can also act as heterogeneous nucleation sites for the liquid. The combined effect is the possibility of greater nucleation event as compared to initial hypoeutectic composition, therefore leading to grain refinement of the system.

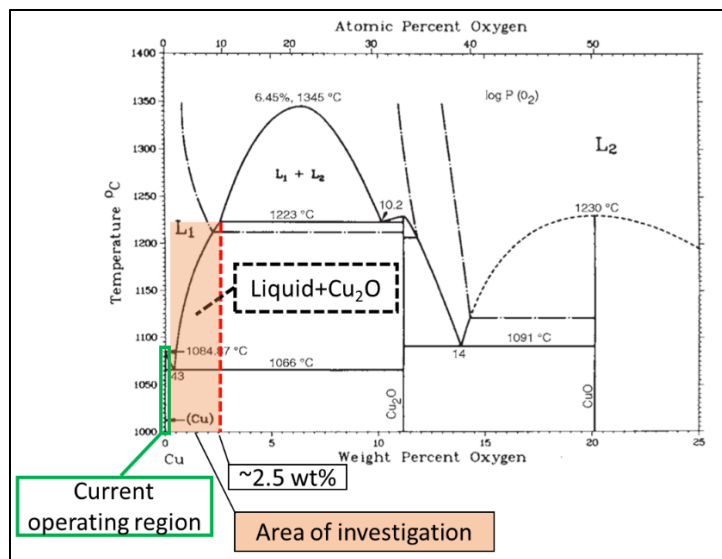


Figure 4-2. Cu-O phase diagram, adapted from (Davis, 2001).

Three different hypereutectic oxygen concentrations along with the current hypoeutectic concentration were chosen for the experimental study: 0.5 wt.%, 1.0 wt.%, and 1.5 wt.%. Reasons for selecting these three levels of concentration were the following. First, as per the phase diagram, a miscibility gap exists between ~2.5 wt.% and 10.2 wt.% which may lead to the formation of undesirable phases upon solidification. Second, as the diffusivity of oxygen in solid copper is low, it will take a much longer time to eliminate the excess oxygen by vacuum annealing process through the dissociation of cuprous oxides if the initial concentration is very high. Third, the chosen levels are not very close to each other, which allows examination of the effect of a rather steep liquidus curve at the hypereutectic region which manifests in drastic differences in the growth restriction factor.

The CET model presented in the previous chapter is applied to these three hypereutectic oxygen concentrations to obtain quantitative results of the solidification phenomena and the columnar-to-equiaxed transition curve. For the ease of reporting, following names will be used for these three powder types. Powder with initial oxygen concentration of 0.5 wt.%, 1.0 wt.%, and 1.5 wt.% will be called hyper-low, hyper-med, and hyper-high copper powders, respectively. However, thermodynamic data for these concentration levels are not found in literature, and subsequently, ThermoCalc software is used for the determination of partition coefficient and liquidus slope calculation. The TCCU2 software database is used for these calculations, and both equilibrium and non-equilibrium Scheil calculations are made. The partition coefficients of all

three powder types at given temperature are calculated using the ratio between the solute concentration in the solid fraction and solute in the liquid fraction. Liquidus slopes are calculated by measuring the change in temperature for a unit change in concentration at a given temperature. The other non-compositional parameters are kept intact in the CET model simulation, whose values are presented in Table 3-2 in the previous chapter.

4.4.2 Thermal analysis of powder using differential scanning calorimetry (DSC)

As reported by Bermingham, et al. (2019), other than the influence of the optimal process parameters, the evolution of lower thermal gradient also depends on the release of latent heat of solidification of the growing S/L interface. This latent heat is a function of interface growth rate and can affect the extent of undercooling in the liquid melt. In order to examine the effect of different levels of oxygen content on the latent heat of solidification, a series of thermal analyses are done using a TA SDT650 Differential Scanning Calorimetry (DSC) instrument. Only one heating-cooling cycle is carried out for each powder type with a heating rate of 20°C/min to 1150°C, followed by a similar cooling rate to room temperature. A constant inert atmosphere is maintained using nitrogen gas flowing through the furnace chamber at a volumetric rate of 100 mL/min. Test powder batches are made by heating copper powder in a lab furnace at 250°C under air for different time durations so that cuprous oxides form on the powder particles. The powder is mechanically stirred multiple times during the heating process to avoid any agglomeration of sintered particles. After the heating process, the oxidized powder is kept in an inert glove box to cool down to room temperature and analyzed for its oxygen content using the LECO OH836. For the DSC thermal analysis, powder samples weighing between 90-100 mg are poured into alumina crucibles which have been calibrated with the reference crucible beforehand. Before running the actual thermal cycle, nitrogen gas is fed into the system for 30 minutes at a volumetric rate of 200 mL/min to clear out air impurities. Temperature, time, and normalized heat flow are recorded throughout the cycle, and are analyzed later for the calculation of thermodynamic factors. After a cycle was finished, the solidified copper powder is imaged using a 12.3 MP Grasshopper USB 3.0 camera equipped with a Canon 100 mm lens. These photographs are analyzed for qualitative assessment of wetting of liquid copper as a function of oxygen content.

4.4.3 Single layer experiment for process parameter selection

Flowability and spreadability of powder feedstock are important factors in a PBF process as they control the quality of the powder bed, and therefore, the surface characteristics. Since copper powder sinters at elevated temperatures, its flowability reduces as the substrate is heated to a higher temperature range. However, as the surface oxide increases in an oxidized copper powder, its flowability enhances due to the increase in activation energy for sintering. While the effect of oxides on flowability is positive, its lower thermal and electrical conductivities lead to charge build-up during EB-PBF process that results in smoking events causing serious qualitative problems with the powder bed. Therefore, it is necessary to understand the constraints related to the processing of copper powder with high oxide contents. To address this issue, single layer experiments are conducted for different substrate temperature, melt current, and scan velocity combinations for all three powder types.

A circular OFHC copper plate is machined with six pockets with a diameter of 25.4 mm and a depth of 3.5 mm. The pockets are separated from each other by 33 mm so that thermal effect of one will be negligible on its neighboring pockets. These pockets are then filled with hyper-low, hyper-med, and hyper-high copper powder in a circular fashion with specific care taken to level them off with the top face of the substrate plate. Each type of powder is made by blending 99.9% pure cuprous oxide obtained from Alfa Aesar with a precursor pure copper powder to their exact stoichiometric weight fractions for this initial experimental run. Each variant is replicated once to examine the effects of different melt current and scan velocities for a given substrate temperature. The experimental plan with important process-related parameters is presented in Table 4-1 below. It is to be noted that the powder inside those pockets is not pressed or sintered in advance. A blind hole at the center of the substrate plate is drilled from its bottom side to insert a thermocouple underneath the plate, which is utilized to monitor the substrate temperature throughout the process. The substrate plate is placed on top of the build piston to avoid a direct pathway for conductive heat transfer, effectively insulating the plate from the system. A circular area of 25 mm diameter at the center is scanned with highly defocused beam for substrate heating purposes in steps of 50°C to the desired temperature. Since the process is extremely fast, a Fastcam SA-X2 1000K high-speed camera equipped with 100 mm Canon lens is used to capture the extent of smoking events as a function of applied process parameters at frame rate of 12,500 per second. A rectangle of 10 mm by 10 mm is scanned individually inside each pocket with respective process parameters, and

a ten-minute gap is given in between two pockets to stabilize the substrate temperature from overheating. The overall set up is shown in Figure 4-3 along with the table for process parameters.

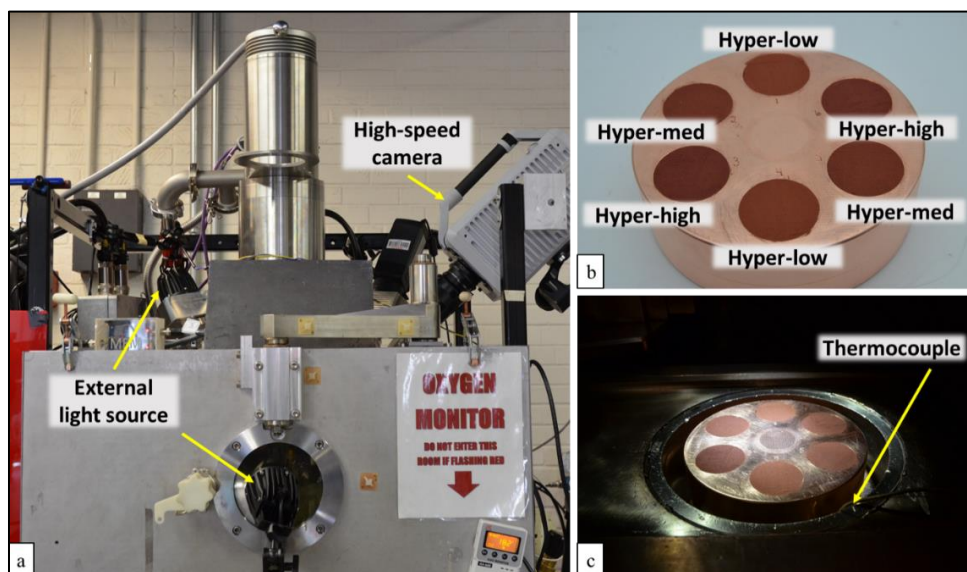


Figure 4-3. a. High speed camera and external light sources set up on Arcam A2 machine; b. Substrate plate with six pockets filled with different powder variants; c. Substrate plate placed inside machine on top of build piston.

Table 4-1. Melt current and scan velocity values for the pocket experiment at different substrate temperatures.

Block #	Oxygen content (wt.%)	Bed temperature					
		Experiment #1: 450°C		Experiment #2: 525°C		Experiment #3: 600°C	
		Current	Speed	Current	Speed	Current	Speed
1	0.5	16	1300	16	1300	14	1150
2	1	16	1300	16	1300	14	1150
3	1.5	16	1300	16	1300	14	1150
4	0.5	18	1450	14	1150	12	1000
5	1	18	1450	14	1150	12	1000
6	1.5	18	1450	14	1150	12	1000

4.4.4 Feasibility study via experimental builds with hypoeutectic high oxygen content powder

Processing space with moderately high oxygen content powder within the hypoeutectic region of Cu-O phase diagram is examined through a series of experimental builds. Although the

DSC study and the literature review of solutal effect on equiaxed grain formation indicate at higher chances of CET with higher solute concentration, oxygen content is limited to ~0.1 wt.% in these builds. While having such amount of oxygen still helps in restricting the grain growth, reduction of the resultant copper oxide remains feasible with the vacuum annealing process conducted for reasonably long durations. Characterization of the powder feedstock is done through Microtrac S3500 and JEOL 6010LA for powder size distribution and overall powder morphology analyses, respectively. It is to be noted here that the powder was hydrogen treated at 400°C as per the method shown by Ledford, et al. (2019), and subsequent oxygen pickup was a result of storing the powder for long time in an air environment. Oxygen content is measured using LECO OH836 before each build to ascertain powder composition consistency. Blocks of 10 × 10 × 10 mm size are printed on a circular OFHC copper plate measuring 86 mm diameter and 40 mm thickness with a layer height of 40 μm in an Arcam A2 machine, similar to the tensile test samples. Power analyzer is turned off to prevent the machine from overriding the speed and melt current values. Other process related parameters are shown below in Table 4-2. Note that some of the blocks are turned off during their fabrication due to the defects such as curled up edges, high porosities, melt balling etc. that compromised the overall block quality.

Since copper powder with high oxygen content flows better at high temperature than pure copper, substrate temperature is aimed at ~450°-500°C during these builds. However, because of the high conductivity of OFHC copper substrate, the temperature goes down very fast, and the gets stable around 350°-375°C. In the last experimental build, high preheat I currents and preheat II are enabled to keep the substrate at high temperature throughout the build. From the thermal model calculations shown in the previous chapter, high substrate temperatures in the range of 500°-600°C are favorable for the CET. Therefore, in the last build, it is expected that a favorable processing condition is attained in terms of substrate temperature along with the solutal effect of moderately high oxygen content present in the powder.

A particular sequence of plate heating is used for all the builds. Sweep current is set to 10, 15 and 25 mA in three successions. Initially, only 10 mA sweep current is used such that the charge build-up around the substrate plate is not enormous. After it reaches to 150°C, the sweep current is increased to 15 mA until the temperature reaches 300°C. After that, the build piston is moved up and down to break off the sintered powder around the plate such that the piston does not get stalled during the build. The maximum sweep current is used in the end to reach the desired plate

temperature. This successive plate heating procedure is required to prevent smoking of the powder when high oxygen content is present.

Table 4-2. Process parameters used in the fabrication of blocks during the feasibility study builds.

Blocks that are turned off due to defects are given in italics fonts.

Build	Sample #	Current (mA)	Power (W)	Velocity (mm/s)	Line offset (mm)	Velocity*Line offset*Layer thickness	Energy density (J/mm³)
Build 1	<i>1</i>	8	<i>480</i>	<i>1000</i>	<i>0.13</i>	<i>5.2</i>	<i>92.3</i>
	<i>2</i>	<i>10</i>	<i>600</i>	<i>1150</i>	<i>0.13</i>	<i>5.98</i>	<i>100.3</i>
	<i>3</i>	12	720	1300	0.13	6.76	106.5
	<i>4</i>	8	<i>480</i>	<i>1300</i>	<i>0.13</i>	<i>6.76</i>	<i>71.0</i>
	<i>5</i>	<i>10</i>	<i>600</i>	<i>1450</i>	<i>0.13</i>	<i>7.54</i>	<i>79.6</i>
	<i>6</i>	<i>12</i>	<i>720</i>	<i>1600</i>	<i>0.13</i>	<i>8.32</i>	<i>86.5</i>
	<i>7</i>	12	720	1600	0.13	8.32	86.5
	<i>8</i>	<i>10</i>	<i>600</i>	<i>1750</i>	<i>0.13</i>	<i>9.1</i>	<i>65.9</i>
	<i>9</i>	<i>12</i>	<i>720</i>	<i>1900</i>	<i>0.13</i>	<i>9.88</i>	<i>72.9</i>
Build 2	<i>1</i>	<i>12</i>	<i>720</i>	<i>1600</i>	<i>0.13</i>	<i>8.32</i>	<i>86.5</i>
	<i>2</i>	16	960	1600	0.13	8.32	115.4
	<i>3</i>	18	1080	1600	0.13	8.32	129.8
	<i>4</i>	<i>20</i>	<i>1200</i>	<i>1600</i>	<i>0.13</i>	<i>8.32</i>	<i>144.2</i>
	<i>5</i>	<i>12</i>	<i>720</i>	<i>1800</i>	<i>0.13</i>	<i>9.36</i>	<i>76.9</i>
	<i>6</i>	16	960	1800	0.13	9.36	102.6
	<i>7</i>	18	1080	1800	0.13	9.36	115.4
	<i>8</i>	20	1200	1800	0.13	9.36	128.2
	<i>9</i>	<i>12</i>	<i>720</i>	<i>2000</i>	<i>0.13</i>	<i>10.4</i>	<i>69.2</i>
	<i>10</i>	16	960	2000	0.13	10.4	92.3
	<i>11</i>	18	1080	2000	0.13	10.4	103.8
	<i>12</i>	20	1200	2000	0.13	10.4	115.4
	<i>13</i>	<i>12</i>	<i>720</i>	<i>2200</i>	<i>0.13</i>	<i>11.44</i>	<i>62.9</i>
	<i>14</i>	16	960	2200	0.13	11.44	83.9
	<i>15</i>	18	1080	2200	0.13	11.44	94.4
	<i>16</i>	20	1200	2200	0.13	11.44	104.9
Build 3	<i>1</i>	12	720	1400	0.13	7.28	98.9
	<i>2</i>	14	840	1400	0.13	7.28	115.4
	<i>3</i>	16	960	1500	0.13	7.8	123.1
	<i>4</i>	16	960	1800	0.13	9.36	102.6
	<i>5</i>	12	720	1600	0.13	8.32	86.5
	<i>6</i>	14	840	1600	0.13	8.32	101.0
	<i>7</i>	16	960	1700	0.13	8.84	108.6
	<i>8</i>	16	960	2000	0.13	10.4	92.3
	<i>9</i>	<i>12</i>	<i>720</i>	<i>1800</i>	<i>0.13</i>	<i>9.36</i>	<i>76.9</i>

Table 4-2. Continued.

	10	14	840	1800	0.13	9.36	89.7
	11	16	960	1900	0.13	9.88	97.2
	12	16	960	2200	0.13	11.44	83.9
	13	12	720	1800	0.13	9.36	76.9
	14	14	840	2000	0.13	10.4	80.8
	15	16	960	2100	0.13	10.92	87.9
	16	16	960	2400	0.13	12.48	76.9

The overall process map is shown in Figure 4-4. Process parameters are chosen such that the volumetric energy density is within the dense processing space of pure copper. However, the oxygen content present in the powder poses challenges in terms of the melt theme, wherein both low and high melt current settings result in either porosity or swelling based on the scanning speed. Therefore, high current-high velocity or low current-low velocity parameters are not considered in these builds.

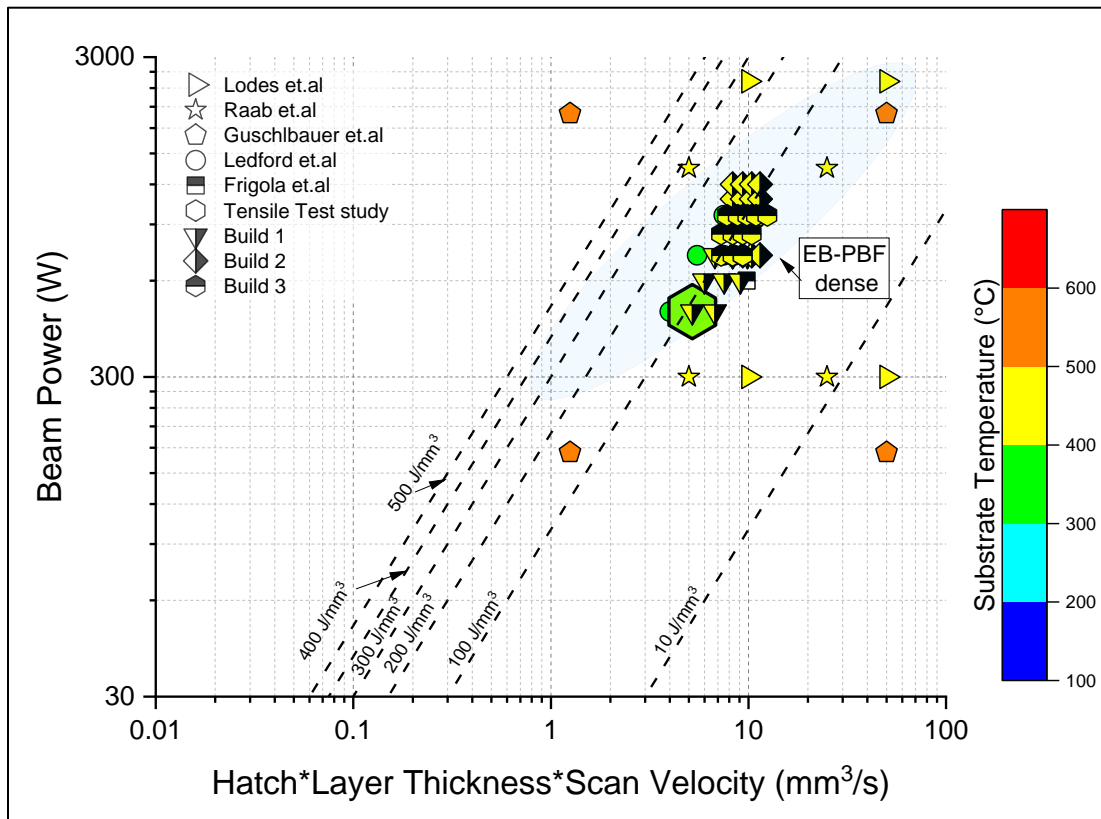


Figure 4-4. Processing space of the experimental builds in comparison to the literature and the tensile study conducted in the first phase of research.

4.4.5 Microstructural and mechanical characterization of the build specimens

Microstructure of selected specimens from all three builds are characterized using a Hirox KH7700 optical microscope after the specimens are sectioned along the build direction, and then mounted and polished. Before etching with Ammonium Persulphate, four micrographs are taken of each specimen to obtain the optical density. Selected samples are viewed under JELO 6010LA SEM in secondary electron imaging mode. Specimen that produced equiaxed grain along the build direction, is further viewed in the FEI Quanta 3D for higher magnification and better resolution of the individual grain. To characterize the mechanical strength of the fabricated parts, microhardness measurements are taken on these selected samples using a LECO M400 instrument with Vickers indenter. A load of 100 gf and a dwell time of 10 seconds are used for each of the ten indentations that are made along the build direction with a 500 μm distance in between each indentation. The average of these ten values are then reported for each of the tested samples.

4.4.6 Vacuum annealing of selected build specimens

Since vacuum annealing reduces the oxygen content in EB-PBF fabricated copper by the dissociation process evidenced in the tensile specimen spreadsheet in Appendix A, Table 6-4, selected specimens from these three builds are vacuum annealed at 950°C in a Thermo-Scientific vacuum tube furnace under a pressure of 5×10^{-5} mbar (shown in Figure 4-5) several times. Given the high starting oxygen content in the solids, annealing time is progressively increased to 24 and 48 hours considering the slow rate of diffusion of oxygen in solid copper (Magnusson and Frisk, 2013). Afterwards, oxygen content of the annealed samples is measured using LECO OH836.

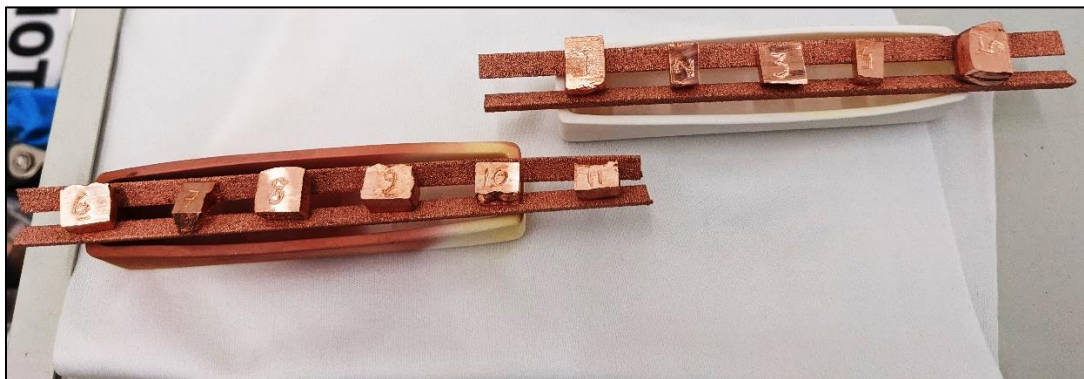


Figure 4-5. Specimens kept on pure copper bars in alumina crucible before vacuum annealing.

4.5 Results and Discussion

4.5.1 Effect of oxygen concentration on CET

In general, solutes that promote columnar-to-equiaxed transition in metallic alloy systems tend to push the transition line further in the direction of columnar region. This facilitates the formation of equiaxed grains for larger thermal gradients which would have resulted into columnar grains if the concentration were lower. However, before delving into the CET model results for different oxygen concentrations, evaluation of thermodynamic properties through ThermoCalc software is presented first because of the scarcity of any published data on these entities of hypereutectic Cu-O system. Figure 4-6 shows here the non-equilibrium Scheil solidification curves for hypoeutectic (0.1 wt.%, referred to as Hypo henceforth) and all three hypereutectic Cu-O systems where the abscissa represents the solid mole fraction, and the ordinate represents the system temperature (1060°C - 1200°C).

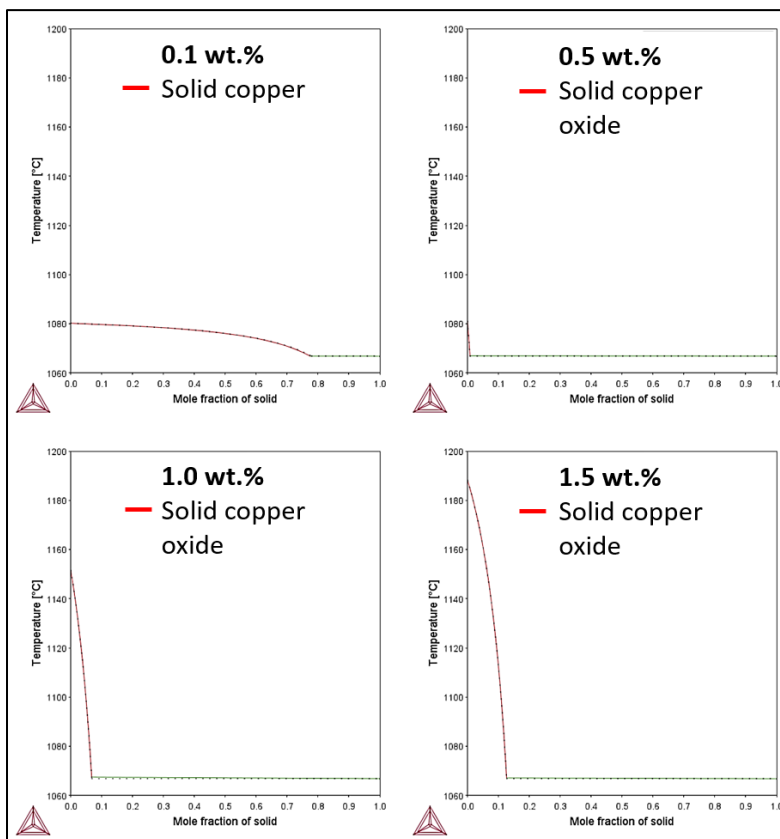


Figure 4-6. Non-equilibrium Scheil curves for copper with different oxygen concentration; obtained using ThermoCalc.

Following features can be gleaned from these solidification graphs.

1. For hypoeutectic copper system
 - a. Temperature range of solidification is low ($\sim 14^{\circ}\text{C}$)
 - b. Fraction of primary copper phase is high, and the eutectic fraction is low
2. For hypereutectic copper system, as the oxygen concentration increases
 - a. Solid copper oxide fraction increases while eutectic fraction decreases
 - b. Starting solidification temperature increases
 - c. Temperature range of solidification increases (from $\sim 14^{\circ}\text{C}$ to $\sim 122^{\circ}\text{C}$)

In order to calculate the partition coefficients and liquidus slopes from the Scheil curves, solid mass fraction is calculated first using the molar mass information of the system. Next, the oxygen concentration in solid is calculated using the stoichiometry of the phase, and thereby, the oxygen concentration in the liquid is calculated by subtracting the former from the initial oxygen concentration. The ratio between the two gives the partition coefficient, while the liquidus slope is calculated as the change in temperature for a unit change in solute concentration. It is seen from Figure 4-7 that the partition coefficient for hyper-low, hyper-med and hyper-high agree very well with those calculated from equilibrium phase diagram for a given temperature range.

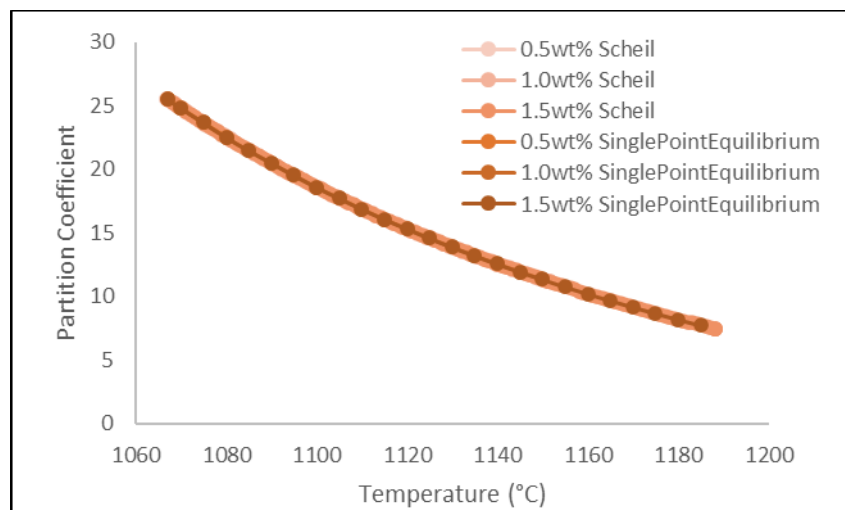


Figure 4-7. Partition coefficient of hypereutectic copper systems from both Scheil and equilibrium phase diagram calculations.

Once these thermodynamic parameters have been evaluated, CET calculation for different Cu-O systems is undertaken using the process steps described in the previous chapter. The CET

curves along with other related phenomena are presented sequentially in Figures 4-8 to 4-11, followed by detail discussion on the respective model outcomes. Partition coefficients of 11.35, and liquidus slopes of 84.99, 89.99, and 95.10 are used for hyper-low, hyper-med, and hyper-high copper systems, respectively. The other non-compositional parameters are kept at the same level as in the CET calculation of hypoeutectic system.

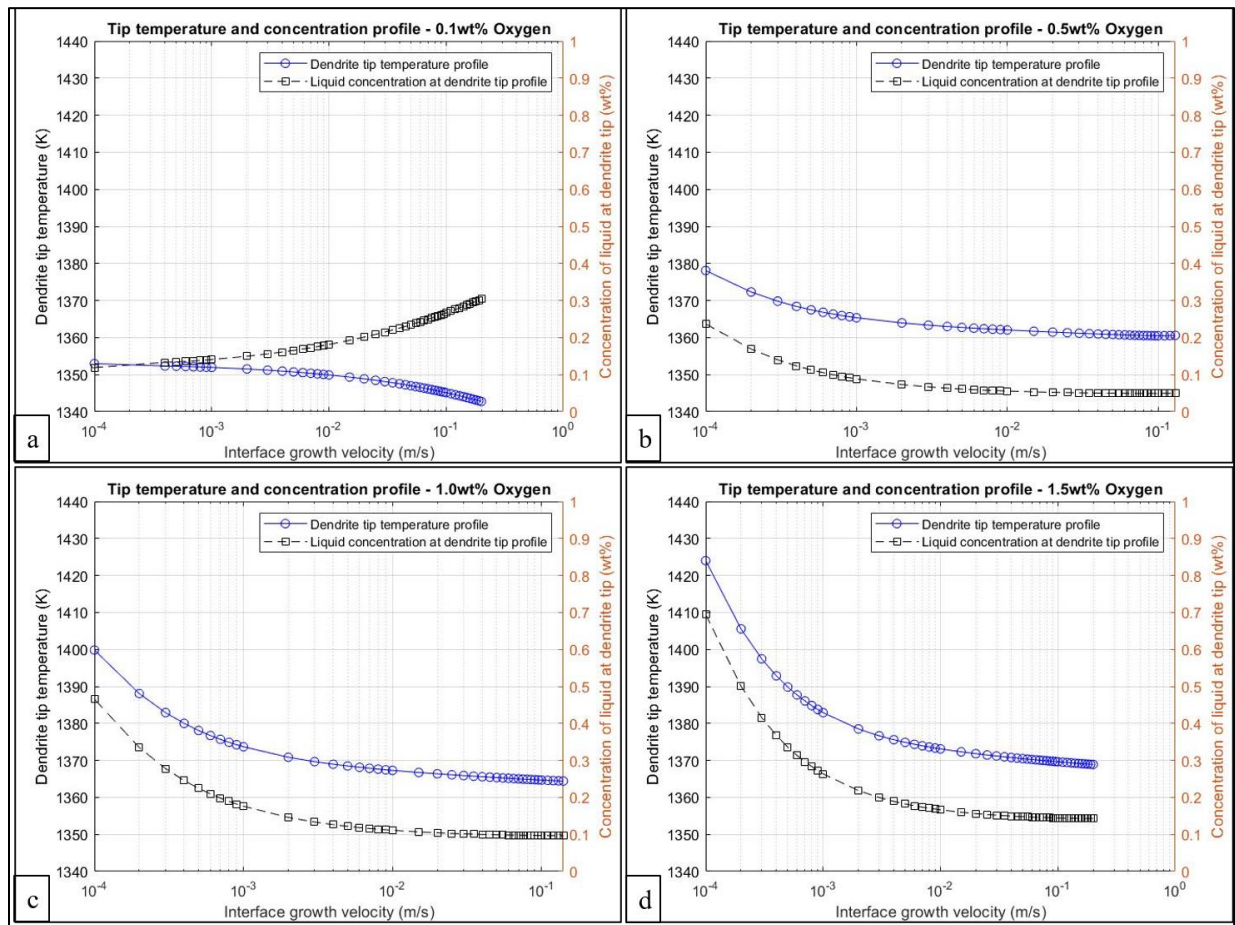


Figure 4-8. Tip temperature (blue line) and solute concentration in the liquid at dendrite tip (black line) for different solidification growth velocities. a. Hypoeutectic, b. Hyper-low, c. Hyper-med, d. Hyper-high.

As illustrated in Figure 4-8, a common trend of high tip temperatures at low solidification velocities and vice versa can be seen across all oxygen concentration levels. As shown in Equation 31 in the previous chapter, tip temperature depends on liquidus slope, initial concentration, and total undercooling for a given velocity. This trend hence suggests that undercooling increases

significantly as a function of solidification velocity for all solute levels as the other two factors remain relatively unaffected with change in velocity. Moreover, it is noted that for a given growth velocity (especially when the value is at the high end), the tip temperature is higher in systems with higher oxygen content. This phenomenon is caused by the combined effects of two attributes of the respective systems: liquidus slope increases as the oxygen content increases, and more solute depletion occurs as the initial solute concentration increases. As a consequence, the temperature difference between the solid and liquid increases as a function of increasing solute concentration resulting in higher undercooling at a given solidification velocity. This feature can be clarified using the undercooling profile ahead of dendrite tip for three different growth velocities as shown in Figure 4-9.

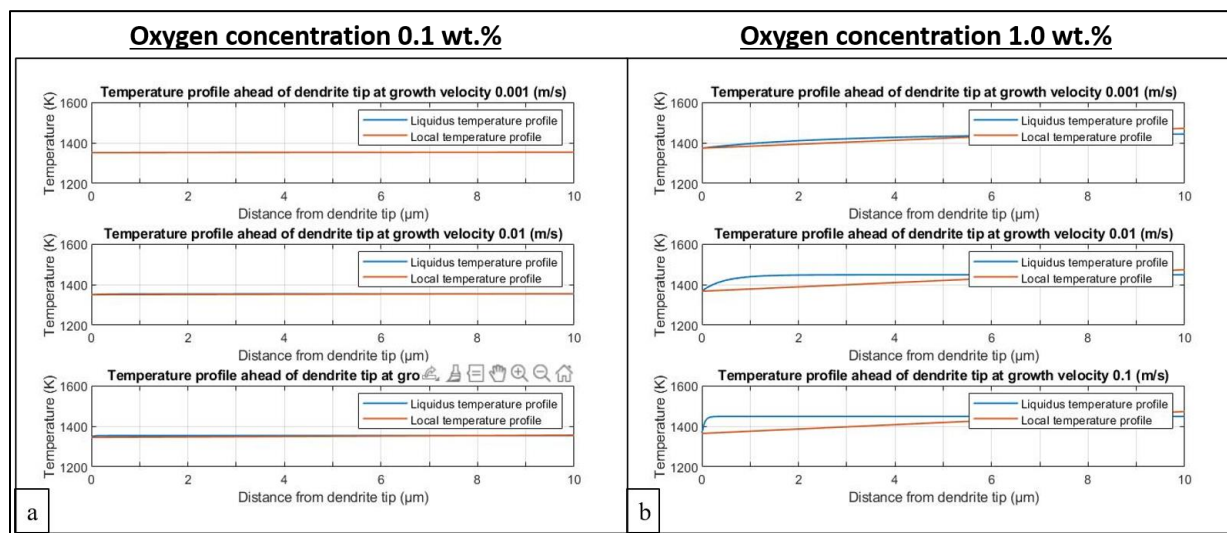


Figure 4-9. Liquidus and local temperature profiles as a function of growth velocities of 0.001 m/s, 0.01 m/s, and 0.1 m/s; a. Hypoeutectic, b. Hyper-med copper oxygen system.

It can be seen that undercooling at low solidification velocities is low for the representative copper alloy systems shown in Figure 4-9, and the undercooling increases as a function of velocity. This is further illustrated in Figure 4-10 below for all four types of copper-oxygen systems at same velocity conditions. This is largely because of the increase in constitutional undercooling where solute rejection (hypoeutectic) or solute depletion (hypereutectic) effects become more prominent at high solidification velocities. The calculated values of other three undercooling factors (thermal, curvature, and kinetic) remain more or less insignificant with respect to the constitutional

undercooling, and hence the overall trend of total undercooling is dictated by the solute concentration profile in the liquid ahead of dendrite tip as shown in Figure 4-8. As the hyper-high copper alloy depletes more solute during its β -phase formation, the liquid ahead of S/L interface lacks more solute at higher solidification velocities, thus resulting in very high total undercooling values compared with other three conditions. Therefore, it can be inferred that higher initial solute concentration leads to better possibilities of nucleating equiaxed grains ahead of S/L interface owing to their enhanced undercooling effects.

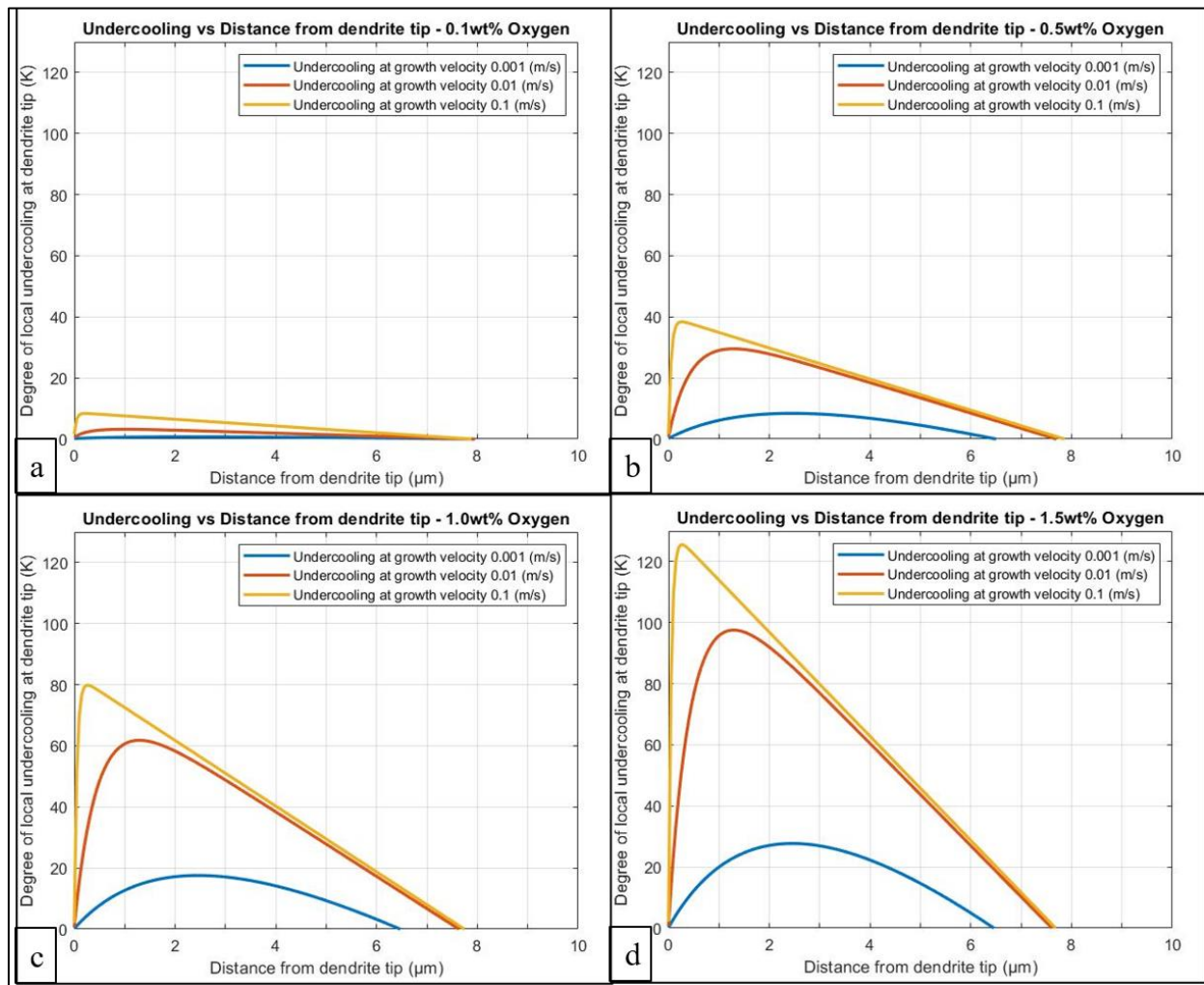


Figure 4-10. Total undercooling for different solidification velocities. a. Hypoeutectic, b. Hyper-low, c. Hyper-med, d. Hyper-high.

This, in turn, affects the CET by expanding the favorable processing space for equiaxed grain development as the solute content in the alloy is increased. Figure 4-11a below shows the

CET for hypoeutectic and all three hypereutectic copper oxygen systems explored here; along with a comparison graph of total undercooling among all system variants presented in Figure 4-11b. The latter shows that as the liquid concentration approaches more toward the eutectic point, total undercooling achieved near the interface increases as a result of greater liquidus temperature difference between the solid and liquid.

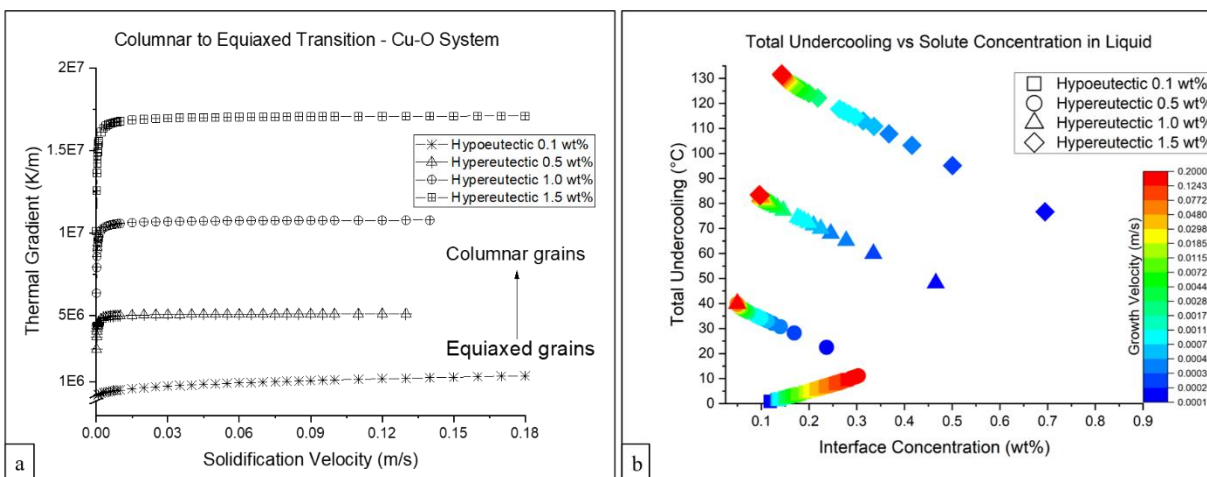


Figure 4-11. a. Columnar-to-equiaxed transition of all copper-oxygen alloy variants; b. Total undercooling as a function of interface solute concentration and solidification velocity; Color bar represents solidification velocity (0.0001 m/s to 0.2 m/s within the limit of stability).

However, estimation of these CET phenomena depends largely on the formulation and assumptions made for rapid solidification processes which should be interpreted with caution. Solute concentration required in casting for equiaxed grain at a comparable thermal gradient is far below than that in AM. For example, Chen, et al. (2016) made several assumptions independent of velocity which in turn affected the solidification kinetics so much that the same principles cannot be used for rapid solidification process.

4.5.2 DSC results of powder with different oxygen concentration

DSC thermal analysis of copper powder with different oxygen content is presented below in Table 4-3 along with relevant temperature measurements taken at important timesteps of phase changes. As seen in the table, an increase in solute content decreases the liquidus and solidus temperature of the system, with the solidus changing with a steeper gradient. This creates a larger solidification range and greater undercooling where liquid copper is deeply undercooled ahead of

solidifying interface. Although the examined powder batches do not have any hypereutectic variant, it is expected to maintain a comparable trend to what has been observed in hypoeutectic copper. As the solute concentration increases, the fraction of eutectic liquid also increases for hypoeutectic alloy conditions (Reed-Hill, 1973), which reduces the peak cooling temperature as observed across all specimens. The undercooling is calculated as the difference between liquidus and solidus temperature, while the heat of solidification (enthalpy of fusion) is calculated within the TRIOS® software by integrating the area underneath the cooling curve from the baseline temperature. These two output variables are shown in Figure 4-12 below for the respective copper oxygen systems.

Table 4-3. DSC results of copper powder with different oxygen concentration and different particle size distributions.

	Oxygen wt. ppm	Solidus Temp (°C)	Liquidus Temp (°C)	Peak Cooling Temp (°C)	Peak Melting Temp (°C)	Undercooling (°C)
15-53µ Powder	200	1078.59	1082.97	1065.74	1095.6	4.38
	600	1075.48	1081.08	1064.69	1092.27	5.6
	1400	1072.52	1080.24	1053	1087.18	7.72
	2300	1070.2	1079.27	1052.45	1082.89	9.07
53- 106µ Powder	300	1077.47	1080.16	1063.89	1092.78	2.69
	850	1076.05	1079.86	1062.4	1090.89	3.81
	1100	1074.34	1079.64	1052.11	1089.15	5.3
	2850	1067.94	1077.87	1051.86	1080.26	9.93

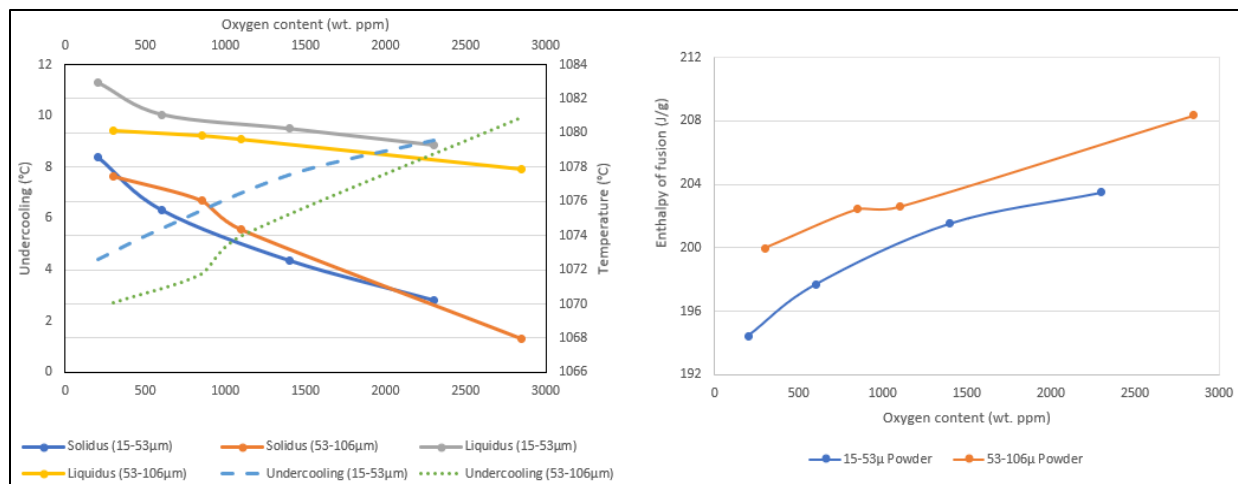


Figure 4-12. Left: Temperature and undercooling values; Right: Latent heat of solidification (enthalpy of fusion) values of different copper powder samples.

Here, during the initial phase, two different particle size distributions were examined in the DSC analysis. As identified in (Bermingham et al., 2019; Greer and Quested, 2006; StJohn et al., 2011), bigger particle sizes have greater potency in acting as heterogeneous nucleants. As can be seen from the results, the powder samples having a PSD of 53-106 μm have resulted in higher undercooling and higher release of latent heat during the solidification process. This is because of their lower surface area to volume ratio which aids in more release of energy during a specific transformation process. Another advantage of using bigger size inoculants is that some particles remain partially un-melted during the melting process, and can act as heterogeneous nucleation sites within the liquid melt, favoring for more grain refinement, as shown by Bermingham, et al. (2019).

Another interesting observation from the DSC experiment is the effect of oxygen content on the wetting of liquid copper melt. From Figure 4-13, it is seen that as the oxygen concentration increases, the contact angle of the solidified bead decreases with the alumina substrate. This effect of oxides on contact angle of solidifying metals has been published for several other metallic systems (Chaklader et al., 1968; Eustathopoulos et al., 2001; Hong et al., 1994; Shirazy et al., 2012). However, no established literature has been found for wetting on a copper substrate, as in the case of EB-PBF fabrication of copper. Nevertheless, the observation gives a qualitative insight as to the increased wettability of copper with increased oxygen content.

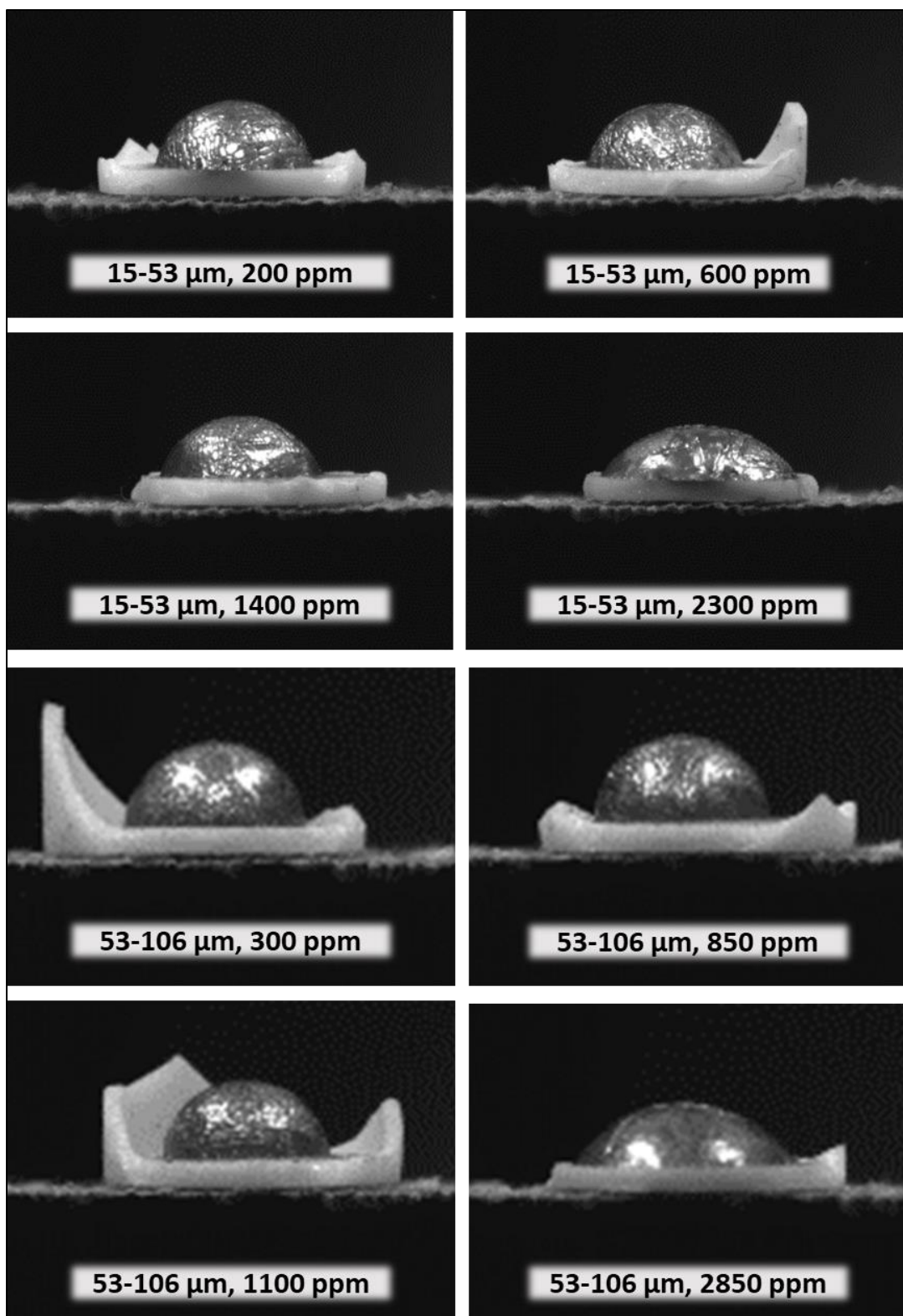


Figure 4-13. Image of solidified copper bead on alumina crucible for qualitative assessment of contact angles; Respective powder size distribution and oxygen concentration in wt. ppm are shown in each image.

4.5.3 Single layer pocket experiment results

The single layer pocket experiment was conducted for finding a feasible process window for the fabrication of high oxygen bearing copper powder by qualitatively analyzing the extent of smoking as a function of processing conditions. The results are shown below in Figure 4-14.

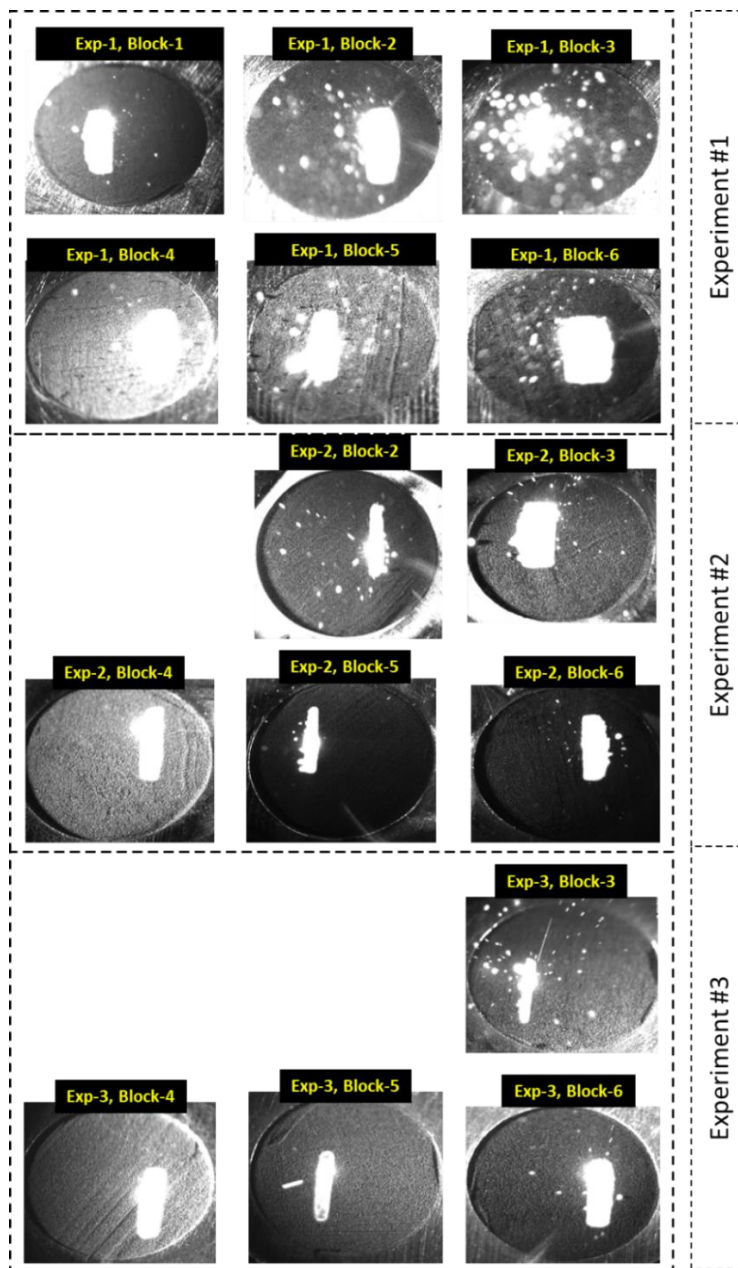


Figure 4-14. High-speed image snapshots during the scanning of different powder pockets. Identifier of each image is shown on top of the same, and the respective process conditions can be obtained from **Table 4-1**.

From the high-speed image movie, it is found out that high substrate temperature leads to better sintering of the powder bed which minimizes the smoking event as described earlier. At lower bed temperature, a higher fraction of hypereutectic copper powder flies away from the powder bed. This repulsive nature of the electron beam is reduced for powder with a lower oxygen content as that builds up lower static charges compared with hyper-high alloy powder even at low substrate temperatures. From Figure 4-14, it is realized that a high powder bed temperature will be beneficial for processing such hypereutectic copper powder. However, the individual effects of other process parameters such as melt current and scan velocities are analyzed through the microstructural observation of the polished surface layer. It is seen that when the melt current is very low (for example 12 mA), the powder bed is not sufficiently melted, and un-melted powder particles have a larger area fraction than that of solid bulk copper. The melt current and scan velocities are chosen such that a speed function of 20 can be maintained for all pockets, assuring a comparable melt pool dimension. However, as the thermal conductivity and specific heat of oxidized copper are different than those of pure copper, using the usual processing space are unsuccessful, and only the high current scenarios result into successful melting conditions. Figure 4-15 illustrates the representative microstructures of hyper-low, hyper-med, and hyper-high solids processed at 450°C bed temperature, 1300 mm/s scan velocity, and 16mA melt current.

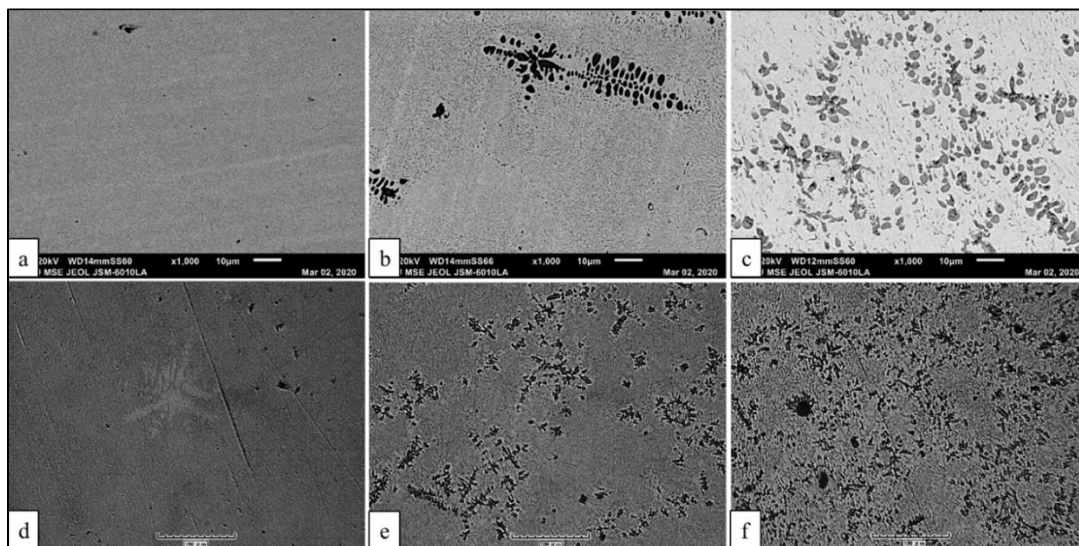


Figure 4-15. Microstructure of single solid layer from different powder types. Top row represents SEM images (scale bar 10 μm), bottom row represents optical microscope images (scale bar 100 μm). (a, d): Hyper-low; (b, e): Hyper-med; (c, f): Hyper-high.

It is seen that hyper-low does not have pronounced dendritic β -phase as the other two, and it mostly has a clean microstructure with very refined grains. The dendritic structure seen in the optical image is larger in size than those found in other two types. It is inferred that higher oxygen concentration leads to sharper dendritic radius according to the results obtained from CET model simulation which ultimately breaks from the main branch, and the several dendritic grains seen in hyper-med and hyper-high powder pockets are these fragmented dendrites. This fragmentation of dendrite branches can lead to the generation of equiaxed grains as they can act as heterogeneous nucleation sites, as observed in conventional casting (Kobayashi and Shingu, 1988; Spittle, 2006).

4.5.4 Results of the feasibility study builds

Although the pocket experiment results show that hyper-high powder batch can lead to a refined grain structure, fabricating copper components with such high oxygen content is seemingly unrealistic considering the demand of purity in their applications. Therefore, the feasibility study builds were done using a hydrogen treated copper powder batch that picked up oxygen with time (0.115 wt.%) with the particle size distribution shown in Figure 4-16a below. It is seen that that the particle size distribution is not changed much across three builds. The oxygen content also remains relatively similar. Figure 4-16b shows the SEM image of the powder morphology that clearly demonstrates the effects of the hydrogen treatment, as reported by Ledford, et al. (2019).

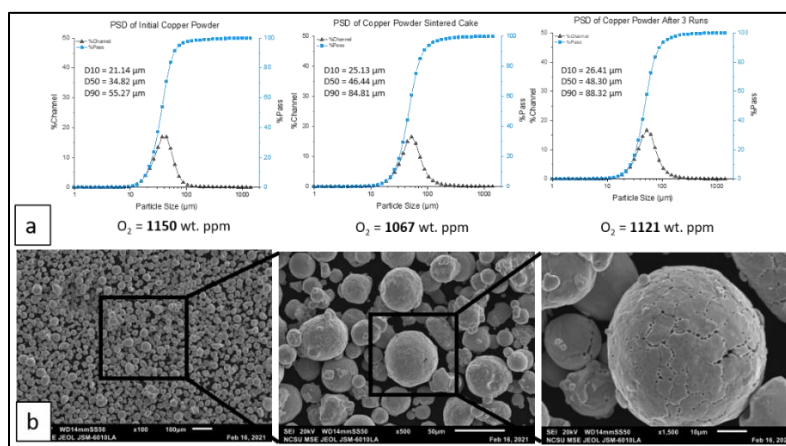


Figure 4-16. Feasibility studies build powder characterization. a. Particle size distribution and oxygen content of virgin powder, sintered cake around the powder bed, and the final build. b. SEM images of virgin powder at 100 X, 500 X, and 1500 X.

The overall build pictures are shown in Figure 4-17 below. It is seen that the top surface of build 1 looks very clean compared with the other two builds. Especially, build 3 has a wavy, heavily sintered powder bed around the solids that affected the powder flow and the appearance of the fabricated solids. Majority of the fabricated blocks has swelled edges due to high material transport phenomenon. In each build, a few samples are turned off during their fabrication (shown in Table 4-2) due to either bad fusion to the base plate, or excessive swelling caused by high input energies. Also, the powder cake in build 3 could not be cleaned without cutting the parts off of the plate as the powder was heavily sintered due to the high process temperature used in that build.

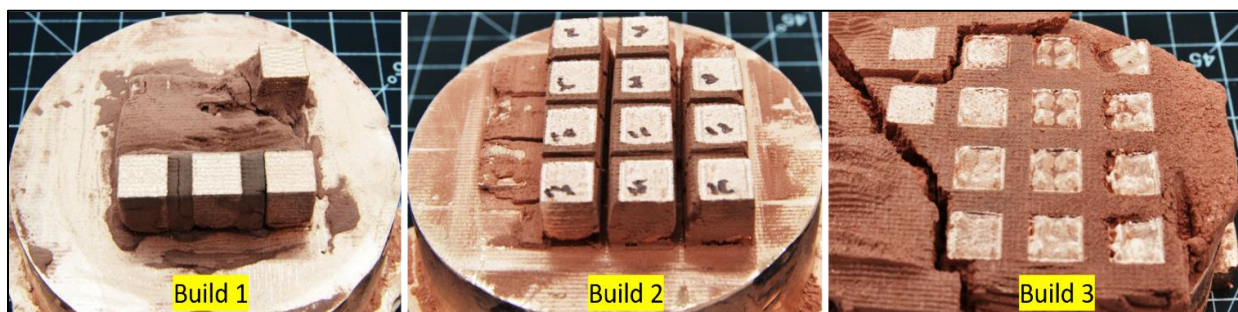


Figure 4-17. Picture of the experimental builds.

As mentioned earlier, both preheating I and preheating II are turned on during build 3 to stabilize the substrate temperature at the desired level of 450°-500°C. At this high substrate temperature and high preheating current settings, the powder bed sinters more easily than the other ones, and therefore, the powder bed of build 3 looks visibly different than the other two. This temperature difference among the three builds is shown in Figure 4-18 below.

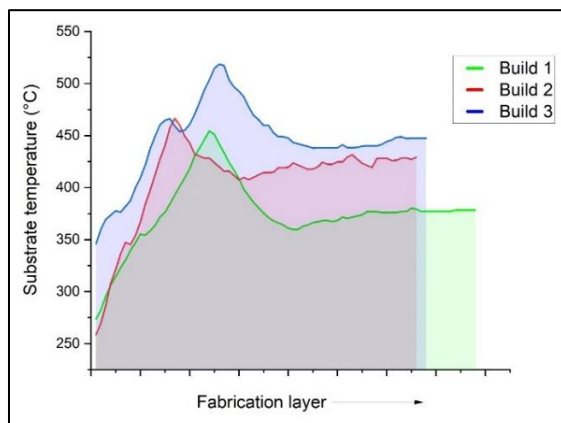


Figure 4-18. Substrate temperature data from log-files for all experimental builds.

4.5.5 Thermal model and CET prediction of selected specimens

Selected specimens from all builds are simulated in the thermal model, and the resultant G and V are plotted on the CET map modeled with 0.1 wt.% oxygen content. Specimens are selected such that the overall range of volumetric energy density is considered in these simulations. Figure 4-19A shows the individual data points within this map, and the chosen samples for simulation are shown in red circles. Green circles represent the samples that are analyzed for microstructure and microhardness.

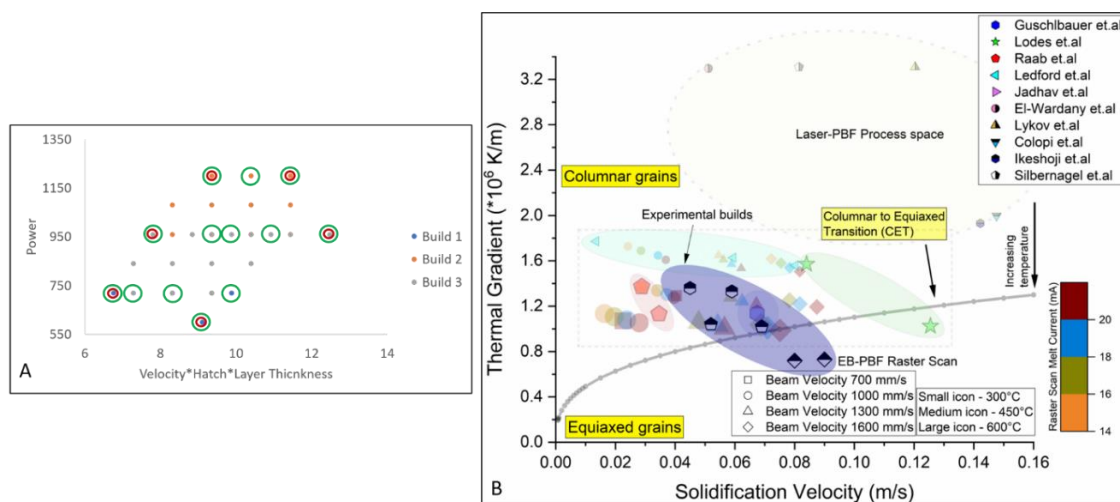


Figure 4-19. A. Process map for the experimental builds. Green circles show selected specimens for microstructural and hardness analyses; red circles show selected specimens for thermal model simulation. B. Thermal model results mapped onto the CET map for the selected specimens. Probable outcomes of all other specimens are enclosed in the blue oval shape.

Thermal model results of the selected specimens suggest that while build 1 and build 2 samples will most likely have columnar grain structure, build 3 may have samples with equiaxed microstructure. This is primarily due to the lower thermal gradients obtained in build 3 due to its increased substrate temperature, and the effect of oxygen in reducing the thermal conductivity of the powder bed. The prediction is shown in Figure 4-19B and analyzed with the optical and SEM grain structure images in the subsequent sections. It is noted that the highest current utilized in build 3 is 16 mA, and therefore, the CET prediction will move upward to the columnar grain region as the melt current is reduced to 12 and 14 mA. Therefore, it is expected that all other samples will have G and V values enclosed within the confidence domain shown as a blue oval.

4.5.6 Microstructural analysis of selected specimens

Microstructure along the build direction for the selected specimens is shown in Figure 4-20 which illustrates the effect of both processing conditions and solute concentration in the grain structure of EB-PBF processed copper. Build direction is from bottom to top for all the samples.

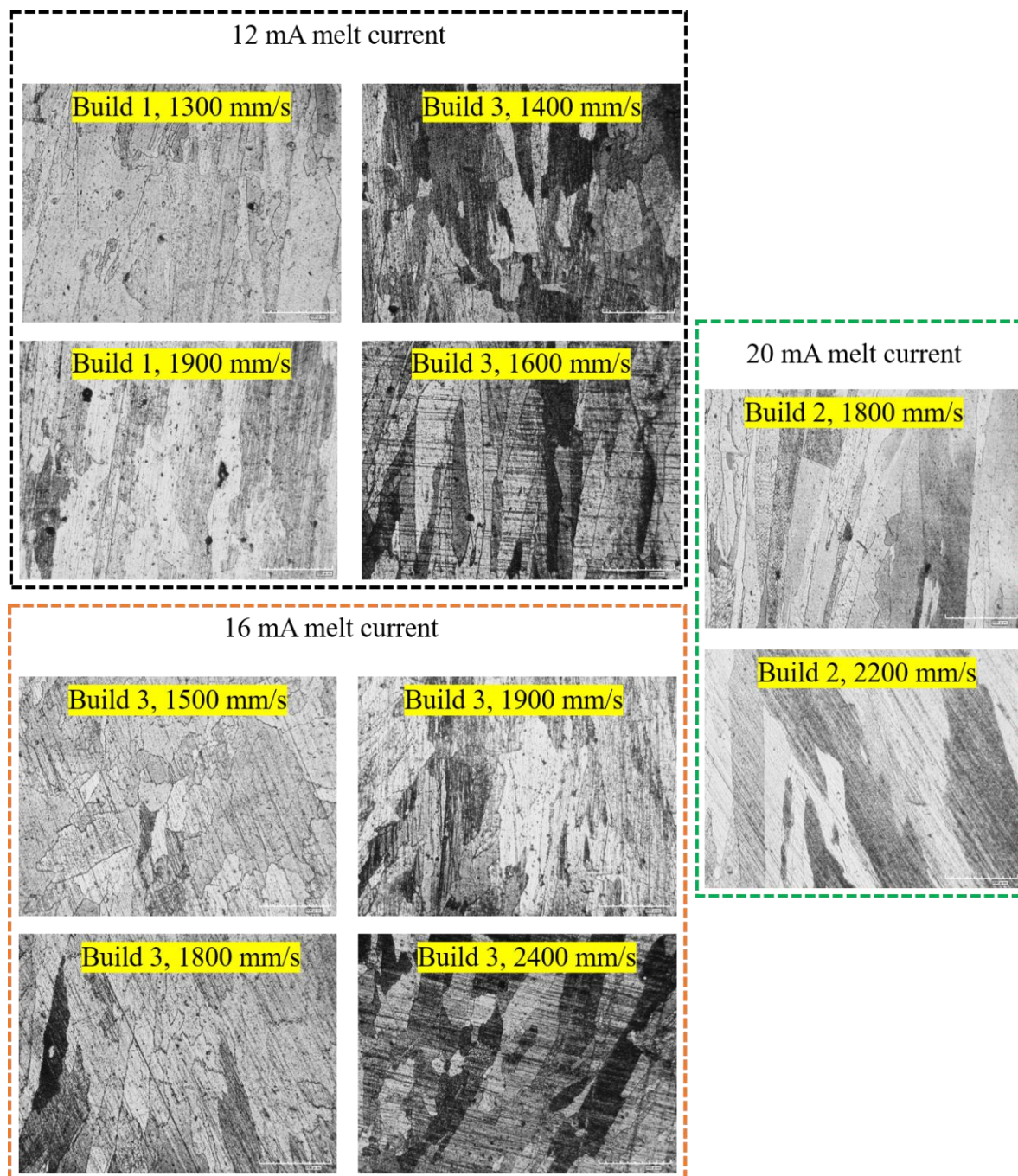


Figure 4-20. Optical microstructure of selected specimens from the feasibility study builds. Scale bar shows 200 μm .

It is seen that the microstructure for both 12 mA and 20 mA current is dominated by usual columnar grains seen in regular copper. This is in accord with the CET model results that suggest a columnar grain structure for such process parameters mainly because of the process temperature attained in the fabrication of those samples ($\sim 375^{\circ}\text{C}$ for build 1, and $\sim 400^{\circ}\text{C}$ for build 2, as can be seen in Figure 4-18). However, the solutal effect of oxygen is seen in the growth restriction of the columnar grains that now spans a few hundred micrometers instead of a millimeter range observed in the pure copper samples, as reported in the tensile test study. From the Cu-O phase diagram, it is observed that upon solidification, copper oxides precipitate out to the grain boundary while pure copper solidifies first. Therefore, with this solute concentration used in this study, it is unlikely that pronounced heterogeneous nucleation is initiated by first solidified copper oxide during solidification of these samples. On contrary, it is assumed that the direction of thermal gradient and the growth restriction imposed by the oxides are the reasons for the grain selection and overall microstructure morphology observed in the samples. Figure 4-21 illustrates such differences in the microstructure where the sample fabricated with 0.1 wt.% oxygen content shows a refined grain structure in both transverse and parallel to the build direction, as compared with the sample fabricated with ~ 0.05 wt.% oxygen content.

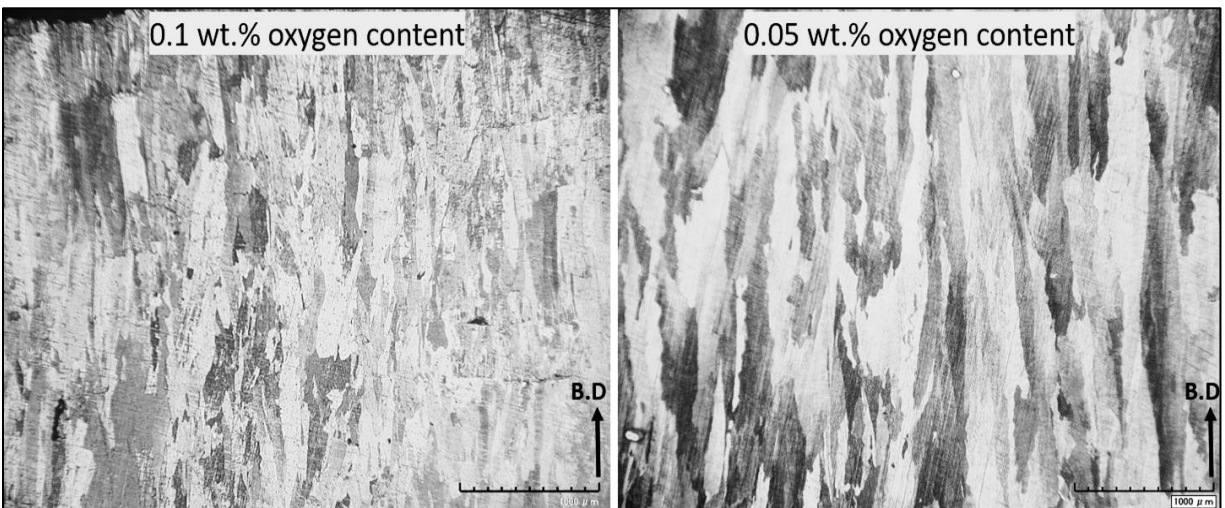


Figure 4-21. Effect of oxygen in restricting the columnar grain growth. Build direction is shown with black arrow; scale bar shows 1000 μm .

However, for build 3, which is run at a higher substrate temperature than the other two, the CET model suggests a possible equiaxed grain structure in the samples that have 16 mA currents. This is seen in the optical microstructure in Figure 4-22 that demonstrates non-columnar equiaxed grain in one of the samples fabricated in build 3. In order to examine the source of the columnar grains seen predominantly in the microstructure of the selected samples and the equiaxed grains seen in this specific sample, SEM images with higher magnification are taken for representative samples that lie on the extreme corners of the volumetric energy density process map as per Figure 4-19.

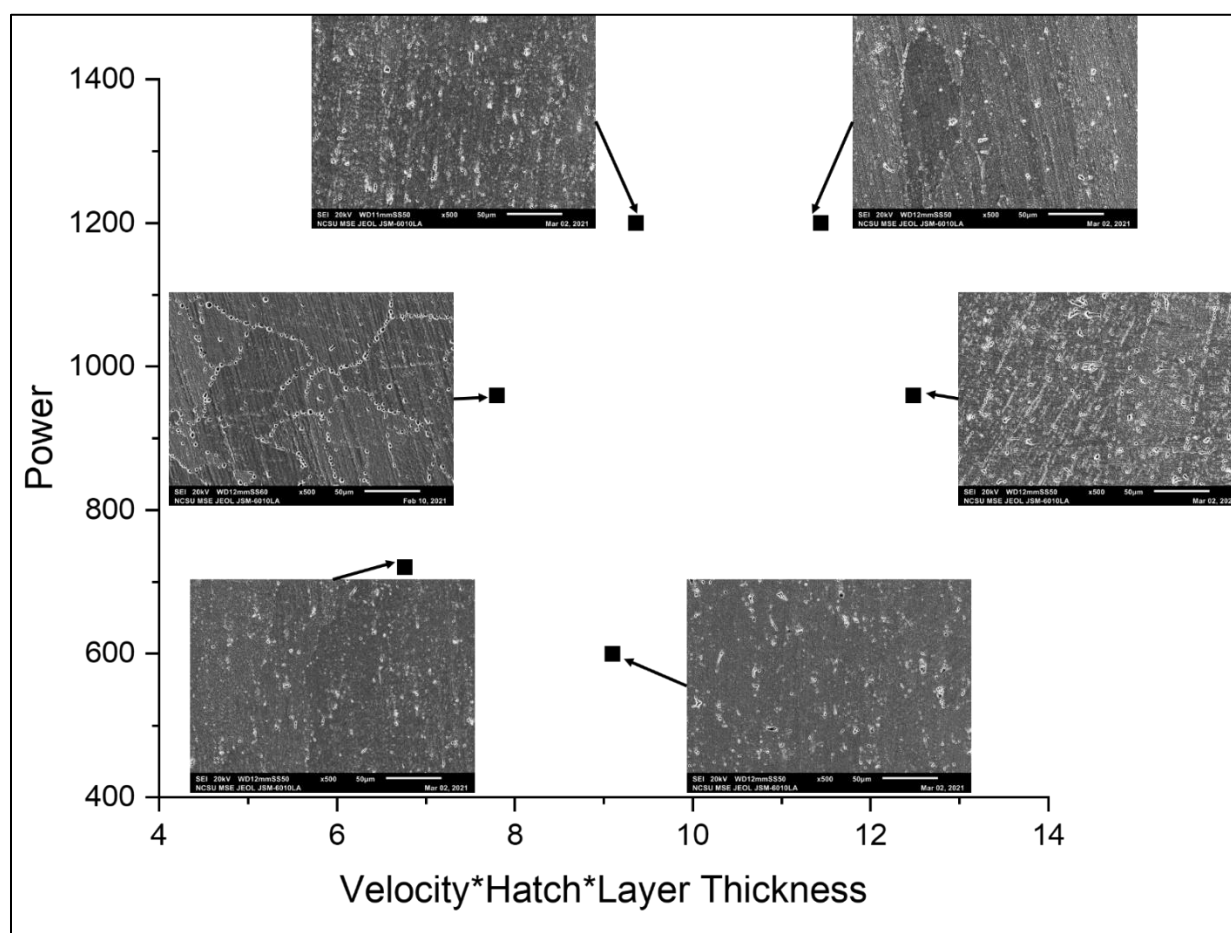


Figure 4-22. SEM images of selected specimens from the feasibility study builds. Note that samples are chosen such that the overall volumetric energy density is covered. Scale bar shows 50 μm .

As per Figure 4-22, all samples show columnar grains of different widths and lengths with etch pits of grain boundary cuprous oxides except for sample 3 from build 3 that shows equiaxed grain structure along the build direction. Majority of these oxides are in micrometer scale lengths, and they decorate the grain boundaries. Since the range of undercooling for hypoeutectic Cu-O system is between 10°C - 20°C for different solidification velocity and thermal gradient conditions, it is postulated that copper gets solidified first, and these copper oxides get pushed to the grain boundaries at the end of the solidification process. Thus, with this level of oxygen content in the powder feedstock, it is unlikely that copper oxides will promote heterogeneous nucleation and the microstructure is controlled by the rate of nucleation (Powell and Hogan, 1968). Instead, the oxide precipitates help reduce the grain growth in one direction when assisted by a change in the thermal gradient direction.

However, the equiaxed grain structure seen in one of the fabricated samples in build 3 calls for further investigation as to understand the reason behind such grain structure. A montage of the optical microscopy images is shown in Figure 4-23 that clearly illustrates equiaxed grains from the base to almost half of the build height, and then a transition to columnar microstructure until the build finished.

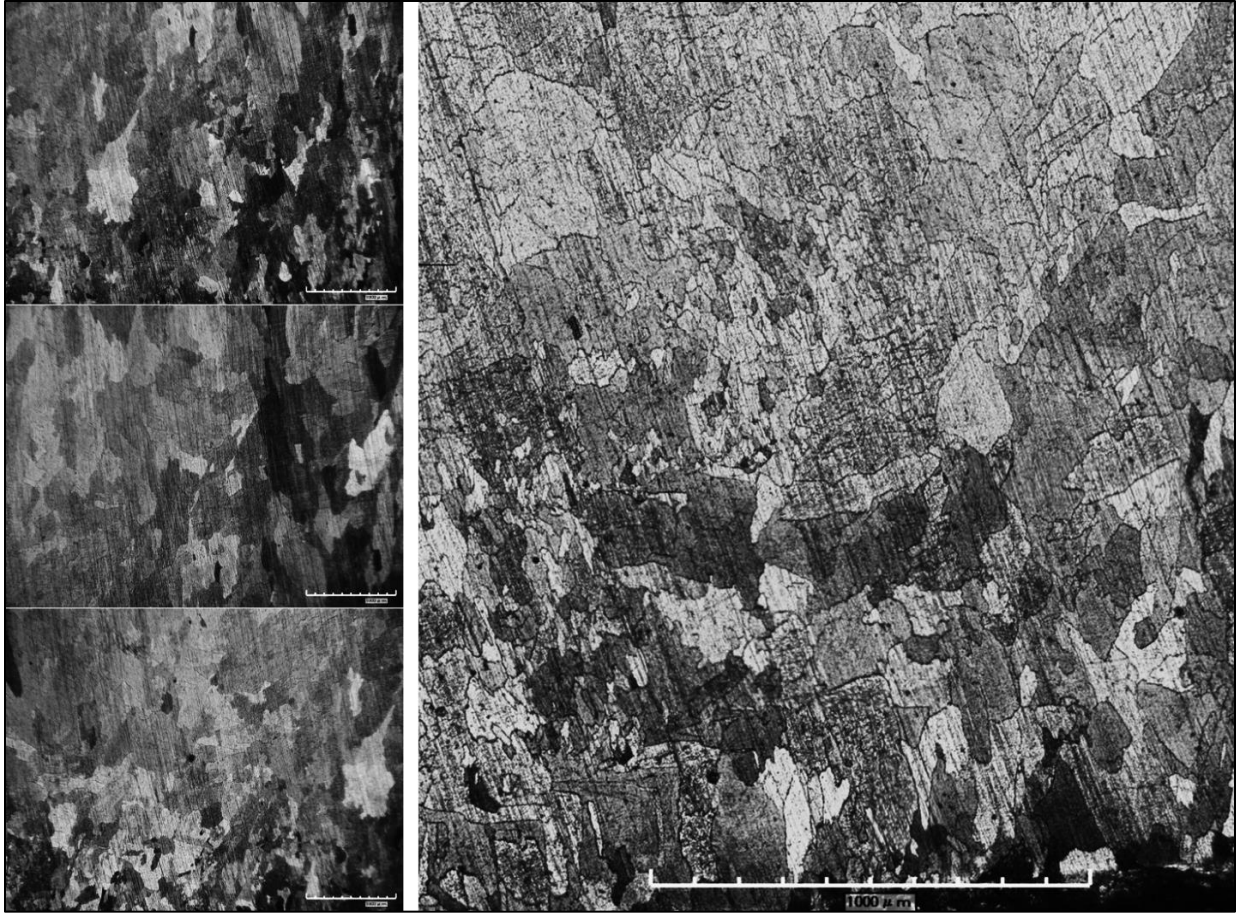


Figure 4-23. Optical microscope image montage for the sample with equiaxed grains along the build direction. Scale bar is 1000 μm .

Grains in the sample with the equiaxed microstructure grow almost transverse to the build direction. However, there is a gradient in the grain orientation wherein the grains orient themselves less transverse and more parallel to the build direction as the build height increases. As the total undercooling at the dendrite tip depends on this relative orientation angle with the build direction (Hadadzadeh et al., 2018), undercooling increases as the grains orient more transverse to the build direction, and vice versa. This enhanced undercooling promotes further equiaxed grain formation, and the process continues as long as other solidification conditions are constant. The SEM montage image of this sample shows such arrangement of equiaxed grains for a bigger field of view where they grow across several melt pools almost perpendicular to the build direction (see Figure 4-24) near the bottom half of the sample.

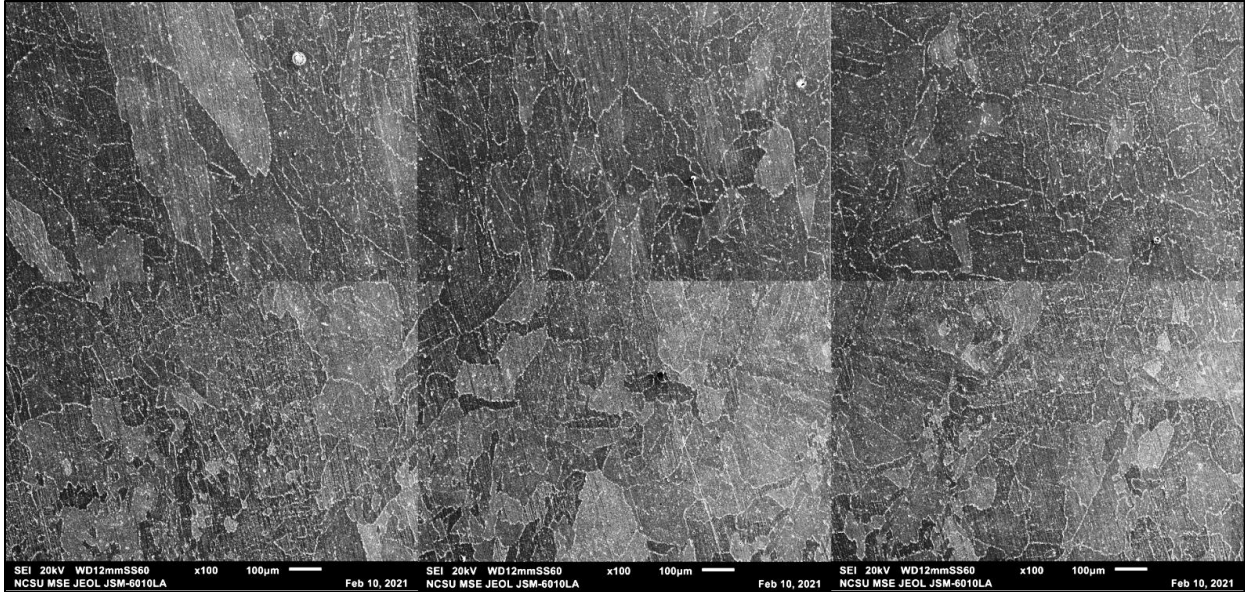


Figure 4-24. SEM image montage for the sample with equiaxed grains along the build direction. Scale bar is 100 μm .

To further gauge the magnitude of grain refinement and extent of equiaxed grain formation, higher magnification images are acquired in FEI Quanta 3D field emission gun. Figure 2-25 shows the grain structure and orientation of the solidified dendrites within the macro-grains in both the regions of equiaxed and columnar grains. From Figure 4-25, the effect of grain orientation is seen on the overall grain morphology selection. In the equiaxed region, solidified dendrites of copper and copper oxide particles arrange in a close-pack structure with multiple growth directions.

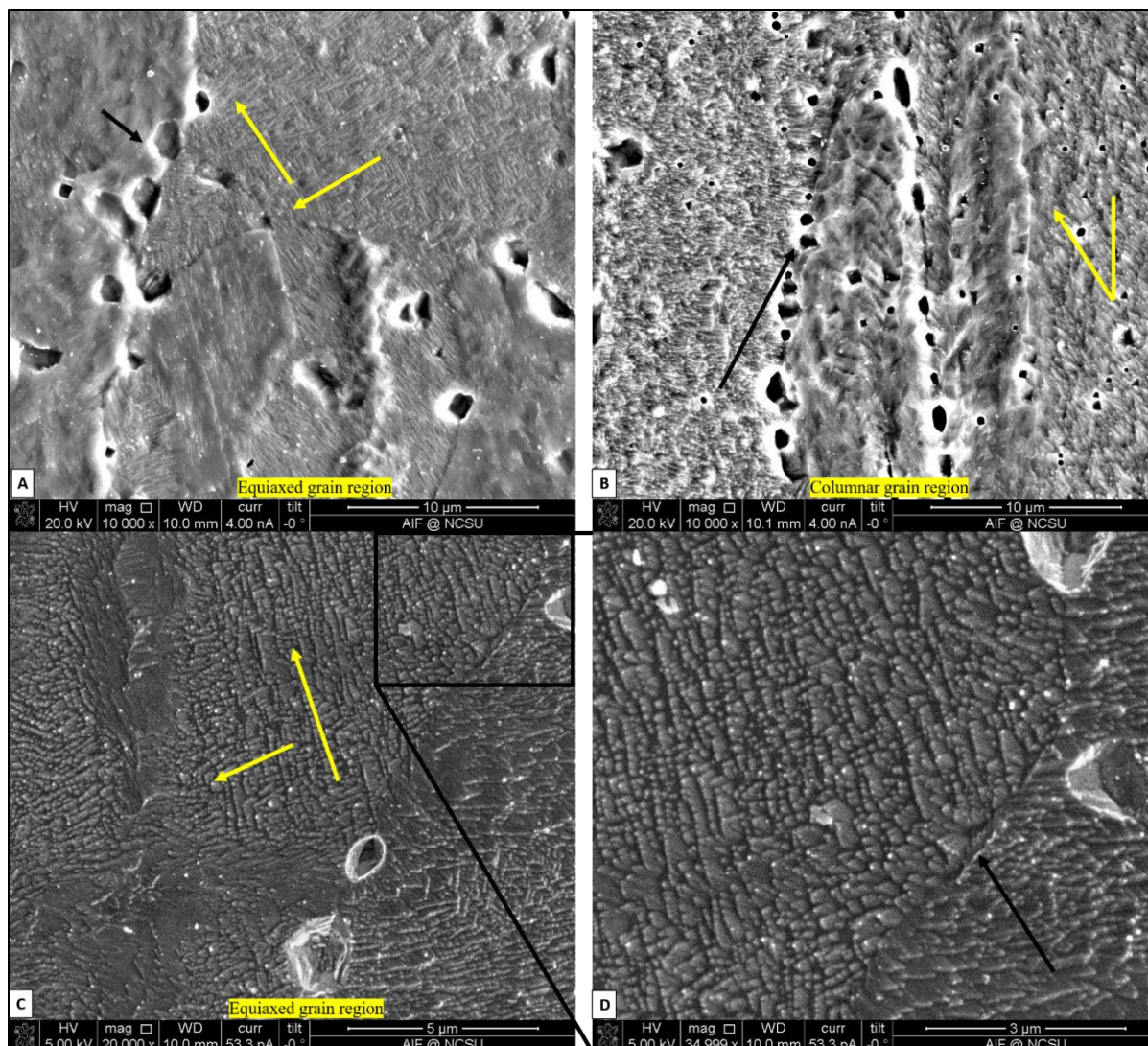


Figure 4-25. A. Equiaxed grain region, B. Columnar grain region, C-D. Dendrite structures within equiaxed grains. Yellow arrows show the direction of grain growth, Black arrow in A and B indicates the oxides at the grain boundary, and in C it indicates just the grain boundary. Note the different scale lengths.

Especially seen in Figure 4-25C-D is such random orientation of dendrites within a single grain grown transverse to the build direction. Within each grain, copper oxides, from sub-micrometer to several micrometer length scales, precipitate out to the grain boundaries, and create the observed etch pits once the solid is etched with Ammonium Persulphate. The direction of grain growth is assisted with the thermal gradient and solidification velocity condition, and the growth of individual grains is restricted by the presence of oxides that pin the grain boundary and deters

the grain boundary mobility during the fabrication. However, in contrast, the columnar region does not present with such multi-direction of dendrites within a grain. Further, between two neighboring grains, the orientational difference is significantly lower than the grains in the equiaxed region. This restricts the nucleation of equiaxed grain and favors the growth of already solidified columnar grains from the previous layer, as found out in the samples fabricated with pure copper powder in Chapter 3.

4.5.7 Density and microhardness characterization of the selected specimens

Physically examining the selected samples reveals surface connected porosities or defects that deteriorated overall part quality. However, with the Quantachrome Pycnometer 1200E density measurement, the carrier gas seeps into these porosities resulting in a high density. Therefore, to measure density of the selected fabricated specimens, unetched optical microscope images are used. The TEY images generated during these builds according to the method published by Ledford, et al. (2020) are useful in qualitatively monitor the build surface since any surface defect or irregularities have high relative contrast with the solid (shown in Appendix C). However, these images lead to erroneous density measurements as the threshold value cuts off the porosities that have contrast between the solid copper and the surface irregularities. Nevertheless, these TEY images are useful in the sense that they produce the upper limit of density, besides providing an educated knowledge of the beam movement and overall energy deposition on the substrate plate.

Table 4-4. Relative density and microhardness values of selected specimens from feasibility study build.

		Relative density		Microhardness (HV0.1)	
		Mean (%)	Std. deviation (%)	Mean	Std. deviation
Build 1	Sample 3	99.3	0.10	75.3	4.8
	Sample 8	99.0	0.12	68.4	9.2
	Sample 9	99.4	0.08	63.8	3.7
Build 2	Sample 8	99.5	0.13	68.1	4.0
	Sample 12	98.7	0.47	70.3	2.3
	Sample 16	99.4	0.19	74.6	6.0
Build 3	Sample 1	99.2	0.17	79.3	9.2
	Sample 3	99.5	0.08	67.8	1.8
	Sample 4	99.3	0.11	78.9	13.8

Table 4-4. Continued.

	Sample 5	99.6	0.09	67.0	2.9
	Sample 11	99.2	0.05	72.8	6.3
	Sample 15	99.4	0.10	66.6	2.8
	Sample 16	99.4	0.29	64.7	2.8

From the density measurements, it is seen that the adopted processing space of high oxygen content powder is capable of producing parts with near full density. Further, there is no apparent correlation between density and process parameters, as found out in the pure copper specimens fabricated in the previous chapter. Both of these are in contrast to the results in L-PBF processing of pure copper by Yan, et al. (2020), and in accord with the findings of Guschlbauer, et al. (2018). Microhardness, on the other hand, is almost similar to what has been found for samples tested in the tensile and microhardness measurement study, with some occasional high values. Interestingly, microhardness is seen to correlate well with the process parameter, especially the volumetric energy density. Similar to the observations made in case of pure copper samples in the previous chapter, samples from these three builds also demonstrate a peak of microhardness at moderate energy density, and a drop on both sides where either the energy density is lower or higher. What is even more noteworthy is that the sample which has equiaxed grain structure, possesses the most uniform hardness values across the build height (lowest standard deviation). Figure 4-26 shows this influence of process parameters on the microhardness measurement of the samples.

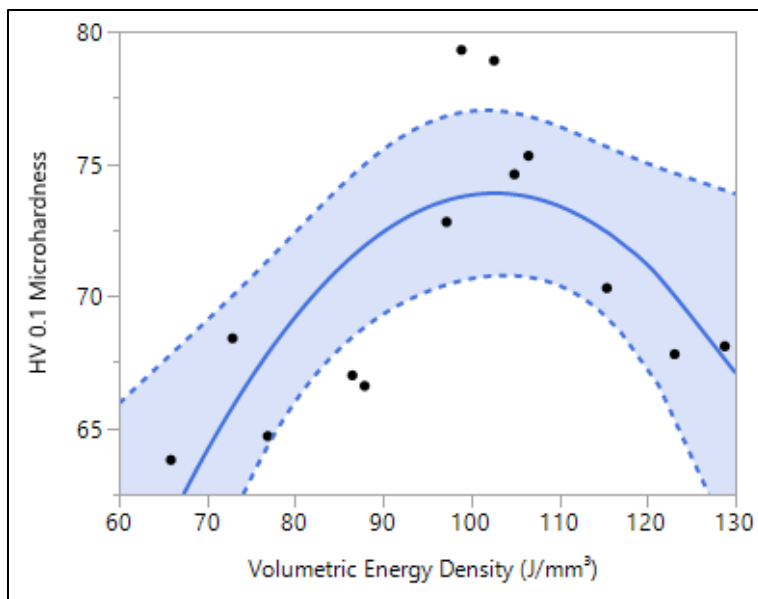


Figure 4-26. Influence of volumetric energy density on the microhardness of selected samples.

Although density of the samples is lower than the pure copper samples measured and shown earlier, this increased hardness values for some samples are ascribed to the higher oxygen content present in the solid that strengthens the material. These oxides precipitate and pin the grain boundaries, providing grain boundary and precipitation strengthening to the material during its deformation. Similar increase in microhardness is reported by Ramirez, et al. (2011) where arrays of copper oxides along the grain boundary are seen to provide precipitation hardening to the copper blocks in both transverse and parallel to build direction.

4.5.8 Vacuum annealing of selected specimens

In order to purify the fabricated copper specimens after their EB-PBF processing, vacuum annealing is conducted at 950°C for 24 and 48 hours. Oxygen content measurements through LECO are shown in Figure 4-27. A starting solid oxygen content similar to what is measured in the feedstock powder, is seen to decrease as the duration of the process increased. However, the final oxygen content after vacuum annealing for 48 hours is still outside the range of ETP copper powder that usually contains between 400 – 600 wt. ppm oxygen (Davis, 2001). It is believed that a further increased annealing schedule can lead to greater purity given the slow diffusion rate of oxygen and thickness of the fabricated samples. The equiaxed microstructure in sample 3 is seen to be unaffected during the vacuum annealing process, and therefore, this extra step of post-process

proves beneficial to reduce the oxygen content in the starting powder without altering the obtained equiaxed microstructure. It is expected that even higher oxygen content in starting powder may give rise to a greater equiaxed grain fraction, as observed from the pocket experiment, and a longer annealing schedule will be necessary to reduce the oxygen content. Nevertheless, this approach shows a great potential to produce equiaxed grains along the build direction in EB-PBF of copper.

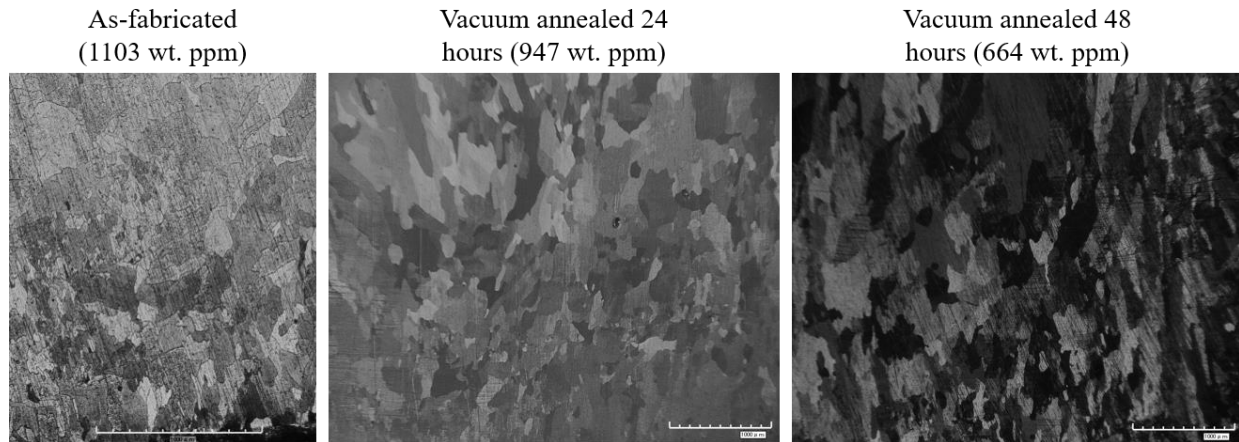


Figure 4-27. Oxygen content and microstructure of sample 3 from build 3 before and after vacuum annealing process.

4.6 Conclusions

Grain refinement through oxygen addition can be beneficial in EB-PBF processing of copper as oxygen has high growth restriction factor compared with the other elements found in the powder feedstock. Moreover, it is seen that CET becomes easier even at high thermal gradients for higher solute concentration as the latter produces high undercooling ahead of solid liquid interface. DSC studies also show that latent heat of solidification increases as the solute content in the powder increases, and that helps in the reduction of contact angle of wetting liquid copper. As the latent heat release and thermal mixing due to high solidification velocity generate the favorable nucleation condition, copper powder with hyper-eutectic oxygen content processed at high beam scanning velocities and melt current has the potential to produce equiaxed grains. Moreover, it is seen through high-speed imaging technique that higher substrate temperature can be exercised when the feedstock powder has high number of oxides, thus resulting in lower thermal gradients. However, due to the application requirements, large fraction of impurities is not favorable in

copper components, and therefore, in this study, the oxygen content is limited to a hypo-eutectic concentration of 0.1 wt.%. It is seen from the experimental builds that when processed with favorable process parameters that lead to low thermal gradient and high solidification velocity, it can produce equiaxed grains along the build direction. However, due to high thermal conductivity of solid copper, even slight changes in processing conditions reverts the microstructure back to columnar grains, albeit, with greater refinement. Throughout, all samples show much refined microstructure compared with the tensile samples fabricated in the same machine. The interdependence theory proposed by Bermingham, et al., (2019), Easton, et al. (2016), and StJohn, et al. (2011) can be used to shed more light on the formation mechanism of equiaxed grain in the presence of a high Q-factor solute. According to the theory, both potency and spatial distribution play significant role in nucleating new grains and promoting equiaxed grains. Since the oxides form at the later part of the solidification process and they are not numerously abundant within the powder feedstock, the ability to form equiaxed grains depend more on the thermal conditions during the solidification. As and when the gradient shifts from favorable region to a steeper one, the microstructure shifts to the columnar epitaxy from the previously solidified equiaxed region. Additionally, if the temperature of the substrate is too high as the build progresses, the diffusion length of solutes increases, leading to less number of nucleation events (Fernández et al., 2018). This is further supported by the interdependence theory for the allowable diffusion length and the distances between nucleating particles for equiaxed grains to develop. Nevertheless, it is expected that increasing the initial oxygen concentration within a hypoeutectic region can instill more growth restriction and more abundancy of nucleating particles, thus promoting the probability of equiaxed grains further. However, the vacuum annealing process need to be scheduled accordingly so that samples can be annealed for much longer time at 950°C to dissociate and evaporate the large amount of initial oxygen. If this post-processing step can be optimized, this approach shows promising results in terms of grain refinement and columnar-to-equiaxed transition in EB-PBF processing of copper that can achieve more isotropic material properties.

5 Summary of research

5.1 Overall research objective

State-of-the-art on the additive manufacturing of pure copper focuses primarily on the development of a suitable processing space that leads to good part densities and acceptable properties. Although significant progress is made in understanding and developing the process physics and required system modifications, respectively, process-structure-property relationship for AM copper is revisited in this research with the following objectives to bridge some of the gaps identified in the state-of-the-art.

Besides electrical and thermal conductivity, mechanical property of additive manufactured pure copper is of interest for its applicability in real-life components. Further, different types of post-processes are usually adopted by the AM industries either to enhance the part properties, or to deliberately alter its microstructural features. However, the effect of such post-processes on AM copper in general, and EB-PBF copper in particular, is not well reported. In literature, most of the characterization is done in the as-fabricated condition, whereas post-processes like heat treatment or HIP are common in the AM processing of other materials. However, HIP in powder metallurgy and annealing in different processing environment conditions are well documented for fabrication of copper components. Therefore, in the first phase of this research, effects of HIP and annealing are investigated on the microstructural changes and subsequent mechanical properties of EB-PBF processed pure copper. We hypothesize that HIP will further increase the part densities obtained in the as-fabricated condition, while annealing conducted under a vacuum atmosphere at a certain temperature will reduce the oxide impurities and eliminate their deleterious effects in downstream high-end applications.

Delving more into the structure-property relationship, it is usually seen that morphological anisotropy contributes to property anisotropy of the materials. EB-PBF processed copper generally produces epitaxial columnar grains along the build direction and equiaxed grains transverse to the build direction. This leads to morphological anisotropy based on part orientations within the build volume, and consequently results in different properties when measured in different directions. It becomes more pronounced when the grain size in transverse direction measures hundreds of micrometers as opposed to several millimeter-long grains parallel to the build direction. This type of

grain structure difference is common in most of the materials processed through the PBF systems, due to the layer-by-layer melting and remelting of previously solidified layers. Nevertheless, progress is made in alloy material systems such as Ti-6Al-4V or IN718 where different methods are adopted to alter the columnar microstructure with a near equiaxed microstructure along the build direction. It is noted that of these methods, process parameter modification and addition of grain refining solute or potent nucleant particles are more frequently utilized in tailoring or changing the microstructure than the others. However, use of such microstructure refining methods and their evaluation in PBF processing of copper are yet unreported, and call for a deeper insight to examine the prospect of more microstructural isotropy. Therefore, in the second phase of this research, both methods are modeled and experimentally evaluated to assess the possibility of producing equiaxed grains along the build direction. From the viewpoint of just modifying the process parameters, we hypothesize that high substrate temperature along with high melt currents can lead to favorable solidification conditions for equiaxed grain formation by reducing the overall thermal gradient. On the solutal effect on grain refinement and grain modification, we investigate the possibility of using the oxides present in the powder feedstock since oxygen has high growth restriction factor in the solidification of copper.

5.2 Contribution of this research

First phase of this research demonstrates that mechanical properties of EB-PBF processed copper depends significantly on the collective influence of build orientation, dislocation movement along the grain boundaries, and the spatial distribution of second phase copper oxides. It is further demonstrated that both HIP and vacuum annealing lead to slight coarsening of grains along with the coalescence of oxides that reduce strength while increasing the ductility. It is also shown that vacuum annealing at 950°C efficiently dissociates the copper oxides, and the oxygen content in the specimen reduces by ~40%. Overall, it is shown that of all mechanical properties, elongation to failure is mostly affected by the build orientation, whereas yield strength is observed to be influenced by post-processing. To summarize, the results enrich the knowledge of post-processing in EB-PBF fabricated copper by linking the observed properties with the microstructural changes.

Second phase of this research utilizes a numerical thermal model along with a CET map generated for Cu-O system based on the feedstock powder composition. Process parameters such

as melt current, scanning speed, and substrate temperature are simulated via the thermal model to obtain temperature profiles within the simulated domains, and ultimately, the thermal gradient and solidification velocity information. Preliminary experiments show that achieving a transition to equiaxed grains from columnar ones just by modifying process parameters is challenging in the EB-PBF processing of pure copper. The second approach of using a more oxidized powder helps in retaining the heat due to lower thermal conductivity of the powder and subsequently reduces the thermal gradient. Equiaxed grains is observed in portions of the solid made from this powder and is validated by the CET predictions. In aggregate, it is proposed that the CET model and the numerical thermal can be used to make educated estimates of the obtainable microstructure and indicates to the direction in which process parameter and/or feedstock composition can be changed to get a CET in EB-PBF processed copper.

5.3 Future work

The following experimental aspects of the EB-PBF processing of copper is envisioned with respect to the works conducted during this research.

1. It is seen that both HIP and vacuum annealing have adverse effects on the strength of copper at the examined process parameters. Although HIP increases the part density and vacuum annealing enhances the part purity, this reduced yield strength and UTS will affect the design of its application. In a recent study by Ganor, et al. (2021), it is shown that different HIP parameters affect the same material (Ti-6Al-4V) in different ways, wherein a certain HIP temperature can increase the density without coarsening of the grains. Since only a select process parameter for both HIP and vacuum annealing is examined in this study, it warrants for further research on characterizing the effects of different parameters for a given post-process. In other words, optimization of HIP and vacuum annealing process is required to make them more effective post-processing routes for EB-PBF processed copper. Further, a few research directions are presented in Appendix A that can help explain the differences in properties seen in the samples as a function of post-processing. Although a more detailed work is necessary to draw conclusions from these analyses, the methods utilized here have proven to be useful in explaining properties in other material systems in additive manufacturing. Therefore,

- it seems prudent to further characterize the microstructure-property dependency by adhering to these proposed directions.
2. Achieving a CET by just modifying the process parameters is challenging for copper due to its high thermal conductivity. At high substrate temperatures, powder flowability also becomes an issue, and a successful stable build becomes difficult. However, the oxidized copper powder relaxes some of the processing constraints in addition to its effectiveness as a growth restricting phase in the system. Several aspects of using such powder still need to be investigated, viz. operating at hyper-eutectic region with the hypothesis of more heterogeneous nucleation and enhanced undercooling, optimizing the vacuum annealing process to reduce such high number of oxides and increase the part purity, understanding the microstructural relationship between the nucleating oxide and nucleated copper etc. Such detailed knowledge will help the user understand the process better, and make appropriate modifications based on the microstructural requirements. Further, optimization of processing high purity copper at high substrate temperature is required that can lead to a stable equiaxed grain formation along the build direction. It is envisioned that with the use of in-situ temperature monitors, it is possible to control the substrate temperature, and subsequently achieve equiaxed grains in copper parts by adjusting the process parameters dictated by the thermal model and the CET map.

REFERENCES

- Anderson, T.D., DuPont, J.N., DebRoy, T., 2010. Origin of stray grain formation in single-crystal superalloy weld pools from heat transfer and fluid flow modeling. *Acta Mater.* 58, 1441–1454. <https://doi.org/10.1016/j.actamat.2009.10.051>
- Atkinson, H.V., Davies, S., 2000. Fundamental aspects of hot isostatic pressing: An overview. *Metall. Mater. Trans. A* 31, 2981–3000. <https://doi.org/10.1007/s11661-000-0078-2>
- Bai, Y., Wagner, G., Williams, C.B., 2017. Effect of Particle Size Distribution on Powder Packing and Sintering in Binder Jetting Additive Manufacturing of Metals. *J. Manuf. Sci. Eng.* 139. <https://doi.org/10.1115/1.4036640>
- Bai, Y., Williams, C.B., 2015. An exploration of binder jetting of copper. *Rapid Prototyp. J.* <https://doi.org/10.1108/RPJ-12-2014-0180>
- Baker, H., 1992. *ASM Handbook, Volume 3, Alloy Phase Diagrams.* ASM International.
- Balart, M.J., Patel, J.B., Fan, Z., 2015. Grain refinement of DHP copper by particle inoculation. *Int. J. Cast Met. Res.* 28, 1–247. <https://doi.org/10.1179/1743133615Y.0000000005>
- Balart, M.J., Patel, J.B., Gao, F., Fan, Z., 2016. Grain Refinement of Deoxidized Copper. *Metall. Mater. Trans. A* 47, 4988–5011. <https://doi.org/10.1007/s11661-016-3671-8>
- Barkia, B., Aubry, P., Haghi-Ashtiani, P., Auger, T., Gosmain, L., Schuster, F., Maskrot, H., 2020. On the origin of the high tensile strength and ductility of additively manufactured 316L stainless steel: Multiscale investigation. *J. Mater. Sci. Technol.* 41, 209–218. <https://doi.org/10.1016/j.jmst.2019.09.017>
- Birmingham, M., StJohn, D., Easton, M., Yuan, L., Dargusch, M., 2020. Revealing the Mechanisms of Grain Nucleation and Formation During Additive Manufacturing. *JOM* 72, 1065–1073. <https://doi.org/10.1007/s11837-020-04019-5>
- Birmingham, M.J., StJohn, D.H., Krynen, J., Tedman-Jones, S., Dargusch, M.S., 2019. Promoting the columnar to equiaxed transition and grain refinement of titanium alloys during additive manufacturing. *Acta Mater.* 168, 261–274. <https://doi.org/10.1016/j.actamat.2019.02.020>
- Bontha, S., Klingbeil, N.W., Kobryn, P.A., Fraser, H.L., 2009. Effects of process variables and size-scale on solidification microstructure in beam-based fabrication of bulky 3D structures. *Mater. Sci. Eng. A* 513–514, 311–318. <https://doi.org/10.1016/j.msea.2009.02.019>

- Bontha, S., Klingbeil, N.W., Kobryn, P.A., Fraser, H.L., 2006. Thermal process maps for predicting solidification microstructure in laser fabrication of thin-wall structures. *J. Mater. Process. Technol.* 178, 135–142. <https://doi.org/10.1016/j.jmatprotec.2006.03.155>
- Calignano, F., Manfredi, D., Ambrosio, E.P., Biamino, S., Lombardi, M., Atzeni, E., Salmi, A., Minetola, P., Iuliano, L., Fino, P., 2017. Overview on Additive Manufacturing Technologies. *Proc. IEEE* 105, 593–612. <https://doi.org/10.1109/JPROC.2016.2625098>
- Campolongo, F., Cariboni, J., Saltelli, A., 2007. An effective screening design for sensitivity analysis of large models. *Environ. Model. Softw.* 22, 1509–1518. <https://doi.org/10.1016/j.envsoft.2006.10.004>
- Cantor, B., O'Reilly, K. (Eds.), 2003. Solidification and casting, Series in materials science and engineering. Institute of Physics Pub, Bristol [England].
- Carreker, R.P., Hibbard, W.R., 1953. Tensile deformation of high-purity copper as a function of temperature, strain rate, and grain size. *Acta Metall.* 1, 654–663. [https://doi.org/10.1016/0001-6160\(53\)90022-4](https://doi.org/10.1016/0001-6160(53)90022-4)
- Chaklader, A.C.D., Armstrong, A.M., Misra, S.K., 1968. Interface Reactions Between Metals and Ceramics: IV, Wetting of Sapphire by Liquid Copper-Oxygen Alloys. *J. Am. Ceram. Soc.* 51, 630–633. <https://doi.org/10.1111/j.1151-2916.1968.tb12634.x>
- Chen, K., Chen, X., Ding, D., Shi, G., Wang, Z., 2016. Heterogeneous nucleation effect of in situ iron-rich nanoparticles on grain refinement of copper alloy. *Mater. Lett.* 168, 188–191. <https://doi.org/10.1016/j.matlet.2016.01.027>
- Chen, Y., Cheng, M., Song, H., Zhang, S., Liu, J., Zhu, Y., 2014. Effects of lanthanum addition on microstructure and mechanical properties of as-cast pure copper. *J. Rare Earths* 32, 1056–1063. [https://doi.org/10.1016/S1002-0721\(14\)60183-6](https://doi.org/10.1016/S1002-0721(14)60183-6)
- Chen, Y., Zhang, S., Song, H., Cheng, M., Li, H., Liu, J., 2016. Sudden transition from columnar to equiaxed grain of cast copper induced by rare earth microalloying. *Mater. Des.* 91, 314–320. <https://doi.org/10.1016/j.matdes.2015.11.083>
- Colopi, M., Caprio, L., Demir, A.G., Previtali, B., 2018. Selective laser melting of pure Cu with a 1 kW single mode fiber laser. *Procedia CIRP*, 10th CIRP Conference on Photonic Technologies [LANE 2018] 74, 59–63. <https://doi.org/10.1016/j.procir.2018.08.030>

- Cordero, Z.C., Meyer, H.M., Nandwana, P., Dehoff, R.R., 2017. Powder bed charging during electron-beam additive manufacturing. *Acta Mater.* 124, 437–445. <https://doi.org/10.1016/j.actamat.2016.11.012>
- Cziegler, A., Geraseva, O., Schumacher, P., 2017. Numerical and Experimental Investigation of the Influence of Growth Restriction on Grain Size in Binary Cu Alloys. *Metals* 7, 383. <https://doi.org/10.3390/met7090383>
- Cziegler, A.K., Schumacher, P., 2017a. Investigation of the correlation between growth restriction and grain size in Cu alloys. *Int. J. Cast Met. Res.* 30, 251–255. <https://doi.org/10.1080/13640461.2017.1290910>
- Cziegler, A.K., Schumacher, P., 2017b. Investigation of the correlation between growth restriction and grain size in Cu alloys. *Int. J. Cast Met. Res.* 30, 251–255. <https://doi.org/10.1080/13640461.2017.1290910>
- Cziegler, A.K., Schumacher, P., 2016. Preliminary Investigation of the Grain Refinement Mechanism in Cu Alloys, in: Tiryakioğlu, M., Jolly, M., Byczynski, G. (Eds.), *Shape Casting: 6th International Symposium*. Springer International Publishing, Cham, pp. 159–166. https://doi.org/10.1007/978-3-319-48166-1_20
- Davis, J.R. (Ed.), 2001. *Copper and copper alloys*, ASM specialty handbook. ASM International, Materials Park, OH.
- DebRoy, T., Wei, H.L., Zuback, J.S., Mukherjee, T., Elmer, J.W., Milewski, J.O., Beese, A.M., Wilson-Heid, A., De, A., Zhang, W., 2018. Additive manufacturing of metallic components – Process, structure and properties. *Prog. Mater. Sci.* 92, 112–224. <https://doi.org/10.1016/j.pmatsci.2017.10.001>
- Dieter, G.E., 1976. *Mechanical metallurgy*, 2nd ed, Materials Science and Engineering Series. McGraw Hill, USA.
- Easton, M.A., Qian, M., Prasad, A., StJohn, D.H., 2016. Recent advances in grain refinement of light metals and alloys. *Curr. Opin. Solid State Mater. Sci., Recent Advances in Solidification Microstructure- Experiments and Computational Analysis* 20, 13–24. <https://doi.org/10.1016/j.cossms.2015.10.001>
- El-Gaaly, A.A.A., 2019. *Optimization Models for Melting Patterns in Powder Bed Fusion Additive Manufacturing*. (PhD Thesis). North Carolina State University, Raleigh.

- El-Wardany, T.I., She, Y., Jagdale, V.N., Garofano, J.K., Liou, J.J., Schmidt, W.R., 2018. Challenges in Three-Dimensional Printing of High-Conductivity Copper. *J. Electron. Packag.* 140, 1–14. <https://doi.org/10.1115/1.4039974>
- Emissivity - Metals | Fluke Process Instruments [WWW Document], 2021. . Emissivity - Met. URL <https://www.flukeprocessinstruments.com/en-us/service-and-support/knowledge-center/infrared-technology/emissivity-metals> (accessed 5.15.21).
- Eskin, D.G., 2008. *Physical Metallurgy of Direct Chill Casting of Aluminum Alloys, Illustrated.* ed, *Advances in Metallic Alloys.* CRC Press. <https://doi.org/10.1201/9781420062823>
- Eustathopoulos, N., Drevet, B., Muolo, M.L., 2001. The oxygen-wetting transition in metal/oxide systems. *Mater. Sci. Eng. A* 300, 34–40. [https://doi.org/10.1016/S0921-5093\(00\)01790-1](https://doi.org/10.1016/S0921-5093(00)01790-1)
- Fernández, R., Cabeza, S., Mishurova, T., Fernández-Castrillo, P., González-Doncel, G., Bruno, G., 2018. Residual stress and yield strength evolution with annealing treatments in an age-hardenable aluminum alloy matrix composite. *Mater. Sci. Eng. A* 731, 344–350. <https://doi.org/10.1016/j.msea.2018.06.031>
- Fezi, K., Krane, M.J.M., 2016. Uncertainty Propagation In Numerical Modeling Of Direct Chill Casting, in: *Light Metals.* Presented at the The Minerals, Metals & Materials Society, p. 6.
- Francois, M.M., Sun, A., King, W.E., Henson, N.J., Tournet, D., Bronkhorst, C.A., Carlson, N.N., Newman, C.K., Haut, T.S., Bakosi, J., Gibbs, J.W., Livescu, V., Vander Wiel, S.A., Clarke, A.J., Schraad, M.W., Blacker, T., Lim, H., Rodgers, T., Owen, S., Abdeljawad, F., Madison, J., Anderson, A.T., Fattebert, J.-L., Ferencz, R.M., Hodge, N.E., Khairallah, S.A., Walton, O., 2017. Modeling of additive manufacturing processes for metals: Challenges and opportunities. *Curr. Opin. Solid State Mater. Sci.* 21. <https://doi.org/10.1016/j.cossms.2016.12.001>
- Frazier, W.E., 2014. Metal Additive Manufacturing: A Review. *J. Mater. Eng. Perform.* 23, 1917–1928. <https://doi.org/10.1007/s11665-014-0958-z>
- Frigola, P., Agustsson, R.B., Boucher, S., Murokh, A., Rosenzweig, J., Travish, G., Faillace, L., Cormier, D., Mahale, T., 2008. A Novel Fabrication Technique for the Production of RF Photoinjectors. Presented at the European Particle Accelerator Conference, Genoa, Italy, p. 3.

- Frigola, P., Harrysson, O.A., Horn, T.J., West, H., Aman, R.L., Rigsbee, J.M., Ramirez, D.A., Murr, L.E., Medina, F., Wicker, R.B., Rodriguez, E., 2014. Fabricating Copper Components with Electron Beam Melting. *Adv. Mater. Process.* 5.
- Gamzina, D., Luhmann, N.C., Ledford, C., Horn, T., Karakaut, I., Lin, L., Frigola, P., 2017. Additive vacuum electronics: Electron beam melting of copper, in: 2017 Eighteenth International Vacuum Electronics Conference (IVEC). Presented at the 2017 Eighteenth International Vacuum Electronics Conference (IVEC), pp. 1–2. <https://doi.org/10.1109/IVEC.2017.8289495>
- Ganor, Y.I., Tiferet, E., Vogel, S.C., Brown, D.W., Chonin, M., Pesach, A., Hajaj, A., Garkun, A., Samuha, S., Shneck, R.Z., Yeheskel, O., 2021. Tailoring Microstructure and Mechanical Properties of Additively-Manufactured Ti6Al4V Using Post Processing. *Materials* 14. <https://doi.org/10.3390/ma14030658>
- Garcia Sanchez, D., Lacarrière, B., Musy, M., Bourges, B., 2014. Application of sensitivity analysis in building energy simulations: Combining first- and second-order elementary effects methods. *Energy Build.* 68, 741–750. <https://doi.org/10.1016/j.enbuild.2012.08.048>
- Gäumann, M., Bezençon, C., Canalis, P., Kurz, W., 2001. Single-crystal laser deposition of superalloys: processing–microstructure maps. *Acta Mater.* 49, 1051–1062. [https://doi.org/10.1016/S1359-6454\(00\)00367-0](https://doi.org/10.1016/S1359-6454(00)00367-0)
- Gäumann, M., Trivedi, R., Kurz, W., 1997. Nucleation ahead of the advancing interface in directional solidification. *Mater. Sci. Eng. A*, Ninth International Conference on Rapidly Quenched and Metastable Materials 226–228, 763–769. [https://doi.org/10.1016/S0921-5093\(97\)80081-0](https://doi.org/10.1016/S0921-5093(97)80081-0)
- German, R.M., 1996. *Sintering Theory and Practice*. John Wiley & Sons Inc., New York, NY.
- Ghahremaninezhad, A., Ravi-Chandar, K., 2011. Ductile failure in polycrystalline OFHC copper. *Int. J. Solids Struct.* 48, 3299–3311. <https://doi.org/10.1016/j.ijsolstr.2011.07.001>
- Gockel, J., Beuth, J., Taminger, K., 2014. Integrated control of solidification microstructure and melt pool dimensions in electron beam wire feed additive manufacturing of Ti-6Al-4V. *Addit. Manuf., Inaugural Issue* 1–4, 119–126. <https://doi.org/10.1016/j.addma.2014.09.004>

- Gokuldoss, P.K., Kolla, S., Eckert, J., 2017. Additive Manufacturing Processes: Selective Laser Melting, Electron Beam Melting and Binder Jetting-Selection Guidelines. Mater. Basel Switz. 10. <https://doi.org/10.3390/ma10060672>
- Greer, A.L., Bunn, A.M., Tronche, A., Evans, P.V., Bristow, D.J., 2000. Modelling of inoculation of metallic melts: application to grain refinement of aluminium by Al–Ti–B. Acta Mater. 48, 2823–2835. [https://doi.org/10.1016/S1359-6454\(00\)00094-X](https://doi.org/10.1016/S1359-6454(00)00094-X)
- Greer, A.L., Quedstedt, T.E., 2006. Heterogeneous grain initiation in solidification. Philos. Mag. 86, 3665–3680. <https://doi.org/10.1080/14786430500198486>
- Guan, S., Solberg, K., Wan, D., Berto, F., Welo, T., Yue, T.M., Chan, K.C., 2019. Formation of fully equiaxed grain microstructure in additively manufactured AlCoCrFeNiTi0.5 high entropy alloy. Mater. Des. 184, 108202. <https://doi.org/10.1016/j.matdes.2019.108202>
- Guschlbauer, R., Burkhardt, A.K., Fu, Z., Körner, C., 2020. Effect of the oxygen content of pure copper powder on selective electron beam melting. Mater. Sci. Eng. A 779, 1–8. <https://doi.org/10.1016/j.msea.2020.139106>
- Guschlbauer, R., Momeni, S., Osmanlic, F., Körner, C., 2018. Process development of 99.95% pure copper processed via selective electron beam melting and its mechanical and physical properties. Mater. Charact., Metal Additive Manufacturing: Microstructures and Properties 143, 163–170. <https://doi.org/10.1016/j.matchar.2018.04.009>
- Hadadzadeh, A., Amirkhiz, B.S., Li, J., Mohammadi, M., 2018. Columnar to equiaxed transition during direct metal laser sintering of AlSi10Mg alloy: Effect of building direction. Addit. Manuf. 23, 121–131. <https://doi.org/10.1016/j.addma.2018.08.001>
- Helmer, H., Bauereiß, A., Singer, R.F., Körner, C., 2016. Grain structure evolution in Inconel 718 during selective electron beam melting. Mater. Sci. Eng. A 668, 180–187. <https://doi.org/10.1016/j.msea.2016.05.046>
- Herzog, D., Seyda, V., Wycisk, E., Emmelmann, C., 2016. Additive manufacturing of metals. Acta Mater. 117, 371–392. <https://doi.org/10.1016/j.actamat.2016.07.019>
- Heussen, D., Bremen, S., 2017. Green Light for New 3D Printing Process [WWW Document]. Press Release 2017-8-30. URL <https://www.ilt.fraunhofer.de/en/press/press-releases/press-release-2017/press-release-2017-08-30.html> (accessed 6.30.19).
- Higuera, O.F., Cabrera, J.M., 2013. Microstructure influencing physical and mechanical properties of electrolytic tough pitch copper produced by equal channel angular pressing. Mech.

- Mater., Nanostructured Materials 67, 9–14.
<https://doi.org/10.1016/j.mechmat.2013.07.011>
- Hong, K.T., Imadojemu, H., Webb, R.L., 1994. Effects of oxidation and surface roughness on contact angle. *Exp. Therm. Fluid Sci.* 8, 279–285. [https://doi.org/10.1016/0894-1777\(94\)90058-2](https://doi.org/10.1016/0894-1777(94)90058-2)
- Horn, T., Karakurt, I., Ledford, C., Gonzalez, M., Gamzina, D., Luhmann, N.C., Lin, L., 2018. Additively manufactured WR-10 copper waveguide, in: 2018 IEEE International Vacuum Electronics Conference (IVEC). Presented at the 2018 IEEE International Vacuum Electronics Conference (IVEC), pp. 409–410. <https://doi.org/10.1109/IVEC.2018.8391526>
- Horn, T.J., Gamzina, D., 2020. Additive Manufacturing of Copper and Copper Alloys, in: Bourell, D.L., Frazier, W., Kuhn, H., Seifi, M. (Eds.), *Additive Manufacturing Processes*. ASM International, pp. 388–418. <https://doi.org/10.31399/asm.hb.v24.a0006579>
- Horn, T.J., Harrysson, O.L.A., 2012. Overview of Current Additive Manufacturing Technologies and Selected Applications. *Sci. Prog.* 95, 255–282. <https://doi.org/10.3184/003685012X13420984463047>
- Hu, Z., Mahadevan, S., 2017. Uncertainty quantification and management in additive manufacturing: current status, needs, and opportunities. *Int. J. Adv. Manuf. Technol.* 93, 2855–2874. <https://doi.org/10.1007/s00170-017-0703-5>
- Hunt, J.D., 1984. Steady state columnar and equiaxed growth of dendrites and eutectic. *Mater. Sci. Eng., Solidification Microstructure: 30 Years after Constitutional Supercooling* 65, 75–83. [https://doi.org/10.1016/0025-5416\(84\)90201-5](https://doi.org/10.1016/0025-5416(84)90201-5)
- Hutasoit, N., Rashid, R.A.R., Palanisamy, S., Duguid, A., 2020. Effect of build orientation and post-build heat treatment on the mechanical properties of cold spray additively manufactured copper parts. *Int. J. Adv. Manuf. Technol.* 110, 2341–2357. <https://doi.org/10.1007/s00170-020-06010-5>
- Hyun, S.K., Murakami, K., Nakajima, H., 2001. Anisotropic mechanical properties of porous copper fabricated by unidirectional solidification. *Mater. Sci. Eng. A* 299, 241–248. [https://doi.org/10.1016/S0921-5093\(00\)01402-7](https://doi.org/10.1016/S0921-5093(00)01402-7)
- Ikeshoji, T.-T., Nakamura, K., Yonehara, M., Imai, K., Kyogoku, H., 2018. Selective Laser Melting of Pure Copper. *JOM* 70, 396–400. <https://doi.org/10.1007/s11837-017-2695-x>

- Jadhav, S.D., Dadbakhsh, S., Goossens, L., Kruth, J.-P., Van Humbeeck, J., Vanmeensel, K., 2019. Influence of selective laser melting process parameters on texture evolution in pure copper. *J. Mater. Process. Technol.* 270, 47–58. <https://doi.org/10.1016/j.jmatprotec.2019.02.022>
- Jadhav, S.D., Goossens, L.R., Kinds, Y., Hooreweder, B.V., Vanmeensel, K., 2021. Laser-based powder bed fusion additive manufacturing of pure copper. *Addit. Manuf.* 42, 101990. <https://doi.org/10.1016/j.addma.2021.101990>
- Jenkins, W.D., Digges, T.G., Johnson, C.R., 1957. TENSILE PROPERTIES OF COPPER, NICKEL, AND 70-PERCENT-COPPER-30-PERCENT- NICKEL AND 30-PERCENT-COPPER-70-PERCENT-NICKEL ALLOYS AT HIGH TEMPERATURES. *J Res. Natl Bur Stand. Vol: 58.* <https://doi.org/10.6028/jres.058.027>
- Kaden, L., Matthäus, G., Ullsperger, T., Engelhardt, H., Rettenmayr, M., Tünnermann, A., Nolte, S., 2017. Selective laser melting of copper using ultrashort laser pulses. *Appl. Phys. A* 123, 596. <https://doi.org/10.1007/s00339-017-1189-6>
- Karlsson, J., Sjögren, T., Snis, A., Engqvist, H., Lausmaa, J., 2014. Digital image correlation analysis of local strain fields on Ti6Al4V manufactured by electron beam melting. *Mater. Sci. Eng. A* 618, 456–461. <https://doi.org/10.1016/j.msea.2014.09.022>
- Khairallah, S., Anderson, A., Rubenchik, A., King, W., 2016. Laser powder-bed fusion additive manufacturing: Physics of complex melt flow and formation mechanisms of pores, spatter, and denudation zones. *Acta Mater.* 108, 36–45. <https://doi.org/10.1016/j.actamat.2016.02.014>
- Knapp, G.L., Raghavan, N., Plotkowski, A., DebRoy, T., 2019. Experiments and simulations on solidification microstructure for Inconel 718 in powder bed fusion electron beam additive manufacturing. *Addit. Manuf.* 25, 511–521. <https://doi.org/10.1016/j.addma.2018.12.001>
- Kobayashi, K.F., Shingu, P.H., 1988. The solidification process of highly undercooled bulk Cu-O melts. *J. Mater. Sci.* 23, 2157–2166. <https://doi.org/10.1007/BF01115783>
- Kok, Y., Tan, X.P., Wang, P., Nai, M.L.S., Loh, N.H., Liu, E., Tor, S.B., 2018. Anisotropy and heterogeneity of microstructure and mechanical properties in metal additive manufacturing: A critical review. *Mater. Des.* 139, 565–586. <https://doi.org/10.1016/j.matdes.2017.11.021>

- Kommel, L., Hussainova, I., Volobueva, O., 2007. Microstructure and properties development of copper during severe plastic deformation. *Mater. Des.* 28, 2121–2128. <https://doi.org/10.1016/j.matdes.2006.05.021>
- Kumar, A., Bai, Y., Eklund, A., Williams, C.B., 2017. Effects of Hot Isostatic Pressing on Copper Parts Fabricated via Binder Jetting. *Procedia Manuf.* 10, 935–944. <https://doi.org/10.1016/j.promfg.2017.07.084>
- Kumar, A.Y., Wang, J., Bai, Y., Huxtable, S.T., Williams, C.B., 2019. Impacts of process-induced porosity on material properties of copper made by binder jetting additive manufacturing. *Mater. Des.* 182, 1–12. <https://doi.org/10.1016/j.matdes.2019.108001>
- Kumar, N.K., Roy, B., Das, J., 2015. Effect of twin spacing, dislocation density and crystallite size on the strength of nanostructured α -brass. *J. Alloys Compd.* 618, 139–145. <https://doi.org/10.1016/j.jallcom.2014.08.131>
- Kurz, W., Bezençon, C., Gäumann, M., 2001. Columnar to equiaxed transition in solidification processing. *Sci. Technol. Adv. Mater.* 2, 185–191. [https://doi.org/10.1016/S1468-6996\(01\)00047-X](https://doi.org/10.1016/S1468-6996(01)00047-X)
- Kurz, W., Fisher, D.J., 1984. *Fundamentals of solidification*, 2nd ed. Trans Tech Publications.
- Kurz, W., Fisher, D.J., 1981. Dendrite growth at the limit of stability: tip radius and spacing. *Acta Metall.* 29, 11–20. [https://doi.org/10.1016/0001-6160\(81\)90082-1](https://doi.org/10.1016/0001-6160(81)90082-1)
- Kurz, W., Giovanola, B., Trivedi, R., 1986. Theory of microstructural development during rapid solidification. *Acta Metall.* 34, 823–830. [https://doi.org/10.1016/0001-6160\(86\)90056-8](https://doi.org/10.1016/0001-6160(86)90056-8)
- Lassila, D.H., LeBlanc, M.M., Magness, F.H., 1994. The effect of grain size on deformation and failure of copper under dynamic loading. *J. Phys.* IV 04, C8-195-C8-199. <https://doi.org/10.1051/jp4:1994828>
- Ledford, C., Rock, C., Carriere, P., Frigola, P., Gamzina, D., Horn, T., 2019. Characteristics and Processing of Hydrogen-Treated Copper Powders for EB-PBF Additive Manufacturing. *Appl. Sci.* 9, 1–22. <https://doi.org/10.3390/app9193993>
- Ledford, C., Tung, M., Rock, C., Horn, T., 2020. Real Time Monitoring of Electron Emissions during Electron Beam Powder Bed Fusion for Arbitrary Geometries and Toolpaths. *Addit. Manuf.* 101365. <https://doi.org/10.1016/j.addma.2020.101365>
- Lee, Y.S., Kirka, M.M., Raghavan, N., Dehoff, R.R., 2017. Simulation of Spot Melting Scan Strategy to Predict Columnar to Equiaxed Transition in Metal Additive Manufacturing, in:

- Proceedings of the 28th Annual International Solid Freeform Fabrication Symposium. Presented at the Solid Freeform Fabrication, Texas, p. 13.
- Lewandowski, J.J., Seifi, M., 2016. Metal Additive Manufacturing: A Review of Mechanical Properties. *Annu. Rev. Mater. Res.* 46, 151–186. <https://doi.org/10.1146/annurev-matsci-070115-032024>
- Li, X., Tan, W., 2018. Numerical investigation of effects of nucleation mechanisms on grain structure in metal additive manufacturing. *Comput. Mater. Sci.* 153, 159–169. <https://doi.org/10.1016/j.commatsci.2018.06.019>
- Lian, Y., Gan, Z., Yu, C., Kats, D., Liu, W.K., Wagner, G.J., 2019. A cellular automaton finite volume method for microstructure evolution during additive manufacturing. *Mater. Des.* 169, 107672. <https://doi.org/10.1016/j.matdes.2019.107672>
- Liu, G., Zhang, G.J., Ding, X.D., Sun, J., Chen, K.H., 2004. The influences of multiscale-sized second-phase particles on ductility of aged aluminum alloys. *Metall. Mater. Trans. A* 35, 1725–1734. <https://doi.org/10.1007/s11661-004-0081-0>
- Liu, P., Wang, Z., Xiao, Y., Horstemeyer, M.F., Cui, X., Chen, L., 2019. Insight into the mechanisms of columnar to equiaxed grain transition during metallic additive manufacturing. *Addit. Manuf.* 26, 22–29. <https://doi.org/10.1016/j.addma.2018.12.019>
- Liu, P.W., Ji, Y.Z., Wang, Z., Qiu, C.L., Antonysamy, A.A., Chen, L.-Q., Cui, X.Y., Chen, L., 2018. Investigation on evolution mechanisms of site-specific grain structures during metal additive manufacturing. *J. Mater. Process. Technol.* 257, 191–202. <https://doi.org/10.1016/j.jmatprotec.2018.02.042>
- Lodes, M.A., Guschlbauer, R., Körner, C., 2015. Process development for the manufacturing of 99.94% pure copper via selective electron beam melting. *Mater. Lett.* 143, 298–301. <https://doi.org/10.1016/j.matlet.2014.12.105>
- Lord, J.D., Roebuck, B., Morrell, R., Lube, T., 2010. Aspects of strain and strength measurement in miniaturised testing for engineering metals and ceramics. *Mater. Sci. Technol.* 26, 127–148. <https://doi.org/10.1179/026708309X12584564052012>
- Lu, W., Zhai, W., Wang, J., Liu, X., Zhou, L., Ibrahim, A.M.M., Li, X., Lin, D., Wang, Y.M., 2021. Additive manufacturing of isotropic-grained, high-strength and high-ductility copper alloys. *Addit. Manuf.* 38, 101751. <https://doi.org/10.1016/j.addma.2020.101751>

- Lykov, P.A., Safonov, E.V., Akhmedjanov, A.M., 2016. Selective Laser Melting of Copper. *Mater. Sci. Forum* 843, 284–288. <https://doi.org/10.4028/www.scientific.net/MSF.843.284>
- Magnusson, H., Frisk, K., 2013. Self-diffusion and impurity diffusion of hydrogen, oxygen, sulphur and phosphorus in copper 33.
- Mahamood, R.M., Akinlabi, E.T., Shukla, M., Pityana, S., 2014. Revolutionary Additive Manufacturing: An Overview. *Lasers Eng. Old City Publ.* 27, 161–178.
- Mahbooba, Z., West, H., Harrysson, O., Wojcieszynski, A., Dehoff, R., Nandwana, P., Horn, T., 2017. Effect of Hypoeutectic Boron Additions on the Grain Size and Mechanical Properties of Ti-6Al-4V Manufactured with Powder Bed Electron Beam Additive Manufacturing. *JOM* 69, 472–478. <https://doi.org/10.1007/s11837-016-2210-9>
- Masuno, S., Tsukamoto, M., Tojo, K., Asano, K., Asuka, K., Funada, Y., Sakon, Y., 2017. Metal powder bed fusion additive manufacturing with 100W blue diode laser. *Int. Congr. Appl. Lasers Electro-Opt.* 2017, P130. <https://doi.org/10.2351/1.5138180>
- Meyers, M.A., Andrade, U.R., Chokshi, A.H., 1995. The effect of grain size on the high-strain, high-strain-rate behavior of copper. *Metall. Mater. Trans. A* 26, 2881–2893. <https://doi.org/10.1007/BF02669646>
- Molinari, A., Lonardelli, I., Demetrio, K., Menapace, C., 2010. Effect of the particle size on the thermal stability of nanostructured aluminum powder: dislocation density and second-phase particles controlling the grain growth. *J. Mater. Sci.* 45, 6739–6746. <https://doi.org/10.1007/s10853-010-4768-x>
- Mooney, B., Kourousis, K.I., Raghavendra, R., Agius, D., 2019. Process phenomena influencing the tensile and anisotropic characteristics of additively manufactured maraging steel. *Mater. Sci. Eng. A* 745, 115–125. <https://doi.org/10.1016/j.msea.2018.12.070>
- Morris, M.D., 1991. Factorial Sampling Plans for Preliminary Computational Experiments. *Technometrics* 33, 161–174.
- Murr, L.E., Gaytan, S.M., Ramirez, D.A., Martinez, E., Hernandez, J., Amato, K.N., Shindo, P.W., Medina, F.R., Wicker, R.B., 2012. Metal Fabrication by Additive Manufacturing Using Laser and Electron Beam Melting Technologies. *J. Mater. Sci. Technol.* 28, 1–14. [https://doi.org/10.1016/S1005-0302\(12\)60016-4](https://doi.org/10.1016/S1005-0302(12)60016-4)

- Myers, M., Blythe, E.A., 1981. Effects of oxygen, sulphur, and porosity on mechanical properties of cast high-purity copper at 950°C. *Met. Technol.* 8, 165–170. <https://doi.org/10.1179/030716981803275604>
- Nieh, T.G., Nix, W.D., 1981. Embrittlement of copper due to segregation of oxygen to grain boundaries. *Metall. Trans. A* 12, 893–901. <https://doi.org/10.1007/BF02648354>
- Pankow, M., Justusson, B., Waas, A.M., 2010. Three-dimensional digital image correlation technique using single high-speed camera for measuring large out-of-plane displacements at high framing rates. *Appl. Opt.* 49, 3418–3427. <https://doi.org/10.1364/AO.49.003418>
- Pelaprat, J.-M., Finuf, M., Fritz, R., Zediker, M., 2018. Seeing Things in a New Light. *Laser Tech. J.* 15, 39–41. <https://doi.org/10.1002/latj.201800028>
- Plotkowski, A., Kirka, M.M., Babu, S.S., 2017a. Verification and validation of a rapid heat transfer calculation methodology for transient melt pool solidification conditions in powder bed metal additive manufacturing. *Addit. Manuf.* 18, 256–268. <https://doi.org/10.1016/j.addma.2017.10.017>
- Plotkowski, A., Rios, O., Sridharan, N., Sims, Z., Unocic, K., Ott, R.T., Dehoff, R.R., Babu, S.S., 2017b. Evaluation of an Al-Ce alloy for laser additive manufacturing. *Acta Mater.* 126, 507–519. <https://doi.org/10.1016/j.actamat.2016.12.065>
- Powell, G.L.F., Hogan, L.M., 1968. The Undercooling of Copper and Copper-Oxygen Alloys. *Trans. Metall. Soc. AIME* 242, 6.
- Promoppatum, P., Yao, S.-C., Pistorius, P.C., Rollett, A.D., 2017. A Comprehensive Comparison of the Analytical and Numerical Prediction of the Thermal History and Solidification Microstructure of Inconel 718 Products Made by Laser Powder-Bed Fusion. *Engineering* 3, 685–694. <https://doi.org/10.1016/J.ENG.2017.05.023>
- Que, Z., Lee, J., Cheng, W., Han, S., Jung, H., Euh, K., 2013. Microstructure Evolution of the Cu-Cr Hypereutectic Alloys During Directional Solidification, in: Jung, H.-K., Kim, J.T., Sahama, T., Yang, C.-H. (Eds.), *Future Information Communication Technology and Applications: ICFICE 2013, Lecture Notes in Electrical Engineering*. Springer Netherlands, Dordrecht, pp. 939–947. https://doi.org/10.1007/978-94-007-6516-0_103
- Raab, S.J., Guschlbauer, R., Lodes, M.A., Körner, C., 2016. Thermal and Electrical Conductivity of 99.9% Pure Copper Processed via Selective Electron Beam Melting. *Adv. Eng. Mater.* 18, 1661–1666. <https://doi.org/10.1002/adem.201600078>

- Rafi, H.K., Karthik, N.V., Gong, H., Starr, T.L., Stucker, B.E., 2013. Microstructures and Mechanical Properties of Ti6Al4V Parts Fabricated by Selective Laser Melting and Electron Beam Melting. *J. Mater. Eng. Perform.* 22, 3872–3883. <https://doi.org/10.1007/s11665-013-0658-0>
- Raghavan, N., Dehoff, R., Pannala, S., Simunovic, S., Kirka, M., Turner, J., Carlson, N., Babu, S.S., 2016. Numerical modeling of heat-transfer and the influence of process parameters on tailoring the grain morphology of IN718 in electron beam additive manufacturing. *Acta Mater.* 112, 303–314. <https://doi.org/10.1016/j.actamat.2016.03.063>
- Raghavan, N., Simunovic, S., Dehoff, R., Plotkowski, A., Turner, J., Kirka, M., Babu, S., 2017. Localized melt-scan strategy for site specific control of grain size and primary dendrite arm spacing in electron beam additive manufacturing. *Acta Mater.* 140, 375–387. <https://doi.org/10.1016/j.actamat.2017.08.038>
- Ramirez, D.A., Murr, L.E., Martinez, E., Hernandez, D.H., Martinez, J.L., Machado, B.I., Medina, F., Frigola, P., Wicker, R.B., 2011. Novel precipitate–microstructural architecture developed in the fabrication of solid copper components by additive manufacturing using electron beam melting. *Acta Mater.* 59, 4088–4099. <https://doi.org/10.1016/j.actamat.2011.03.033>
- Reed-Hill, R.E., 1973. *Physical Metallurgy Principles*, 2nd ed, University series in Basic Engineering. PWS-KENT, Boston, MA.
- Rhodin, T.N., 1950. Low Temperature Oxidation of Copper. I. Physical Mechanism1a. *J. Am. Chem. Soc.* 72, 5102–5106. <https://doi.org/10.1021/ja01167a079>
- Romero, J.S., Cruchaga, M.A., Celentano, D.J., 2013. Evaluation of Formation and Evolution of Microporosity in Anodic Copper Solidification Processes: Simulation and Experimental Validation. *Metall. Mater. Trans. B* 44, 624–652. <https://doi.org/10.1007/s11663-013-9815-y>
- Rosenthal, D., 1946. The theory of moving sources of heat and its application to metal treatments. *Trans. Am. Soc. Mech. Eng.*
- Saeidi, K., Akhtar, F., 2018. Subgrain-controlled grain growth in the laser-melted 316 L promoting strength at high temperatures. *R. Soc. Open Sci.* 5, 172394. <https://doi.org/10.1098/rsos.172394>

- Sames, W.J., List, F.A., Pannala, S., Dehoff, R.R., Babu, S.S., 2016. The metallurgy and processing science of metal additive manufacturing. *Int. Mater. Rev.* 61, 315–360. <https://doi.org/10.1080/09506608.2015.1116649>
- Sanders, P.G., Eastman, J.A., Weertman, J.R., 1997. Elastic and tensile behavior of nanocrystalline copper and palladium. *Acta Mater.* 45, 4019–4025. [https://doi.org/10.1016/S1359-6454\(97\)00092-X](https://doi.org/10.1016/S1359-6454(97)00092-X)
- Seifi, M., Salem, A., Beuth, J., Harrysson, O., Lewandowski, J.J., 2016. Overview of Materials Qualification Needs for Metal Additive Manufacturing. *JOM* 68, 747–764. <https://doi.org/10.1007/s11837-015-1810-0>
- Shamsujjoha, Md., Agnew, S.R., Fitz-Gerald, J.M., Moore, W.R., Newman, T.A., 2018. High Strength and Ductility of Additively Manufactured 316L Stainless Steel Explained. *Metall. Mater. Trans. A* 49, 3011–3027. <https://doi.org/10.1007/s11661-018-4607-2>
- Shirazy, M.R.S., Blais, S., Fréchet, L.G., 2012. Mechanism of wettability transition in copper metal foams: From superhydrophilic to hydrophobic. *Appl. Surf. Sci.* 258, 6416–6424. <https://doi.org/10.1016/j.apsusc.2012.03.052>
- Silbernagel, C., Gargalis, L., Ashcroft, I., Hague, R., Galea, M., Dickens, P., 2019. Electrical resistivity of pure copper processed by medium-powered laser powder bed fusion additive manufacturing for use in electromagnetic applications. *Addit. Manuf.* 29. <https://doi.org/10.1016/j.addma.2019.100831>
- Spittle, J.A., 2006. Columnar to equiaxed grain transition in as solidified alloys. *Int. Mater. Rev.* 51, 247–269. <https://doi.org/10.1179/174328006X102493>
- StJohn, D.H., Qian, M., Easton, M.A., Cao, P., 2011. The Interdependence Theory: The relationship between grain formation and nucleant selection. *Acta Mater.* 59, 4907–4921. <https://doi.org/10.1016/j.actamat.2011.04.035>
- Tan, L.K., Li, Y., Ng, S.C., Lu, L., 1999. Effects of rare earth additions on structures and properties of rapidly solidified copper alloys. *Mater. Sci. Technol.* 15, 169–179. <https://doi.org/10.1179/026708399101505716>
- Thijs, L., Montero Sistiaga, M.L., Wauthle, R., Xie, Q., Kruth, J.-P., Van Humbeeck, J., 2013. Strong morphological and crystallographic texture and resulting yield strength anisotropy in selective laser melted tantalum. *Acta Mater.* 61, 4657–4668. <https://doi.org/10.1016/j.actamat.2013.04.036>

- Thompson, N., Wadsworth, N., Louat, N., 1956. Xi. The origin of fatigue fracture in copper. *Philos. Mag.* 1, 113–126. <https://doi.org/10.1080/14786435608238086>
- Torre, F., Lapovok, R., Sandlin, J., Thomson, P., Davies, C.H.J., Pereloma, E., 2004. Microstructures and properties of copper processed by equal channel angular extrusion for 1-16 passes. *Acta Mater.* 52, 4819–4832. <https://doi.org/10.1016/j.actamat.2004.06.040>
- Tran, T.Q., Chinnappan, A., Lee, J.K.Y., Loc, N.H., Tran, L.T., Wang, G., Kumar, V.V., Jayathilaka, W.A.D.M., Ji, D., Doddamani, M., Ramakrishna, S., 2019. 3D Printing of Highly Pure Copper. *Metals* 9, 756. <https://doi.org/10.3390/met9070756>
- Trevisan, F., Calignano, F., Lorusso, M., Lombardi, M., 2017. Selective laser melting of chemical pure copper. Presented at the Euro PM, Milan.
- Verhulp, E., van Rietbergen, B., Huiskes, R., 2004. A three-dimensional digital image correlation technique for strain measurements in microstructures. *J. Biomech.* 37, 1313–1320. <https://doi.org/10.1016/j.jbiomech.2003.12.036>
- Vincent, C., Silvain, J.F., Heintz, J.M., Chandra, N., 2012. Effect of porosity on the thermal conductivity of copper processed by powder metallurgy. *J. Phys. Chem. Solids* 73, 499–504. <https://doi.org/10.1016/j.jpcs.2011.11.033>
- Wang, G., Ouyang, H., Fan, C., Guo, Q., Li, Zhiqiang, Yan, W., Li, Zan, 2020. The origin of high-density dislocations in additively manufactured metals. *Mater. Res. Lett.* 8, 283–290. <https://doi.org/10.1080/21663831.2020.1751739>
- Wang, T., Zhu, Y.Y., Zhang, S.Q., Tang, H.B., Wang, H.M., 2015. Grain morphology evolution behavior of titanium alloy components during laser melting deposition additive manufacturing. *J. Alloys Compd.* 632, 505–513. <https://doi.org/10.1016/j.jallcom.2015.01.256>
- Wang, Z., Palmer, T.A., Beese, A.M., 2016. Effect of processing parameters on microstructure and tensile properties of austenitic stainless steel 304L made by directed energy deposition additive manufacturing. *Acta Mater.* 110, 226–235. <https://doi.org/10.1016/j.actamat.2016.03.019>
- Wei, C.-N., Bor, H.-Y., Chang, L., 2008. Effect of Hot Isostatic Pressing on Microstructure and Mechanical Properties of CM-681LC Nickel-Base Superalloy Using Microcast. *Mater. Trans.* 49, 193–201. <https://doi.org/10.2320/matertrans.MER2007088>

- White, A.H., Germer, L.H., 1942. The Rate of Oxidation of Copper at Room Temperature. *Trans. Electrochem. Soc.* 81, 305–319. <https://doi.org/10.1149/1.3071381>
- Wu, J.-H., Zhang, S.-H., Song, H.-W., Chen, Y., 2018. Columnar to equiaxed transition mechanism of pure copper induced by La. *Mater. Sci. Technol.* 34, 1759–1767. <https://doi.org/10.1080/02670836.2018.1480875>
- Xie, J., Kar, A., 1999. Laser welding of thin sheet steel with surface oxidation. *Weld. J. - WELD* J 78.
- Yan, X., Chang, C., Dong, D., Gao, S., Ma, W., Liu, M., Liao, H., Yin, S., 2020. Microstructure and mechanical properties of pure copper manufactured by selective laser melting. *Mater. Sci. Eng. A* 789, 139615. <https://doi.org/10.1016/j.msea.2020.139615>
- Yang, K.V., Rometsch, P., Davies, C.H.J., Huang, A., Wu, X., 2018a. Effect of heat treatment on the microstructure and anisotropy in mechanical properties of A357 alloy produced by selective laser melting. *Mater. Des.* 154, 275–290. <https://doi.org/10.1016/j.matdes.2018.05.026>
- Yang, K.V., Shi, Y., Palm, F., Wu, X., Rometsch, P., 2018b. Columnar to equiaxed transition in Al-Mg(-Sc)-Zr alloys produced by selective laser melting. *Scr. Mater.* 145, 113–117. <https://doi.org/10.1016/j.scriptamat.2017.10.021>
- You, Z., Lu, L., 2015. Effect of Strain Rate on Tensile Ductility and Fracture Behavior of Bulk Nanotwinned Copper. *Adv. Eng. Mater.* 17, 1754–1759. <https://doi.org/10.1002/adem.201500073>
- Zakirov, A., Belousov, S., Bogdanova, M., Korneev, B., Stepanov, A., Perepelkina, A., Levchenko, V., Meshkov, A., Potapkin, B., 2020. Predictive modeling of laser and electron beam powder bed fusion additive manufacturing of metals at the mesoscale. *Addit. Manuf.* 35, 101236. <https://doi.org/10.1016/j.addma.2020.101236>
- Zhang, D., Qiu, D., Gibson, M.A., Zheng, Y., Fraser, H.L., StJohn, D.H., Easton, M.A., 2019. Additive manufacturing of ultrafine-grained high-strength titanium alloys. *Nature* 576, 91–95. <https://doi.org/10.1038/s41586-019-1783-1>
- Zhang, Q., Chen, J., Lin, X., Tan, H., Huang, W.D., 2016. Grain morphology control and texture characterization of laser solid formed Ti6Al2Sn2Zr3Mo1.5Cr2Nb titanium alloy. *J. Mater. Process. Technol.* 238, 202–211. <https://doi.org/10.1016/j.jmatprotec.2016.07.011>

- Zhang, Q, Chen, J., Wang, L., Tan, H., Lin, X., Huang, W., 2016. Solidification Microstructure of Laser Additive Manufactured Ti₆Al₂Zr₂Sn₃Mo_{1.5}Cr₂Nb Titanium Alloy. *J. Mater. Sci. Technol.* 32, 381–386. <https://doi.org/10.1016/j.jmst.2015.11.019>
- Zhao, Y., Zhang, Y., Zhao, H., Li, X., Li, Y., Wen, L., Yan, Z., Huo, Z., 2015. Epitaxial growth of hyperbranched Cu/Cu₂O/CuO core-shell nanowire heterostructures for lithium-ion batteries. *Nano Res.* 8, 2763–2776. <https://doi.org/10.1007/s12274-015-0783-1>
- Zhou, G.W., 2009. TEM investigation of interfaces during cuprous island growth. *Acta Mater.* 57, 4432–4439. <https://doi.org/10.1016/j.actamat.2009.06.005>

6 APPENDICES

6.1 Appendix A

6.1.1 Literature review of AM of pure copper

Table 6-1. EB-PBF processing of pure copper.

Bed temp.	Beam Current	Scan speed	Scan strategy	Hatch	Layer thickness	PSD	Grain size average	Powder purity	Powder O2	Solid density	Reference
500-600°C	NA	NA	90° rotation	0.05 mm	NA	Mean = 55 μm	NA	99.99%-99.8%	NA	NA	Frigola et al. (2014)
400°C	5-42mA	2000-10000mm/s	NA	0.1mm	50μm	45-106μm	10-50μm in XY, few mm in Z	99.94%	NA	99.95%	Lodes et al. (2015)
380°C, 450°C	5-22.5mA	1000-5000mm/s	Meandering	0.1mm	50μm	45-105μm	NA	99.91%	400 ppm	99.95%	Raab et al. (2016)
530°C	2.9-33.3 mA	250-10000mm/s	Meandering, 90° rotation b/w layer	0.1mm	50μm	55.4-110μm	NA	99.95%	188 ppm	99.50%	Guschlbauer et al. (2018)

Table 6-2. BJ processing of pure copper.

Sintering time	Sintering/HIP schedule	Sintering atmosphere	Layer thickness	Powder distribution	Grain average size	Powder purity	Solid density	Reference
0.5,3 HRS	450, 1075°C+ HIP-1075°C, 206 Mpa,2 hrs.	Hydrogen	70μm	17μm, 25μm, Bimodal-30 and 5μm	34μm, 24.1μm, 25.8μm	NA	97.3% after HIP	Kumar et al. (2019)
0.5,3 HRS	450, 1075°C+ HIP-1075°C, 206 Mpa,2 hrs.	Hydrogen	70μm	Bimodal - 30μm, 5μm	NA	NA	99.47% after HIP	Kumar et al. (2017)
0.5,2-6/0.5,1,2-6 hrs.	450,1000-1090/450,700,1040-1080°C	Air-vacuum/Hydrogen	100, 80μm	75μm, 16μm, 15μm	NA	91%, 95.3%, 96.4%	63.2%,77.6%, 85.5%	Bai & Williams

Table 6-3. L-PBF processing of pure copper.

Beam power	Power input	Beam dia.	Scan speed	Scan strategy	Hatch	Layer thickness	PSD	Powder purity	Solid density	Grain size average	Reference
1000 W	600-800 W	40 μm	200-600mm/s	Bi-directional+90° rotation	0.07-0.09mm	30 μm	22.7-47.1 μm	99.95%	98%	NA	Jadhav et al. (2019)
300 W	200-300 W	NA	600-1000mm/s	NA	NA	NA	NA	NA	91%	NA	El-Wardany et al. (2018)
200 W	100-200 W	35 μm	100-300mm/s	NA	0.12mm	50 μm	Mean = 32.52 μm	NA	88.10%	NA	Lykov et al.(2016)
1000 W	200-1000 W	78 μm	1000-4000mm/s	45° rotation	0.07mm	50, 100 μm	16-45 μm	99.90%	97.80%	NA	Colopi et al. (2018)
NA	15-25 W	35 μm	300-2500mm/s	90° rotation	0.015mm	30 μm	<35 μm	99%	NA	NA	Kaden et al. (2017)
1000 W	800 W	NA	300mm/s	Bi-directional serpentine	0.025-0.12mm	50 μm	Mean = 28.2 μm	99.90%	96.60%	NA	Ikeshoji et al. (2017)
200 W	100-200 W	35 μm	50-1250mm/s	Stripes, Islands, Rotation, Nested	0.05-0.175mm	30, 45, 60 μm	Mean = 38 μm	99.90%	85.80%	Mean = 14 μm along XY	Silbernagel et al. (2019)
90 W	49.6-76.6 W	NA	10-250mm/s	90° rotation	NA	50-100 μm	NA	NA	NA	NA	Pogson et al. (2003)
100 W	100 W	200 μm	50mm/s	NA	NA	100 μm	<63 μm	NA	NA	NA	Masuno et al. (2017)
200W	195 W	100 μm	400mm/s	67° rotation	0.08mm	30 μm	6-14 μm	NA	83.01%	Mean = 0.25 μm in XY, 15-75 μm in XZ	Trevisan et al. (2017)
400 W	150-350W	100 μm	200-1000 mm/s	67° rotation	0.08mm	30 μm	17-50 μm	99.9%	99.1%	NA	Yan et al. (2020)

6.1.2 Tensile test data**Table 6-4.** Tensile test sample spreadsheet.

Sample #	Orientation in the build	Post-process	UTS (MPa)	Yield strength (MPa)	Elongation (%)	Solid Oxygen Content	Density (g/cm³)
1	Vertical	As-fabricated	181.6645	103.421	-	418	8.87
2	Vertical	HIP	173.0871	77.911	-	386	8.94
3	Vertical	HIP	173.5315	75.842	67.19	293	8.91
4	Vertical	As-fabricated	177.8917	96.527	-	418	8.86
5	Vertical	As-fabricated	184.4307	126.912	63.28	418	8.88
6	Vertical	HIP	176.5703	75.780	59.38	417	8.91
7	Vertical	As-fabricated	184.3678	117.211	58.59	418	8.87
8	Vertical	HIP	172.6282	79.290	-	420	8.92
9	Horizontal	As-fabricated	227.4477	135.137	31.25	438	8.89
10	Vertical	As-fabricated	168.1706	95.148	46.2	474	8.86
11	Vertical	Annealed	155.8532	44.816	53.2	168	8.90
12	Vertical	As-fabricated	166.6323	75.842	47.4	474	8.89
13	Vertical	Annealed	157.2438	46.195	55.8	248	8.90
14	Horizontal	Annealed	196.4395	47.574	36.8	243	8.91
15	Horizontal	As-fabricated	207.8938	82.737	31.1	474	8.88
16	Horizontal	Annealed	199.6445	48.953	37.1	227	8.90
17	Horizontal	As-fabricated	214.1419	85.840	31	500	8.88

Table 6-4. Continued.

18	Horizontal	As-fabricated	212.0332	89.632	22.6	500	-
19	Horizontal	HIP	195.6936	79.290	31.99	569	8.92
20	Horizontal	HIP	193.0329	89.632	28.95	519	8.91
21	Horizontal	HIP	191.9101	75.842	41.4	601	8.92
22	Horizontal	HIP	196.4845	74.463	33.5	464	8.92
23	Vertical	Annealed	175.279	58.605	71	356	8.91
24	Vertical	Annealed	176.219	59.088	70.1	220	8.92
25	Vertical	HIP	180.781	63.777	62.5	509	8.93
26	Horizontal	As-fabricated	194.5654	113.764	23.27	618	8.91
27	Horizontal	Annealed	194.877	61.363	43.9	421	8.93
28	Horizontal	Annealed	195.6036	62.053	36.98	394	8.92
29	Horizontal	Annealed	191.077	62.742	45.38	250	8.92
30	Horizontal	HIP	200.8566	84.806	-	481	8.92
31	Horizontal	HIP	197.0706	89.287	39.8	482	8.93
32	Horizontal	HIP	194.8652	95.148	38.48	489	-
33	Horizontal	HIP	195.9415	110.316	34.5	428	8.93

6.1.3 Future directions for better understanding of the effects of post-processing

To further investigate the difference in properties as a function of treatment conditions, X-oriented horizontal samples from each treatment condition were analyzed in a Rigaku SmartLab X-ray Diffractometer under high resolution XRD mode. Samples were taken from the grip section end after the tensile test and were polished similar to the metallographic samples used for grain structure visualization. For XRD measurements, operating conditions of 40 kV voltage, 44 mA current, and a step size of 0.01° at a scan rate of $0.5^\circ/\text{min}$ were used. Instrumental broadening was corrected using a LaB_6 specimen run under similar optics conditions. Figure 6-1 shows the peak profiles for all three conditions where it is observed that the as-fabricated condition has low height and wide peaks compared to HIP and vacuum annealed condition for (111) and (200) planes.

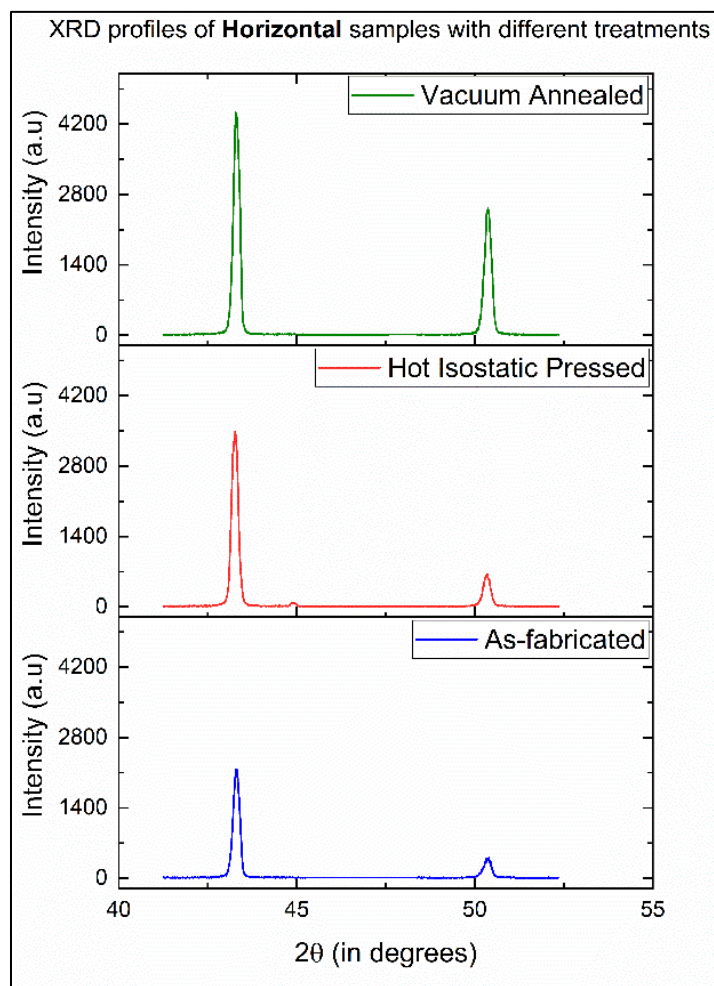


Figure 6-1. XRD peak profiles for X-oriented samples under different treatment conditions.

It is well-known that peak broadening, after due refinement with Rietveld and instrumental broadening, is related to the crystallite size variation where small crystallite sizes broaden the peak profiles and lead to larger micro-strain (Molinari et al., 2010; Shamsujjoha et al., 2018). Although crystallite size and grain size are different attributes for a direct comparison, similar trend is observed in the optical micrographs where slight grain coarsening is recorded for heat treated samples. This in turn results in lower micro-strains in the vacuum annealed and HIP specimen (0.0017% and 0.0018%, respectively) compared with as-fabricated condition (0.0021%). Further, these XRD profiles were used in estimating dislocation density as per the method adopted by Kumar, et al. (2015). Since such method relies on the calculation of crystallite sizes, HRTEM images were taken for an as-fabricated and a HIP specimen to calculate dislocation density by linear intercept method from twenty micrographs taken for each specimen (with a foil thickness taken as 85 nm from EFTEM measurements). A relatively good agreement is found between the two methods, and it is noticed that the as-fabricated sample had higher area fraction of dislocations than the HIP specimen, as shown in Figure 6-2. Although such dense network of dislocation is unlikely when conventionally produced copper is heat treated, Wang, et al. (2020) reported dislocation densities $\sim 10^{16}/\text{m}^2$ for L-PBF processed pure copper, and Shamsujjoha, et al. (2018) reported little change in microstructure in L-PBF processed 316L SS even after heat treating at 1100°C , leading to partial recovery of dislocations.

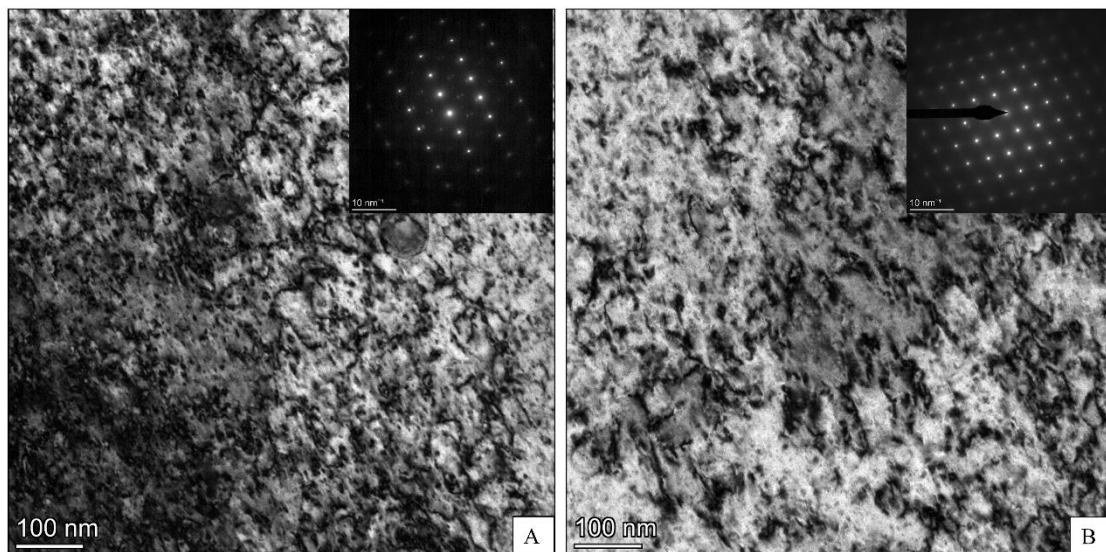


Figure 6-2. Dislocation arrangement in as-fabricated (A) and HIP (B) specimen.

It is suggested that the dense dislocation structure in the as-fabricated specimen compared with the HIP specimen leads to a shorter free dislocation movement path and more dislocation hardening. However, no evidence of sub-structure or cell formation is detected from these TEM images, as opposed to what is observed by Wang, et al. (2020). This is further verified using the Selected area electron diffraction (SAED) pattern shown in the insets for each process condition. Such microstructural difference is assumed to be caused by the formation of very fine equiaxed grains found in the microstructure in the study of Wang, et al. (2020), in contrast with the high-length-scale columnar microstructure seen in this study.

The effect of heat treatment is also seen in the misorientation profile of a vacuum annealed specimen, when compared with the as-fabricated condition. As the specimen is vacuum annealed, misorientations between grains lower down, resulting in lower internal micro-strains, as found out from the XRD profile peak. This leads to increased plasticity for the heat-treated samples for both orientations as compared to the as-fabricated condition. Figure 6-3 shows the misorientation maps for as-fabricated and vacuum annealed specimens used for EBSD analysis.

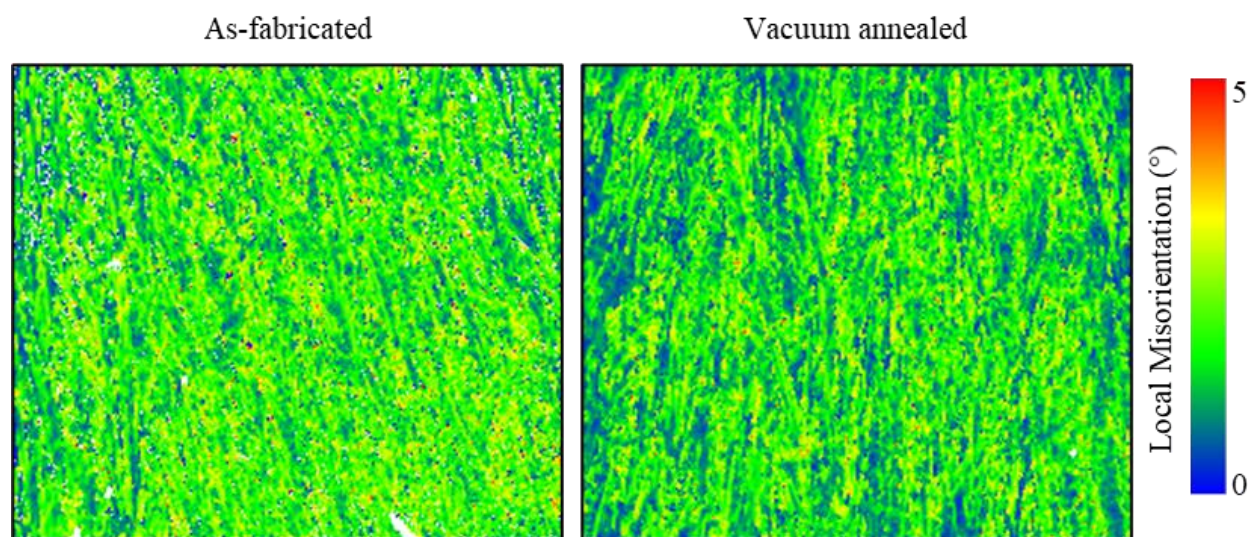


Figure 6-3. Misorientation maps of X-oriented representative as-fabricated and vacuum annealed specimen.

6.2 Appendix B

6.2.1 Analysis of the effect of thermal model assumptions

Within the parameter values presented in Table 3-4, some parameters are approximated in the baseline region observed/reported in the literature body, while others are measured material properties under steady state condition. Since in the model the properties of the substrate plate and powder are assumed to be homogeneous, effect of such variable-value approximation adds another layer of error margin in the final results. Therefore, the effect of three most prominent variables whose values are approximated in this model are subjected to a sensitivity analysis: emissivity (ϵ), beam radius (r_b), and thermal conductivity (k_c). A full-factorial design between these variables is constructed and shown in Table 6-5 below. Beam diameter in an EB-PBF system has been reported with a range of values by different authors, e.g. Zakirov, et al. (2020) used a 500-700 μm beam size for their numerical model simulations, Knapp, et al. (2019) used a defocused 400 μm beam size, although indicating to a much smaller beam size in practice. Ledford, et al. (2020) reported a beam size of 355 \pm 50 μm for the current settings used in their studies, measured by the knife-edge method. For emissivity, values were taken from “Emissivity Values for Metals,” (2021) from Fluke process instruments. Such range of values primarily originates from the surface condition of the feedstock powder and varies between 0.1 and 0.9 for pure and polished to oxidized surface, respectively. For thermal conductivity, the lower extreme value is chosen as 1.5% of the bulk copper according to Raghavan, et al. (2016), while the upper extreme value is selected by extrapolating the works of Vincent, et al. (2012). Among other variables used in the study, the absorption coefficient is found to be reported relatively closely in the literature in agreement with the manufacturer’s specification (Knapp et al., 2019; Raghavan et al., 2016), and is taken as 0.9 in this study. The penetration depth is taken as 20 μm from the works of Lee, et al. (2017).

Table 6-5. Variable values used in the sensitivity analysis of thermal model assumptions.

Variables	Values
Beam radius (μm)	100, 175, 250
Emissivity	0.2, 0.5, 0.8
Thermal conductivity (W/m-K)	10, 50, 90

All simulations are run at a substrate temperature of 300°C, beam velocity of 1600 mm/s, and a melt current of 16 mA. A single timestep from all these simulation results is chosen in each case when the beam is at the center of the domain, and a temperature profile of the spot with the highest temperature in that specific timestep is obtained by the “plot selection over time” function in Paraview. Figure 6-4 shows the overall result where the temperature profile is the mean value in each timestep for all 27 simulation results, and the error bars represent the standard deviation. It is seen that the effect of all these variables is less pronounced in the beginning with low error bars and continues to affect the temperature profile as the beam scans closer to the spot. The error is maximum where the temperature is maximum in the melt-pool due to the concentrated effects from all three variables, and therefore, individual effect of each variable needs to be considered to examine the significance of each.

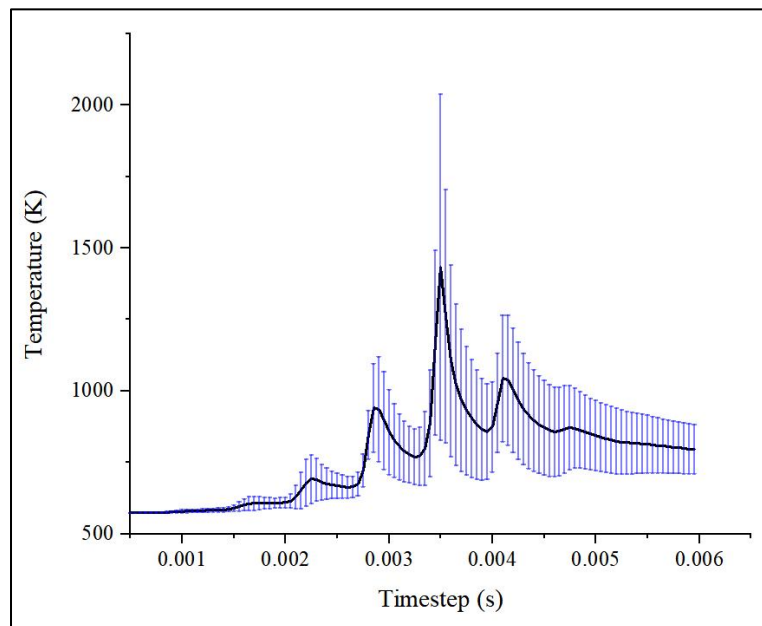


Figure 6-4. Average temperature profile of the selected spot by considering all 27 simulation results.

To elucidate the effect of individual variables, plot from each variable at their three levels are selected for the given nominal level of the other two variables. Following nominal values are used in this study: beam radius of 100 μ m for highly focused beam (Knapp et al., 2019), emissivity of 0.5, and thermal conductivity of 50 W/m-K (Ledford et al., 2019).

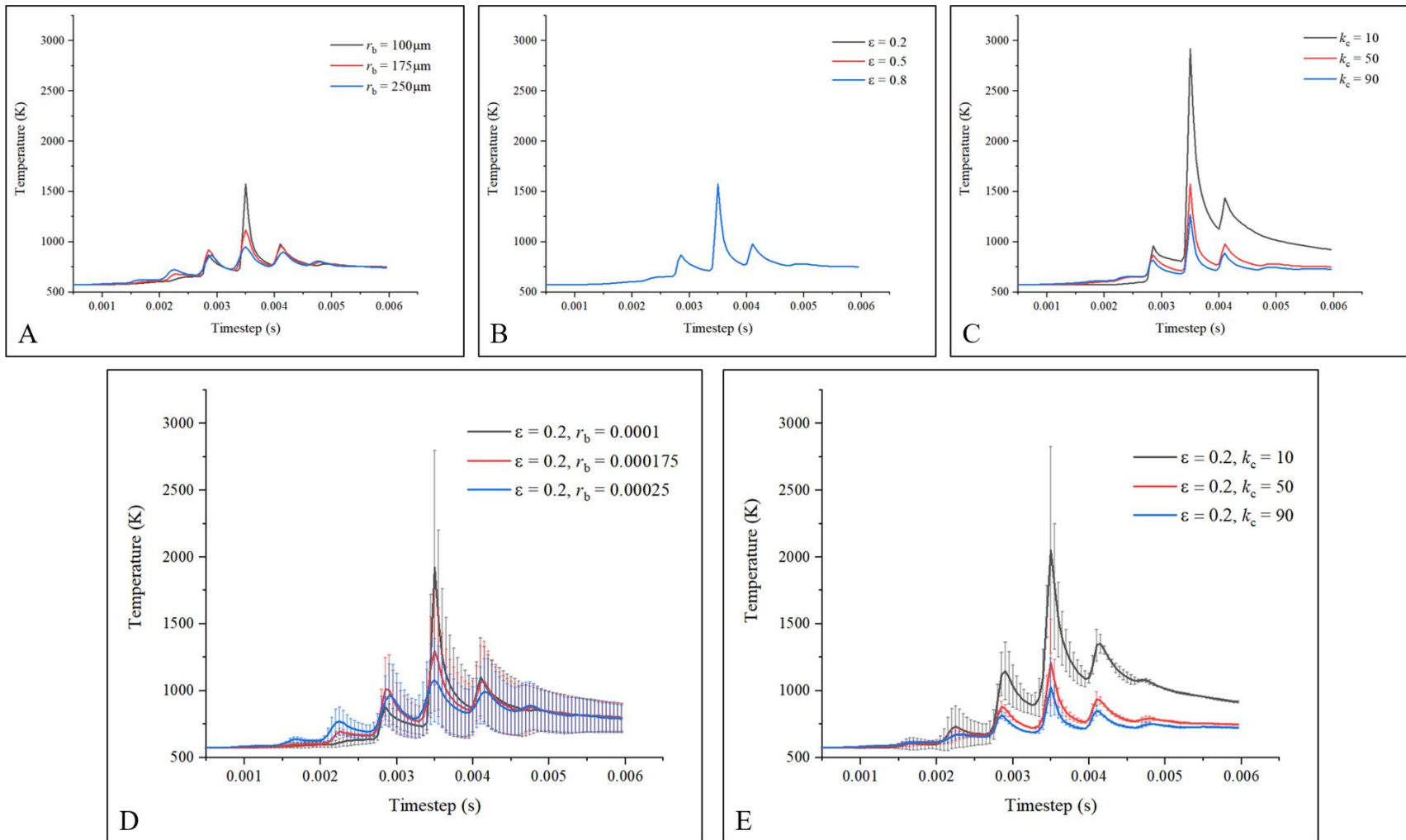


Figure 6-5. Effect of variables in the thermal model on the temperature profiles. Individual effects are shown in (A-C) for beam radius, emissivity, and thermal conductivity, respectively. Coupled effects of Beam radius (D) and thermal conductivity (E) for a given emissivity are shown in (D and E).

From Figure 6-5 (A-C), it is observed that emissivity does not impact the temperature profile for a given value of thermal conductivity and beam radius. However, thermal conductivity affects the results significantly when it is in the lower threshold region. The effect becomes less prominent for the other two levels of thermal conductivity. Similar observation is made from the plots of changing beam radius where very sharp focused beam increases the local temperature in a more significant way than a more defocused beam. Further investigation on the beam radius and thermal conductivity interaction is illustrated in Figure 6-5 (D-E), and it is observed that the effect of thermal conductivity outweighs the beam radius.

6.2.2 Preliminary observations of correlation between thermal model results and microstructure

Investigating the microstructure further from Figure 3-16, it is noticed that the 16 mA samples have the highest grain widths across a row, and the 12 mA samples has the lowest grain widths. From the literature, it is seen that lower hatch offset values lead to more overlap between two adjacent melt pools, and widens the grain width (Helmer et al., 2016), thus reducing the grain aspect ratio. Doing similar analysis of the melt pool dimension using the thermal model reveals that the overlap between two adjacent melt pools increases as the current increases. On contrary, an increase in scan velocity has an opposite effect on the melt pool by reducing the width of the same for same current values. This overall effect is shown in Figure 6-6 below, which partially explains the increase in grain size as the current increases across the row.

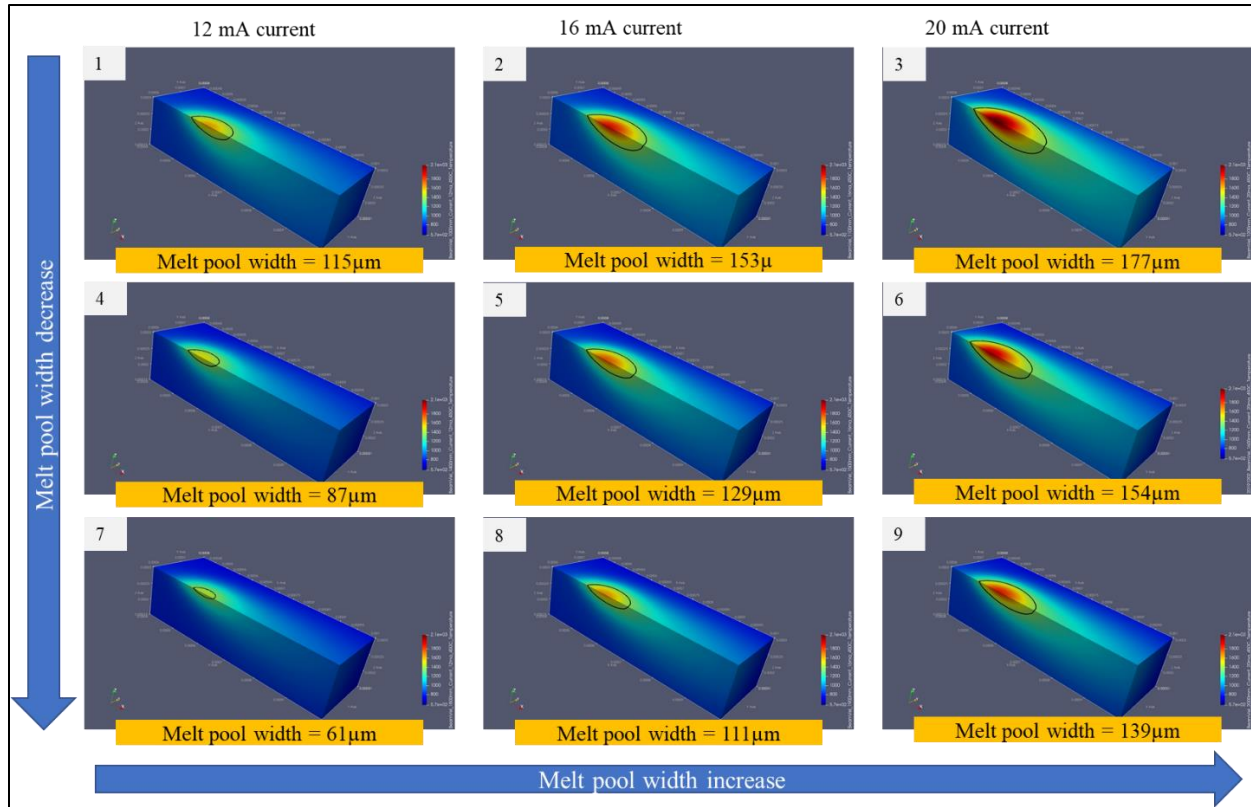


Figure 6-6. Melt pool snapshots from thermal model simulation showing the effect of melt current and scan velocity for the fabricated samples in the experimental build. Note: Only half of the melt pool is shown in the snapshots due to their axial symmetry along the beam direction. Color bar represents a range of 573K-2100K. Sample number is given at top left corner in each snapshot.

However, as mentioned in Chapter 3, grain size is not observed to increase linearly as the current increases. Rather, it is seen that the 16 mA current samples have bigger grains than 12 mA and 20 mA current samples for all different velocities. While this relationship between grain size and melt current setting is not found in the present literature of AM of copper, Yan, et al. (2020) reported a similar trend of density and microhardness in samples fabricated using different process parameter sets that revealed highest density and microhardness values at medium energy densities and a drop at both sides for different energy densities. To factor in the volumetric energy density in explaining the observed differences in grain sizes, a ration between volumetric energy density and cooling rate is used for each sample and is compared with respective grain sizes. The physical significance of this particular ration is the timescale that is required to dissipate the heat generated in each sample. Larger values mean longer time for heat dissipation, and subsequently longer time

for solidification, leading to coarsening of the grains. Figure 6-7 shows this relationship where the ratio value for 16 mA current samples is higher than the other ones and leads to the increase in grain size. This ratio also indicates to a decrease in grain size as the scan velocity increases (i.e., an increase in cooling rate), in accord with the previous thermal model results. It is to be noted that samples 1, 2, and 3 are not shown in the plot as the grain size for sample 2 is not available. Also, the Y-axis denotes respective units for both variables under consideration. While the use of such ratio is not reported in literature, a quantitative assessment can be established in rationalizing the grain size differences for different process parameter setting.

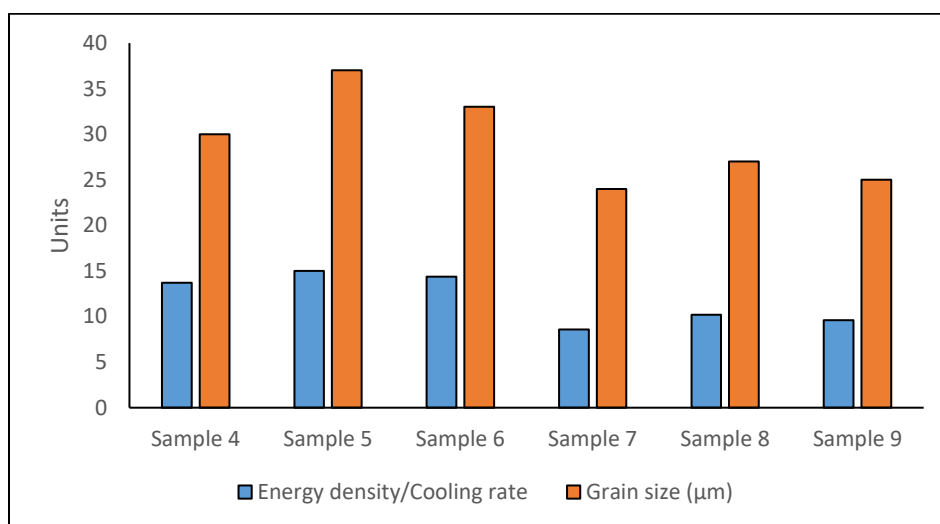


Figure 6-7. Effect of volumetric energy density and cooling rates on the observed grain size for samples 4 to 9.

6.3 Appendix C

6.3.1 TEY images of builds

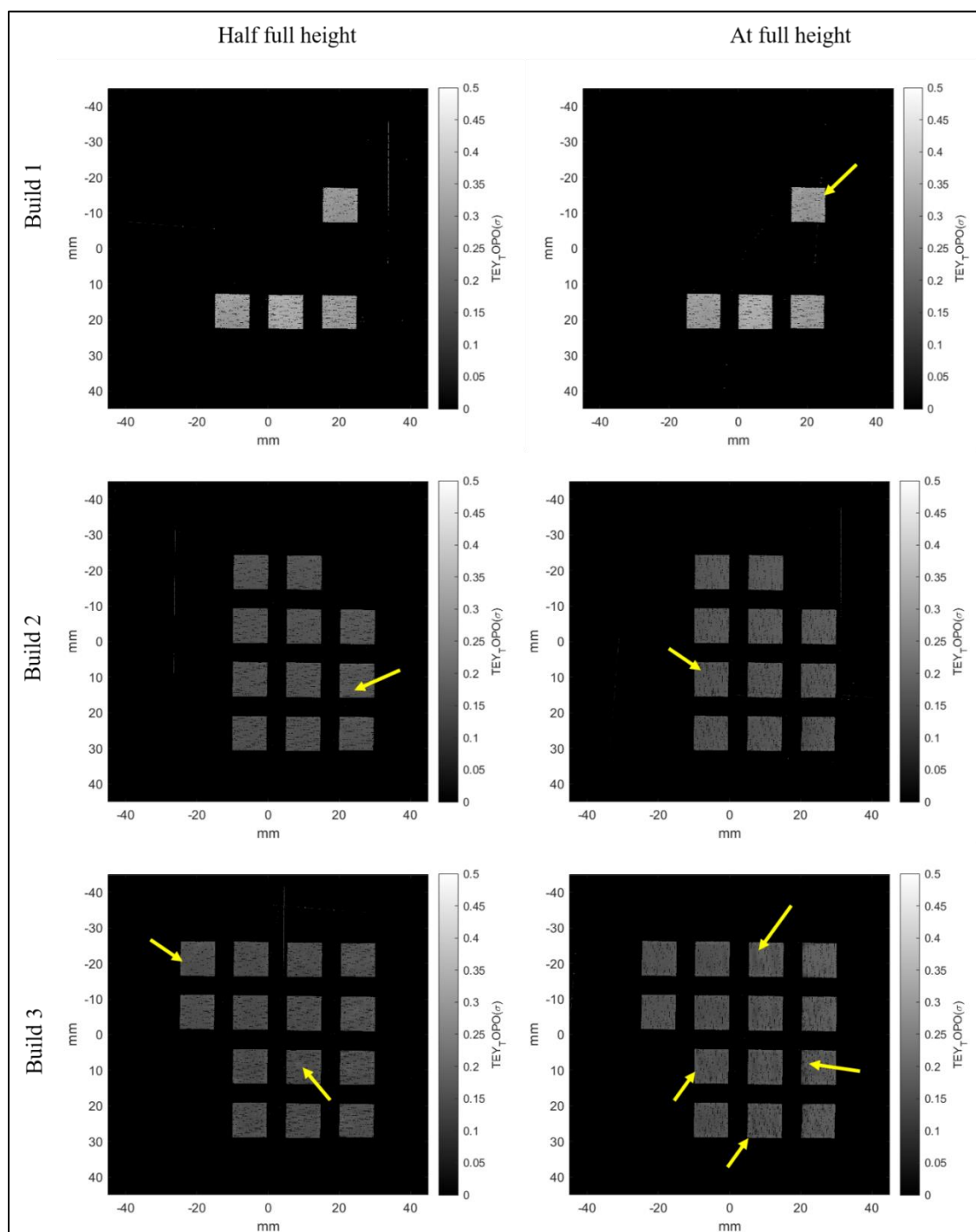


Figure 6-8. TEY images of all three builds at two different stages. Yellow arrows show representative defects detected by the in-situ monitoring method.

6.3.2 Further characterization of equiaxed grains and possible future directions for analysis

To further elucidate the grain structure and its formation mechanism within the equiaxed region, a TEM specimen is prepared according to the method explained in §2.4.5. Figure 6-9 shows a montage of TEM images taken at various locations. As seen in Figure 6-9c-d, subgrain structure is significantly apparent in the equiaxed region where dense dislocation networks outline the subgrains. However, the EDS map presented in Figure 6-9b reveals oxide at or near the grain boundaries in the fabricated sample. Within the hypoeutectic composition of Cu-O system used in this build, it is apparent from the phase diagram that the copper oxides form in the later stage of solidification. This is supported by the finding of Kobayashi and Shingu, (1988) and Powell and Hogan, (1968) in their experiments with hypo-eutectic Cu-O system. Nevertheless, the oxides act as a grain refiner due to their high growth restriction abilities, as found out from the distribution of etch pits in the SEM images shown in Chapter 4.

Although no subgrain structure is seen previously in samples fabricated from pure copper in the tensile test study, Wang, et al. (2020) reported subgrains in pure copper fabricated using an L-PBF system that belong to the areas of equiaxed grains observed near melt pool boundaries. In case of this sample fabricated using moderately oxidized powder, the origin of such subgrain is yet unclear, and a more targeted experiment is required that can address the question. Wang, et al. (2020) have attributed the evolution of subgrains to the dislocation network arrangement, caused primarily by the cyclic heating and cooling of highly localized areas during the process. However, other factors such as internal lattice strains, misorientations between the oxides and primary copper phase etc. can also contribute to the subgrain structure. In that respect, EBSD analysis can prove useful in explaining the internal strain field and local misorientations that can shed more light on the observed microstructural feature.

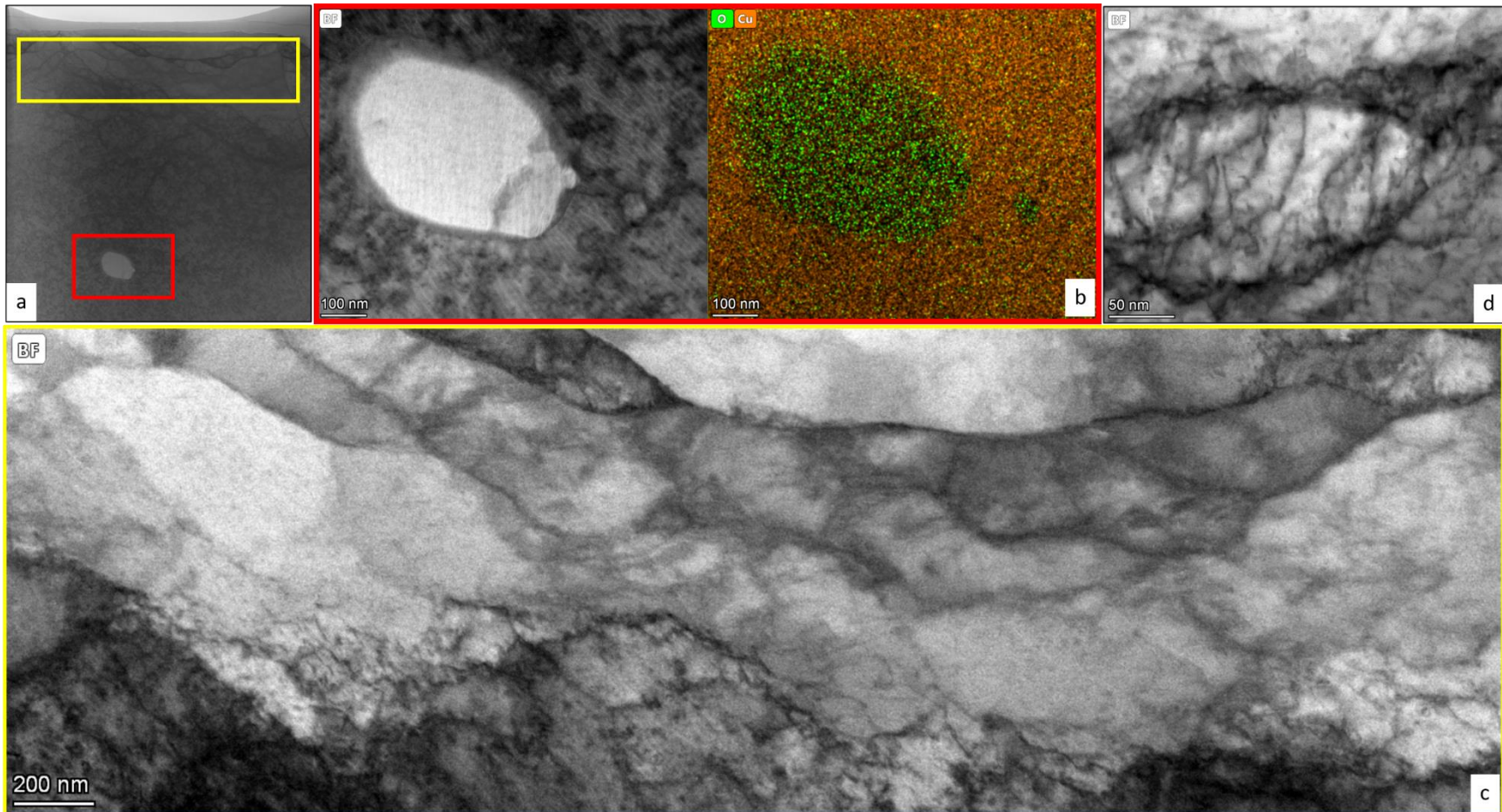


Figure 6-9. a. Lift out specimen for TEM observation; b. EDS map of the particle outlined by red rectangle that clearly shows to be a copper oxide particle; c. tiled image of the top area shown with yellow rectangle, representing the equiaxed subgrains growing transverse to the build direction. d. further magnified image of such subgrain illustrating the distribution of dislocations within the grain and the boundary formed by dense dislocations. Please note the different length scales.